Contents

V.A. Bushuev, A.I. Frank
Depth of Formation of Specular Reflection of X–Rays and Neutrons and its Relationship with the Group Delay Time.....7

V.R. Kocharyan, A.E. Movsisyan, T.R. Muradyan, A.R. Mkrtchyan
Investigation of the Diffraction Phenomena of Thermal Neutrons in Single Crystals under the External Temperature Gradient.....16

V.R. Kocharyan, A.E. Movsisyan, A.V. Shahverdyan, A.S. Gogolev, A.R. Mkrtchyan
2nd Focusing Of Reflected X–Rays From Quartz Single Crystal in The Presence of External Temperature Gradient.....21

V. Sarian, A.R. Mkrtchyan, V. Ermakov, A. Nazarenko, A. Lyubushin, A.R. Meshcheryakov
Hybrid monitoring systems for global processes. The results of the experiment at the first point of the hybrid system.....28

A.R. Mkrtchyan, P.A. Aleksandrov, L.Sh. Grigoryan, A.H. Mkrtchyan, H.F. Khachatryan, M.V. Kovalchuk
Features of Radiation Generated by Bunches of Charged Particles Passing Through the Centre of a Ball.....40

L.Sh. Grigoryan, A.A. Saharian, A.H. Mkrtchyan, H.F. Khachatryan, M.L. Grigoryan, T.A. Petrosyan, H.P. Harutyunyan
Angular Distribution of Intensive Radiation from a Charge Rotating Around a Conductive Ball.....49

A.R. Mkrtchyan, A.S. Abrahamyan
Acoustoplasma State of Matter.....56

A.S. Abrahamyan, A.H. Mkrtchyan, R.Yu. Chilingaryan, A.S. Hakobyan
Minimagnetrons and Their Supply.....64

A.S. Abrahamyan, A.H. Mkrtchyan, R.Yu. Chilingaryan, H.T. Hovhannisyan, S.A. Mkhitaryan, S.M. Petrosyan
New Magnetron Equipment.....71

A.S. Abrahamyan, R.Yu. Chilingaryan, Q.G. Sahakyan
Bilateral Measurements in Electrical Circuits with Gas–Discharge Devices.....75

L.S. Bezhanova, A.K. Atanesyan
Dynamic Processes during Phase Transitions and Structural Transformations in Oriented Liquid Crystal Systems.....84

A.H. Mkrtchyan, A.R. Mkrtchyan, A.K. Atanesyan, G.A. Harutyunyan, S.A. Mkhitaryan, Kh.V. Kotanjyan, S.A. Mirakyan, V.N. Agabekyan, V.V. Nalbandyan, H.R. Muradyan, E.A. Mkrtchyan, E.G. Baghdasaryan, G.G. Tokhmaxyan, S.M. Petrosyan, A.A. Papazyan, E.S. Shadyan
Researches of Acoustic Properties of Some Lakes and Reservoirs of the RA.....92

A.H. Mkrtchyan, A.R. Mkrtchyan, V.V. Nalbandyan, A.S. Hakopyan, I.A. Babayan, A.A. Papazyan, E.S. Shadyan, A.A. Nalbandyan
Detector of Charged Particles Based on Synthesized New Composite Mediums $(Si)_{I}$ $(Csj)_{II}$ $(Ag)_{III}$.....103

A.H. Mkrtchyan, A.R. Mkrtchyan, V.V. Nalbandyan, S.A. Mkhitaryan, G.A. Ayvazyan, A.A. Papazyan, E.S. Shadyan
Detector of Thermal Neutrons Based on Synthesised New Composite Mediums $(Si)_{I}$ $(Lif)_{II}(Csj)_{III}(Ag)_{IV}$.....109

Andrzej Baczmański, Elżbieta Gadalińska , Sebastian Wroński, Przemysław Kot, Marcin Wroński, Mirosław Wróbel, Christian Scheffzük, Gizo Bokuchava, Krzysztof Wierzbanowski
Neutron Diffraction Study of Phase Stresses Evolution in Two Phase Polycrystalline Al/Sic Composite During Elastoplastic Deformation.....114

A.R. Mkrtchyan, A.A.Lalayan, H.S. Eritsyan, A.L.Margaryan
Diffraction on an Aperture Located Between Media With Different Refractive Indices....130

A.M. Yegiazaryan, A.K. Atanesyan
Bragg's X–ray Microscope and X–ray Holography Development Perspectives.....138

V.E. Asadchikov, A.V. Buzmakov, A.S. Ingacheva, Yu.S. Krivonosov, D.A. Zolotov, M.V. Chukalina
Noise Reduction Methods in Laboratory X–ray Microtomography.....141

A.R. Aramyan
The Study of MF Electromagnetic Waves Radiation Caused by the Effects of Solar Radiation on Spacecraft.....147

A.S. Abrahamyan
Cavity Magnetron Spectra.....151

A.S. Abrahamyan, K.V. Hakobyan, Q.G. Sahakyan
The Interaction of the Discharge Modules.....157

S. H. Harutyunyan, L. E. Khachikyan, G. A. Harutyunyan
Generation of Monodisperse Particles.....164

A.G. Sargsyan, S.M. Jomardyan, S.M. Grigoryan, M.A.Ghukasyan, A.A. Shahinyan
X–ray Study of the Lyotropic Mesomoophism pf Sodium Dioctyl Sulfosuccinate–Water System.....170

A.G. Sargsyan, S.M. Jomardyan, S.M. Grigoryan, M.A.Ghukasyan, A.A. Shahinyan
The Study of Lyotropic Mesomorphism of A System of Sodium Pentadecyl Sulfonate–Polyethylene Glycol –Water under the Influence of Temperature.....178

T.R. Muradyan, E.H. Bagdasaryan, S.M. Petrosyan, H.H. Samsonyan, V.R. Kocharyan
Parallel X–ray Beams with Controllable Quantity and Distances under the External Acoustic Fields in Quartz Crystals.....188

H. R. Drmeyan, H. G. Margaryan
X–Ray Diffraction Method of Investigation of Imperfections in Crystals Based on Interpretation of Sectional Topogram.....193

D.V. Roshchupkin, E.V. Emelin, O.A. Plotitcyna, R.R. Fahrtdinov, D.V. Irzhak, V.K. Karandashev, T.V. Orlova, B.S. Redkin, H. Fritze, Yu. Suhak
Advanced Ferroelectric $LiNb_{(1-x)}Ta_xO_3$ Crystal: Crystal Growth, Crystal Structure, Physical Properties.....200

A.Zh. Khachatrian, Zh. R. Panosyan, Zh. B. Khachatryan
A Wave Packet Evolution in the Field of an One–Dimensional Potential.....206

Al.G.Aleksanyan
On Role of Energy Transmission in Mechanisms of Nonradiative Energy Relaxation in Massiv of Quantum Dots.....211

A.R. Mkrtchyan, V.V. Parazian, A.A. Saharian
Transition Radiation of Electron Bunches on Acoustic Superlattices.....214

A.H. Mkrtchyan, V.V. Nalbandyan, A.S. Hakobyan, H.T. Hovhannisyan, K.V. Avetisyan, V.S. Harutyunyan, A.A. Papazyan, E.S. Shadyan
Research of Acoustic Responses of Biological Objects for Detection of Malignancies.....223

A.A. Saharian, A.S. Kotanjyan, A.R. Mkrtchyan, V.Kh. Kotanjyan
Radiation of Surface Polaritons from a Charge Rotating Around a Dielectric Cylinder.....229

A.A. Saharian, A.Kh. Grigoryan, V.V. Parazian
Fermionic Condensate in Two–Dimensional Rings.....238

A.R. Mkrtchyan, A.A. Saharian, L.Sh. Grigoryan, H.F. Khachatryan, A.S. Kotanjyan
Features of Synchrotron Radiation in Presence of a Medium with Negative Permittivity.....248

A.M. Sedrakyan
Variety of Physical Vacuum or Worldwide. Interaction Form in a New Strengthening Space.....257

Depth of Formation of Specular Reflection of X–Rays and Neutrons and its Relationship with the Group Delay Time

V.A. Bushuev[1*], A.I. Frank[2]

[1]M.V. Lomonosov Moscow State University, GSP–1 Moscow, Russia, 119991
[2]International Intergovernmental Organization, Joint Institute for Nuclear Research
6 Joliot–Curie St., Dubna, Moscow Region, Russian Federation, 141980

Abstract: *The problem of the connection of the group delay time (GDT) with the depth in the medium at which the formation of specular reflection of X–rays and neutrons from a semi–infinite homogeneous medium with an ideally sharp interface in the regions up to the threshold of the total external reflection (TER) and above this threshold is discussed. The article has a discussion character and is based on materials that are not included in the review [1].*

1. Introduction

Using the example of reflection of a neutron pulse (wave packet) from two– and three–layer planar structures in a review [1] it was shown that due to some time spent on penetrating radiation deep into the medium and back, the reflection of the pulse occurs with some delay in time with respect to the incident pulse. To a first approximation, this delay is determined by the so–called group delay time (GDT), equal to the derivative in energy from the phase of the amplitude reflection coefficient. The concept of group delay time was introduced into scientific use by Eisenbud, Bohm, and Wigner [2–4] as a measure of the interaction time in quantum mechanics.

In this paper, a seemingly simpler case (in comparison with [1]) is considered, namely, specular reflection of X–rays and neutrons from a semi–infinite homogeneous medium. As is known, the amplitude of specular reflection and the distribution of the field (or wave function) in a medium in the entire range of angles and incidence energies is described by exact Fresnel formulas. Fresnel formulas give exact expressions for the reflection amplitude, field structure, and depth of radiation penetration into the medium, both below the threshold of total external reflection (TER) and above this threshold, but they do not give any answer about the thickness of the near–surface layer in which the reflected wave is formed.

The article discusses the problem of the connection between the GDT and the depth at which the formation of specular reflection of X–rays and neutrons from a semi–infinite homogeneous medium with an ideally sharp interface in regions up to the total external reflection threshold and above this threshold occurs. Calculations show that in the region below the threshold of the TER this formation depth is exactly equal to the penetration depth of the exponentially decaying evanescent wave. However, in the region above the threshold of TER, where the penetration depth of radiation increases significantly, the GDT and the depth of reflection formation, on the contrary, are greatly reduced. Moreover, the GDT increases with increasing absorption in the medium, while the penetration depth decreases.

[*]**E – mail:** *vabushuev@yandex.ru*

It will be shown below that various attempts to determine the relationship between the depth of reflection formation and the GDT lead to some contradictions both in the physics of the phenomenon and in the specific numerical values of this depth, especially in the region above the threshold of the total external reflection. Moreover, a number of questions have not yet received an exhaustive explanation. Our proposed method for estimating the depth of reflection formation based on the first Born approximation in the scattering theory gives highly overestimated results in comparison with direct calculations of the GDT and the reflection time of wave packets. In conclusion, the possible causes of such a sharp discrepancy are briefly discussed.

2. Calculation method

Along with the Goos–Hänchen effect [5, 6], which consists in the longitudinal displacement of the reflected wave beam during its oblique incidence on the surface of the medium (see also [7]), there is a phenomenon of time delay of the reflected pulse with amplitude $A_R(t)$ relative to the incident pulse $\Psi_{in}(t) = A_{in}(t)\exp(-i\omega_0 t)$ with slowly varying complex–valued amplitude $A_{in}(t)$ (see, for example, the review [1] and references therein). In the framework of the spectral approach, it is easy to show that the slowly varying amplitude of the reflected pulse $A_R(t)$ is described by the integral relation

$$A_R(t) = \int_{-\infty}^{\infty} R(\omega) A_{in}(\Omega) e^{-i\Omega t} d\Omega \tag{1}$$

where

$$A_{in}(\Omega) = \frac{1}{2\pi} \int_{-\infty}^{\infty} A_{in}(t) e^{i\Omega t} dt \tag{2}$$

is the spectral amplitude of the incident pulse, $R(\omega) = |R(\omega)|\exp(i\varphi)$ is the amplitude reflection coefficient of a plane monochromatic wave with a frequency ω from an arbitrary structure uniform in a plane perpendicular to its surface, $\varphi(\omega)$ is the reflection phase, $\Omega = \omega - \omega_0$ is the frequency offset, ω_0 is the central radiation frequency of the incident pulse with the spectrum $A_{in}(\Omega)$.

Consider the case when the modulus of the reflection coefficient $|R(\omega)|$ varies rather weakly within the spectrum $A_{in}(\Omega)$. We represent the reflection phase as a decomposition $\varphi(\omega_0 + \Omega) \approx \varphi(\omega_0) + (d\varphi / d\omega) \times \Omega$ and substitute this expression into the integral (1). As a result, up to insignificant phase factors, we obtain that the reflected pulse coincides in shape with the incident pulse, but is time shifted by τ:

$$A_R(t) \approx |R(\omega_0)| A_{in}(t - \tau) \tag{3}$$

where the value τ is called the group delay time and is determined by the ratio

$$\tau = \frac{d\varphi}{d\omega} = \hbar \frac{d\varphi}{dE} \tag{4}$$

If the derivative of the phase in relation (4) is positive, then the pulse is reflected with some positive time delay $\tau > 0$, which is quite natural, since the pulse spends some time on the forward and backward propagation in the medium.

If the derivative (4) is negative, then we arrive at a physically impossible result $\tau < 0$, namely, the pulse is reflected (or begins to be reflected) even before the incident pulse falls on the surface of the medium. Obviously, such a paradox arose due to the oversimplification of the general formula (1) as a result of the expansion of the reflection phase $\varphi(\omega)$ in a series accurate to the first term in Ω. In reality, the spectral dependences of the functions $R(\omega)$ and $A_{in}(\Omega)$ under the sign of the integral in (1) must be taken into account precisely. For this reason, the GDT τ (4) is only an approximate evaluation of the time shift of the reflected pulse.

In a number of examples, it was shown in [1] that, when neutron pulses are reflected from layered structures of finite thickness, the GDT τ can be either positive or negative, which, however, does not contrary to the principle of causality. It turns out that in the case $\tau < 0$ the shape of the reflected pulse is distorted in such a way that the position of its maximum is actually slightly ahead of the maximum of the incident pulse, but the condition $A_R(t) < A_{in}(t)$ is fulfilled for all times $t < 0$.

In this paper, we consider the Fresnel (mirror) reflection of a wave from a homogeneous amorphous semi–infinite medium. The wave functions (or fields) of the incident, reflected, and transmitted radiation have the following form: $\Psi_{in} = A_{in} \exp(i\mathbf{kr})$, $\Psi_R = A_R \exp(i\mathbf{k}_R\mathbf{r})$ and $\Psi_T = A_T \exp(i\mathbf{qr})$, respectively. In this case, for the complex amplitude reflection coefficient $R(\omega) = A_R / A_{in}$ there is the following well–known exact solution:

$$R(\omega) = \frac{k_z - q_z}{k_z + q_z} \tag{5}$$

where k_z and q_z are the values of the z–projections of the wave vectors of the incident plane monochromatic wave in vacuum and in the medium, respectively (the z axis is directed deep into the medium perpendicular to the interface).

For X–ray radiation, the z–projection $k_z = k \sin\theta$, where $k = \omega / c = 2\pi / \lambda$ is the magnitude of the wave vector in vacuum, ω is the frequency, λ is the wavelength, θ is the gliding angle with respect to the surface, $q_z = q_z' + iq_z'' = k(\sin^2\theta + \chi)^{1/2}$ is the z–projection of the wave vector in the medium in the region $z > 0$, $\chi(\omega) = \chi'(\omega) + i\chi''(\omega)$ is the complex polarizability of the medium, and the real value $\chi'(\omega) < 0$ is negative.

For neutrons, by virtue of the potential dispersion law $q^2 = k^2 - k_b^2$, one can restrict oneself to the case of normal incidence. Here $q = q' + iq''$, $k(\omega) = MV / \hbar$ is the wave number of neutrons in vacuum, M is the neutron mass, V is the velocity of incident neutrons with energy $E = \hbar\omega = MV^2 / 2$, k_b is the boundary (critical) value of the wavenumber of neutrons in the

medium, which is determined from the relation $k_b^2 = 4\pi Nb = 2MU/\hbar^2$, where N is the bulk density of nuclei, $b = b' - ib''$ is the complex length of coherent scattering, $U = U' + iU''$ is the effective complex potential of the medium. The neutron reflection coefficient can also be represented in the following form, equivalent to expression (5):

$$R(E) = \frac{\sqrt{E} - \sqrt{E-U}}{\sqrt{E} + \sqrt{E-U}} = |R| e^{i\varphi} \tag{6}$$

The shape of the specular reflection curve $|R(E)|^2$, phase $\varphi(E)$, and GDT $\tau(E)$ substantially depends on the energy of the incident neutron. In accordance with this, we will distinguish two cases: 1) sub–barrier reflection, when $k \le k_b'$ ($E \le U'$), and 2) over–barrier reflection, for which $k > k_b'$ ($E > U'$).

The reflection phase is determined from the general relation $\mathrm{tg}\varphi = R''/R'$. In the case of $E \le U'$ and $U' << U'$ the phase $\varphi = -\mathrm{arctg}(x)$, where $x = 2\sqrt{E(U'-E)}/(2E-U')$. To calculate the GDT τ (4), we use the following simple relations: $\tau = \hbar(d\varphi/dE) = \hbar(d\varphi/dx)(dx/dE)$ and $d\varphi/dx = -d[\mathrm{arctg}(x)]/dx = -1/(1+x^2)$. Taking into account these relations, after a series of mathematical transformations, we obtain the following final expression for the GDT (see also relation (12) in [1]):

$$\tau = \frac{\hbar}{\sqrt{E(U'-E)}} \tag{7}$$

From formula (7) it follows that the GDT is maximum at energies $E \to 0$ and $E \to U'$. In a real situation, of course, it is necessary to take into account the absorption, i.e. imaginary part of the potential U'', which leads to the disappearance of the divergence, which is done on a computer by numerically differentiating the reflection phase $\varphi(E)$.

3. Results and discussion

The Fig. 1 shows the dependencies of the reflection phase, the reflection coefficient modulus, and its real and imaginary parts on the neutron energy. It should be noted that on the scale adopted here it may seem that the phase of reflection is zero at an energy $E > U'$ above the threshold of total external reflection (TER). In reality, this phase is simply very small, since in this region the phase is determined by the imaginary part of the potential $U'' << U'$ (see also formula (9) below).

The depth of radiation penetration into the medium is determined by the ratio $L_z = 1/\mathrm{Im}(q_z)$. In the region below of the threshold of TER for neutrons, i.e. at energy $E < U'$, the value L_z is equal to the attenuation depth of the evanescent wave: $L_z = 1/(k_b'^2 - k^2)^{1/2}$. From the most general intuitive considerations, we can assume that the delay time is equal to $\tau_z = 2L_z/V$. Here, the lower index z indicates that this delay time is obtained from the

assumption of the double passage of neutrons (deep into the medium and up to the interface) of the near–surface layer with an effective thickness equal to the penetration depth L_z.

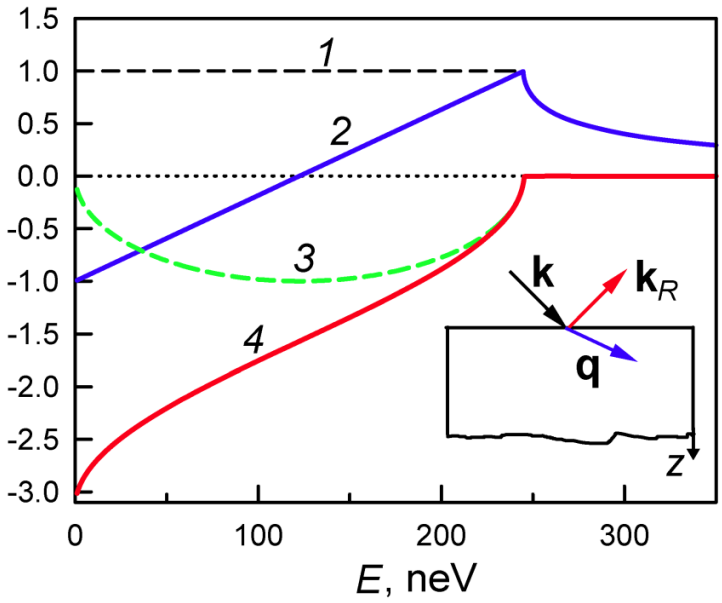

Fig. 1. The module of the amplitude reflection coefficient $|R|$ (curve *1*), the real R' (curve *2*) and imaginary R'' (curve *3*) parts, as well as the reflection phase φ (curve *4*) depending on the energy of neutrons incident on a semi–infinite nickel medium. The inset shows the location and orientation of the wave vectors of the incident, reflected and transmitted waves

The most surprising thing is that this estimated time τ_z exactly coincides with the GDT obtained from the exact relation $\tau = d\varphi / d\omega$ (1) (see curves 2 and 3 in Fig. 2). Indeed, taking into account the relations $E = \hbar^2 k^2 / 2M$, $U' = \hbar^2 k_b'^2 / 2M$, and also $\hbar k = MV$ and $L_z = 1/\mathrm{Im}(q_z)$ from formula (7), it is easy to obtain that

$$\tau = \frac{2M}{\hbar k\sqrt{k_b'^2 - k^2}} = \frac{2}{V\,\mathrm{Im}(q_z)} = \frac{2L_z}{V} \equiv \tau_z \qquad (8)$$

From this we can conclude that the depth of reflection formation L_R coincides with the depth of penetration into the medium, i.e. $L_R = L_z$. The reasons for this coincidence are completely incomprehensible, since there is no backward wave $\sim\exp(-iq_z z)$ in a semi–infinite medium (see the inset in Fig. 1), and the assumption that the neutron velocity is equal V in the medium and in the vacuum, and even in the field of total external reflection, does not correspond to reality. In the field of TER, the *z*–projection of the wave vector is purely imaginary and it is not entirely correct to talk about the neutron velocity.

Nevertheless, rigorous calculations show that the delay time τ_z of the reflected pulse $A_R(t)$ is in very good agreement with the GDT calculated by the formula $\tau = d\varphi / d\omega$ (see

curves *2* and *3* in Fig. 2 in the region $E < U'$). At this scale in Fig. 2, it may seem that in the region above the threshold of total external reflection the GDT $\tau = 0$, but this is not so, although indeed the group delay time is very short (see below for more details).

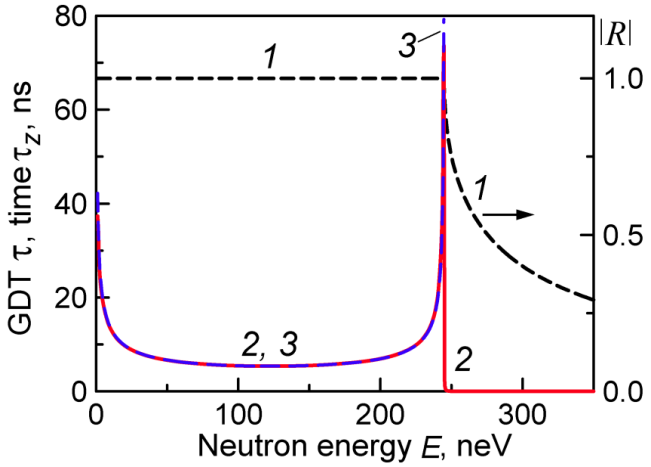

Fig. 2. The dependence of the reflection coefficient modulus $|R|$ (curve *1*, right scale), GDT τ (curve *2*) and the estimated time $\tau_z = 2L_z / V$ (curve *3*) on the neutron energy E when they are reflected from a semi–infinite nickel medium ($U'_{\mathrm{Ni}} = 245$ neV). Curve *3* is shown in the energy region up to 245.1 neV, since then it increases very sharply

Similar results are also valid for X–ray radiation, for which in the region of total external reflection $(\theta < \theta_c = |\chi'|^{1/2})$ the group delay time is determined by the ratio $\tau = 2\theta / [\omega(\theta_c^2 - \theta^2)^{1/2}]$, and the depth of mirror reflection formation is equal to $L_z = \tau c / (2\sin\theta)$

In the region above the total external reflection threshold, the penetration depth L_z increases significantly, while the GDT and, consequently, the depth of reflection formation $L_R = \tau n V / 2$, on the contrary, decrease significantly, where $n = [1 - (k_b / k)^2]^{1/2}$ is the refractive index (see Tables 1 and 2). Here, the lower index R means that the depth of formation L_R in the region above the TER threshold is determined according to the GDT τ, i.e. derivative (4) of the reflection coefficient phase R. Moreover, with a decrease in absorption, i.e. with a decrease in the imaginary parts b'' for neutrons and χ'' for X–rays, the depth L_z of radiation penetration into the medium increases, while the GDT decreases:

$$\tau = \frac{M k_b'^2}{\hbar k (k^2 - k_b'^2)^{3/2}} \frac{b''}{b'}, \quad (E > U') \tag{9}$$

$$\tau = 2 \frac{\chi''(\omega_0)}{\chi'(\omega_0)} \frac{\omega_0^2}{\omega^3}, \quad (\theta > \theta_c) \tag{10}$$

It can be seen from Tables 1 and 2 that in the region above the TER threshold, group delay times τ are much shorter than the period T of incident waves, and the corresponding depths of mirror reflection formation are generally comparable or even much smaller than atomic

sizes. In this regard, the interpretation of the results obtained above within the framework of existing concepts based on the Fresnel formula, encounters certain difficulties.

Table 1. Group delay time τ and the depth of formation of neutron reflection L_R from nickel depending on the energy E of incident neutrons ($U' = 245$ neV, $U'' = 0.024$ neV, period $T \approx 8$ ns).

Energy E, neV	**200**	**240**	**244**	**250**	**270**
GDT τ, ns	6.9	18.9	41.8	0.04	0.004
Depth L_R, Å	215	642	1430	0.22	0.04

Table 2. Group delay time τ and depth L_R of formation of reflection of X–ray CuK_α –radiation ($\lambda = 1.54$ Å) from silicon depending on the angle of incidence θ (critical angle of TER $\theta_c = 13.4$ arc.min, wave period $T = 0.5$ as).

Angle θ, arc.min	**10**	**13**	**14**	**20**	**30**
GDT τ, as	0.18	0.64	0.08	0.007	0.005
Depth L_R, Å	95	264	28	1.8	0.8

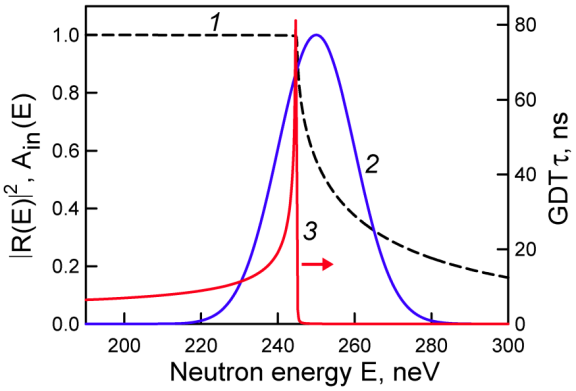

Fig. 3. *1* – reflection coefficient $|R(E)|^2$, *2* – spectrum of the incident neutron pulse $A_{in}(E)$ with central energy $E_{in} = 250$ neV and spectral width $\Delta E = 10$ neV (pulse duration $\tau_{in} = 66$ ns), *3* – dependence of the group delay time $\tau = \hbar(d\varphi / dE)$ with a narrow sharp peak at energy $E = U'$ on energy (right scale), $U'_{\mathrm{Ni}} = 245$ neV

It is interesting to compare the real time shift Δt of the reflected pulse, calculated according to the exact formula (1), with the value of the GDT τ (4). It must be borne in mind here that the calculation results depend not only on the central neutron energy E_{in}, which can be both above and below the threshold of total external reflection, but also on the duration of the incident pulse τ_{in}. This is due to the fact that the pulse has a finite spectral width $\Delta E = \hbar / \tau_{in}$, therefore, the "tail" of the spectrum $A_{in}(E)$ can penetrate into the total reflection region, in which

the group delay time τ is relatively large, even if the energy of the incident pulse $E_{in} > U'$ is higher than the threshold (see Fig. 3 and Fig. 4).

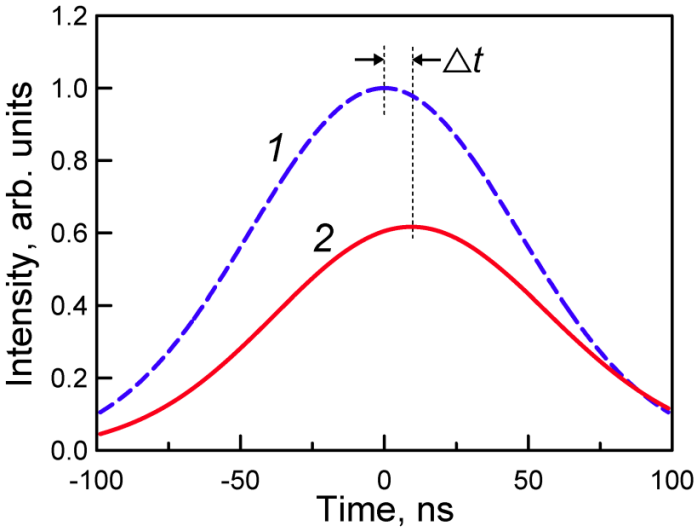

Fig. 4. The intensity of the incident (curve *1*) and reflected (curve *2*) pulses. The duration of the incident pulse $\tau_{in} = 66$ ns, the group delay time at the energy $E_{in} = 250$ neV is equal to $\tau = 0.044$ ns, the real time shift $\Delta t = 9.5$ ns, which is much more than the GDT τ (4)

For comparison, we note that in the region up to the threshold of total external reflection, if $E_{in} = 220$ neV and $\Delta E = 10$ neV, then the real time shift $\Delta t = 9.5$ ns, that is only a little more than the GDT $\tau = 8.9$ ns. However, if $E_{in} = 240$ neV and $\Delta E = 10$ neV, then the real time shift $\Delta t = 13.8$ ns, which is less than the GDT $\tau = 18.9$ ns, is precisely because the "tail" of the spectrum penetrate into the region above the TER threshold. With increasing pulse duration, i.e. with a decrease in the width of its spectrum by 10 times, the values Δt and τ are practically compared ($\Delta t = 32.9$ ns and $\tau = 30.4$ ns at energy $E_{in} = 243$ neV, spectral width $\Delta E = 1$ neV, and the pulse duration $\tau_{in} = 660$ ns). In the case of a relatively short pulse, even at energy $E_{in} = 270$ neV $> U'_{\mathrm{Ni}}$=245 neV and $\Delta E = 10$ neV, a real time delay is equal to $\Delta t = 0.38$ ns, which is almost two orders of magnitude larger than the GDT $\tau = 0.004$ ns, despite the very small amplitude of the spectrum $A_{in}(E)$ in the region below the TER threshold.

It is clear that to exclude the influence of the "tails" of the spectrum $A_{in}(E)$, especially in the region below the TER threshold in the case when $E_{in} > U'$, it is necessary to use sufficiently long pulses. However, this raises the problem of determining extremely small time delays against the background of such long pulses.

Calculations of the group delay time τ and the depth of reflection formation $L_R \approx 1/(2k_z)$ within the framework of the first Born approximation of the scattering theory in the kinematic region above the TER threshold, where $q_z \approx k_z$, give highly overestimated results compared to the depth L_R obtained both from the GDT (4), (8)–(10), and with the calculation of

the reflection time based on rigorous calculations of the amplitudes of the reflected pulses $A_R(t)$ (1).

It is possible that the role of a backward wave in a medium is played by a nonradiative wave of delayed excitation in a dispersive medium characterized by a spectral refractive index $n(\omega)$. On the other hand, it is not entirely clear whether the macroscopic "bulk" and "structureless" concepts of polarizability $\chi(\omega)$, scattering length b, and effective potential U can be transferred to microscopic regions with thicknesses much smaller than the wavelength and atomic sizes. It is possible that our a priori idea of the relationship between the reflection time, the depth of formation of the reflected pulse and the velocity of wave propagation in matter may also be incorrect.

This work was supported by the Russian Foundation for Basic Research (Grant No. 19–02–00218).

References.

1. Bushuev V. A., Frank A. I., Physics – Uspekhi, **61**, 952 (2018).
2. Eisenbud L., "The formal properties of nuclear collisions", Doctoral dissertation (Princeton University, 1948).
3. Bohm D., *Quantum Theory* (New York: Prentice–Hall, 1951).
4. Wigner E. P., Phys. Rev. **98**, 145 (1955).
5. Goos F., Hänchen H., Ann. der Phys. **1**, 333 (1947).
6. Goos F., Lindberg–Hänchen H., Ann. der Phys. **5**, 251 (1949).
7. Artmann K., Ann. der Phys. **2**, 87 (1948).

Investigation of the Diffraction Phenomena of Thermal Neutrons in Single Crystals under the External Temperature Gradient

V.R. Kocharyan*, A.E. Movsisyan, T.R. Muradyan, A.R. Mkrtchyan

Institute of Applied Problems of Physics NAS RA
25 Hr. Nersissian Str., Yerevan, Republic of Armenia, 0014

Abstract: The reflection of thermal neutron beams from a quartz single crystal was investigated in the Laue geometry under the external influences. The scattering of thermal neutrons in crystal is described by the Schrödinger equation. The controllability of a neutron beam in space and time is analyzed and its parameters are estimated (relative maximum intensity, the angular and energy distribution of obtained beams etc.).

Keywords: thermal neutron, diffraction, reflection, quartz crystal

1. Introduction

Thermal neutrons are used in the areas of local structural analyses, investigation of magnetic characteristics of micro and nano structures, neutron absorption therapy, as well as in the material science, biology and condensed matter physics. Nowadays thermal neutrons are more successfully used in neutron absorption therapy by using the neutron sources of nuclear reactors when the object is also radiated by the gamma rays. For decreasing the intensity of gamma rays the beam coming out from a reactor is passed through a bismuth filter, but in this case the intensity of the neutron beam significantly decreases too, that unfortunately requires increasing the irradiation time. To achieve higher intensities and free from gamma radiation, it is important to have a thermal neutron lens with controlled parameters. Theoretical and experimental works on controllability of X–ray and neutron beam parameters in space and time under external influences (temperature gradient and ultrasound) laid grounds for creation of basic elements of thermal neutrons optics. First the effect of complete transfer of X–rays from a transmission direction to the reflection one was observed in [1, 2] in the Laue geometry in quartz single crystals under the influence of either a temperature gradient or ultrasonic vibrations. In [3, 4] it was shown both theoretically and experimentally that by means of acoustic field and temperature gradient one can control the position of the focus of reflected radiation in space and time, as well as to convert a spherical wave into a flat one. In [5, 6] it was shown that the angular width of completely transferred X–ray radiation depends on the thickness of a test specimen and operating parameters of external influences. In [7] a new scheme of high resolution X–ray diffractometer based on acoustic monochromator was developed and realized. Later on a complete transfer of thermal neutron beams from the primary direction to the reflection one from atomic planes (1011) of quartz single crystals in the presence of temperature gradient was experimentally obtained in [8] for the first time by diffraction in the Laue geometry. In [9] the diffraction of a neutron beam in single crystals under external influences (acoustic vibrations and

*E – mail: *Vahan2@yandex.ru*

temperature gradient) was theoretically considered in the Laue geometry. The experimental results were obtained to agree well with the theory.

In the present work the process of thermal neutron diffraction was investigated in the Laue geometry under the presence of temperature gradient in single–crystals. The scattering of thermal neutrons in crystal is described by the Schrödinger equation.

2. Diffraction of thermal neutrons from quartz crystal under the external temperature gradient, results and discussion

Reflection of thermal neutrons beam from the Quartz single crystal in the Laue geometry under the external influences was investigated theoretically. The scattering of thermal neutrons in crystal is described by the Schrödinger equation

$$\Delta\Psi\left(\vec{r}\right)+k^2\Psi\left(\vec{r}\right)=\frac{2mV\left(\vec{r}\right)}{\hbar^2}\Psi\left(\vec{r}\right)$$

where ***Ψ(r) –*** is the neutron wave function, ***V (r)*** – the interaction potential of neutron in crystal, *k* and *m* – the wave number and mass of neutron, correspondingly, and *ħ* – the Plank constant.

The potential for deformed crystals is as follows:

$$V\left(\vec{r}\right)=\sum_m V_m e^{-2\pi i\vec{h}_m(\vec{r}-\vec{U}(\vec{r}))}$$

where V_m –are the Fourier amplitudes of the potential, h_m –the vector of reciprocal lattice and *r* the radius vector, *U(r)* is a function of atomic displacement in crystal from equilibrium position.

We consider the diffraction of thermal neutrons on *X*–cut quartz crystal for the symmetric Laue geometry under temperature gradient perpendicular to the reflecting atomic planes $(10\bar{1}1)$. In this case *h* has only *hx* component and, hence, only *Ux(x, z)* component of displacement function can be considered, and at definite distance from a heating face of crystal *Ux* may be represented as

$$U_x=\frac{t^2-(t-2z)^2}{8R}$$

where *t* – is the crystal thickness, *R* – the radius of curvature of reflecting atomic planes.

Assuming that a plane monochromatic wave is incident on the crystal, the boundary conditions on the front surface of crystal corresponding to z = 0 , will be:

$$\Psi_0\left(x,0\right)=\Psi_{inc.}$$

$$\Psi_h\left(x,0\right)=0$$

Using boundary conditions and displacement function, we finally have for $\Psi_h(z)$

$$\Psi_h(z)=\frac{\beta_h\Psi_{ins}}{2\sqrt{W(0)W(z)}}\left(\exp\left(\frac{2A-\mathrm{Im}(\beta_h\beta_{\bar{h}})}{\mathrm{Re}(\beta_h\beta_{\bar{h}})}f(z)-\mathrm{Im}(\beta_0)z\right)\exp\left(i[\varphi(z)+\phi_1(z)+f(z)]\right)\right.$$
$$\left.-\exp\left(\frac{\mathrm{Im}(\beta_h\beta_{\bar{h}})-2A}{\mathrm{Re}(\beta_h\beta_{\bar{h}})}f(z)-\mathrm{Im}(\beta_0)z\right)\exp\left(-i[\varphi(z)+\phi_2(z)+f(z)]\right)\right)$$

where

$$f(z)=\frac{2Az+\alpha-At+\sqrt{(2Az+\alpha-At)^2+\mathrm{Re}(\beta_h\beta_{\bar{h}})}}{\alpha-At+\sqrt{(\alpha-At)^2+\mathrm{Re}(\beta_h\beta_{\bar{h}})}},$$

$$\varphi(z)=\frac{(2Az+\alpha-At)\sqrt{(2Az+\alpha-At)^2+\mathrm{Re}(\beta_h\beta_{\bar{h}})}-(\alpha-At)\sqrt{(\alpha-At)^2+\mathrm{Re}(\beta_h\beta_{\bar{h}})}}{4A},$$

$$\phi_{1,2}(z)=\pm\left(\mathrm{Re}(\beta_0)+2\alpha\right)z\pm A\left(zt-z^2\right), \qquad A=\frac{\pi h}{2R}$$ – deformation parameter

In Fig. 1 shows the intensity of reflected beam of 50 meV thermal neutrons versus deformation parameter A (inverse proportional to the radius of curvature) of reflecting atomic planes $(10\bar{1}1)$ of quartz single crystals with thicknesses 1 cm, 3 cm and 5 cm. It is seen in the figure that the intensity of reflected beam increases with decreasing curvature in reflecting atomic planes, reaches the maximum value (i.e. the plane monochromatic beam of thermal neutrons completely transfers to the reflection direction), and then slowly decreases.\

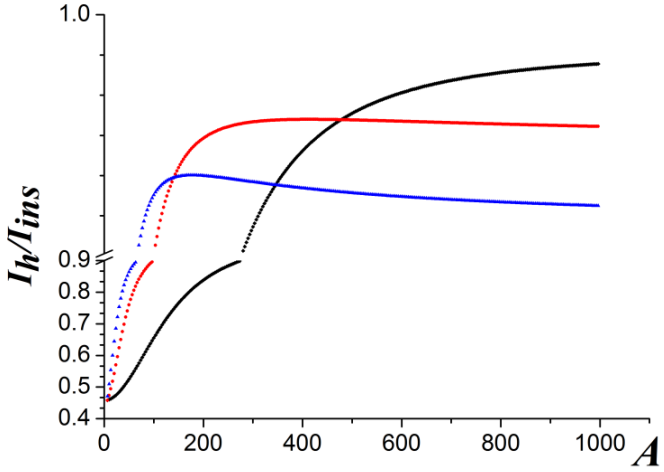

Fig. 1. Intensity of reflected beam of thermal neutrons with energy of 50 meV vs the deformation parameter of $(10\bar{1}1)$ reflecting atomic planes for thicknesses of quartz single crystal: 1) t=1cm, 2) t=3cm, 3) t=5cm

The calculated rocking curves of reflecting atomic planes $(10\bar{1}1)$ of quartz single crystal are given in Fig. 2 for different A parameters. As is seen in the figure, with increasing A (decreasing radius of curvature) the rocking curve is slowly widened, and the maximum value of relative intensity is increased by reaching unity (case of complete transfer). The rocking curves abruptly widen as the radius of curvature of reflecting plane further increases.

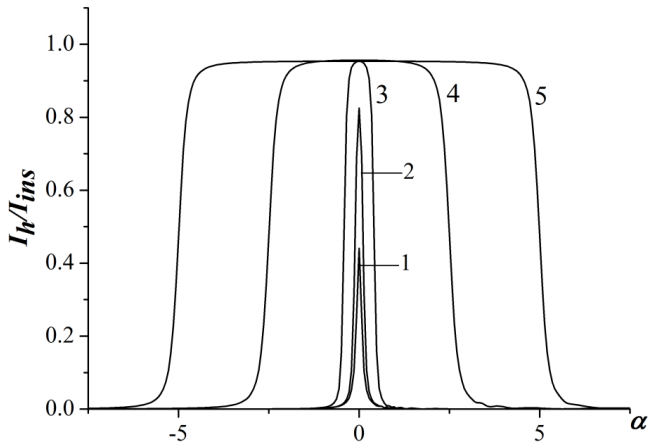

Fig.2. Rocking curves of reflecting atomic planes $(10\bar{1}1)$ of 3 cm thickness quartz single crystal for different values of A parameter: 1) A=0, 2) A=70, 3) A=250, 4) A=500, 5) A=1000

The calculated rocking curves of reflecting atomic planes $(10\bar{1}1)$ for different thicknesses of quartz single crystal for the value of $A = 10^5$ (radius of curvature 10 m) for thermal neutrons with an energy of 50 meV are given in Fig. 3. It is seen from the figure 3, that at a certain value of A parameter the thicker is the crystal, the wider is the rocking curve, i.e., the greater is the angular aperture of completely transferred beam of thermal neutrons. For example, 1 cm thickness quartz single crystal, the atomic planes of which have 10m curvature of camber, completely reflects thermal neutrons with angular aperture ~6–7', and 5 cm thickness crystal completely reflects ~30'. When the radius of curvature of reflecting atomic planes $(10\bar{1}1)$ of the quartz single crystal is ~1 m, completely reflected are thermal neutrons with angular aperture of ~3°.

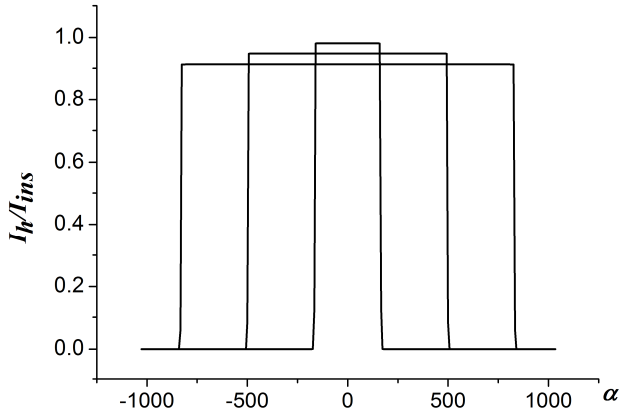

Fig. 3. Rocking curves of reflecting atomic planes $(10\bar{1}1)$ of quartz single crystal for the value of $A = 10^5$ (radius of curvature 10 m) for thermal neutrons with an energy of 50 meV:
1) t=1cm, 2) t=3cm, 3) t=5cm

3. Conclusion

Thus, with decreasing curvature of reflecting atomic planes $(10\bar{1}1)$ of a quartz single crystal, the intensity of reflected beam of thermal neutrons increases, and then reaching the maximum value (i.e., a flat monochromaticity beam of thermal neutrons is completely transferred to the direction of reflection) begins to slowly decrease. As the thermal neutrons are absorbed much less as compared with X–rays (the absorption length ~50 cm), one can separate from a primary beam a neutron beam with large spectral and angular width using a temperature gradient or acoustic field, applied to several centimeters thickness quartz single crystal, and transfer that to the reflection direction.

This work was supported by the RA MES State Committee of Science, in the frames of the research project No 18T–1C395.

References.

1. Mkrtchyan, A.R., Navasardian, M.A., and Mirzoyan, V.K., Pis'ma v ZhTF, 1982, vol. 8, p. 677.
2. Mkrtchyan, A.R., Navasardian, M.A., Gabrielyan, R.G., etc., Pis'ma v ZhTF, 1983, vol. 9, p. 1181.
3. Mkrtchyan, A.R., Navasardian, M.A., Gabrielyan, R.G., Kocharian, L.A., and Kuzmin, R.N., Solid St.Commun., 1986, vol. 59, p. 147.
4. Mkrtchyan, A.R., Gabrielyan, R.G., Aslanyan, A.A., etc., Izvestiya AN Arm. SSR, Fizika, 1986, vol. 21, p. 297.
5. Noreyan, S.N., Mirzoyan, V.K., and Kocharyan, V.R., Izvestiya Natsional'noi Akademii Nauk Armenii, Fizika, 2004, vol. 39, p. 124.
6. Mkrtchyan, A.R., Bagdasaryan, A.S., Khlopuzyan, S.G., and Kocharyan, V.R., Nelineinyi mir (Nonlinear world), 2015, vol. 13, p. 47.
7. Mkrtchyan, A.R., Mkrtchyan, A.H., Kocharyan, V.R., Movsisyan, A.E., Dabagov, S.B., and Potylicyn, A.P., J. Contemp. Phys. (Armenian Ac. Sci.), 2013, vol. 48, p. 141.
8. Mkrtchyan, A.R., Kocharyan, L.A., Navasardyan, M.A., etc., Izvestiya AN Arm. SSR, Fizika, 1986, vol. 21, p. 287.
9. Mkrtchyan, A.R., Gabrielyan, R.G., Unanyan, O.A., and Beglaryan, A.G., Izvestiya AN Arm. SSR, Fizika, 1986, vol. 21, p. 313.
10. Noreyan, S.N., Mirzoyan, V.K., and Kocharyan, V.R., Poverkhnost'. Rentgenovskie, sinkhrotronnye I neitronnye issledovaniya (Surface Investigation. X–ray, Synchrotron and Neutron Techniques), 2004, vol. 1,p. 18.

2nd Focusing Of Reflected X–Rays From Quartz Single Crystal in The Presence of External Temperature Gradient

V.R. Kocharyan[1*], A.E. Movsisyan[1], A.V. Shahverdyan[1], A.S. Gogolev[2], A.R. Mkrtchyan[1,2]

[1]Institute of Applied Problems of Physics NAS RA
25 Hr. Nersissian Str., Yerevan, Republic of Armenia, 0014
[2]National Research Tomsk Polytechnic University
30 Lenin Avenue, Tomsk, Russian Federation, 634050

Abstract: With a view to obtaining the basic elements of hard X–rays (>30 keV) with controllable parameters, in the present work the principles and regularities of hard X–ray reflection in quartz single crystals under the influence of temperature gradient were considered in the Laue geometry. It was demonstrated that with the help of temperature gradient it is possible to separate a beam with large angular and spectral width from the white beam, to transfer that to the reflection direction, to focus and change the focal length, i. e., to control the beam parameters within wide limits. It was experimentally shown that in the presence of temperature gradient in X–cut quartz single crystal it was possible to obtain a two–dimensional bending of reflecting atomic planes $(10\bar{1}1)$ depending on the position and shape of heater, and thereby ensure the possibility of two–dimensional focusing of X–ray radiation at reflection from these planes. It is noteworthy that the degree of bending depends on the thermal expansion coefficient in the given direction. Consequently, in case of appropriate choice of crystal, of its cut and the family of reflecting atomic planes, one can provide such a two–dimensional bending, at which a point focus of reflected X–ray radiation is obtained. It is also shown that under these conditions the integrated intensity of reflected X–ray radiation increases by several orders of magnitude, and the angular width in mutually perpendicular directions is controllable.

Keywords: X–ray, focusing, temperature gradient, quartz

1. Introduction

The development and improvement of new methods for controlling the parameters of X–rays is important for elaboration of new, more sensitive and universal X–ray optical elements required for development of micro– and nanoresolution methods of the tomography of biological objects, for determination of the perfection of micro– and nanostructures. One of the most important tasks in controlling the parameters of X–rays is its focusing. The methods of X–ray focusing are rapidly developed in connection with elaboration of X–ray sources and technologies of preparation of focusing elements. The efforts on elaboration and production of focusing elements were based on refraction, reflection, and diffraction phenomena. In some conventional X–ray devices the focusing Fresnel–zone plates [1, 2], refracting elements [3] or the elements of total internal reflection [4] were used. The boundaries of applicability of these elements are determined by the refractive index of the materials, from which they are made. Utilized in some focusing instruments are multilayer structures with variable thicknesses of layers [5] and curved

[*]**E – mail:** *vahan2@yandex.ru*

single crystals [6–8], from which the diffracted X–rays are focused. As is commonly known, for X–rays elements even of rough configuration devices an extremely high precision manufacturing is required.

An important requirement in present–day focusing systems is a precise control of the position of focus, that may be realized with the help of controlled bending of crystal planes of lenses (single crystals) under external influences (acoustic oscillations, temperature gradient) [9–12]. It is known that with the help of temperature gradient applied perpendicular to $(10\bar{1}1)$ atomic planes of x–cut quartz single crystal, one can control the radius of curvature of atomic plans [13] and the interplanar distances [14]. In these works one of the faces of a rectangular parallelepiped of quartz parallel to atomic planes $(10\bar{1}1)$ is heated, whereas the other faces freely exchange heat with the environment (air). As was shown in [10–14], under these conditions the reflected X–rays are focused only in the reflection plane, i. e., the atomic planes are bent about the perpendicular axis of reflecting planes [15, 16].

The aim of the present work is to study the phenomenon of X–ray diffraction from quartz single crystal in the presence of a temperature gradient that creates a two–dimensional bending, that, in its turn, leads to the two–dimensional focusing of reflected X–ray radiation.

2. Experimental Part and Results

In this experiment the white spectrum of X–ray radiation from Ag BSV–29 X–ray tube at 50 kV voltage and 4 mA anode current was used. The focal point of the tube is 0.4×0.8 mm2. For two–dimensional collimation of X–ray radiation a slit of 0.5 mm in diameter was placed at 13 cm distance from the source. The tested sample was arranged at 19.5 cm distance from the slit. Perpendicular to the direction of beam propagation at distances of 20 and 40 cm from the sample a two–coordinate X–ray detector was installed, the matrix of which was 256×256 pixels, the size of each pixel (resolution) being 55×55 μm2. The experimental setup is given in Fig. 1. The sample was 0.7 cm thick rectangular plate of x–cut quartz single crystal of 3×3 cm2 area. The crystal sample was made in such a way that one of its ribs was parallel to the family of $(10\bar{1}1)$ atomic planes. As is seen in Fig. 1, 1 cm long cylindrical heater of 1 mm in diameter was arranged in the central part of this rib, and all other ribs freely exchanged heat with air. Owing to such a geometry, the heater not only produces in quartz single crystal a temperature gradient perpendicular to reflecting $(10\bar{1}1)$ atomic planes, but also provides temperature gradient from the crystal center to other ribs, that is in directions of y– and z–axes.

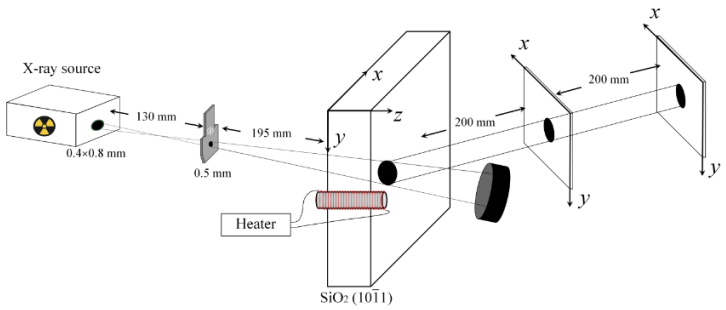

Fig. 1. Experimental setup

In [17] it was shown that the normal component of temperature gradient to reflecting atomic planes, coinciding with x–axis in Fig. 1, brings only to changes in interplanar distances, and the tangential component – to bending of these atomic planes. As was noted above, in the geometry of described experiment a temperature gradient is produced from the center of single crystal along y– and z–axes. In our case these axes are parallel to reflecting $(10\bar{1}1)$ atomic planes, i. e., an appropriate condition for two–dimensional bending of these planes is formed. The axis of heater is arranged parallel to z–axis, as a result of which the value of temperature gradient along yaxis exceeds that along z–axis. This geometry was selected intentionally so that the radius of curvature (inverse proportional to the value of temperature gradient) of reflecting atomic planes $(10\bar{1}1)$ to be less along y–axis, than that along z–axis. In experiments the heater temperature changed from room temperature (18°C) to 400°C. The front distribution of the intensity of reflected 40 keV X–ray radiation from reflecting atomic planes $(10\bar{1}1)$ was recorded at different distances from quartz single crystal for different values of heater temperature. During the experiment a multiple increase in the integral intensity of reflected X–ray radiation was observed depending on the increase in heater.

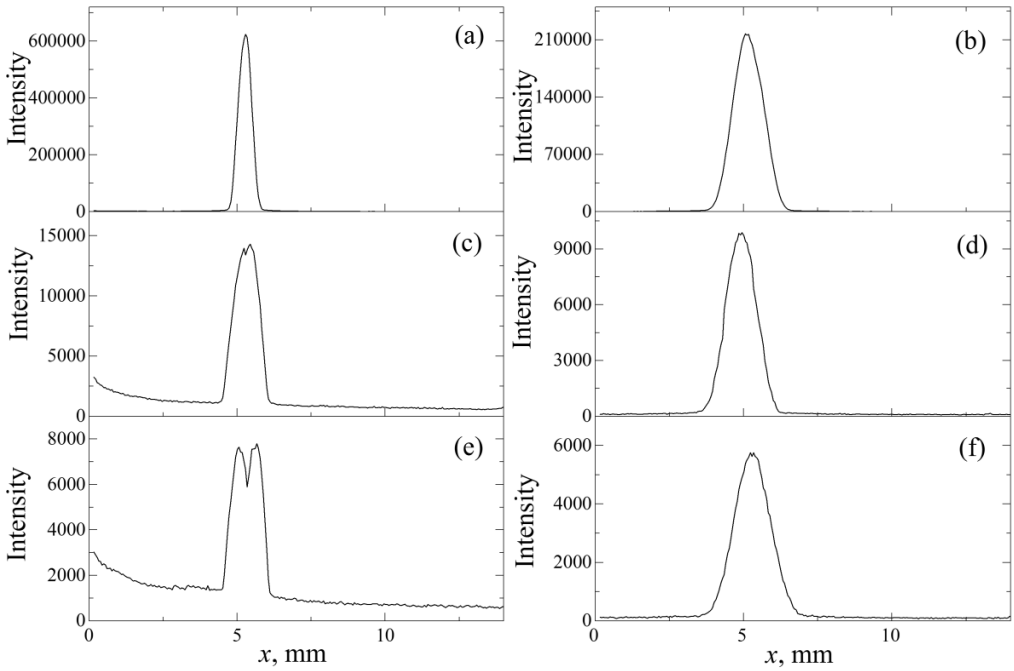

Fig. 2. Intensity distribution of reflected 40 keV X–ray radiation in the reflection plane at distances 20 cm (a, c, e) and 40 cm (b, d, f) from quartz single crystal for different values of heater temperature: 400°C (a, b), 70°C (c, d), and 18°C (e, f) temperature. Figure 2 shows the intensity distribution of reflected X–ray radiation along x–axis at various distances from quartz single crystal for different values of heater temperature

Figure 3 shows the intensity distribution of reflected X–ray radiation along y–axis at various distances from quartz single crystal for different values of heater temperature. Figure 4 shows the front distribution of the intensity of reflected X–ray radiation at distances of 20 and 40 cm from quartz single crystal for different values of heater temperature (18, 70, and 400°C).

3. Discussion

As is seen from intensity distributions of reflected X–ray radiation at 20 and 40 cm distances from quartz single crystal in the absence of external influences (18°C) shown in Fig. 2, the beam in the reflection plane is slightly diverging with the distance from the single crystal. In Fig. 3 it is clearly seen that in the absence of external influences the reflected X–ray radiation in the direction perpendicular to the reflection plane has significant divergence amounting to ~34' due to the collimation of primary beam.

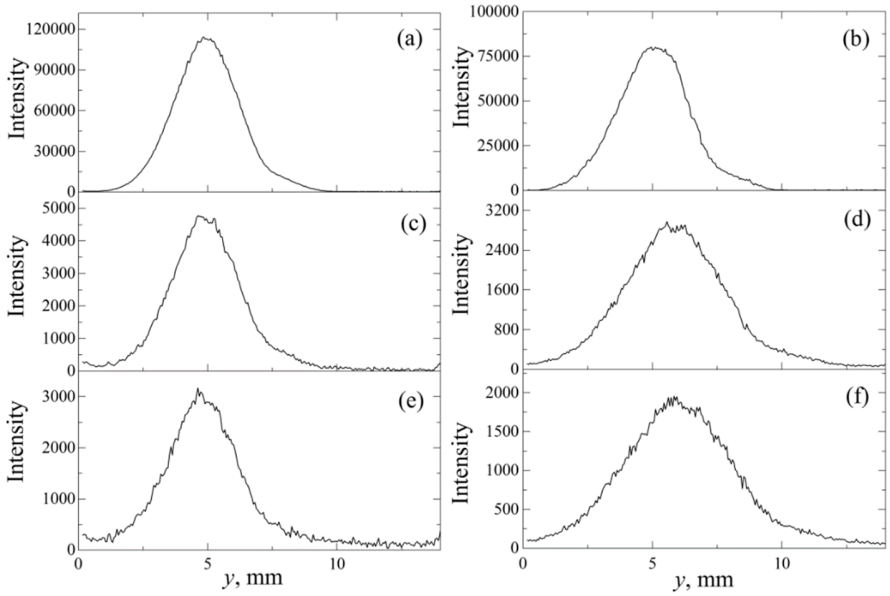

Fig. 3. Intensity distribution of reflected 40 keV X–ray radiation perpendicular to the reflection plane at 20 cm (a,c,e) and 40 cm (b,d,f) distances from quarz single crystal for different values of heater temperature: 400°C (a, b), 70°C (c, d), and 18°C (e, f).

It follows from Fig. 2 that when the heater temperature is 70°C, the intensity of reflected beam increases almost twice as much and the intensity distribution at 20 cm distance is notably changed (the central part grows much intensively than the lateral parts). This notwithstanding, the cross–section of Xray beam does not change at 20 cm distance in the reflection plane, but at 40 cm distance it slightly decreases, i. e., in the reflection plane X–ray beam does not diverge. It follows from Fig. 3 that in the direction perpendicular to reflection plane at heater temperature of 70°C respectively at 20 and 40 cm distances from the crystal, the cross–sections of X–ray beams are almost unchanged compared with cases without of external influences.

When the temperature of heater reaches to 400°C, the intensity of reflected beam increases by two orders of magnitude as it seen in Figs. 2 and 3. Along with that, at the distance of 20 cm the curve of intensity distribution of reflected X–ray beam in the reflection plane is narrowed almost two times as much, and at the distance of 40 cm is increased in comparison with the case without external influences. It follows from Fig. 3 that at heater temperature of 400°C the width of intensity distribution curve of X–ray beam does not change at the distance of 20 cm in the perpendicular direction, and at 40 cm distance the curve narrows considerably compared with the case without external influences and the X–ray beam does not diverge.

It is much clearly demonstrated in Fig. 4, where the frontal intensity distributions at 20 and 40 cm distances from quartz single crystal are given at heater temperature of 18, 70 and 400°C.

Taking into account that the spatial resolution of detector in the horizontal and vertical directions is 55 μm, one can measure in these images the angular width of X–ray radiation in mutually perpendicular directions with accuracy ~2'.

The values of the spatial width of reflected beam (as determined at half–height of the intensity distribution) and angular widths in mutually perpendicular directions at 20 and 40 cm distances for heater temperatures of 18, 70 and 400°C are given in Table 1. In the table Δx_1 and $\Delta x2$ are the spatial widths of beam in the reflection plane, and Δy_1 and Δy_2 are the spatial widths of beam in the perpendicular plane at 20 and 40 cm distances, respectively. In the last two columns of the table the measured results of the angular widths of X–ray radiation in mutually–perpendicular directions $\Delta\theta_x$ and $\Delta\theta_y$ are given respectively. As is seen from the cited values, in the absence of external influences the reflected X–ray radiation has a divergence of ~5' in the reflection plane, and ~30' in the plane perpendicular to that. The beam of X–rays is focused in the reflection plane and the focus approaches the crystal as the heater temperature increases, and in the perpendicular plane, where the divergence of beam is significant ~30', the angle of divergence gradually decreases and at 400°C temperature it reduces to ~3'.

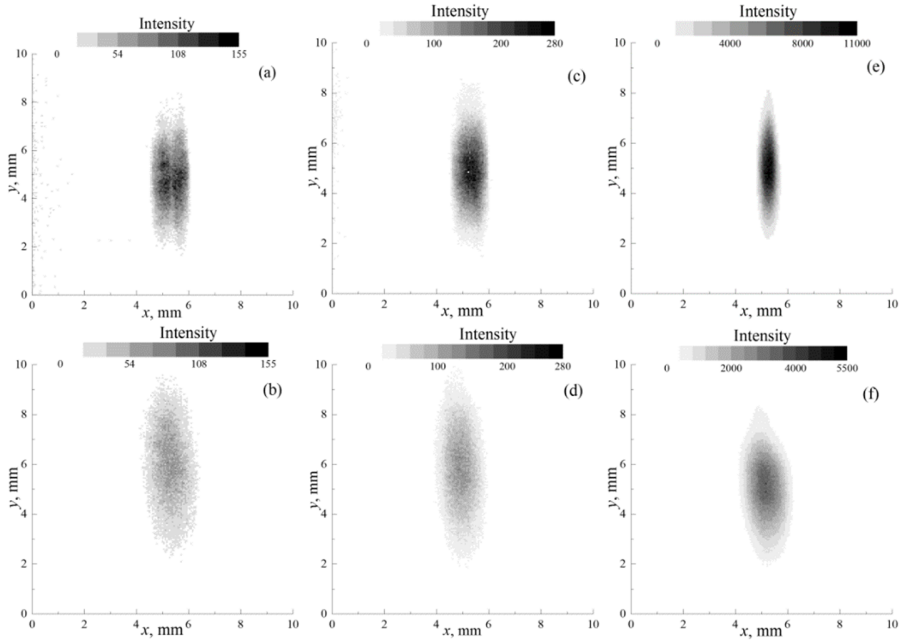

Fig. 4. Frontal intensity distribution of reflected 40 keV X–ray radiation at 20 cm (a,c,e) and 40 cm (b,d,f) distances from quartz single crystal for different values of heater temperature: 18°C (a,b), 70°C (c, d), and 400°C (e,f)

Keeping in mind that as the observed reflection is from the white spectrum of anode radiation, it is evident that the focusing is geometrical and occurs due to the bending of reflecting atomic planes. It is seen from Table 1 values of $\Delta\theta x$ and $\Delta\theta y$, that the maximum difference of the angular width of reflected X–ray radiation in the reflection plane changes less (~18'), than in the perpendicular plane (~23'). This means that as was assumed at the start of experiment, the radius

of curvature of atomic planes (10–11) in the direction of y–axis, perpendicular to the reflection plane, is less than along z–axis.

It is noteworthy that the degree of bending depends on the thermal expansion coefficient in the given direction. Consequently, in case of appropriate choice of crystal, of its cut and the family of reflecting atomic planes, one can provide such a two–dimensional bending, at which a point focus of reflected X–ray radiation is obtained.

Table 1. Values of spatial and angular width of reflected beam at 20 cm and 40 cm distances for different temperature of heater values

3	**Δx_1, mm**	**Δy_1, mm**	**Δx_2, mm**	**Δy_2, mm**	**$\Delta\theta_x$, angular min**	**$\Delta\theta_y$, angular min**
18	1.265	2.97	1.54	4.62	4.73	28.36
70	1.045	2.915	1.1	4.07	0.94	19.85
400	0.495	2.75	1.26	2.915	13.15	2.84

4. Conclusions

It is noteworthy that the degree of bending depends on the thermal expansion coefficient in the given direction. Consequently, in case of appropriate choice of crystal, of its cut and the family of reflecting atomic planes, one can provide such a two–dimensional bending, at which a point focus of reflected X–ray radiation is obtained. It is also shown that under these conditions the integrated intensity of reflected X–ray radiation increases by several orders of magnitude, and the angular width in mutually perpendicular directions is controllable.

Acknowledgments

This work was supported by the RA MES Science Committee, in the frames of the research project №18T–1C395.

References.

1. David, C., Nöhammer, B., and Ziegler. E., *Appl. Phys. Lett.*, 2002, vol. 79, p. 1088.
2. Grigoriev, M., Fakhrtdinov, R., Irzhak, D., Firsov, Al., Firsov, An., Svintsov, A., Erko, A., and Roshchupkin, D., *Opt. Commun.*, 2017, vol. 385, p. 15.
3. Snigirev, A. and Snigireva, I., *C. R. Physique.*, 2008, vol. 9, p. 507.
4. Yumotoa, H., Mimura, H., Matsuyama, S., and Hara. H., *Rev. Scient. Instr.*, 2005, vol. 76, p. 063708.
5. Kang, H.C., Yan, H., Winarski, R.P., Holt, M.V., Maser, J., Liu, C., Conley, R., Vogt, S., Macrander, A.T., and Stephenson, G.B., *Appl. Phys. Lett.*, 2008, vol. 92, p. 221114.
6. Levonyan, L.V. and Balyan, M.K., *Phys. Stat. Sol. (a)*, 1993, vol. 140, p. 247.
7. Khlopuzyan, S.H., *Armenian J. Physics*, 2015, vol. 8, p. 73.
8. Irzhak, D. and Roshchupkin, D., *J. Appl. Phys.*, 2014, vol. 115, p. 244903.
9. Gabrielyan, R.G. and Aslanyan, H.A., *Phys. Stat. Sol. (b)*, 1984, vol. 123, p. K97.
10. Kocharyan, V.R., *J. Contemp. Phys*. (*Armenian Ac. Sci.*), 2017, vol. 52, p. 392.

11. Mkrtchyan, A.R., Navasardian, M.A., Gabrielyan, R.G., Kocharian, L.A., and Kuzmin, R.N., *Solid State Communications*, 1986, vol. 59, p. 147.
12. Margaryan, V.V., Hayrapetyan, K.T., Noreyan, S.N., Khachatryan, V.A., Kiziridi, A.A., and Aloyan, L.R., *J. Contemp. Phys*. (*Armenian Ac. Sci*.)*,* 2017, vol. 52, p. 264.
13. Mirzoyan, V.K., Noreyan, S.N., and Kocharyan, V.R., *Izvestiya Akademii Nauk Arm., Fizika*, 2005, vol. 40, p. 53.
14. Kocharyan, V.R., Gogolev, A.S., Movsisyan, A.E., Beybutyan, A.H., Khlopuzyan, S.G., and Aloyan, L.R., *J. Appl. Crystallography*, 2015, vol. 48, p. 853.
Noreyan, S.N., Mirzoyan, V.K., and Kocharyan, V.R., *Poverkhnost' Rentgenovskie, sinkhrotronnye i neitronnye issledovaniya*, 2004, no. 1, p.18.

Hybrid monitoring systems for global processes. The results of the experiment at the first point of the hybrid system

V. Sarian[1*], A.R. Mkrtchyan[2], V. Ermakov[3], A. Nazarenko[4], A. Lyubushin[5], R. Meshcheryakov[6]

[1] Federal State Unitary Enterprise Radio Research and Development Institute(NIIR)
16 Kazakova Str., Moscow, Russian Federation,195964
[2] Institute of Applied Problems of Physics NAS RA
25 Hr. Nersissian Str., Yerevan, Republic of Armenia, 0014
[3] V.I. Vernadsky Institute of Geochemistry and Analytical Chemistry of Russian Academy of Sciences
19 Kosygina str., Moscow, Russian Federation, 119991
[4]Federal State Unitary Enterprise Radio Research and Development Institute (NIIR)
16 Kazakova Str., Moscow, Russian Federation, 105064
[5] Schmidt Institute of Physics of the Earth of Russian Academy of Sciences
10–1 Bolshaya Gruzinskaya str., Moscow, 123242
[6] V. A. Trapeznikov Institute of Control Sciences of Russian Academy of Sciences
65 Profsoyuznaya street, Moscow, Russian Federation,117997

The team of authors represented by Saryan V.K., Nazarenko A.A., Ermakov V.V., Lyubushin A.A. and Meshcheryakov R.V. hard survives the death of our co–author, dear friend and outstanding physicist, academician of the National Academy of Sciences of the Republic of Armenia Alpik Rafaelovich Mkrtchyan. Once again, we express our sincere condolences to the relatives and friends of A.R. Mkrtchyan, Director of IPPA Mkrtychyan A.G.– corresponding member of NAS RA, the entire team of the IPPF NAS RA, and we hope to continue those started with A.R. Mkrtychyan works.

This article presents our recent collaboration with Mkrtchyan A.R.

***Abstract**: This article is a continuation of the topic with which Sarian V.K. and A.R. Mkrtchyan [7] spoke at «International Conference on Electron, Positron, Neutron and X–Ray Scattering under External Influences & International School named after G. A. Askaryan 16–22 October 2017» «Invitation to the use of a powerful experimental ground created in the Russian Federation for monitoring the global processes based on new information technologies».*

The first point of the hybrid network was organized at the beginning of 2018 with the participation of scientists and specialists of the Federal State Unitary Enterprise NIIR, GEOKHI RAS, IPE RAS, IAPP NAS RA, ICS RAS and others at the field national center for complex environmental and biogeochemical studies of the GEOHI RAS, which is located on a geological base Moscow State University in the village N. Unal of North Ossetia (RF). The report will describe the measuring equipment used and discuss the significance of the results of measurements for short–term, medium–term and long–term forecasts of global processes, including emergency situations. The experiments will be continued from 2020 to 2021. It is planned to expand the experiment in potentially seismic areas in Kamchatka and Armenia. Similar experiments will be conducted at national training sites in the countries of the Asia–Pacific region in

[*]**E – mail**: *sarian@niir.ru, ermakov@geokhi.ru, apn@niir.ru, lyubushin@yandex.ru, mrv@ipu.ru*

accordance with the decision of the 58th meeting of the Working Group on Telecommunications and Information in the framework of the Asia–Pacific Economic Cooperation (APEC), which was held at the end of 2018 in Taipei (Chinese Taiwan). Similar experiments will be carried out at national training sites in the countries of the Asia–Pacific region in accordance with the decision of the 58th meeting of the Working Group on Telecommunications and Information in the framework of the Asia–Pacific Economic Cooperation (APEC), which was held at the end of 2018 in Taipei (Chinese Taiwan). At this meeting, the authors made a keynote speeches.

In the future, on this basis, it is planned to establish an international interdisciplinary collaboration of scientists and specialists on the formulation of development goals and regulations on the use of the created global hybrid monitoring system for global processes of natural and technogenic origin.

The relevance of the presented work is very great, since Improving the adaptive capabilities of a person in conditions of increasing technogenesis and increasing the risk of human and material losses from emergencies of natural and technogenic origin is a vital task (the task of survival) of modern civilization.

The article will consist of five sections:

1. Tasks to be solved with the help of hybrid monitoring systems.
2. Developed solutions.
3. Interdisciplinary research and international cooperation from 2016 to 2019. Research results.
4. The world's first experimental site of a hybrid monitoring system.
5. Further research plans (directions and scope).

1. Tasks to be Solved Using Hybrid Monitoring Systems

Statistics captures radical decrease in human and material losses from global emergencies of natural origin (hereinafter – emergencies) in today's world.

Each year, various global emergencies of natural origin cause unjustifiably large material and human losses in different parts of the Earth. These losses are equally high for both developed and developing countries. According to statistics, the risks of losses due to emergency situations, as a rule, increase annually in all countries of the world due to a noticeable increase in the frequency of emergency situations (earthquakes, tsunamis, floods, landslides, etc.). The situation seemed so bleak, that in 1997, a final and probably non–appealable sentence was passed by seismologists: "earthquakes cannot be predicted – that's the point.

But despite such a harsh verdict, these processes are so sensitive for all countries that in many countries, large amounts of money are still being spent on research to develop a reliable system of medium– and long–term forecasting, but their predictive potential is still so small that these predictions do not yet have economic values, and they are completely ignored in all countries. Indeed, all economic activity in the whole region (or megalopolis) will not be stopped for an indefinite time on the grounds that, according to scientific observations in this region, there may be an earthquake in the future.

Among the causes of increasing technogenesis should be attributed desynchronization reduction between the pace and scale of the introduction of new technologies, urbanization processes and other factors of increasing technogenesis and scientific research. The inevitable consequence of the victory of the fourth industrial revolution (digitalization), which all countries are striving for today, if not take urgent measures, will be a further increase in the environmental

technogenesis. The diagram below illustrates the reasons for the increase in technogenesis associated with globalization processes.

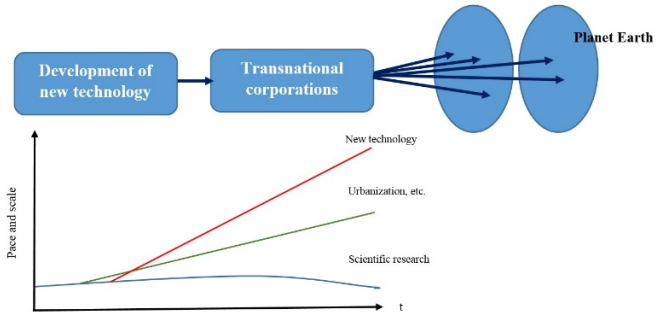

Fig.1. The decrease in desynchronization indicators

The decrease in desynchronization indicators is associated not only with the gap between the pace and scale of the introduction of new technologies, but also with the processes of urbanization and other factors of increasing technogenesis and scientific research. The anthropogenic burden on nature is increasing due to growing trends in the concentration of the population in megacities, the construction of smart cities, an increase in the pace of life and mobility of the population (including the development of mass tourism), rapid changes in technology, etc. Science is serious lags behind in studying the environmental impact of this burden, especially in developing countries.

2. Developed solutions

Choosing solutions, we decided not to abandon the use of existing national and, for a number of tasks, combined into global networks for monitoring earthquakes and other emergencies, although at present they have extremely low predictive potential and record only emerging emergencies. Today, the indicators are mainly used for scientific research of physical processes in the bowels of the Earth, development of models of the Earth's dynamics and internal structure, study of Earth's seismicity and earthquake source physics, seismic zoning, development of theory and computer science, technology for interpreting geophysical data, etc.

We supplemented the existing solutions with new ones, implementing a new mass service based on modern ICT, primarily Internet of things (IoT) technology – individualized subscriber rescue management (ISRM) in the event of global emergencies (earthquakes, floods, etc.) that reduce human and material losses of not less than 90%. We emphasize that this service can be available to any user of an existing infocommunication network at any time and in any place and provides individual rescue control in the event of any type of emergency.

These works are described in detail in [1, …, 25].

A key point in the possibility of implementing such a service for any type of emergency was the proposal to create a hybrid network for monitoring natural emergencies, which differs from existing networks in that sensors based on the Internet of things are installed in the vicinity of the existing measuring station of the existing network. The joint processing of the signals of all sensors will make it possible to detect precursor signals, for example, earthquakes, before the

start of earthquakes, and thereby ensure the evacuation of people to a safe area before the start of an emergency. In Fig. 2 is a block diagram of a hybrid monitoring network.

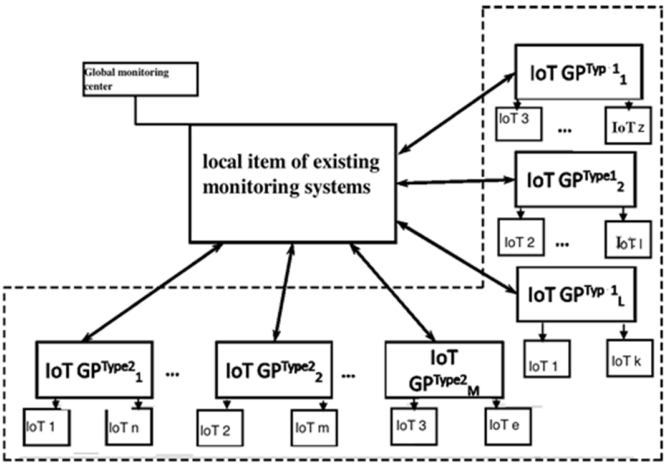

Fig.2. The block diagram of a hybrid monitoring network

3. Interdisciplinary research and international cooperation from 2016 to 2019. Research results.

Global emergencies of technogenic and natural origin, for example, earthquakes, do not recognize state borders and academic disciplines. Earthquake–related natural disasters needed to reduce interdisciplinary and international research and collaboration. Therefore, from the very first steps of our research, much attention is paid to probation proposals of technical decisions at reputable international venues such as ITU, ESCAP (Economic and the Social Commission for Asia and the Pacific), bringing together five regional commissions United Nations, APEC Forum. These organizations, in accordance with the resolution adopted by the General Assembly on June 3, 2015, the Sendai Framework for Disaster Risk Reduction 2015–2030, much attention is paid to the study of the possibilities of using ICT to prevent natural and man–made disasters origin, response to them and in the restoration of damage, calling for widespread international cooperation. The same tasks are included in the program of achieving 17 goals. UN Sustainable Development.

The following are the steps for forming an interdisciplinary team. Steps for forming an interdisciplinary team

2016 – NIIR, RF + IPPF NAS RA, RA

2017 + IFZ RAS, RF + GEOKHI RAS + NIIR–Svyaz LLC, etc.

2018 + IPU RAS + Kyrgyz Academy of Sciences + Serbian Academy of Sciences

2017 – 2019 Scientists from the USA, India, China, the Republic of Korea, Japan, Malaysia, Australia, and the Philippines also showed interest in this work.

We paid great attention to the wide testing of the proposed solutions at such authoritative expert sites as ITU, APEC, ESCAP, articles were published in leading scientific and technical journals, reports were made at international conferences in Atlanta, Brussels, Geneva, Taipei, Moscow, and others. fragments of the system were demonstrated at international exhibitions in Geneva, Hanover, Hong Kong, Moscow, etc. [25,…34]

4. The world's first experimental site of a hybrid monitoring system

The APEC TEL 58 session in Taipei approved the decision to establish national pilot sites in APEC countries. In Russia, such a site was created in 2019 in the North Caucasus.

The territory of the Unal depression is located in the mountainous region of North Ossetia (Fig.3, 4.), where lead–zinc deposits are located and almost all the mining industry of the republic is concentrated. It is a technogenic zone of increased environmental hazard. The main sources of environmental pollution by lead, cadmium, copper, zinc are: Arkhon–Kholstinsky dumps, Mizursky mining and processing plant (GOK) and the Unal tailing dump (pulp). The content of heavy metals (HM) in soils, waters, and biota is markedly increased here relative to their natural background, especially lead.

Fig.3. The world's first experimental site of a hybrid monitoring system

The base is located in a highly seismic mountainous area at an altitude of 900 m above sea level on the slopes of the Rocky Range. In the basin of the mountain rivers of North Ossetia, avalanches, glaciers, landslides, mudflows, earthquakes and floods are frequent. To date, the base has been used for the work of local geologists who control natural disasters. The territory of the Unal depression is located in the mountainous region of North Ossetia, where lead–zinc deposits are located and almost all the mining industry of the republic is concentrated. It is a technogenic zone of increased environmental hazard. The main sources of environmental pollution by lead, cadmium, copper, zinc are: Arkhon–Kholstinsky dumps, Mizursky mining and processing plant (GOK) and the Unal tailing dump (pulp). The content of heavy metals (HM) in soils, waters, and biota is markedly increased here relative to their natural background, especially lead.

The base is located in a highly seismic mountainous area at an altitude of 900 m above sea level on the slopes of the Rocky Range. In the basin of the mountain rivers of North Ossetia, avalanches, glaciers, landslides, mudflows, earthquakes and floods are frequent. To date, the base has been used for the work of local geologists who control natural disasters.

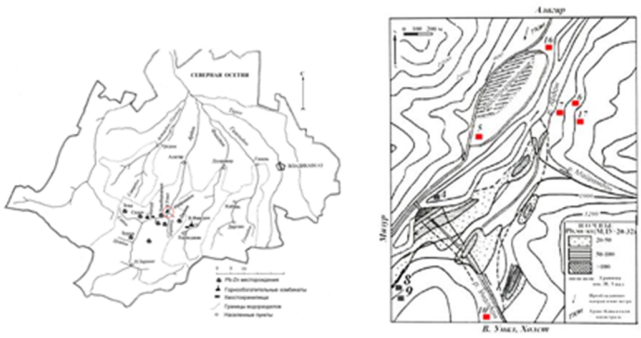

Fig.4. Area of work. Experimental sites.

Equipment of the experimental site:

a) Sensors,

b) Wireless equipment,

c) Ionospheric station,

d) Addition of signals from sensors, including signals from sensors of the nearest seismic station and joint processing to identify the synchronization effect.

a) Sensors.

Real–time monitoring of biogeochemical parameters using a system of existing sensors and sensors, for example, such as Stevens Hydra Probe Field Portable soil monitoring system, VAISALA GMT220 carbon dioxide sensor, RADEX MR107 radon indicator, UKR–1MTs mercury analyzer, 3000 IP mercury sensor, portable gas analyzer of mercury vapor in the air and other gases, ORP sensor (Redox) – redox potential pH S406 DG, digital optical oxygen sensor S423 / C / OPT, etc.

b) Wireless equipment.

Due to the small number of installed sensors (six in total) on the territory of the experimental site (Fig.5.), a local wireless network was used to transfer data from these sensors to the addition device for joint processing, despite the fact that its parameters at the sensor installation points were extremely unstable (temporary scheme) and require another solution that is available in the Russian Federation.

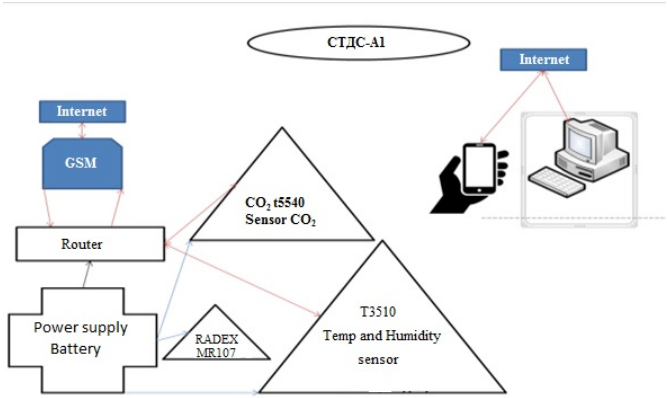

Fig.5. The temporary connecting diagrams of the geographically distributed sensors

The two figures (Fig.6, 7) below show the results of real measurements.

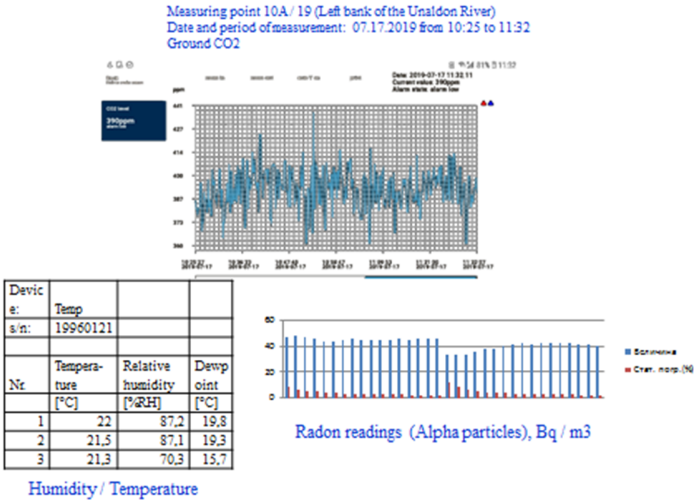

Device:	Temp		
s/n:	19960121		
Nr.	Tempera-ture	Relative humidity	Dewp oint
	[°C]	[%RH]	[°C]
1	22	87,2	19,8
2	21,5	87,1	19,3
3	21,3	70,3	15,7

Fig.6. The results of real measurements. Date and period of measurement: 07.17.2019 from 10:25 to 11:32

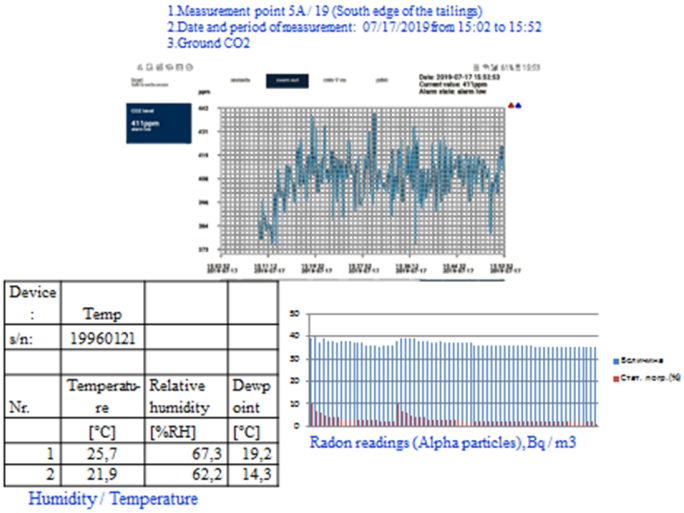

Device:	Temp		
s/n:	19960121		
Nr.	Temperatu-re	Relative humidity	Dewp oint
	[°C]	[%RH]	[°C]
1	25,7	67,3	19,2
2	21,9	62,2	14,3

Fig.7. The results of real measurements. Date and period of measurement: 07.17.2019 from 15:02 to 15:52

c) Ionospheric station – Complex of sounding of the ionosphere "Rainbow", fully domestic equipment.

The Rainbow vertical and oblique sounding ionosphere complex is designed for vertical, oblique and radiotomographic sounding and real–time real–time determination of the ionosphere parameters (Fig.8.), as well as the formation and continuous monitoring of the regional ionosphere model and its correction according to sounding data.

The Rainbow ionosphere sounding complex is currently unique and one of the best in the world, among similar equipment.

The uniqueness of the equipment lies in the high resolution, which allows you to record the precursors of earthquakes at their initial occurrence in the ionosphere.

The resolution of the equipment reaches 50 meters in the ionosphere and allows you to continuously monitor the dynamics of changes in the total electronic content in different layers of the ionosphere.

It should be noted that the Rainbow equipment also has the ability to record earthquake precursors at a great distance (including over the ocean) due to oblique sounding of the ionosphere over 3,000 kilometers. For this, equipment is located at intervals of up to 3,000 km (including on the islands).

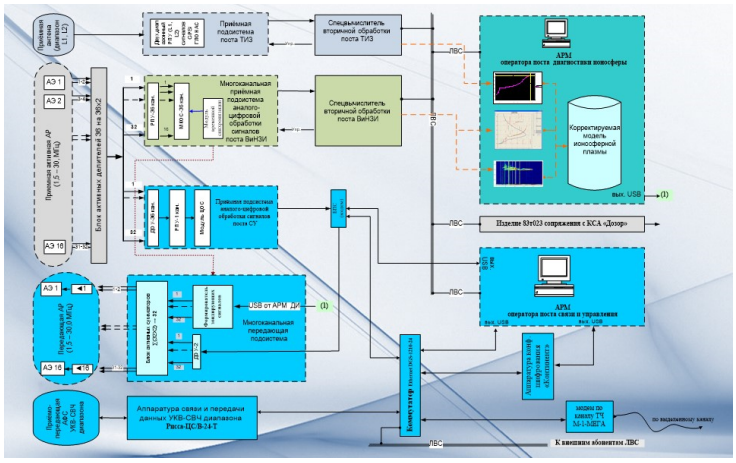

Fig.8. The block diagram of the Rainbow vertical and oblique sounding ionosphere complex

d)Addition of signals from sensors, including signals from sensors of the nearest seismic station and joint processing to identify the synchronization effect.

This item will be implemented in the future.

In spite of this, the objectives of the first stage of work at the experimental site of the hybrid monitoring system are to put together all the equipment and try to connect to the communication networks and find out the compatibility of the interfaces of individual devices to develop a user interface concept for such experimental sites. Ultimately, this is a step towards designing and testing a software product for effective product interaction, which would be delivered from the experimental section of the hybrid system to users: a) operators of situational centers and b) subscribers of mass IUSA services.

In principle, the goals of the first stage, as all participants admittedly, have been achieved.

5. Further research plans (directions and scope)

Briefly describe plans for further work:

– Introduce a new wireless network at the test site that fully meets all research objectives.

Duplex based domestic networks universal service for inhabitants in sparsely populated points of residence on the territory of the Russian Federation and the new low cost sustainable telecommunication network for the countryside. These are entirely domestic development. Created by the “Russian Communications Corporation", part of the state Rostec Corporation. This development is protected by patents.

In Fig. 9 a block diagram of a traditional and new wireless communication system is shown. From a comparison of the block diagrams, it can be seen that the new system can provide wireless access to objects even in sparsely populated areas, which makes it economically feasible to use the information interaction of the remote center of the hybrid network and the IoT–based sensors located in the pilot area.

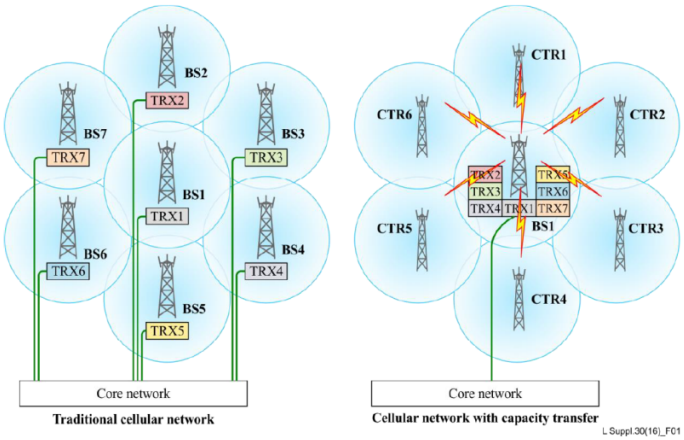

Fig.9. Cellular network with capacity transfer principle

– Implement the function of adding signals from sensors, including signals from sensors of the nearest seismic station, and ensure their joint processing to identify the synchronization effect.

– Continue the work of the experimental site, transferring measurements to the round–the–clock mode with remote multi–user control, including with foreign experimental sites, which, according to the APEC decision, should be deployed at the end of this year or at the beginning of the next in the Republic of Korea and Taipei.

– To expand the network of pilot sites in the country in Kamchatka, as well as in Kyrgyzstan and Armenia. The beginning of such practical work in Armenia was dreamed by our dear friend and co–author of this article, academician of the National Academy of Sciences of Armenia Alpik Rafaelovich Mkrtychyan, and we are obliged to bring these plans to life.

Actively research the search for sensors based on IoT–living (including humans) and oblique objects located in the vicinity of the experimental site to identify sensitive sensors of emergency precursors that are specific to this region.

– Embed services in new promising:

— communication systems, such as 5G and 2030 networks for providing individualized subscriber rescue management (ISRM) anywhere and anytime, so that the proposed solution to radically reduce the risk of emergency losses could be implemented on the whole planet;

— KVNO systems;

— e–medicine systems, etc.

– To increase the effectiveness of biogeochemical monitoring of ecosystems through the widespread introduction of dynamic studies of processes occurring in ecosystems, including by testing physiological sensors: vascular pulsation, muscle tremors, tension etc. in a large number of animals and humans. These non–specific parameters may give a surge in case of emergency.

– To expand our collaboration and set ourselves the goal – to achieve, no later than 2021, an international mega–grant for this work.

References.

1. Mkrtchyan A.R., Sarian V..K. Towards the integration of Earth sciences and the Internet of things., General meeting of the NAS RA, Department of Physics and Astrophysics, Yerevan April 12, 2016
2. Butenko V., Nazarenko A., Sarian V. and oth. Personal safety in emergency. Innovative application for mobile phones. ITU News, no. 3, pp. 47–49, 2012.
3. Butenko V., Nazarenko A., Sarian V. and oth. Applications of wireless sensor networks in next generation networks; technical paper. ITU–T, pp. 94–97, 2014.
4. Sarian V. Internet of things technology – a powerful catalyst functioning single digital space. ITU Regional Workshop on the Internet of Things (IoT) and Future Networks, Saint Petersburg, Russia, 19–20 June 2017. (Электронный ресур) https://www.itu.int/en/ITU–D/Regional–Presence/CIS/Pages/EVENTS/2017/06_Saint_Petersburg/06_SPB_Presentations.aspx
5. Ermakov V.V. Geochemical ecology and biochemical criteria for assessing the ecological state of biosphere taxa ”// Geochemistry. 2015. no.3. pp 203–221.
6. Sarian V.K., Nazarenko, A.P. Lyubushin A.A. Creating a hybrid monitoring network of global processes of natural and man–made disasters on the planet Earth, using geo–technologies of the Internet of things (GeoIoT). First Forum GeO IoT World, 2016, 25–28 may 2016, Brussels. (Электронный ресурс) https://niir.ru/wp–content/uploads/2013/12/NIIR_Viliam–Sarian.pdf
7. Sarian V., Mkrtchyan A. , Invitation of the use of powerful experimental ground created in Russian federation for monitoring the global processes based on new information technologies // IAPP NAS RA, International Conference on Electron, Positron, Neutron and X–ray Scattering under External Influences and International School named after G. A. Askarian, 16–22 October 2017, Yerevan–Meghi, Armenia.
8. ITU–T 2016 Y.2239 «Requirements for information control network and related application».
9. Recommendation Y.2222 «Sensor control networks and related applications in a next generation network environment» ITU–T, Geneva. – April 2013.
10. Recommendation Y.2221 «Requirements for support of ubiquitous sensor network (USN) applications and services in the NGN environment» ITU–T, Geneva. – January 2010
11. Recommendation Y.4100 «Common requirements of Internet of Things» ITU–T, Geneva. – June 2014
12. Recommendation Y.4102 «Requirements for Internet of Things devices and operation of Internet of Things applications during disaster» ITU–T. Geneva. – February 2015
13. Recommendation Y.4103 (2014) «Common requirements for Internet of things (IoT) applications» ITU–T. Geneva. – October 2014

14. Recommendation Y.4121 «Requirements of an Internet of Things enabled network for support of applications for global processes of the Earth» ITU–T. Geneva. – June 2018.
15. Butenko V.V., Nazarenko A.P., Saryan V.K. Mass infocommunication services based on coordinate–temporal and navigation support (second stage) // "Fundamental and applied coordinate–temporal and navigation support" (KVNO–2013) April 15, 2013
16. Nazarenko A.P., Saryan V.K. Navigation of Internet things: prospects, problems, solutions // “Fundamental and applied coordinate–time and navigation support” (KVNO–2015), April 2015.
17. Nazarenko A.P., Saryan V.K. On the increasing role of the administration of KVNO services at the present stage // “Fundamental and applied coordinate–time and navigation support” (KVNO–2017), April 17, 2017.
18. Nazarenko A.P., Saryan V.K. The fundamentals of creating a global system of individualized management of rescue of people in case of emergencies using promising technologies KVNO // "Fundamental and applied coordinate–time and navigation support" (KVNO–2019), April 15–19, 2019
19. Draft ITU–T Recommendation Y.smart–evacuation «Framework of Smart Evacuation during emergencies in Smart Cities and Communities» (Geneva, 4–15 September 2017).
20. Draft ITU–T Recommendation Y.disaster_notification «Framework of the disaster notification of the population in Smart Cities and Communities» (Cairo, 6–15 May, 2018).
21. ITU–T 2017 Y.3051 «The basic principles of trusted environment in ICT infrastrature».
22. Lyubushin A. Forecast of a seismic disaster in Japan on March 11, 2011 on the analysis of microseismic noise: force, time, place. URL: http://lnfm1.sai.msu.ru/grav /russian/life/chteniya/sagit2011/Lyubushin_Japan_2011.pdf
23. Lyubushin A. Prognostic properties of low frequency seismic noise// Natural Science, 2012, 4(8A), pp. 659–666.
24. Lyubushin A., Dynamic estimate of seismic danger based on multufractal properties of low frequency seismic noise// Natural Hazards, 2014, 70 (1), pp. 471–483.
25. Sarian V. Cooperation Program on Creating a Common Interoperable Approach to Improving the Efficiency of Existing Disaster Management Systems based on ICT. APEC TEL Workshop, Moscow, 30.11.2015.
26. Ermakov V. and Saryan V. Nowaday development of biogeochemical methods as an approach towards integrated knowledge system by use of modern information and communication technologies. Challenges of Green Economy, University «Union–Nikola Tesla», Beograd, pp. 57–76, 2018.
27. Sarian V., Ermakov V. and Jovanovic L. The role of earthquakes and waterfloods monitoring system, Ecologica, Zemun: Akademskaizdanja, vol. 25 no. 92, pp. 1001–1004, 2018

28. Sarian V., Nazarenko A. Improving the efficiency of the use of ICT to radically reduce losses in the event of global emergencies. Workshop «Earthquakes and Waterfloods Monitoring System with the application of the Internet of Things», The 58th APEC Telecommunications and Information Working Group Meeting, Taipei, Chinese Taipei, 2018.
29. Sarian V. and Nazarenko A. Mass service of individualized control for the population rescue in the event of all kinds of emergency situation. ITU Regional Workshop on Network 2030 jointly with ITU Forum on Future Applications and Services. Perspective 2030, Saint Petersburg, Russia, 21–23 May 2019. URL: https://www.itu.int/en/ITU–T/Workshops–andSeminars/201905/Pages/programme.aspx
30. Sarian V., Yakoubovsky R. and Salomatina E. Emergency situation in Smart Cities. Points of Application ICT 2030. ITU Regional Workshop on Network 2030 jointly with ITU Forum on Future Applications and Services. Perspective 2030, Saint Petersburg, Russia, 21–23 May 2019. URL: https://www.itu.int/en/ITU–T/Workshops–and–Seminars/201905/Pages/programme.aspx
31. Sarian V. Workshop «Earthquakes and Waterfloods Monitoring System with the application of the Internet of Things (IoT)». October 01, 2018 Taipei.
32. Ermakov V., Sarian V. Geochemical ecology and its significance in present biocheric research. World Congress of Geochemistry «Current trends and innovation in Geochemistry», November 18–19, 2017, Atlanta, USA.
33. Saryan V.K., Meshcheryakov R.V., Nazarenko A.P. Problems and opportunities of a hyperlinked world / V international conference “Engineering & Telecommunications – En&T”. MIPT, 2018.
34. Meshcheryakov R.V., Saryan V.K. The consequences of the inevitable transformation of all interacting objects in a single infocommunication system of the Internet of things // IT Standard Conference, 2019, Moscow.

Features of Radiation Generated by Bunches of Charged Particles Passing Through the Centre of a Ball

A.R. Mkrtchyan[1], P.A. Aleksandrov[2], L.Sh. Grigoryan[1*], A.H. Mkrtchyan[1], H.F. Khachatryan[1], M.V. Kovalchuk[2]

[1] Institute of Applied Problems of Physics NAS RA
25 Hr. Nersissian Str., Yerevan, Republic of Armenia, 0014
[2] National research centre "Kurchatov institute"
1 Akademika Kurchatova pl., Moscow, Russian Federation, 23182

Abstract: *We investigate the radiation generated by a train of bunches crossing a ball. The expressions for the spectral and angular distributions of the radiation energy is obtained for a general case of the dispersion law for the material of the ball. The consideration is based on the corresponding exact analytical solutions of Maxwell's equations. The numerical results are given for a dielectric ball. The possibility for the appearance of strong peaks in the spectral distribution of the radiation energy is demonstrated. The wavelengths corresponding to these peaks are of the order of the ball radius. A visual explanation of this phenomenon is provided.*

1. Introduction

The presence of a medium may essentially influence on the characteristics of high–energy electromagnetic processes, giving rise to new types of phenomena [1–6]. Well known examples of this kind are the Cherenkov Radiation (CR) [1,2,7,8], the diffraction and transition [3,4] types of radiations. The operation of a large number of sources for generation of the electromagnetic radiation in various spectral ranges is based on the interaction of relativistic electrons with matter [5]. In particular, the interfaces separating different media can be used for the control of radiation fluxes emitted by various systems.

The Synchrotron Radiation (SR) of a charged particle rotating in a homogeneous medium has been considered in [7] (see also [2,8]), where it has been shown that the interference between SR and CR leads to nontrivial consequences. New features in the spectral–angular distribution of the radiation intensity appear in the case of a charge rotation in an inhomogeneous medium. Exactly solvable problems for the radiation from a charge rotating in spherically and cylindrically symmetric media have been considered in a series of papers, started in [9,10] (see also [11,12] and references therein).

The modern accelerators may generate relativistic and monoenergetic short bunches with submillimeter length and with a relatively large number of electrons ($>10^9$). Such bunches allow to generate high–power quasi–coherent terahertz radiation, that is of considerable interest for applications in physics, chemistry and biology [13]. High intensity narrow–band and coherent terahertz CR generated by a bunch passing through a hollow channel inside a waveguide filled with a dielectric was directly observed in [14]. The use of a waveguide filled by dielectric plates with given separations between them leads to the further increase of the output power [15].

[*] **E – mail:** *levonshg@mail.ru*

The theory predicts another possibility for a significant increase in the CR intensity. It is related to the fact that the recent accelerators allow to generate trains of bunches with submillimeter separations. Tuning the distance between bunches, in [16] a powerful resonant (or, so–called, parametric [17]) coherent terahertz CR has been observed on a single waveguide mode. A different choice for the separation of bunches, allowing the generation of resonant CR on a large number of neighboring waveguide modes, was proposed in [18]. A clear explanation of this phenomenon is given in [18].

The radiation from a relativistic electron, crossing a ball (with an arbitrary dielectric function $\varepsilon(\omega)$ and with magnetic permeability $\mu = 1$) through its center, was studied in [19,20] (see also the references therein). It was shown, that the spectral distribution of radiation generated by the relativistic particle inside a ball at specified frequencies is strongly influenced by the ball–vacuum boundary.

In the present paper, we investigate the radiation by a train of one–dimensional electron bunches passing through the center of a ball made of a dielectric, a conductor, or a composite material. The possibility for generation of quasi–coherent CR by a train of equidistant bunches of relativistic electrons is shown. The radiation energy is evaluated for the case of a dielectric ball.

2. Problem setup and the radiation intensity

We consider a train of electron bunches flying through the center of a ball with dielectric function $\varepsilon(\omega)$ and immersed in vacuum. The magnetic permeability for the material of the ball will be assumed to be unity (non–magnetic material). It is also assumed that there is an external field (for example, electric), which supports the uniform motion of particles inside the ball.

Fig.1. A train of electron bunches flying through the center of a ball

In [9] a method is proposed for the evaluation of the Green function of the electromagnetic field in a medium consisting of $N \geq 1$ spherically–symmetric layers having a common center and different dielectric permittivities. Based on this method, a formula is derived for the energy of radiation from a charged particle moving along an arbitrary trajectory in such medium. The special cases of a charged particle rotating around or inside a dielectric ball have been investigated in [21,11] (see also the references given therein). Another example of a charged particle uniformly moving along a straight line through the center of a ball with the radius r_b and the dielectric permittivity ε_b, immersed in a homogeneous medium with permittivity ε_1, is discussed in [19] (see Fig. 2).

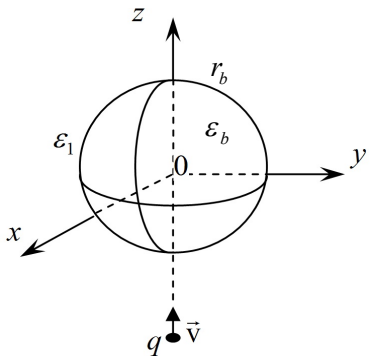

Fig.2. A particle flying from a medium into a ball

Assuming that the trajectory of the particle is described by the equation $z = \mathrm{v}t$, the corresponding current density can be written as

$$\vec{j}(\vec{r},t) = \frac{q\vec{\mathrm{v}}}{\pi r^2 \sin\theta}\begin{cases}\delta(r-\mathrm{v}t)\delta(\theta) & \text{for} \quad t>0\\ \delta(r+\mathrm{v}t)\delta(\theta-\pi) & \text{for} \quad t<0\end{cases} \tag{1}$$

where q and v are the charge and velocity of the particle, and θ is the polar angle of spherical system of coordinates r,θ,φ. For the corresponding Fourier transform one has

$$\vec{j}(\vec{r},\omega) = \frac{1}{2\pi}\int \vec{j}(\vec{r},t)e^{i\omega t}dt = \frac{q\vec{\mathrm{v}}}{2\pi^2 \mathrm{v} r^2 \sin\theta}[\delta(\theta)e^{i\frac{\omega}{\mathrm{v}}r} + \delta(\theta-\pi)e^{-i\frac{\omega}{\mathrm{v}}r}] \tag{2}$$

Expanding $\vec{j}(\vec{r},\omega)$ in spherical vectors $\vec{X}^{(\mu)}_{lm}$ [22], we can evaluate the corresponding expansion coefficients:

$$j^{lm}_{\mu}(r) \equiv \int \vec{j}(\vec{r},\omega)\vec{X}^{(\mu)*}_{lm}d\Omega. \tag{3}$$

As a result we find

$$j^{lm}_1 = \frac{q\delta_{m0}}{2\pi\, r^2}\sqrt{\frac{2l+1}{4\pi}}[e^{i\frac{\omega}{\mathrm{v}}r} - (-1)^l e^{-i\frac{\omega}{\mathrm{v}}r}], \qquad j^{lm}_2 = j^{lm}_3 = 0 \tag{4}$$

Similarly, one can expand the vector potential $\vec{A}(\vec{r},\omega)$ of the electromagnetic field in spherical vectors $\vec{X}^{(\mu)}_{lm}$. In the Lorentz gauge the expansion coefficients A^{lm}_{μ} are given by the expressions

$$\frac{(2l+1)cr_b^2}{4\pi}\begin{bmatrix}A^{lm}_1(r)\\ A^{lm}_2(r)\end{bmatrix} = \begin{bmatrix}lu_{\underline{l-1}} + (l+1)u_{\underline{l+1}}\\ \sqrt{l(l+1)}(u_{\underline{l-1}} - u_{\underline{l+1}})\end{bmatrix}^{lm}_r + \gamma_l[lB^{lm}_{\underline{l-1}} - (l+1)B^{lm}_{\underline{l+1}}]\begin{bmatrix}lP_{\underline{l-1}} + (l+1)P_{\underline{l+1}}\\ \sqrt{l(l+1)}(P_{\underline{l-1}} - P_{\underline{l+1}})\end{bmatrix}_{(r,r_b)} \tag{5}$$

(for details see [9,11]). The magnetic type multipoles ($\mu = 3$) are not generated and $A^{lm}_3(r) = 0$. Here

$$u^{lm}_{\underline{l_1}}(r) \equiv \int_0^{\infty} P_{\underline{l_1}}(r,x)j^{lm}_1(x)x^2dx$$

$$B^{lm}_{\underline{l_1}} = \frac{q\delta_{m0}}{2\pi}\sqrt{\frac{2l+1}{4\pi}}\{\lambda_0 j_l(\lambda_0 r_b)\int_{r_1}^{\infty} h^{(1)}_{\underline{l_1}}(\lambda_1 x)[e^{i\frac{\omega}{\mathrm{v}}x} - (-1)^l e^{-i\frac{\omega}{\mathrm{v}}x}]dx + \tag{6}$$

$$+ \lambda_1 h^{(1)}_l(\lambda_1 r_b)\int_0^{r_b} j_{\underline{l_1}}(\lambda_0 x)[e^{i\frac{\omega}{\mathrm{v}}x} - (-1)^l e^{-i\frac{\omega}{\mathrm{v}}x}]dx\}$$

with the notations

$$\gamma_l = \frac{1/\varepsilon_b - 1/\varepsilon_1}{l z_{l-1}^l + (l+1) z_{l+1}^l}, \quad \lambda_0 = \frac{\omega}{c}\sqrt{\varepsilon_b}, \quad \lambda_1 = \frac{\omega}{c}\sqrt{\varepsilon_1}$$

$$z_\upsilon^l = \frac{\lambda_1 j_\upsilon(\lambda_0 r_b) h_l^{(1)}(\lambda_1 r_b)/\varepsilon_1 - \lambda_0 j_l(\lambda_0 r_b) h_\upsilon^{(1)}(\lambda_1 r_b)/\varepsilon_b}{\lambda_1 j_\upsilon(\lambda_0 r_b) h_l^{(1)}(\lambda_1 r_b) - \lambda_0 j_l(\lambda_0 r_b) h_\upsilon^{(1)}(\lambda_1 r_b)} \tag{7}$$

and $h_l^{(1)}(y) = j_l(y) + i n_l(y)$ ($j_l(y)$ and $n_l(y)$ are the spherical Bessel and Neumann functions respectively). In (6) the following notations are used

$$f_{\underline{l}}(\tau) \equiv f_l(\tau)/[\lambda_0 j_{l-1}(\lambda_0 r_b) h_l^{(1)}(\lambda_1 r_b) - \lambda_1 j_l(\lambda_0 r_b) h_{l-1}^{(1)}(\lambda_1 r_b)] \tag{8}$$

and for the fields outside the ball ($r > r_b$) one has

$$P_l(r, r_b) = h_l^{(1)}(\lambda_1 r) j_l(\lambda_0 r_b) \tag{9}$$

From the relations

$$h_l^{(1)}(x) \approx (-i)^{l+1} \frac{e^{ix}}{x}, \qquad j_l(x) \approx \frac{1}{x}\sin(x - l\pi/2), \qquad x >> l \tag{10}$$

for the spherical Bessel and Hankel functions [23,24] it follows that at large distances from the ball one has

$$A_\mu^{lm}(r) \approx \delta_{m0} a_\mu^l \frac{e^{i\lambda_1 r}}{\lambda_1 r} + \ldots, \qquad r \to \infty \tag{11}$$

Here

$$\begin{bmatrix} a_1^l \\ a_2^l \end{bmatrix} = \frac{(-i)^l q}{c r_1^2 \sqrt{\pi(2l+1)}} \begin{bmatrix} l \mathrm{w}_{\underline{l-1}} - (l+1)\mathrm{w}_{\underline{l+1}} \\ \sqrt{l(l+1)}(\mathrm{w}_{\underline{l-1}} + \mathrm{w}_{\underline{l+1}}) \end{bmatrix}, \qquad a_3^l = 0 \tag{12}$$

and

$$\mathrm{w}_{l_1} \equiv J_{l_1}(<) + i\lambda_1 r_b^2 \left[a_{l_1}^{(12)} J_{l_1}(>) + a_{l_1}^{(22)} H_{l_1} \right] + \gamma_l j_{l_1}(\lambda_0 r_b) \left[l Q_{\underline{l-1}} - (l+1) Q_{\underline{l+1}} \right] \tag{13}$$

In (13) the following notations are introduced

$$J_{l_1}(<) \equiv \int_0^{r_b} j_{l_1}(\lambda_0 x)[e^{i\frac{\omega}{\mathrm{v}}x} - (-1)^l e^{-i\frac{\omega}{\mathrm{v}}x}]dx, \quad J_{l_1}(>) \equiv \int_{r_b}^{\infty} j_{l_1}(\lambda_1 x)[e^{i\frac{\omega}{\mathrm{v}}x} - (-1)^l e^{-i\frac{\omega}{\mathrm{v}}x}]dx,$$

$$H_{l_1} \equiv \int_{r_b}^{\infty} h_{l_1}^{(1)}(\lambda_1 x)[e^{i\frac{\omega}{\mathrm{v}}x} - (-1)^l e^{-i\frac{\omega}{\mathrm{v}}x}]dx, \qquad Q_{l_1} = \lambda_0 j_l(\lambda_0 r_b) H_{l_1} + \lambda_1 h_l^{(1)}(\lambda_1 r_b) J_{l_1}(<) \tag{14}$$

According to [9] the spectral–angular and spectral distributions of the radiation energy (during the all time of the charge motion) are determined by the expressions

$$\frac{dI_1}{d\omega\, d\Omega} = \frac{c}{\sqrt{\varepsilon_1}} \left| \sum_l a_2^l \vec{X}_{l0}^{(2)} \right|^2 \tag{15}$$

and

$$\frac{dI_1}{d\omega} = \frac{c}{\sqrt{\varepsilon_1}} \sum_l \left| a_2^l \right|^2 \tag{16}$$

respectively.

We now turn to the study of the spectral distribution of energy emitted by a train of electron bunches over the entire time of its movement:

$$\int F(\omega) I_1(\omega) d\omega \equiv \int I(\omega) d\omega \tag{17}$$

Here, $I_1(\omega)$ is the spectral density of the energy emitted by a single electron and $F(\omega)$ is the structure factor of the train of electron bunches. In what follows we will assume that the transverse size of the bunches is much smaller compared with the radius of the ball and with the radiation wavelength.

The structure factor in (17) is presented in the form [25, 26]

$$F = n_e[1 - f_e(\omega) f_{tr}(\omega)\,] n_b + n_e^2 f_e(\omega) n_b^2 f_{tr}(\omega) \tag{18}$$

It is determined by the coherence factor of electrons inside the bunches:

$$f_e = \exp(-\omega^2 \sigma^2 / \mathrm{v}^2) \tag{19}$$

(we assume Gaussian distribution of electrons with standard deviation σ), and by the coherence factor for the radiation of bunches inside the train:

$$f_{tr} = \frac{\sin^2(\omega d n_b / 2\mathrm{v})}{n_b^2 \sin^2(\omega d / 2\mathrm{v})} \tag{20}$$

Here, d is the distance between the bunches, n_e is the number of electrons in the bunch, n_b is the number of bunches in the train. From (20) it follows that the train of bunches (with characteristic size essentially smaller than the radiation wavelength: $\sigma << 2\pi c / \omega$) radiates coherently $f_e(\omega) \approx 1,\ f_{tr}(\omega) = 1$ on discrete frequencies

$$\omega_m = \frac{2\pi \mathrm{v}}{d} m\,, \qquad m = 1,2... \tag{21}$$

(the frequency of emitted electromagnetic waves is proportional to the repetition frequency), and quasi–coherently $f_e(\omega) \approx 1,\ 0.5 < f_{tr}(\omega) \le 1$ near these frequencies with the bandwidth

$$\Delta\omega_{n_b} = \frac{\pi \mathrm{v}}{d \cdot n_b} \sim \frac{1}{n_b} \tag{22}$$

3. Numerical results and their visual explanation. Ball made of melted quartz

3.1. Radiation from a single electron

In this section we describe the features of the radiation for a ball made of melted quartz. The corresponding dielectric permittivity is given by [27] $\varepsilon_b = \varepsilon_b' + i\varepsilon_b'' = 3.78(1 + 0.0001i)$. In Fig. 3 (see [19]) we display the spectral distribution of the radiated energy from an electron of the energy 2 MeV, flying through the center of the ball with radius $r_b = 4\,\mathrm{cm}$ (full curve).

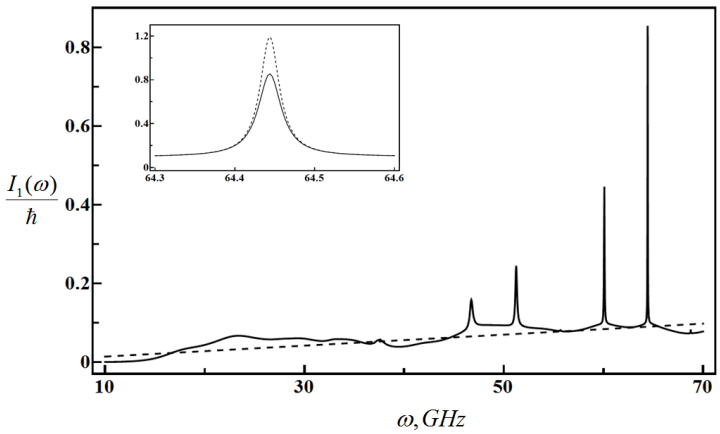

Fig.3. Spectral distribution of the radiated energy from an electron of energy 2 MeV flying through the center of the ball of melted quartz (full curve). The dashed curve corresponds to the motion of electron in a homogeneous medium with $\varepsilon_b = \varepsilon_b'$ provided the radiation is accumulated over the length of the path $2r_b$ (ball diameter). The Cherenkov condition is satisfied (for the graph in the upper left corner, see below)

Noteworthy is the fact that

1. sharp peaks are observed on certain "resonant" frequencies (for example, $\omega_0 \approx 64.45$ GHz) with the wavelength of the order r_b, whose height is almost an order of magnitude higher than at neighboring frequencies. This circumstance indicates a strong effect of the ball – vacuum interface on the CR generated by the particle in the ball material.

Numerical calculations show that

2. Taking into account the dielectric losses of the material of the ball has practically no effect on the radiation intensity, with the exception of the vicinity of "resonant" frequencies. In the vicinity of these selected frequencies, even small losses of radiation energy in the material of the ball (as, for example, in melted quartz) noticeably reduce the intensity of radiation. This fact is seen in the graph shown in the upper left corner of Fig.3, where the dotted curve corresponds to the case of the absence of dielectric losses.

The foregoing can be explained by the fact that

3. the radiation amplification is caused by the constructive superposition of electromagnetic waves, multiply reflected from the inner surface of the ball.

3.2. Radiation from a train of electron bunches

In Fig. 4 we have plotted the spectral distribution of the radiation energy generated by a train of electron bunches flying through a dielectric ball made of melted quartz

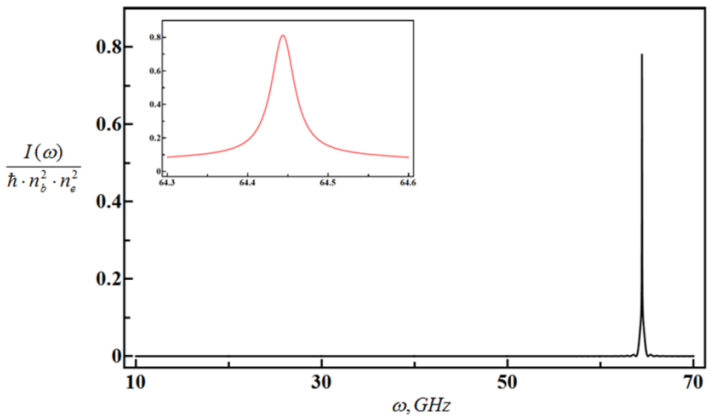

Fig.4. Spectral distribution of the radiation energy from a train of electron bunches of energy 2 MeV flying through the center of a ball of melted quartz, $n_e = 10^9$, $n_b = 100$, $d \cong 2{,}8$ cm. Other parameters are the same as those for Fig.3

The power of quasi–coherent radiation generated by a train of bunches in the range $\omega_0 \pm \Delta\omega/2$ is given by

$$P \cong \frac{\mathrm{v}}{l} \int_{\omega_0-\Delta\omega/2}^{\omega_0+\Delta\omega/2} F(\omega) I_1(\omega) d\omega \cong \frac{\mathrm{v}}{l} \Delta W \cdot n_e^2 \cdot n_b^2 \sim 1\,\mathrm{kw} \tag{23}$$

where

$$\Delta W = \int_{\omega_0-\Delta\omega/2}^{\omega_0+\Delta\omega/2} I_1(\omega) d\omega \sim 1.3 \cdot 10^{-8}\ \text{eV}, \qquad \omega_0 \approx 64.45\ \text{GHz} \tag{24}$$

$\Delta\omega \sim 50\,\mathrm{MHz}$, $n_e \approx 10^9$ is the number of electrons in the bunch, $n_b = 100$ is the number of bunches and $l = n_b d \cong 2{,}8\,\mathrm{m}$ is the length of the train.

The emergence of powerful quasi–coherent radiation is related to the fact that:

a) for given choice of the values of system parameters, one of the resonant frequencies of the ball is equal to the repetition frequency of the bunches, $\omega_0 = \dfrac{2\pi\mathrm{v}}{d}$ (compare with (21)). In this case, the train of bunches will radiate coherently at this resonant frequency of the ball, with the highest spectral density:

$$I(\omega_0) = F(\omega_0) I_1(\omega_0), \qquad \text{where} \qquad F(\omega_0) \approx n_e^2 n_b^2 \tag{25}$$

and

b) is quasi–coherent:

$$I(\omega) = F(\omega) I_1(\omega), \qquad \text{where} \qquad F(\omega) \geq n_e^2 n_b^2 / 2 \tag{26}$$

in the entire frequency range $\omega \in [\omega_0 - \Delta\omega/2, \omega_0 + \Delta\omega/2]$, because

$$\Delta\omega < \Delta\omega_{n_b}, \quad \text{i.e.} \quad n_b < \pi\mathrm{v}/d\Delta\omega \tag{27}$$

4. Conclusions

1. We have investigated the possibility of generating quasi–coherent CR by a train of equidistant one–dimensional electron bunches flying through the center of a ball made of a dielectric, a conductor, or of a composite material.
2. In the case of a melted quartz ball, it was shown that with a special choice of the distance between the bunches $d \cong 2.8\,\text{cm}$, the resonant quasi–coherent CR of 100 bunches is formed near the resonant frequency $\omega_0 \approx 64.45 GHz$ in a narrow frequency band $\Delta\omega \cong 50 MHz$.
3. In a real situation (a) a train of three–dimensional bunches is generated instead of one–dimensional ones, and (b) this train should move along a hollow channel cuted through the ball (to reduce ionization losses). The influence of these factors will be insignificant if the radius of the channel is much smaller than the wavelength of radiation and larger than the transverse dimensions of the bunch.
4. It is proposed to use this phenomenon for the development of high–power and narrow–band sources of electromagnetic waves in the giga–terahertz frequency range.

Acknowledgments

The work of L.Sh.G. and H.F.Kh. was supported by the RA Committee of Science, in the frames of the research project №18T–1C397.

References.

1. Jelley J.V., Cherenkov Radiation and its Applications, Pergamon Press, London (1958).
2. Zrelov V.P., Vavilov–Cherenkov Radiation and its Applications in High Energy Physics, Atomizdat, Moscow (1968) (in Russian).
3. Garibian G.M., Yan Shi, X–Ray Transition Radiation, AN Arm. SSR Press, Yerevan (1983) (in Russian).
4. Ginzburg V.L., Tsytovich V.N., Transition Radiation and Transition Scattering, Adam Hilger, Bristol (1990).
5. Rullhusen P., Artru X., Dhez P., Novel Radiation Sources Using Relativistic Electrons, World Scientific, Singapore (1998).
6. Potylitsin A.P., Electromagnetic Radiation of Electrons in Periodic Structures, Springer, Berlin (2011).
7. Tsytovich V.N., Westnik MGU, **11,** 27 (1951) (in Russian).
8. Kitao K., Prog. Theor. Phys., **23**, 759 (1960).
9. Arzumanyan S.R., Grigoryan L.Sh., Saharian A.A., Izv. Nats. Akad. Nauk Arm., Fiz. (Engl. Transl.: J. Contemp. Phys.), **30**, 99 (1995).
10. Grigoryan L.Sh., Kotanjyan A.S., Saharian A.A., Izv. Nats. Akad. Nauk Arm., Fiz. (Engl. Transl.: J. Contemp. Phys.), **30**, 239 (1995).
11. Grigoryan L.Sh., Khachatryan H.F., Arzumanyan, S.R., Grigoryan, M.L., Nucl. Instr. and Meth., B **252**, 50 (2006).
12. Saharian A.A., Kotanjyan A.S., J. Phys., A **38**, 4275 (2005).

13. Williams G.P., Reports on Progress in Physics, **69**, 301 (2006).
14. Cook R., Tikhoplav A.M., Tochitsky S.Y., Travish G., Williams O.B., Rosenzweig J.B., Phys. Rev. Lett., **103**, 095003 (2009).
15. Grigoryan L.Sh., Mkrtchyan A.R., Khachatryan H.F., Arzumanyan S.R., Wagner W., J. Phys.: Conf. Ser., **357**, 012004 (2012).
16. Andonian G., Williams O., Wei X., Niknejadi P., Hemsing E., Rosenzweig J. B., Muggli P., Babzien M., Fedurin M., Kusche K., Malone R., Yakimenko V., Appl. Phys. Lett., **98**, 202901 (2011).
17. Fainberg Y.B., Khizhniak N.A., Zh. Eksp. Teor. Fiz., **32**, 883 (1957) (in Russian).
18. Grigoryan L.Sh., Khachatryan H.F., Saharian A.A., Kotanjyan Kh.V., Arzumanyan S.R., Grigoryan M.L., Izv. Nats. Akad. Nauk Arm., Fiz. (Engl. Transl.: J. Contemp. Phys.), **40**, 155 (2005).
19. Arzumanyan, S.R., J. Phys.:Conf. Series, **357**, 012008 (2012).
20. Grigoryan L.Sh., Mkrtchyan A.H., Khachatryan H.F., Proceedings of the Int. Conf. on "Electron, Positron, Neutron and X–Ray Scattering under External Influences", Yerevan, Armenia, 47 (2016).
21. Grigoryan L.Sh., Khachatryan H.F., Arzumanyan S.R., Izv. Nats. Akad. Nauk Arm., Fiz. (Engl. Transl.: J. Contemp. Phys.), **37**, 327 (2002).
22. Berestetskii V.B., Lifshitz E.M., Pitaevskii L.P., Quantum Electrodynamics, Nauka, Moscow (1980) (in Russian).
23. Jackson J.D., Classical Electrodynamics, John Willey & Sons, New York–London (1962).
24. Korn G.A., Korn T.M., Mathematical Handbook, McGraw Book Company, New York (1968).
25. Korkhmazian N.A., Gevorgian L.A., Petrosian M.L., Zh. Tekh. Fiz., **47**, 1583 (1977) (in Russian).
26. Nikitin M.M., Epp V.Ya. Undulator Radiation, Energoatomizdat Press, Moscow (1988) (in Russian).
27. Voronkova E.M., Grechushnikov B.N., Distler G.I., Petrov I.P., Optical Materials for Infrared Technology, Nauka, Moscow (1965) (in Russian).

Angular Distribution of Intensive Radiation from a Charge Rotating Around a Conductive Ball

L.Sh. Grigoryan[1*], A.A. Saharian[1], A.H. Mkrtchyan[1], H.F. Khachatryan[1], M.L. Grigoryan[1], T.A. Petrosyan[1], H.P. Harutyunyan[2]

[1] Institute of Applied Problems of Physics NAS RA
25 Hr. Nersissian Str., Yerevan, Republic of Armenia, 0014
[2] National Polytechnic University of Armenia
105 Teryan St., Yrevan, Republic of Armenia, 0009

Abstract: *The angular distribution of the radiation from a relativistic charged particle uniformly rotating about a conductive ball in its equatorial plane is studied. The magnetic permittivity of the ball is assumed to be one. The work is based on the corresponding exact analytic solutions of Maxwell's equations. The generalized Drude–Lorentz–Sommerfeld formula for the dielectric function of the conductive ball is used in numerical calculations.*
Earlier it was shown that localized and high–amplitude oscillations of the electromagnetic field can be generated at a given harmonic inside the ball at a certain (resonant) particle rotation frequency. Herewith, at large distances from the trajectory of the particle, these localized oscillations are accompanied by intense radiation at the same harmonic, which is many times more intense than the analogous radiation in the case when the ball is absent. The possibilities of using this phenomenon to develop sources of quasi–monochromatic electromagnetic radiation in the range from giga– to terahertz frequencies are discussed.

1.Introduction

The presence of matter may essentially influence to the radiation of charged particle, which may have important practical applications. For example, in the presence of flat interfaces between media relativistic particle generates transition radiation [1,2]. Opportunities for radiation of a charged particle are expanded at the transition from open (flat) to a half–closed (cylindrically symmetric) or closed (spherically symmetric) boundary between two media.

It is important to mention that if the source of the field is moving near the boundary, in addition to the volume waves also surface waves (SW) can be generated on the boundary. Moreover, the phase velocity of the latter can be much smaller than that for the volume waves. This may have important practical applications.

This work is devoted to this topic. The electromagnetic field of the charged particles rotating around a metallic ball was studied in [3]. However, in [3] it was not investigated the possibility of SW generation inside a conductive ball. In [4] the radiation of a charged particle uniformly rotating around a conductive ball, in its equatorial plane has been investigated (see also [5]). The angular distribution of the radiation from a charged particle rotating along an equatorial orbit around a dielectric ball is studied in [6]. In this work the angular distribution of the radiation from a relativistic charged particle uniformly rotating about a conductive ball is studied.

[*] **E – mail:** *levonshg@mail.ru*

2. The description of problem

Now consider the uniform rotation $\mathrm{v} = const$ of a relativistic electron in the equatorial plane of a conductive ball in the magnetic field, in empty space (see Fig.1).

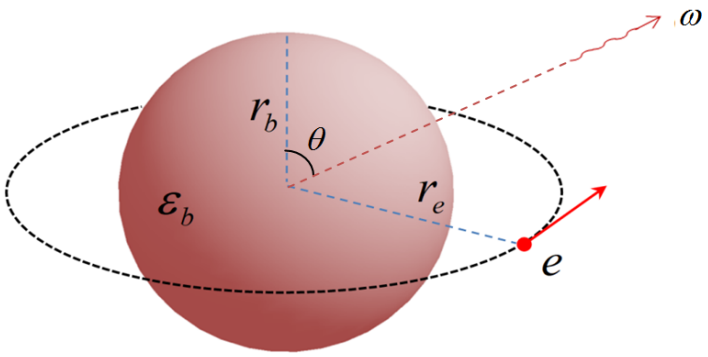

Fig.1. A relativistic electron rotating about a ball in its equatorial plane

The permittivity of medium is the following step function of radial coordinate *r*:

$$\varepsilon(r) = \varepsilon_b + (1-\varepsilon_b)\Theta(r-r_b) \tag{1}$$

where r_b is the radius of ball and $\varepsilon_b = \varepsilon_b' + i\varepsilon_b''$ is the complex valued permittivity of the ball material and $\Theta(x)$ –is the Heaviside step function. The magnetic permeability of the substance of the ball is taken to be unity. The uniform rotation of electron (with speed v and orbital radius r_e) entails radiation at some discrete cyclic frequencies (harmonics) $\omega_k = k\mathrm{v}/r_e$ with the harmonic number $k = 1,2,3\ldots$. It is convenient to introduce the following dimensionless quantity:

$$W_{kT} / \hbar\omega_k \equiv N_k \tag{2}$$

(the number of emitted quanta). Here W_{kT} is the energy radiated at cyclic frequency ω_k during one period $T = 2\pi r_e / \mathrm{v}$ of electron gyration, and $\hbar\omega_k$ is the energy of corresponding electromagnetic wave quantum. Let us also introduce the angular distribution $n_k(\theta)$ of the number of emitted quanta determined by the equation

$$N_k = \int_0^\pi n_k(\theta)d\theta \tag{3}$$

where θ is the corresponding polar angle.

It is known [7,8] that if the space as a whole is filled with a transparent and homogeneous substance (with constant dielectric permittivity ε) then

$$N_k(\infty;\mathrm{v},\varepsilon) = \frac{N_0}{\beta\sqrt{\varepsilon}}[2\beta^2 J_{2k}'(2k\beta) + (\beta^2 - 1)\int_0^{2k\beta} J_{2k}(x)dx] \tag{4}$$

$$n_k(\infty;\mathrm{v},\varepsilon) = \frac{N_0 \cdot k}{\sqrt{\varepsilon}}\sin\theta \times [ctg^2(\theta)J_k^2(k\beta\sin\theta) + \beta^2 J_k'^2(k\beta\sin\theta)] \tag{5}$$

where $N_0 = 2\pi e^2 / \hbar c \cong 0.0459$, $\beta = \mathrm{v}\sqrt{\varepsilon}/c$ and $J_k(x)$ is the Bessel function of integer order. The case $\varepsilon = 1$ of these formulae corresponds to the synchrotron radiation in vacuum (see, e.g., [9,10]).

In [11–13] (see also [14,15]) the following expression was derived:

$$N_k(\text{ball};\mathrm{v},x,\varepsilon_b)=\frac{2N_0}{k}\sum_{s=0}^{\infty}(\,|\,a_{kE}(s)\,|^2+|\,a_{kH}(s)\,|^2) \tag{6}$$

for the number of quanta emitted by the electron during one revolution around a dielectric ball. In this case the angular distribution of the number of emitted quanta is determined by the equation

$$n_k(\theta)=\frac{16\pi^2N_0}{k}\sin\theta\cdot\left|\sum_{s=0}^{\infty}(-1)^s[a_{kE}(s)\vec{X}^{(2)}_{k+2s,k}(\theta,0)+i\cdot a_{kH}(s)\,\vec{X}^{(3)}_{k+2s+1,k}(\theta,0)]\right|^2 \tag{7}$$

where $\vec{X}^{(\mu)}_{lm}$ are spherical vectors of electric ($\mu=2$) and magnetic ($\mu=3$) types, $x=r_b/r_e<1$ and

$$a_{kE}(s)=kb_l(E)P_l^k(0)\sqrt{\frac{(l-k)!}{l(l+1)(2l+1)(l+k)!}},\qquad l=k+2s$$

$$a_{kH}(s)=b_l(H)\sqrt{\frac{(2l+1)(l-k)!}{l(l+1)(l+k)!}}\left.\frac{dP_l^k(y)}{dy}\right|_{y=0},\qquad l=k+2s+1 \tag{8}$$

are dimensionless amplitudes describing the contributions of electric (E) and magnetic (H) type multipoles respectively, $P_l^k(y)$ are the associated Legendre polynomials and $b_l(E)$, $b_l(H)$ are the following factors depending on k,v,x and ε_b:

$$b_l(E)=(l+1)b_{l-1}(H)-lb_{l+1}(H)+x^{-2}(1-\varepsilon_b)[j_{\underline{l-1}}(xu_b)+j_{\underline{l+1}}(xu_b)][h_{\underline{l-1}}(u)+h_{\underline{l+1}}(u)]\frac{l(l+1)u_bj_l(xu_b)}{lz^l_{l-1}+(l+1)z^l_{l+1}}$$

$$b_l(H)=iu[j_l(u)-h_l(u)\frac{\{j_l(xu_b),j_l(xu)\}_x}{\{j_l(xu_b),h_l(xu)\}_x}],\quad u=k\mathrm{v}/\mathrm{c}\,,\quad u_b=k\mathrm{v}\sqrt{\varepsilon_b}/c \tag{9}$$

Here $h_l(y)=j_l(y)+i\mathrm{n}_l(y)$ and $j_l(y)$, $\mathrm{n}_l(y)$ are spherical Bessel and Neumann functions respectively. In (9) we used the following notations:

$$\{a(x\alpha),\ b(x\beta)\}_x\equiv a\frac{\partial b}{\partial x}-\frac{\partial a}{\partial x}b,\ f_{\underline{l}}(x)\equiv f_l(x)/\{j_l(xu_b),h_l(xu)\}_x$$

$$z^l_\nu\equiv\frac{uj_\nu(xu_b)h_l(xu)\varepsilon_b-u_bj_l(xu_b)h_\nu(xu)}{uj_\nu(xu_b)h_l(xu)-u_bj_l(xu_b)h_\nu(xu)} \tag{10}$$

In the absence of dielectric ball ($\varepsilon_b=1$) the calculations by means of our formulae (6), (7) give the same results as those obtained using the well–known synchrotron radiation theory formulae (4), (5) where $\varepsilon=1$.

The simple analytical function $\varepsilon_b(\omega)$ often used to describe the dispersion law for the substance of conductive ball has the form

$$\varepsilon_b(\omega)=\varepsilon_0-\frac{\omega_p^2}{\omega^2+i\gamma\omega}=\varepsilon_b'(\omega)+i\varepsilon_b''(\omega) \tag{11}$$

(the generalized Drude–Lorentz–Sommerfeld formula). This expression satisfactorily describes the dielectric function of noble metals. For example, for gold [16]

$$\varepsilon_0^{Au}=9.84,\ \hbar\omega_p^{Au}=9.01eV,\quad \hbar\gamma^{Au}=0.072eV \tag{12}$$

The effective parameter $\varepsilon_0>1$ describes the contribution of bound electrons, ω_p is the effective bulk plasma frequency which is associated with effective concentration of free electrons, γ is the phenomenological damping constant of the electron motion.

We will consider electromagnetic oscillations in the frequency range for which

$$\varepsilon_b'(\omega)<0 \tag{13}$$

In this case, the generated electromagnetic oscillations inside the ball must be localized.

3. Numerical results in the gigahertz frequency range

We assumed that (a) the ball is made of a dielectric with a negligible mixture of gold, so that the plasma frequency of the free charge carriers is

$$\omega_p = 3\cdot 10^{10}\, Hz \tag{14}$$

($\omega_p^{Au} = 1.4\cdot 10^{16}\, Hz$). In this case, (b) the dielectric should have a weak dispersion and should absorb light slightly in the gigahertz (GHz) frequency range. For this purpose melted quartz can be used with the dielectric permittivity of [17]

$$\varepsilon_{SiO_2} = 3.78(1+0.0001i) \tag{15}$$

in the mentioned frequency range. The parameter ε_0 in (11) we identified by ε_{SiO_2} because of the small concentration of gold in the substance of the ball. In numerical calculations, two estimated values of parameter $\gamma/\omega_p = 1/125; 1/500$ have been used, where $1/125 \approx \gamma^{Au}/\omega_p^{Au}$ (the ball is entirely made of gold).

Thus, the dielectric function $\varepsilon_b(\omega)$ was calculated from formula (11) with the following values of the parameters

$$\varepsilon_0 \approx \varepsilon_{SiO_2}, \qquad \omega_p = 3\cdot 10^{10}\, Hz, \qquad \gamma/\omega_p = 1/125; 1/500 \tag{16}$$

The results of numerical calculations are shown in Figs. 2–5.

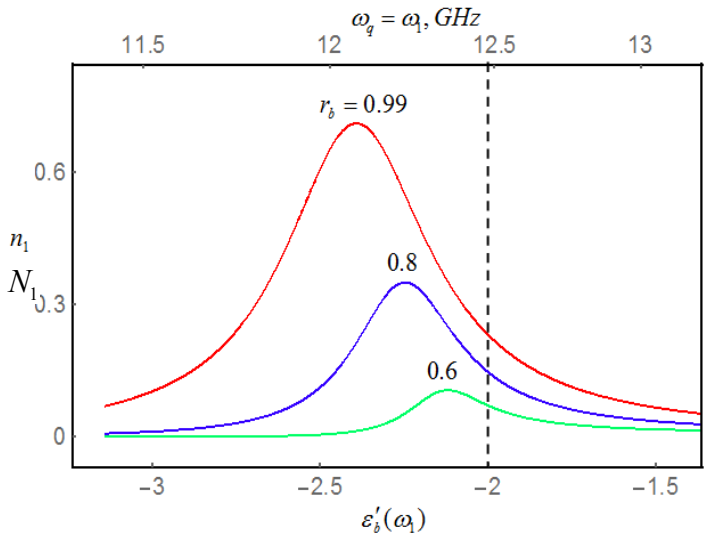

Fig.2. The number of quanta of the electromagnetic field N_1 emitted by the electron at the first harmonic during its one revolution about the conductive ball. Along the axis of abscissa (a) the values of $\omega_q = \omega_1$ (the upper part of the figure) and (b) the values of the real part $\varepsilon_b'(\omega_1)$ of the dielectric constant of the ball (the lower part of the figure) are plotted. The radius of the electron orbit is $r_q = 1$ cm, $\gamma/\omega_p = 1/125$. Near the curves, the values of radius of the ball are indicated

Comparing the course of the curves with $r_b =$ 0.99, 0.8 and 0.6 cm in Fig. 2, we arrive at the following conclusions:

1) The electron generates very intense radiation ($N_1 >> e^2/c\hbar$) if it rotates about a conductive ball at a certain (resonant) frequencies;
2) The resonant frequency ω_q^{res} with which an electron rotates about a conductive ball depends on the ball radius r_b;
3) As the radius of the conductive ball r_b (a) decreases, the maximum of the function N_1 decreases rapidly and (b) the value of the real part of the dielectric function of the ball ε_b' corresponding to this maximum tends to –2.

In Fig.3 the dependence of angular distribution of the number of electromagnetic field quanta n_1 generated by the electron during its one rotation around the ball, on the rotation cyclic frequency ω_q is presented.

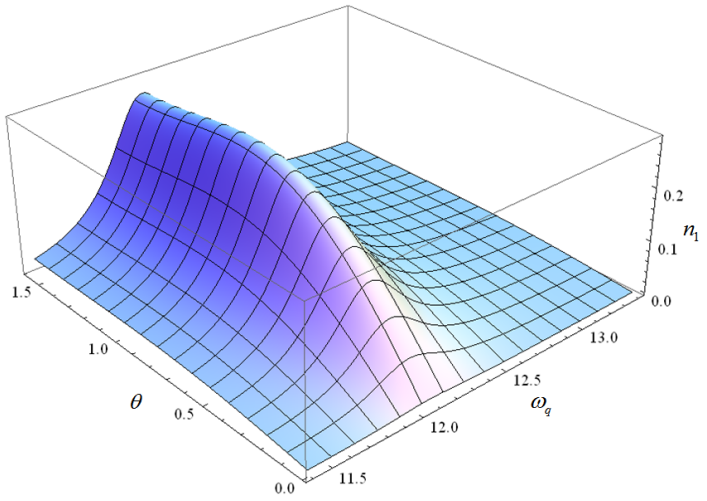

Fig.3. The angular distribution of the number of electromagnetic field quanta n_1 generated by the electron at the first harmonic (during its one rotation around the ball) as a function of rotation cyclic frequency ω_q

It can be seen from Fig.3 that the radiation intensity is just about evenly distributed in the region $\pi/4 < \theta \le \pi/2$ and tends to zero at $\theta \to 0$.

Similar numerical calculations have been done for the second harmonic and for $\gamma/\omega_p = 1/500$. The results are presented in Figs. 4,5.

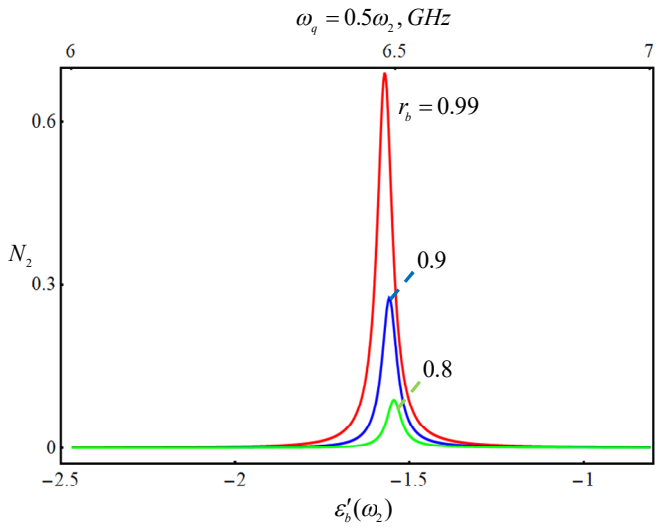

Fig. 4. The same as in Fig.2 for the 2–nd harmonic, $\gamma/\omega_p = 1/500$

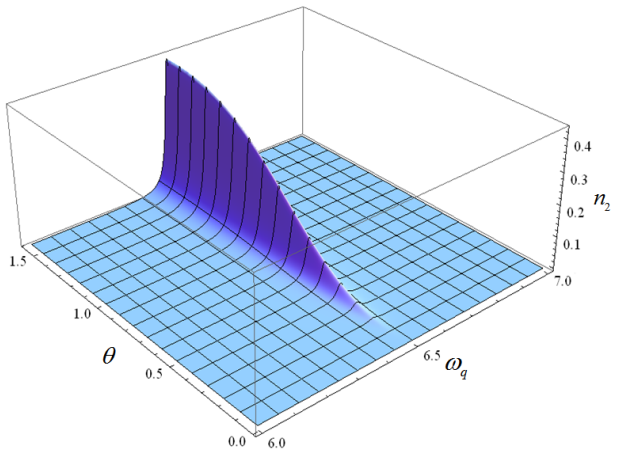

Fig. 5. The same as in Fig.3 for the 2–nd harmonic, $\gamma/\omega_p = 1/500$

Comparing Figs.4;5 with Figs.2;3, we arrive at the following conclusions:

4) For the second harmonic, the peaks are significantly narrower and at decreasing ball radius r_b, the maximum of the function N_2 decreases more rapidly (Fig.4).

5) The angular density of radiation intensity for the 2–nd harmonic is maximal for $\theta = \pi/2$ and rapidly tends to zero at $\theta \to 0$.

4. Conclusions

The angular distribution of the intensive radiation of a charged particle uniformly rotating around a conductive ball, in its equatorial plane has been investigated, taking into account the dispersion of electromagnetic waves inside a conductive ball. It is shown that

1. Charged particle can generate powerful radiation if revolves around a conductive ball at a specific resonant frequency. In [4] it was shown that generation of powerful radiation is due to the fact that at a certain (resonant) particle rotation frequency, localized oscillations of a high–amplitude electromagnetic field (Surface Plasma Waves (SPW)) can be generated inside the ball. Herewith, at large distances from the trajectory of the particle, these localized oscillations are accompanied by intense radiation, which is many times more intense than the analogous radiation in the case when the ball is absent.

2. The angular density of this “resonant” radiation intensity is maximal for $\theta \cong \pi / 2$ and tends to zero at $\theta \to 0$.

3. The linear dimensions of the resonators for SPW may be many times smaller than the linear dimensions of the cavities for the bulk electromagnetic waves. This fact may be used to develop powerful sources of electromagnetic radiation of small sizes.

Acknowledgments

The work was supported by the RA Committee of Science, in the frames of the research project №18T–1C397.

References.

1. Garibian G.M., Yan Shi, X–Ray Transition Radiation, AN Arm. SSR Press, Yerevan (1983) (in Russian).
2. Ginzburg V.L., Tsytovich V.N., Transition Radiation and Transition Scattering, Adam Hilger, Bristol (1990).
3. Magomedov M.R., Izv. Akad. Nauk Arm. SSR, Fiz., **4**, 271 (1969) (in Russian).
4. Mkrtchyan A.H., Grigoryan L.Sh., Khachatryan H.F., Grigoryan M.L., Sargsyan A.V., Resource–Efficient Technologies, **3**, 1 (2018).
5. Torabi M., Shokri B., Physics of Plasmas, **24**, 013114 (2017).
6. Grigoryan L.Sh., Saharian A.A., Khachatryan H.F., Grigoryan M.L., Sargsyan A.V., Petrosyan T.A. XIII International Symposium “Radiation from Relativistic Electrons in periodic Structures, September 16–20, Belgorod, Russia, Book of abstracts, p.45 (2019).
7. Zrelov V.P., Vavilov–Cherenkov Radiation and its Applications in High Energy Physics, Atomizdat, Moscow (1968) (in Russian).
8. Tsytovich V.N., Westnik MGU, **11,** 27 (1951) (in Russian).
9. Ternov I.M., Mikhailin V.V., Khalilov V.R., Synchrotron Radiation and its Applications, Harwood Academic, Amsterdam (1985).
10. Sokolov A.A, Ternov I.M., Radiation from Relativistic Electron, ATP, New York (1986).
11. Arzumanyan S.R., Grigoryan L.Sh., Saharian A.A., Izv. Nats. Akad. Nauk Arm., Fiz. (Engl. Transl.: J. Contemp. Phys.), **30,** 99 (1995).
12. Arzumanyan S.R, Grigoryan L.Sh., Saharian A.A., Kotanjian Kh.V., Izv. Nats. Akad. Nauk Arm., Fiz. (Engl. Transl.: J. Contemp. Phys.), **30**, 106 (1995).
13. Grigoryan L.Sh, Khachatryan H.F., Arzumanyan S.R., Izv. Nats. Akad. Nauk Arm., Fiz. (Engl. Transl.: J. Contemp. Phys.), **33,** 267 (1998).
14. Grigoryan L.Sh, Khachatryan H.F, Arzumanyan S.R., Izv. Nats. Akad. Nauk Arm., Fiz. (Engl. Transl.: J. Contemp. Phys.), **37** 327 (2002).
15. Grigoryan L.Sh., Khachatryan H.F., Arzumanyan, S.R., Grigoryan, M.L., Nucl. Instr. and Meth., B **252**, 50 (2006).
16. Kolwas K., Derkachova A.J., Quant. Spectrosc. & Radiat. Transfer., **114,** 45 (2013).
17. Voronkova E.M., Grechushnikov B.N., Distler G.I., Petrov I.P., Optical Materials for Infrared Technology, Nauka, Moscow (1965) (in Russian).

Acoustoplasma State of Matter

A.R. Mkrtchyan[1,2], A.S. Abrahamyan[1*]

[1]Institute of Applied Problems of Physics NAS RA
25 Hr. Nersissian Str., Yerevan, Republic of Armenia, 0014
[2]National Research Tomsk Polytechnic University
30 Lenin Avenue, Tomsk, Russian Federation, 634050

Abstract: *In our experiments, it was shown that the modulation of the discharge by the current, which contains a direct and variable component, leads to the transition of the plasma to a new state, which was called acoustoplasmic. In this new state, many parameters of acoustoplasma differ from the parameters of the plasma when it is supplied with direct current.*

In the cold plasma of the positive glow discharge column, the electron concentration is determined by the parameters of the external circuit and the modulation of the discharge current.

The modulation of the electron concentration leads not only to the modulation of the level populations, but also to the disturbance of the relative equilibrium of the populations. Those, possible inversion of the populations of individual states, which will lead to the appearance of anomalously strong lines in the emission spectra.

In a non–equilibriumplasma, due to the multi–level energy structure of atoms and molecules, there are dozens of mutually transforming neutral components with different levels of excitation. This property generates various phase transitions (including cascade ones) and selection of some separate states of atoms (including optical transitions).

From this chaos of states, acoustoplasmic structures are formed.

The report presents the experimentally obtained results of studies of acoustoplasma states. All the diversity of the research is presented in the form of a nomogram.

1. Introduction

The concept proposed more than forty years ago by Academician of the National Academy of Sciences of Armenia Alpik Mkrtchyan is as follows: acoustic fields lead to a deformation of the characteristics of the medium and a small amount of acoustic energy due to the collective action of many particles can lead to a significant change in the parameters of the medium and the parameters of radiation with an energy that is much more than the energy of an individual phonon.

In a plasma, an acoustic disturbance forms acoustic parameter superlattices.Plasma with acoustic vibrations excited in it allows this approach to be treated as a new medium – ACOUSTOPLASMA.

The parameters of the acoustoplasma (hereinafter AP) can significantly differ from the parameters of the plasma without acoustic disturbance (hereinafter OP – ordinary plasma). In particular, the behavior of some of the parameters of the AP becomes similar to the behavior of the parameters of a condensed medium.

Most of the experiments cited correspond to the AP obtained by modulating the discharge current in a long cylindrical tube.Those, the length of the tube is much larger than the diameter.Modulation of the discharge current leads to the generation of an acoustic signal in the

***E – mail:** *arbel11@mail.ru*

tube, which interacts with the plasma created by the same discharge current.In addition, it should be taken into account that the discharge tube itself is an acoustic resonator and acoustic modes are possible in it, leading to the appearance of superlattices of parameters [1–4].

Figure 1 shows a diagram of the state of the medium and the main phase transitions (PT).PT can also be in the solid state, for example, topological [5, 6]. First, we consider only the basic thermodynamic transitions.

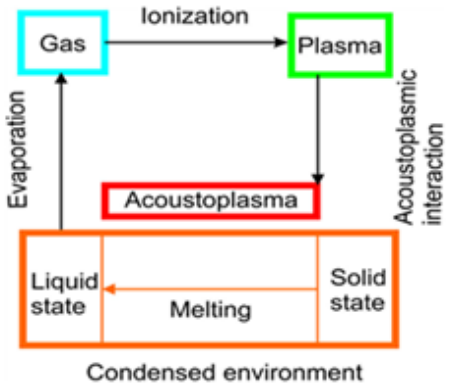

Fig. 1. General diagram of the state of the medium and the main phase transitions (PT)

The first PT is melting. During melting, there can also be various cascade PT, but only the main thermodynamic can be represented. The second PT is evaporation, the transition from liquid to gas. The third PT is ionization, the transition from gas to plasma.

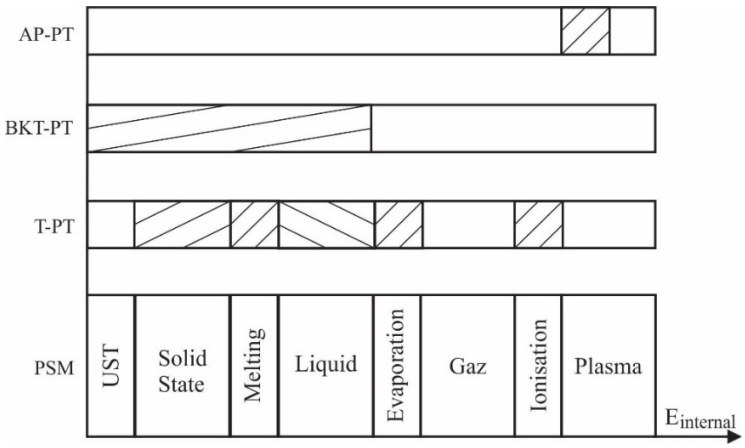

Fig. 2. The hierarchy of PT. The regions of existence of PT are shaded as slanting lines. PSM – the phase state of the matter, UST – ultra small temperatures, T–PT – thermodynamic phase transitions, BKT–PT – topological phase transitions, AP–PT – acoustoplasma phase transitions

The interaction of acoustic waves with OP creates the state of AP. Standing acoustic waves form parameter gratings, long–range order appears and the acoustoplasma medium becomes similar to a condensed medium. We get the fourth PT – the acoustoplasmic one, the transition from plasma without acoustic disturbance to the acoustoplasma state (OP–AP). Then there are various PT in acoustoplasma. Those, it is possible PT of the OP–AP, and between various acoustoplasmic states.

Fig. 2 shows a diagram of PT, which shows in which areas there are thermodynamic PT and non–thermodynamic PT.

The abscissa represents the values of the internal energy of the substance in relative units. On the ordinate axis: PSM – the phase state of the substance in the standard representation, UST – ultra small temperatures, T–PT – thermodynamic phase transitions, BKT–PT – topological phase transitions (Nobel Prize in 2016), Berezinskiy–Kosterlitz–Thouless phase transitions [5, 6], AP–PT – acoustoplasma phase transitions [7].

In Fig. 2, it is noted that PT are also possible in solids and liquids, and the regions of existence of topological and acoustoplasma PT are also noted.

Both AP and OP are self–consistent environments. Adding new control parameters (frequency and depth of modulation of the discharge current, as well as the shape of its variable component) allows you to control almost all the parameters of the AP [3, 4].The depth of modulation is the ratio of the amplitude of the variable component to the value of the constant component.

This allows you to implement new types of devices based on acoustoplasma interaction and to upgrade existing devices.

It is possible that in the future, AP will indeed be called the 5th state of matter. The fact is that the behavior of some of the parameters of the AP is similar to the behavior of a condensed medium. A further increase in energy in the AP also leads to quasi–melting of AP structures (destruction of long–range order) and a return to gas. Even more energy will lead to complete ionization. Those, as if the second coil of a spiral for Fig. 1. Thus, AP can exist only in the region of low–temperature plasma.

2. Generally

Consider how AP differs from OP:

1. In the AP, parameter jumps and PT are possible, so the question arises about the appropriateness of using the continuity formulas and the small increment method that are used for OP;
2. Even the OP, as a self–consistent medium, is non–linear, but some equations can be linearized. AP is a fundamentally non–linear medium and linearization will always lead to errors;
3. A direct current discharge creates a stationary plasma, which manages to reach its equilibrium state.

A high–frequency discharge creates a dynamic plasma in which the characteristic times << of the time of ionization–recombination processes. Quasi–stationary low–frequency discharge creates an AP. A relatively slow restructuring of the regimes leads to the fact that the equilibrium point is restored, but in different coordinate parameters. This is the meaning of PT from the state of OP to state of AP. This is a necessary but not sufficient condition for the existence of the AP.

4. The Maxwell distribution is valid only for a homogeneous and isotropic medium. In OP the Maxwell distribution can be applied with reservations. In AP, due to the strongest anisotropy of the acoustic field in the plasma, the Maxwell distribution is unfair.
5. The OP usually considers pair collisions. In a highly nonequilibrium plasma, which is an AP, collective effects far exceed the effect of pair collisions. Multiple collisions are treated as waves in the plasma.

6. In both OP and AP, ionization nonlinearly depends on concentration, but laws can be different due to different relaxation times and inertia of processes.
7. At times > the period of plasma oscillations, the Debye screening has time to establish. But with low–frequency modulation, the Debye screening receives low–frequency modulation along the screening radius.
8. At low modulation frequencies, ~ 0.1 kHz, almost all processes are quasi–stationary. At frequencies > 0.5–1 kHz, standing acoustic waves can occur along the length of the discharge tube and the mechanical displacement is different and does not simultaneously change in phase at all points of the discharge tube. Thus, in the AP, a situation arises when there is quasistationarity in electrical parameters and not in terms of the acoustic parameters of the tube.
9. In AP, the mobility of ions depends more on mechanical vibrations than on modulation of the electric field strength.
10. Instead of the forces of van der Waals in the OP and AP, the main role is played by the forces of Coulomb. This can lead to the consideration of Coulomb acoustics and Coulomb thermodynamics.
11. The non–isotropy velocity in the OP leads to instability. AP discharge stabilizes some instabilities since reduces fluctuations of non–isotropy.
12. In the positive column of an acoustoplasma glow discharge, current modulation leads to modulation of the electron concentration. Collisions of electrons with atoms in this case lead not only to modulation of the level populations, but also to a violation of the relative equilibrium of the populations. Those, inversion of the populations of individual states is possible, which will lead to the appearance of abnormally strong lines in the emission spectra.
13. In a nonequilibrium low–temperature AP, due to the multilevel energy structure of atoms and molecules, there are dozens of mutually transforming neutral components with different levels of excitation. This property gives rise to various phase transitions (including cascade) and the selection of some individual states of atoms (including optical transitions).
14. In a conventional mechanical system, forced oscillations of large amplitude with a frequency different from the natural frequency of the system can lead to the suppression of own vibrations or to the complex form of their interaction. In the case of AP, an external force can provoke oscillations at other frequencies than the exciting one, and further parametric self–amplification can support these oscillations.
15. In our experiments, acoustic fields in the discharge tube were formed upon modulation of the discharge current, which leads to modulation of heat generation and momentum simultaneously along the entire axis of the discharge. An acoustic wave is excited that is orthogonal to the axis of the discharge. In the general case, this is a spiral wave, but if the modulation frequency is lower than the frequency of existence of spiral waves, then only a longitudinal acoustic wave is excited [8].Thus, in a tube with an AP discharge, acoustic fields orthogonal to the axis of the discharge are much stronger than the acoustic fields along the discharge. This leads to the strongest anisotropy of acoustic fields in the AP during modulation of the discharge current.

Of all this chaos of states, self–consistency of processes in AP leads to the formation of acoustoplasma structures.

Below are the experimental results that were obtained under the direction of A.R. Mkrtchyan at the Laboratory of Applied Problems of Cold Plasma at the Institute of Applied Problems of Physics over the past 22 years.

The whole variety of studies (40 phenomena, 80 experiments) is presented in the form of a diagram in Fig. 3.

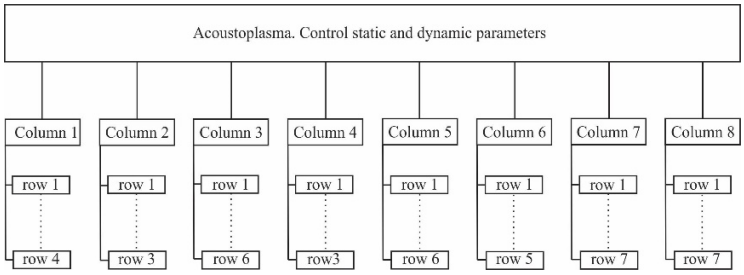

Fig. 3. Diagram of studies of the control of parameters and processes of acoustoplasma states in a laboratory

For almost every element of this diagram, there is at least one publication.

In this diagram, one more column could be added for magnetized acoustoplasma. But work in this area has begun recently.

Column 1. Change of geometric parameters (sizes and trajectories).

row

1- changing the trajectory of discharges;
2- changing of contraction;
3- acoustic turbulence;
4- soliton stopping;

Column 2. Change of optical parameters.

1- integrated brightness;
2- change of spectrum lines and bands;
3- generation of strong spectrum lines;

Column 3. Change of electrical parameters.

1- direct component of voltage and current;
2- alternate component of voltage and current;
3- phase shift between voltage and current;
4- resistance and conductivity;
5- distribution of charges in space and time;
6- change in time RCL–parameters of an equivalent circuit modeling the discharge;

Column 4. Change of acoustic parameters in the acoustoplasma medium.

1- amplification and attenuation of sound;
2- generation of sound;
3- change the speed of sound;

Column 5. Change the thermodynamic parameters.

1- temperature;
2- thermodynamic phase transition;
3- non–thermodynamic phase transition;
4- speed control of the plasma components;
5- control of acoustic streaming;

1. 6– memory relaxation;

Column 6. Change in energy parameters.

1- efficiency;
2- energyinvestigation;
3- energy capacity;
4- luminous efficiency of light sources;
5- stabilization and variation of lasers and light sources;

Column 7. Implementation of new types of devices and processes based on acoustoplasma.

1- development and manufacture of measuring equipment and modernization of the existing one;
2- new power sources for acoustoplasma devices;
3- acoustoplasma light sources;
4- acoustoplasma lasers;
5- acoustoplasma magnetrons;
6- acoustoplasma accelerators;
7- acoustoplasma controlling in plasma chemistry;

Column 8. Methods of processing the results that were used in the measurements.

1- creation of an online laboratory;
2- creation of a multi–channel measuring complex;
3- waveform processing techniques;
4- use of catastrophe theory to determine the presence of phase transitions and catastrophic parameter jumps;5– the use of catastrophe theory in solving incorrectly posed inverse problems;
5- the use of rectangular matrices containing several columns (according to the number of measured parameters) and 120 rows for working with the obtained oscillograms;
6- new software products;

According to the results of the studies, more than 50 works were published, and 7 PhD theses were defended by young laboratory staff and graduate students from 2005 to 2014. A detailed description of all the results obtained far exceeds the possibility of publication in this collection. A detailed description of all the results obtained far exceeds the possibility of publication in this proceedings.

Some of the results obtained on the basis of the fundamental research are given below:

1. A video clip has been created that clearly demonstrates the ability to control plasma using acoustic fields.
2. Designed and manufactured specialized power supplies for gas–discharge devices for operation in the AP mode.
3. Acoustoplasma fluorescent lamps with high light efficiency have been developed. In 2009, Philips, with its Tornado lamp, achieved a luminous efficiency of 90 Lm /W. In our laboratory, in a small series (several hundred lamps) in 1999, a luminous efficiency of 100 Lm/W was obtained. (Luminous efficiency is considered by the total energy consumption of the actual lamp bulb and electronic power circuit).At the same time, the advantage of the bispiral design of fluorescent lamps during their operation in the AP mode was substantiated. Today, almost all fluorescent lamps operate in AP mode, but no one takes this into account.

4. The possibility of increasing the power of a serial CO_2 laser during transition to the acoustoplasma mode instead of supplying with direct current (by 25–30%) is shown. When developing special AP lasers, the energy input into the discharge can be increased several fold and the efficiency of converting the electric pump power to optical power is almost 2 times higher.
5. The effect of one laser module on another in multimodular structures is investigated. It is shown that it is possible to control the magnitude of the mutual influence of the modules.
6. It is shown that in the AP mode of discharge power, it is necessary to measure the current at the input to the anode of the discharge tube and at the exit from the cathode of the discharge tube at the same time. If the current is measured at only one point, then the average values will be correct, and the dynamics of the current will be erroneous. The dynamics of charge changes in the tube will not be taken into account.
7. Designed, manufactured and patented acoustoplasma magnetrons for sputtering.
8. It was experimentally shown that after switching off the external acoustic exposure (only the direct component of the current from the source remains), the AP remains, i.e. keeps memory of his condition. It retains a small modulation of the current, although there is no external modulation of the current. After a certain time (relaxation time, which can reach several minutes), the AP returns to the OP state, i.e. current modulation disappears completely.
9. It has been experimentally shown that in the energy intensity of AP significantly (hundreds of times) exceeds the energy intensity of OP. When the acoustoplasma state is destroyed, this energy can be released in the form of an explosion.
10. The possibility of the existence of phase transitions in the states of various parameters in the AP is shown experimentally. In particular, in some parameters of the AP, the medium after the phase transition becomes similar to a condensed medium.
11. The possibility of accelerating charged particles in an AP discharge is experimentally shown. A mechanism is proposed for the formation of negative conductivity due to acceleration.
12. It has been experimentally shown that during the modulation period in the AP not only the magnitude of the negative charge in the tube changes, but also the electric capacity of the discharge. Those, during the period of modulation in the AP discharge, the electroneutrality of the positive column is almost always violated.
13. The possibility of acoustically controlling the movement of the current – voltage characteristics of the AP discharge along the axes of current and voltage and changing its shape is experimentally shown.
14. The possibility of a significant (tens and hundreds of times) increase in the intensity of individual spectral lines in the AP regime was shown experimentally in molecular gases. Moreover, these lines are highly monochromatic. Monochromatic sources are now being developed on these strong lines.
15. The dependence of the generated acoustic pressure in the AP on the magnitude of the discharge current, modulation frequency, pressure and type of gas or gas mixture is investigated. A convenient empirical formula is obtained for determining the magnitude of the generated acoustic pressure from the "specific generated acoustic pressure". For

different gases and gas mixtures, the specific generated acoustic pressures (3–23 Pa/A torr) were obtained at the frequency of the first acoustic resonance of the discharge tube. With increasing frequency of modulation of the discharge current, the value of the generated acoustic pressure increases.

16. In AP, both amplification and attenuation of sound are possible. Acoustic amplifiers and acoustic screens that attenuate sound can be created on this principle.
17. It is experimentally shown that the AP discharge can be modeled by a parallel oscillatory circuit. One branch is represented by resistance, or resistance, and part of the inductance the other branch is series–connected by capacitance, inductance and resistance. The resonant frequency of the AP discharge does not coincide either with the lower acoustic resonances of the discharge tube or with the electric resonance of the equivalent circuit.
18. A technique has been developed to study the possibility of phase transitions and jumps in the parameters of an AP discharge using the mathematical theory of catastrophes and solving incorrectly posed inverse problems.

This work was carried out using partly the grant Armenia–Belarus (AB–10, 2011), in a small share by grant ISTC A–196–2.

References.

1. MkrtchyanA.R., GalechyanG.A., DivanyanE.G.Izvestia of AN Arm. SSR, Phisika, v.22, pp.231–235, 1987. (In Russian).
2. Galechyan G.A., Mkrtchyan A.R. Acoustoplasma.Apaga, Yerevan, 338p.,2005. (In Russian).
3. Mkrtchyan A.R., Bagdasaryan A.S., Abrahamyan A.S., Kostanyan R.B., Mkrtchyan A.H. Management by the parameters of gas–discharge low–temperature plasma through the acoustic vibrations. Lecture of handing of prize of the name A.M. Prokhorov, 99p.,2009 (In Russian).
4. Mkrtchyan A.R., Mkrtchyan A.H., Abrahamyan A.S. Acoustoplasma is a new state of plasmas. VII Int.Conf.Plasma Phys.and Plasma Technology, PPPT–7, Minsk, Belarus, 17–21 Sept.2012, Proc., v.1, pp.3–5, 2012.
5. Berezinskiy V.L. The destruction of the long–range order in one–dimensional and two–dimensional systems with a countinuous symmetry group. I. Classic systems. Soviet physics JETP, v.59, no.3, pp.493–500, 1971.
6. Kosterlitz J.M., Thouless D.J. J.Phys., C, 6, p.1181, 1973.
7. Abrahamyan A.S., Chilingaryan R.Yu., Sahakyan Q.G. Catastrophe theory and phase transitions study in acoustoplasma. VII Int.Conf.Plasma Phys.and Plasma Technology, PPPT–7, Minsk, Belarus, 17–21 Sept. 2012, Proc., v.1, pp.197–199, 2012.
8. Skudrzyk E. The Foundation of Acoustic. Basic Mathematics and Basic Acoustics. N.Y.,1971.

Minimagnetrons and Their Supply

A.S. Abrahamyan*, A.H. Mkrtchyan, R.Yu. Chilingaryan, A.S. Hakobyan

Institute of Applied Problems of Physics NAS of the Republic of Armenia,
25 Hrachya Nersissian Str., Yerevan, Republic of Armenia, 0014

Abstract: *Today, magnetron sputtering installations use electrical power in kW or even hundreds of kW. Uniform deposition, as a rule, is achieved by significant removal of the substrate from the sprayed cathode. But as the distance between the sputtered cathode and the substrate increases, the degree of clusterization of the particles increases, i.e. on the surface of the substrate sit clusters, rather than individual atoms of the sprayed material. This is not always desirable.*

In addition, difficulties arise in the deposition of multicomponent films. One of the ways to solve this problem is to use partitioned cathodes, when inserts are made from other sprayed materials into the main cathode material. However, the heterogeneity of the cathode leads to instabilities in the burning of the discharge and the associated defect in the deposited layers.

It is more reasonable to use a mosaic of mini–magnetrons, each of which has its own independent power supply, instead of a large–sized magnetron cathode.

The report presents the design of minimagnetrons and experimental research in this area.

1. Introduction

Magnetron ion sputtering systems are modern high–performance atomization systems. One of the first patents for a magnetron atomizer was obtained in the USA in 1988 [1].

This is a new technique on which modern new technologies are based in microelectronics, nanoindustry, plasma chemistry and other areas of science and technology in which thin–film coatings are used.

Today, magnetron sputtering plants use electric power units and even hundreds of kW. The diameter of the sprayed cathodes is from 5 to 40 cm. Naturally, water cooling of both the sprayed cathode and the substrate for sputtering is required. The sputtering rate can reach 15nm / s or more.

2. Experiments and results

A single magnetron is a structure that is shown in Fig. 1. The principle of operation of the magnetron is devoted to a large number of works [2–7].

A is the magnetron magnet system. Depending on the magnetic field strength, the magnetron is called unbalanced when the magnetic field lines intersect the anode plane and balanced when the magnetic field lines mainly close in the cathode region. *B* is sprayed cathode, usually cooled. *C* is the luminous region of the plasma torus. In the region of the plasma torus, a negative charge prevails [7]. *D* is the region of the positive column, electrical quasi–neutral. *E* is the magnetron anode.

*E – mail: arbel11@mail.ru

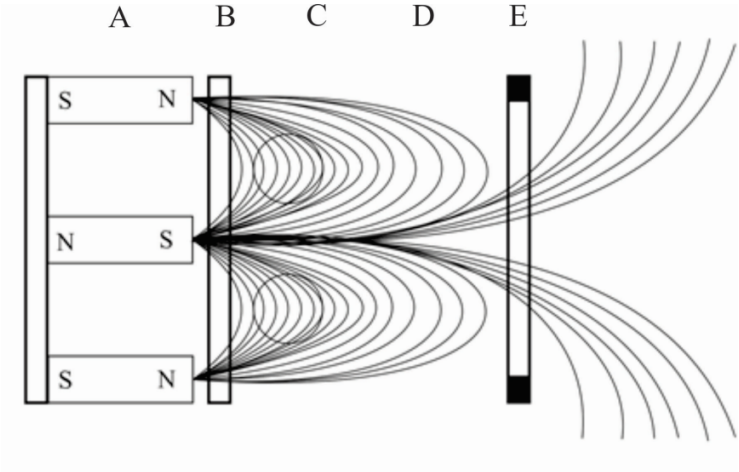

Fig. 1. The scheme of the magnetron for sputtering. *A* is the magnetic system, *B* is the atomized cathode, *C* is the plasma in the form of a ring (torus), *D* is the positive column with magnetic field lines, *E* is the anode

An important feature of the magnetron discharge is the spraying of the cathode material as a result of bombardment by high–energy ions.

During operation of the magnetron, the surface of the anode is contaminated, which requires a periodic shutdown of the spraying process for the cleaning of the anode. A dual magnetron scheme was proposed, in which a separate anode is missed, Fig.2 [8]. Its role is alternately played by the surfaces of two cathodes, combined into a dual structure. Each of the cathodes is contaminated during the time when it works as an anode and is cleaned during the time when it works as a cathode.

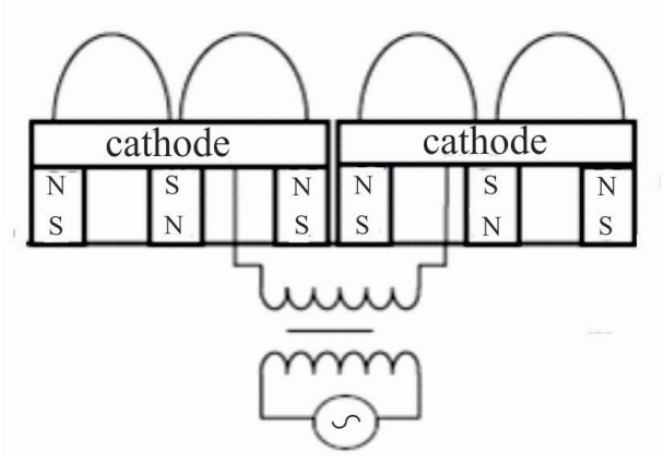

Fig. 2. The dual magnetron system

All of the above magnetrons give a nonuniform deposition. The cathode sputtering diagram taken from [2] is shown in Fig. 3. The uniformity of sputtering is most often achieved by removing the substrates from the sprayed cathode to such a distance that the entire sputtered area is within the range of visible angles of ± 30 – 40° angular degrees. This reduces the sputtering rate and increases the loss of spray material.

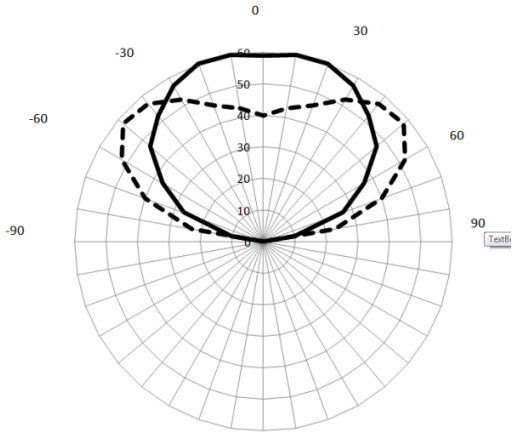

Fig. 3. Sputtering diagram (in polar coordinates). The solid line corresponds to the particle energy of 300 eV, and the dashed one to the energy of 100 eV

Difficulties arise when sputtering multicomponent films. For this, complex cathodes with inserts from different sprayed materials are often used [9]. But each material has its own sputtering speed and this makes it difficult to choose a spraying mode.

Instead of a large magnetron cathode, we propose using a mosaic of minimagnetrons, each of which has its own independent power supply. In this case, for multi–component sputtering on a substrate, different cathode materials can be used for different minimagnetrons, and the possibility of using different sputtering modes makes it possible to obtain films with controlled stoichiometry. In addition, minimagnetrons are easy to combine into dual – paired and even quadrosystems.

Figure 4 shows the developed single minimagnetron with a cathode diameter <45 mm and a plasma torus diameter of 18 mm. The ring–shaped anode had a diameter of 50 mm.

A patent was obtained for the operation of magnetrons in the acoustoplasma mode [10–12].

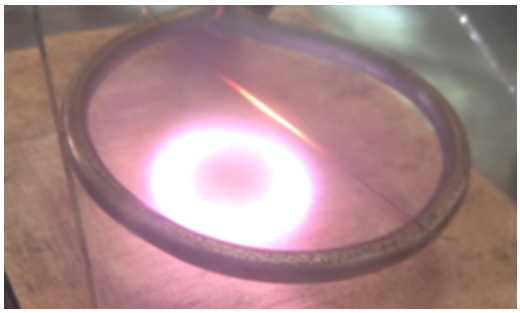

Fig. 4. Single minimagnetron

Due to the small size of the anode ring, the focusing of ions by the anode ring is strongly manifested. The sputtering diagram of such a magnetron is shown in Fig. 5 [12].

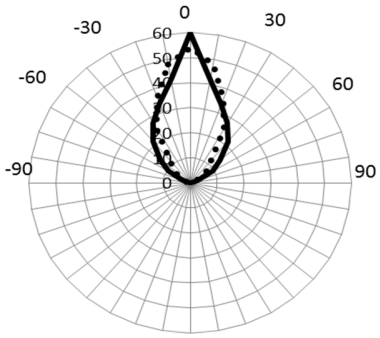

Fig. 5. Sputtering diagram (in polar coordinates). Solid line for acoustoplasma operation; dashed line for direct current. The distance between the cathode and the substrate is 4 cm

As follows from Fig. 5, the sputtering diagram of an individual magnetron has greatly impaired. But the sputtering speed has increased significantly. For a power density applied to the discharge of 90 W/cm^2 (calculated from the area of the plasma torus), the deposition rate of copper at a distance between the cathode and substrate of 4 cm reached 10–13 nm/s. In conventional magnetrons for copper, the deposition rate is 1–2 nm/s [6].

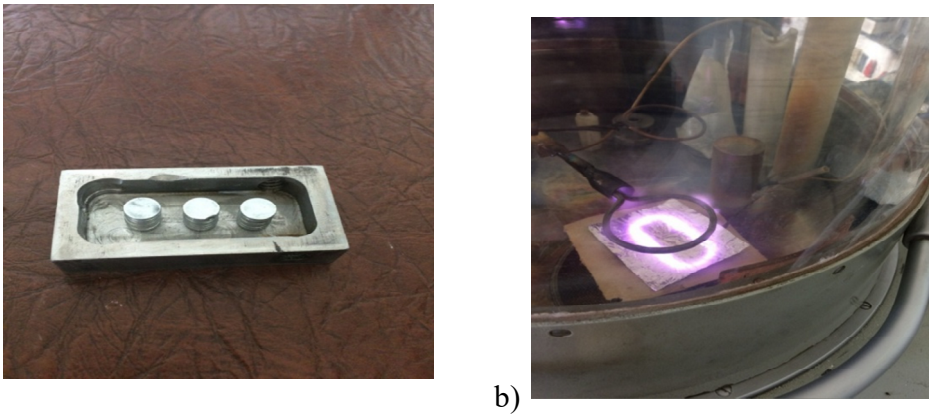

a) b)

Fig. 6. Rectangular planar minimagnetron. a) a picture of the magnetic system; b) a luminous plasma ring in a working magnetron

Figure 6a shows the magnetic system of a rectangular minimagnetron. The external size of a rectangular minimagnetron is 30x60 mm. Three cylindrical permanent magnets with a diameter of 10 mm and a height of 10 mm are visible inside, the distance between the magnetic columns is 5–6 mm. The outer part of the body is made of steel. Fig. 6b shows a working magnetron, the dimensions of the plasma cord are 20x50mm, and the cord width is 5mm. From Fig.6 it can be seen that although the center is not a solid long magnet, but discrete–standing columns, the shape of the plasma cord is the same. This improves the cooling of the magnetic system.

Figure 7 shows an aluminum foil substrate with a deposited layer of copper (Fig. 7a) and (Fig. 7b) a sputtering diagram in rectangular coordinates for a minimagnetron shown in Fig. 4.

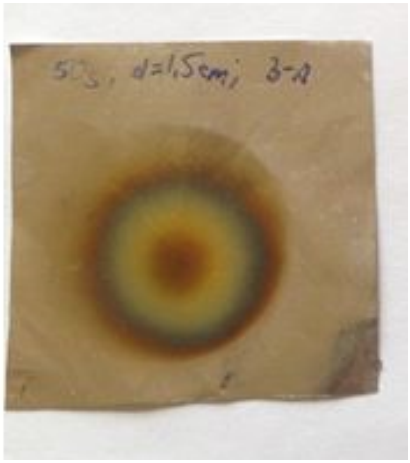

a)

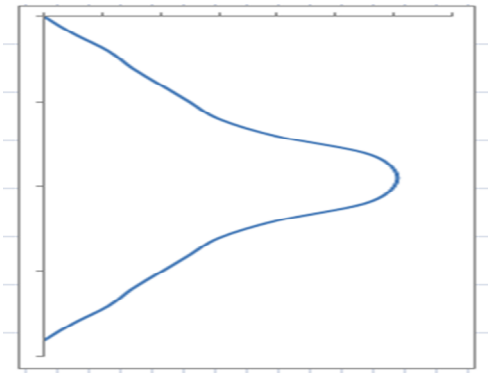

b)

Fig. 7. Suttered substrate (a) and sputtering diagram (b) in rectangular coordinates

As can be seen from Fig. 7, the deposition is nonuniform. But from such minimagnetrons, rectangular or round, you can assemble a block of the required sizes.

Fig. 8 shows how, for a block of 10 minimagnetrons arranged in a line, the uniformity of sputtering improves if each individual magnetron has a sputtering pattern shown in Fig. 7b.

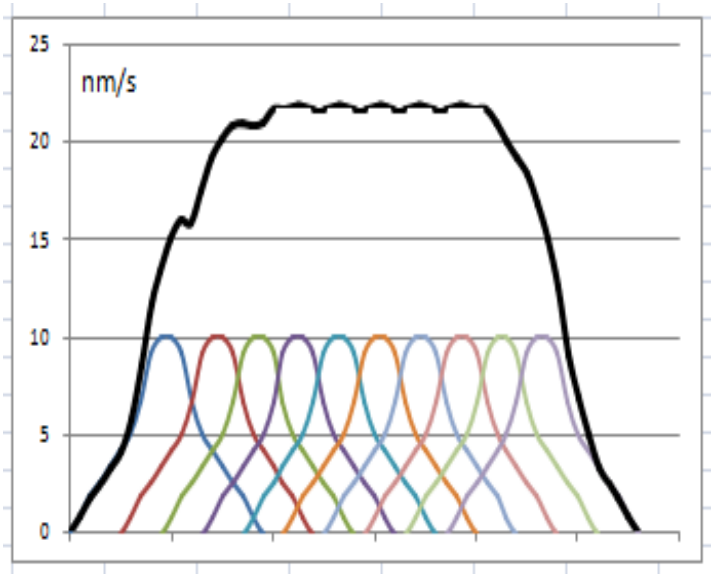

Fig. 8. Uniformity of sputtering for a block of 10 minimagnetrons. The deposition nonuniformity in the middle part can be 1–2%.

In addition, during collective work of minimagnetrons, the deposition rate increases. If for a single minimagnetron the deposition rate was 10 nm/s, then for a team of magnetrons the deposition rate was more than 20 nm/s.

Fig. 9 shows a block of 14 round minimagnetrons, the diameter of each minimagnetron is 12 mm. The diameter of the plasma torus of each of the minimagnetrons is 10 mm. The dimensions of the entire block are 60x80mm. The possibilities of interaction of minimagnetrons with each other, the parameters of magnetic systems, and deposition processes were investigated.

Figure 10a shows the regime when all cathodes have a common power supply and a common anode ring. It can be seen that different minimagnetrons produce plasma rings of different intensities, the operating mode is unstable, intense plasma rings can change their location on the block surface. In Fig. 10b, only 2 neighboring magnetrons work, no power is supplied to the remaining cathodes, even the distance between them is small and the common anode is under potential. A similar regime can be realized in dual magnetrons. In this case, the common anode can be excluded, or left to work in the primary ignition mode.

Fig. 9. Block of round minimagnetrons

a) 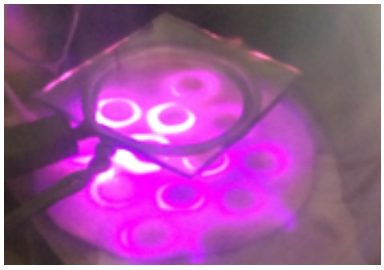 b) 

Fig. 10. Work of assembly of round minimagnetrons. a) all cathodes and anodes have a common power supply, b) power is supplied to two neighboring magnetrons

3. Conclusion

1. When sputtering, instead of one large magnetron, it is proposed to use a system of minimagnetrons located close to each other**.**
2. Choosing the configuration of the block of minimagnetrons, we can obtain uniform deposition over large areas.
3. The minimagnetron assembly can be located relatively close to the sputtered surface, which is important if undesirable clustering occurs at short distances and if it is necessary to reduce the loss of spray material.
4. Thermal loads on each cathode are reduced, which simplifies the cooling system.
5. The possibility of synthesis and sputtering of multicomponent compositions is simplified. different cathodes can be made from different materials.

References.

1. Morrison Jr. Method and apparatus for arc evaporating large area targets. C23C 14/22, US Patent no.4724058.
2. Kashtanov V.P., Smirnov B.M., Hippler R. Magnetron plasma and nanotechnology. *Physics–Uspekhi,* v.177, N5, pp. 573–610, 2007. (In Russian). doi:10.1070/PU2007v050n05ABEH006138
3. Rossnagel S.M. Deposition and redeposition in magnetrons. *J.Vac.Sci. &Technology, A, Surfaces and Films*, v.6, issue 6, November, pp.3049–3054, 1988. doi:10.1116/1.575473.
4. Danilin B.S., Syrchin V.K. Magnetron spray systems. Moscow, Radio and communication, 72p, 1982.
5. Stepanova M., Dew S.K. Estimates of differential sputtering yields for deposition applications. J.Vac.Sci. & Technology A., v.19, no.6, pp.2805–2816, 2001. doi:10.1116/1.1405515
6. Popov V.F., Gorin Yu.N. Processes and installations of electron–ion technology: Textbook for high schools. High school, Moscow, 255p, 1988. (In Russian).
7. Abrahamyan A.S., Mkrtchyan A.H., Chilingaryan R.Yu. Comparison of glow, arc, and magnetron direct current discharges. Resource–Efficient Technologies 2, pp.29–35, 2019. doi:10.18799/24056537/2019/2/237.
8. Struempfel J., Bejster G., Erbkamm W., Rehn S. Sputtering installation with two longitudinally placed magnetrons. C23C 14/34, US Patent no.6361668
9. Glebovskij V.G. Composite target for spraying and method of its production. H01J 37/00; C23C 14/35, RU2392686C1.
10. Mkrtchyan A.H., Mkrtchyan A.R., Abrahamyan A.S., Nalbandyan V.V. The method of acoustoplasma sputtering in vacuum. Patent Armenia, no.3086A.
11. Mkrtchyan A.R., Abrahamyan A.S. Creation of new generation magnetrons based on acoustoplasmic states for surface cleaning and deposition on substrates. *The First Russian Crystallographic Congress*, Moscow, p.177, 2016. (In Russian).
12. Abrahamyan A.S., Mkrtchyan A.H., Nalbandyan V.V., Hovhannisyan H.T., Chilingaryan R.Yu., Hakobyan A.S., Mossoyan P.H. Cleaning and sputtering using planar acoustoplasma magnetron. *Resource–Efficient Technologies,* Tomsk, 3, pp.7–13, 2018. doi:10.18799/24056537/2018/3/197.

New Magnetron Equipment

A.S. Abrahamyan*, A.H. Mkrtchyan, R.Yu. Chilingaryan, H.T. Hovhannisyan, S.A. Mkhitaryan, S.M. Petrosyan

Institute of Applied Problems of Physics NAS of the Republic of Armenia, 25 Hrachya Nersissian Str., Yerevan, Republic of Armenia, 0014

Abstract: *The report present the developed magnetron equipment for the study of sputtering processes and plasma–chemical synthesis of nanoparticles and new materials.*

In the developed equipment, it is possible to simultaneously study up to four different sputtering and synthesis systems, as well as a comparison of different magnetrons (including new ones) under the same conditions in one vacuum volume. The operation of magnetrons is provided with a direct current supply, with high–frequency voltage supply, with a pulse supply and in acoustoplasma mode. The equipment has the possibility to separate the working volume of each of the magnetrons under study from the rest of the vacuum volume.

The possibility of parameters separate control of each of the magnetrons are provided.The diameter of the vacuum chamber is 0.6 m and the volume is ~ 0.15 m^3.

It is envisaged to study systems with solid, liquid and gaseous plasma cathodes.

At the second stage of work, it is supposed to embed the systems for monitoring the thickness of the sprayed layers, ion separator systems, mass spectrometers and other auxiliary devices into the vacuum chamber.

1. Introduction

Today, on many sites, sputtering installations can be found for most of the arising tasks. But most of the proposed installations, as a rule, are designed for a certain range of tasks. The installation under development is intended for research purposes and testing new methods and devices, many of which have not yet been studied, or cannot be carried out using serial equipment.

Today, the installation is in the process of completion, so this publication can be considered as an advance project.

2. Experimental setup

Figure 1 shows the appearance of the installation.

Installation dimensions 900x620x21000mm^3, together with a fully extended lead screw installation height 2500mm. The vacuum bell rises and falls with the spindle (Fig. 2). The inner diameter of the vacuum bell is 500mm, the height is 600mm, the vacuum volume is ~ 0.15m^3.

*E – mail: arbel11@mail.ru

Fig. 1. Appearance of the installation

Fig. 2. The node lifting the vacuum bell

In this installation, in one vacuum volume, 4 independent zones have been created in which up to four different sputtering and synthesis systems can be studied. For example, magnetron, arc and thermal. If necessary, you can transfer the same substrate from one zone to another, performing all the necessary operations in one vacuum cycle.

Each zone has its own systems of gas inlet, pressure control, pumping and control. If necessary, during one vacuum cycle operations, in each zone can be isolated from the others, and at any time this isolation can be removed and the substrate can move from one zone to another.

It is possible to work with single magnetrons, dual ones, quadromagnetrons and blocks of minimagnetrons [1]. The possibility of independent control of each of the magnetrons is provided.

The possibility of working with solid, liquid (including molten) and gaseous vapor–plasma cathodes is provided.

Figure 3 shows the working surface of the lower part of the vacuum chamber. The copper ring on which the rubber seal of the vacuum cap sits is clearly visible. All 4 working areas are visible, they are highlighted by black circles.

Each of the zones contains 4–5 high–voltage inlets for vacuum, rated for voltages up to 20kV and 12 low–voltage inlets. There are also 3 fiber–optic bushings with a diameter of 1mm quartz fiber core. This allows you to enter and output light fluxes of low intensity for spectroscopic control of spraying and powerful light fluxes for processing and forming the necessary structures.

The total number of high–voltage vacuum inlets is 18.

Fig. 3. The working surface of the lower part of the vacuum chamber

In order to make working zones more visible, the central stock with mechanisms for moving the substrates is removed. Creating a good vacuum in the entire vacuum bell volume is difficult and time consuming. Creating a good vacuum in a small area using additional small caps greatly simplifies the task. One of the zones is wearing a small insulating cap. The experiments showed that such a cap made of thin plastic quite well decouples the volume of the small zone and the large vacuum volume.

On the left, the magnetic system of a magnetron with a diameter of 120 mm is visible.

The vacuum system consists of a foreline pump and diffusion pumps made on specially designed magnetrons.

Water cooling of units with low–voltage potential and intra–vacuum oil cooling of high–voltage units are provided. During oil cooling, one of the heat exchangers removes heat from the

object, the other heat exchanger transfers heat to the water cooling system. Small–sized centrifugal pump for oil cooling system was tested for work in vacuum.

The possibility of using heat pipes for cooling is being considered.

Tests were carried out to work inside the vacuum volume of small–sized video and WEB cameras and the necessary devices for this.

The operation of magnetrons is provided for when powered by direct current, with high–frequency and microwave power, with pulse power and acoustoplasma operation.

The vacuum work of micromotors, stepper motors and intra–vacuum hydraulics in vacuum oil for the necessary movements of the substrates and the tool is studied.

All signal circuits are made with shielded cable RK–75, if necessary additional shielding is made.

At the second stage of the work, it is planned to integrate into the vacuum chamber control systems for the thickness of the sputtered layers, ion separator systems, mass spectrometers, and other auxiliary devices.

3. Conclusion

A unique research facility for the study of various processes of deposition and synthesis is described.

Today, the installation is in the process of installation and commissioning, so this publication can be considered as an advance project. Some of the nodes are not described, because they are at the patenting stage.

Bilateral Measurements in Electrical Circuits with Gas–Discharge Devices

A.S. Abrahamyan*, R.Yu. Chilingaryan, Q.G. Sahakyan

Institute of Applied Problems of Physics NAS RA
25 Hr. Nersissian Str., Yerevan, Republic of Armenia, 0014

***Abstract**: If the electrical circuit is unbranched, then usually the current that flows through the circuit is measured only at one point of such a series circuit. If there are LC elements in the circuit, the currents in these elements are considered phase–shifted. When working with gas–discharge devices, and especially if they have a variable component of the discharge current, the situation changes completely. When the current in a low–temperature plasma changes, the degree of ionization and the speed of motion of charged particles change simultaneously.*

In addition, in the acoustoplasma mode, the motion of neutral particles follows to the laws of acoustics, while the movement of ions follows simultaneously both the laws of acoustics and of electrostatics.

The movement of electrons is directly follows the laws of electrostatics, but due to the quasi–neutral nature of the plasma, the movement of electrons is also associated with the movement of ions, i.e. indirectly obeys the acoustic movement of ions. Since the mass of the ion is much larger than that of the electron, the effect of the electron on the movement of the ion can be very often (but not always) neglected. Therefore, in gas–discharge devices, when powered by a current that contains a variable component, it is necessary to simultaneously measure current both from the anode side and from the cathode side.

Dynamic processes will be very different from the average for the period of change in the discharge current. The experimental results of such measurements and a comparison with current measurements at one point in a series circuit with a gas–discharge device are present, for example, not only a change in the dynamic resistance of the discharge, but also a dynamic change in the electrical capacitance of the discharge.

1. Introduction

Let's consider electrical circuits for gas discharge. In electrical engineering, there are two main ways to connect the load to the power source: the circuit of the "voltage generator" and the circuit of the "current generator" [1].

We consider both the main circuit to power the discharge tube.

The circuit of the "voltage generator" is shown in Fig. 1a. The constant resistance R_1 and the voltage–controlled variable resistance R_2 form a voltage divider. The voltage from the midpoint of this divider through the ballast resistance R_b is supplied to the discharge tube with an active resistance R_d. Moreover, R_1, $R_2 << R_b$.

If the resistance R_2 is controlled by a constant voltage, then the resistance R_b is selected so that its value is slightly larger than the differential resistance R_{ddif} of the discharge. In this case, it is necessary to observe the condition of the circuit of the "voltage generator" R_1, $R_2 << (R_d + R_b)$.

*E – mail: *arbel11@mail.ru*

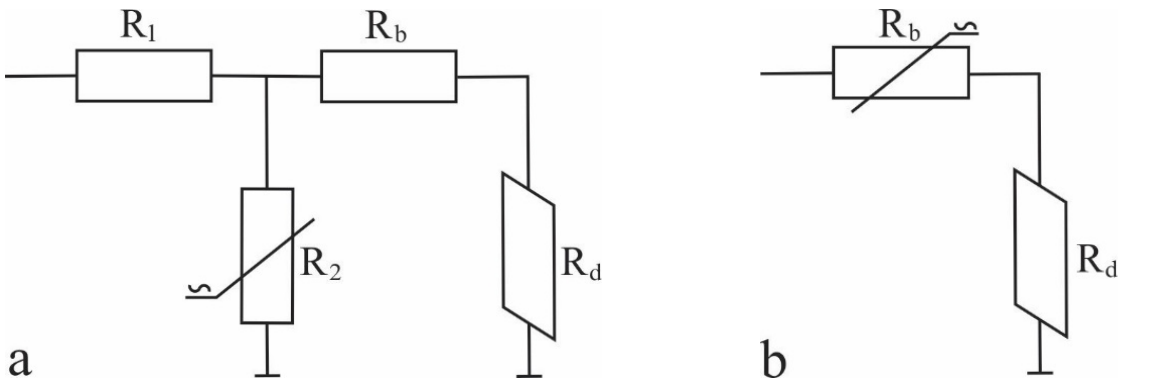

Fig. 1. Schemes for connecting the discharge tube to a power source. R_d is the active resistance of the discharge. a) voltage generator circuit; b) current generator circuit

Recall that, $R_{ddif} = \Delta U_{tub} / \Delta I_{tub}$, where U_{tub} is the voltage between the anode and cathode of the discharge tube, I_{tub} is the current flowing through the discharge tube. For a gas–discharge low–temperature plasma, when the discharge is supplied with direct current, the differential resistance of the discharge is always negative and therefore the positive ballast resistance R_b must be greater than the maximum possible discharge differential resistance, otherwise the unstable operation mode will begin in the circuit.

As a controlled resistance R_2, a high–voltage generator lamp was used. If it is controlled by a sinusoidal alternating voltage, then the voltage at the midpoint of the divider will contain a sinusoidal variable and a constant components – this is the acoustoplasma discharge mode [2, 3].

In the acoustoplasma mode, due to the difference in the shape of the current and voltage from the sinusoidality and phase shift between the current and voltage on the discharge tube, its differential resistance varies significantly. During one period of modulation, the differential resistance of an acoustoplasma discharge can vary from several *kOhm* to several *MOhm*, and can be either positive or negative. R_b is usually ~ 100–200 *kOhm* [4–6]. In this case, the ballast resistance is chosen larger than the differential resistance value $<R_{ddif}>$, averaged over the modulation period, $\{R_b > (<R_{ddif}>)\}$. It is assumed that during the modulation period the unstable regime will not have time to develop.

Fig. 2 shows the behavior of the differential resistance of the discharge tube with the plasma during one period of modulation of the discharge current. It can be seen from Fig. 2 that the behavior of R_{ddif} depends on the frequency of the modulation of the discharge voltage and reaches 400–500 *kOhm* at certain times.

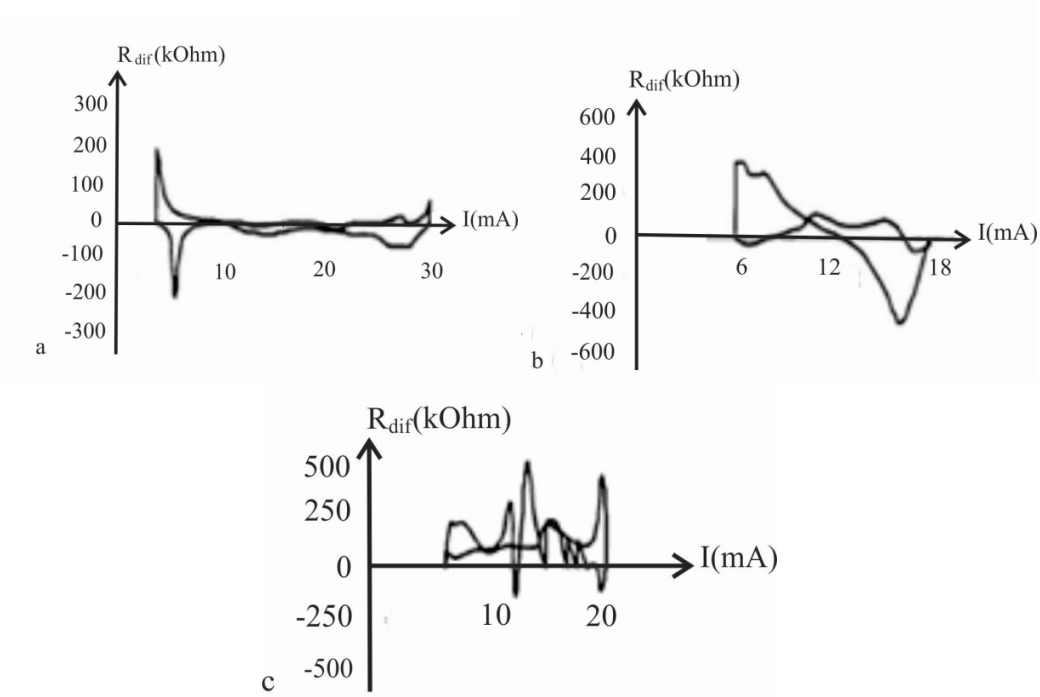

Fig. 2. The change in the differential resistance of the discharge tube during the modulation period for the voltage generator circuit. Gas CO_2: N_2: He = 1: 1: 8, P_0 = 25torr. a) f = 0.1kHz; I_0 = 20mA; $I\sim$ = 6mA; b) f = 1kHz; I_0 = 15mA; $I\sim$ = 3mA; c) f = 15kHz; I_0 = 11mA; $I\sim$ = 9mA

During the modulation period, both the active and reactive discharge resistances can vary significantly. Our experiments showed that the active resistance of the discharge can vary from 50 to 250 kOhm [4–6].

When the “voltage generator” is turned on at those times when the discharge resistance becomes much less than the ballast resistance, the discharge current is entirely determined by the ballast resistance and therefore coincides in phase with the supply voltage. At those times when the discharge resistance becomes greater than the ballast resistance, the discharge current should drop sharply. It was experimentally obtained that if a discharge tends to make a jump due to a phase transition, then its resistance will increase sharply, turning into an analog of a condensed medium. But in this case, the discharge current will also drop sharply. As a result, the phase transition either will not occur or will be so blurred that it may not even be noticed. The phase of the discharge current measured at the grounded cathode will repeat the phase of the input voltage.

Fig. 1b shows a diagram of a "current generator". The controlled ballast resistance R_b changes its value depending on the control voltage. In order to match the current generator circuit, the average values for the period are ($<R_b>$) > ($<R_d>$). The ballast resistance on the electron tube is assembled in such a way that when replacing the discharge tube with an active resistance equal to ($<R_d>$) when the sinusoidal control voltage is applied, the current in the circuit is also sinusoidal. The electronic circuit is assembled in such a way that, even when the discharge resistance changes during the modulation period, the discharge current is maintained in the form that is set by the voltage supplied to the control R_b. Those if the control voltage is sinusoidal, then the current will be sinusoidal. In addition to variable ballast resistance, a constant protective ballast resistance, which is small in comparison with R_d, is connected in series with the tube, this

leads to the fact that the discharge tube itself can be powered by not quite sinusoidal voltage and current.

Despite the apparent simplicity, it is much more difficult to implement the circuit of Fig. 1b than the circuit of Fig. 1a. It is advisable to ground the circuit on the side of the controlled ballast resistance, in this case both electrodes of the discharge tube are under high voltage potential, and the voltage of the audio frequencies containing constant and variable components. This greatly complicates the work and measurements on such an installation.

When the discharge tube is turned on according to the "current generator" scheme, the power supply seeks to maintain the current that sets the control signal. In those moments when the discharge resistance drops, the voltage on the discharge should also fall. But if this moment coincides with an increase in the discharge current, then the voltage drop will be insignificant, or, even, the voltage may increase. Those, voltage tends to repeat the phase of the modulating current. At those moments when the discharge resistance increases simultaneously with an increase in current, the voltage at the discharge will increase sharply. If, together with an increase in resistance, the current drops, then at such moments the voltage at the discharge will also drop, or slightly increase, i.e. in the general case, the voltage at the discharge repeats the phase of the modulating current.

In addition, with an increase in the voltage at the discharge, the ionization conditions change, an increase in voltage increases the ionization and, therefore, reduces the resistance of the discharge. All these effects, together with the self–consistency of the plasma, lead to well–defined phase transitions. Therefore, to study jumps and phase transitions in acoustoplasma, it is advisable to use the "current generator" scheme.

2. Experimental setup

In the experiments described above, the discharge current was measured at one point in the series circuit containing the discharge tube. This is a commonly used method, but for an acoustoplasma discharge this can give erroneous results.

In our experiments on the study of discharge parameters, we used a more complex "current generator" circuit shown in Fig. 3.

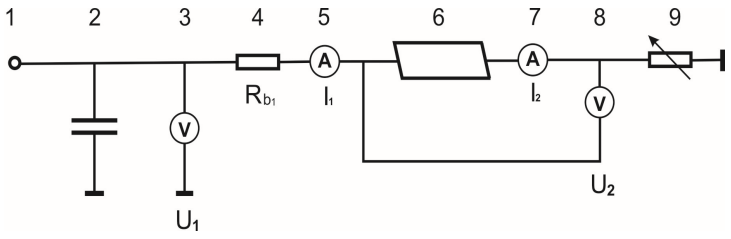

Fig. 3. The discharge tube power scheme used in the experiments

Voltmeter 3 measures the constant high voltage voltage U_1, which is generated by source 1 on the filter capacitor 2. Ballast 4 is protective and limits the maximum current in the circuit, it can be significantly less than the differential resistance of the discharge tube. Milliammeter 5 shows the value of current I1 (or I_a) that flows into the anode of the discharge tube 6. Milliammeter 7 shows the value of current I_2 (I_c) that flows from the cathode of the discharge tube 6. Voltmeter 8 shows the voltage U_2 (or U_{tub}) at the anode–cathode gap discharge

tube. The variable resistance 9 determines the current that flows from the cathode of the discharge tube. The variable resistance 9 is assembled on a high–voltage electron lamp and allows receiving a current close to sinusoidal at the cathode of the discharge tube 6. The filter capacitor 2, a large capacity, provides a short circuit of the alternating current component in a serial circuit, in the entire frequency range of the modulation of resistance 9.

Using special electronic devices, the instantaneous currents measured by milliammeters 5 and 7 and voltmeter 8 were fed to double–beam oscilloscopes, which made it possible to measure the waveforms of currents and voltages. The difference between the discharge current and voltage on the tube from the sinusoidal is due to the processes inside the discharge tube. They are the subject of research.

3. Results of experiment

With direct current in an unbranched electrical circuit, only one point can be measured, i.e. the current I_1 of the milliammeter 5, which flows into the anode of the discharge tube, is considered equal to the current I_2 of the milliammeter 7, which flows from the cathode of the discharge tube. $I_a = I_c = I_0 = \langle I_{tub} \rangle$, where I_0 is a direct current, $\langle I_{tub} \rangle$ is the direct component of the discharge current in a discharge with a modulated current.

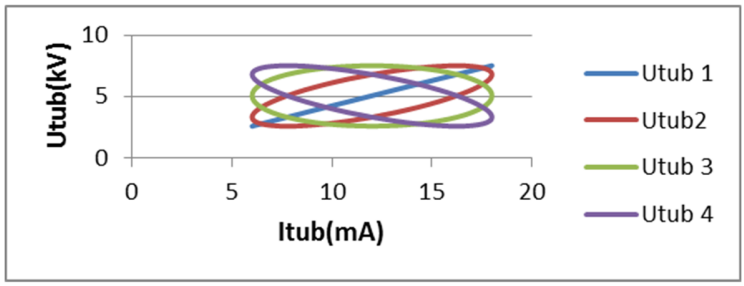

Fig. 4. Designed dynamic current–voltage characteristics when using current–voltage characteristics on a direct current. $U_{tub1} = U_{tub}$ ($\Delta\varphi = 0$); $U_{tub2} = U_{tub}$ ($\Delta\varphi = \pi / 4$); $U_{tub3} = U_{tub}$ ($\Delta\varphi = \pi / 2$); $U_{tub4} = U_{tub}$ ($\Delta\varphi = 3\ \pi / 4$)

If there are L or C elements in the circuit and an alternating sinusoidal current flows along the circuit, then the currents I_1 and I_2 are phase shifted. In this case, the current – voltage characteristic will have the form of Lissajous figures (Fig. 4). The dynamic current–voltage characteristics (CVC) would also look if the CVC, which were obtained for direct current, could be used.

In gas discharge devices, everything is much more complicated.

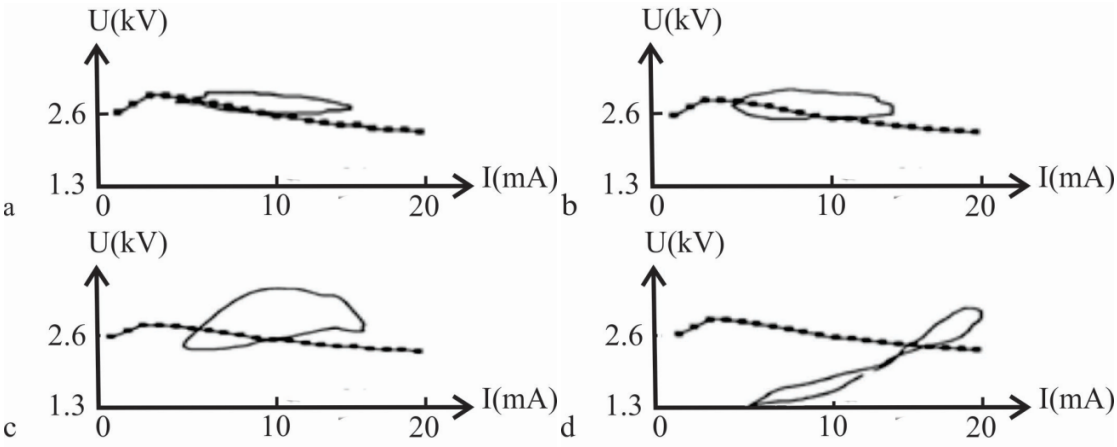

Fig. 5. Dynamic CVC of an acoustoplasma discharge. a) f = 0.1kHz, b) f = 0.3kHz, c) f = 1kHz, d) f = 15kHz. – CV characteristic of a direct current

It can be seen from Fig. 5 that the dynamic CV characteristics of an acoustoplasma discharge depend on the frequency and differ greatly from the Lissajous figures.

When the discharge current is modulated in a low–temperature plasma, the quantity and speed of charged particles also change simultaneously, in addition, the voltage at the discharge can change for other reasons. Therefore, the parameters of the dynamic processes in the plasma and especially in the acoustoplasma will be very different from the average for the period of modulation. It should be noted that both plasma and acoustoplasma are nonlinear media. Therefore, even if one of the first current has a sinusoidal shape, then, due to the nonlinearity of the plasma, the second one will have harmonics. And finally, when the discharge current changes in the plasma, an additional charge can accumulate or dissolve, in this case it is natural that during the modulation period the current values flowing into the tube and flowing out of the tube will differ. All this leads to the fact that in gas–discharge devices, especially when powered by a current that simultaneously contains both constant and variable components, it is necessary to simultaneously measure both the current that flows into the anode and the current that flows from the cathode.

Those, we have not only a change in the dynamic resistance of the discharge, but also a dynamic change in the electric capacitance of the discharge, electron charges and its other parameters.

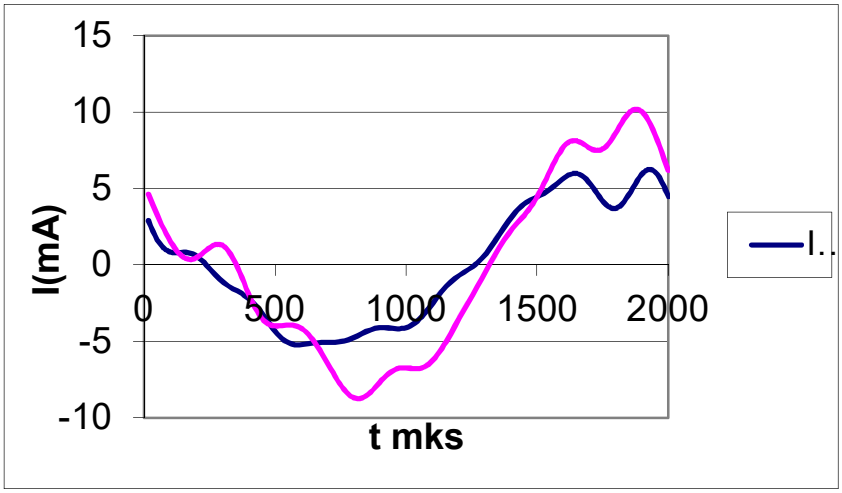

Fig. 6. Change in current values measured from the anode side (I_a) and the cathode side (I_c) during the modulation period

Figure 6 shows the measured current values of the variable component of currents I_c and I_a. Moreover, the direct component of the discharge current $I_0 = \langle I_a \rangle = \langle I_c \rangle = 12$mA; The depth of modulation of the current measured from the side of the cathode $M_{Ic} = 0.83$, the depth of modulation of the current measured from the side of the anode $M_{Ia} = 0.5$. The modulation depth M is the ratio of the amplitude of the variable component of the discharge current $I \sim$ to the value of the direct component of the discharge current ($M = I \sim / I_0$).

Note that in wires and milliammeters, the current is due only to the movement of electrons, and in the anode–cathode gap the current in the plasma is due to the movement of charges of both signs, and effects similar to those that arise in Gunn diodes and avalanche–span diodes described in [7] are possible.

From Fig. 6 it is difficult to say how much the curves I_a and I_c differ from each other.

Table 1 shows the Fourier spectrum of the amplitudes of harmonics I_a and I_c.

From table 1 it is seen that the second harmonic of the current measured from the cathode side is approximately 6 times greater than that measured from the anode side. Those. in the plasma inside the discharge tube, some processes occur, characterized by a second harmonic. Usually this is a parametric pumping process [1].

Table 1. The Fourier spectrum of the amplitudes of the harmonics of the signals shown in Fig. 5.

n	**1**	**2**	**3**	**4**	**5**	**6**
I_c(mA)	7,95	1,28	0,66	0,53	0,63	0,86
I_a(mA)	5,39	0,23	0,22	0,33	0,51	0,33

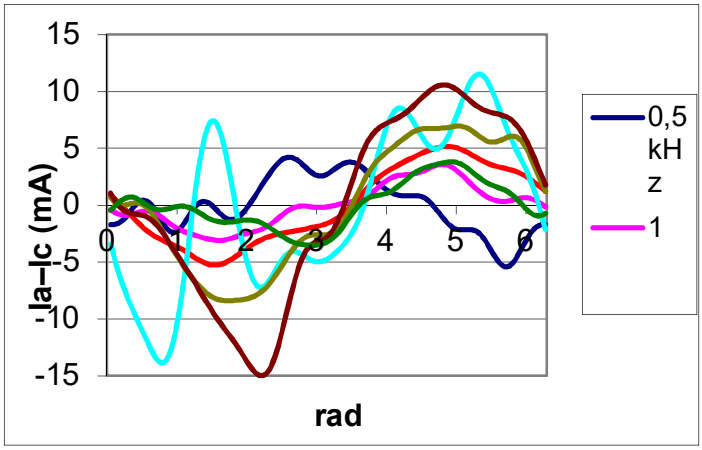

Fig. 7. A family of difference values of simultaneously measured instantaneous values of currents I_a and I_c for different modulation frequencies

Figure 7 shows the difference in instantaneous values (I_a–I_c) for different modulation frequencies. In order to be able to compare the curves for different modulation frequencies along the abscissa axis, the values are plotted in radians. It can be seen from Fig. 7 that the difference in instantaneous values (I_a–I_c) has a complex form. But this difference (I_a–I_c) shows the instantaneous change in charge in the tube during the modulation period. Since we already measure the current in conductors that are connected to the anode and cathode, the electron velocities can be considered the same and large in both conductors and not take into account the change in the electron velocity in the plasma.

Further, by solving direct and inverse problems, we can determine many parameters of the acoustoplasma, which for some reason we could not directly measure.

4. Conclusion

It has been shown that in acoustoplasma discharges and in discharges with alternating current, measuring the discharge current at only one point in the series circuit leads to errors, since this does not take into account the change in charge in the discharge tube itself.

It is necessary to simultaneously measure the current that flows into the anode of the discharge tube and the current that flows from the cathode of the discharge tube.

References.

1. Bessonov L.A. Theoretical Foundations of Electrical Engineering. Visshaia shkola, Moscow, p.774, 1966. (In Russian).
2. Galechyan G.A., Mkrtchyan A.R. Acoustoplasma. Apaga, Yerevan, p.338, 2005. (In Russian).
3. Mkrtchyan A.R., Mkrtchyan A.H., Abrahamyan A.S. Acoustoplasma is a new state of plasmas. VII Intern.Conf.Plasma Physics and Plasma Technology, PPPT–7, Minsk, Belarus, 17–21 Sept.2012, Proc., v.1, pp.3–5, 2012.
4. Abrahamyan A.S., Bezhanyan T.Zh. The dependence of the resonant properties of a gas discharge on the circuit. Laser physics conf. – 2007, Ashtarak, Armenia, 9–12 October 2007, pp.225–228, 2007.

5. Haroyan K.P. Generation and amplification of acoustic waves in a gas–discharge plasma and control of discharge parameters. Ph.D. Dissertation, IAPP NAS RA, Yerevan, Armenia, 2005.
6. Sahakyan Q.G. The solution of incorrectly posed inverse problems in acoustoplasma. Ph.D. dissertation, IAPP NAS RA, Yerevan, Armenia, 2014.
7. Lebedev A.I. Physics of semiconductor devices. Physmatlit, Moscow, 488p., 2008. (In Russian).

Dynamic Processes during Phase Transitions and Structural Transformations in Oriented Liquid Crystal Systems

L.S. Bezhanova, A.K. Atanesyan

Institute of Applied Problems of Physics NAS RA,
25 Hrachya Nersissian Str., Yerevan, Republic of Armenia, 0014

The aim of the study was to obtain numerical values of such dynamic parameters, as orientation relaxation time and ordering, which would offer new technical solutions that would expand the field of practical applications of liquid crystals (LC).

In this paper, we managed to obtain high mobility of molecules in binary systems of nematogens in the solid phase.

Nematic LCs satisfying the below mentioned conditions have been chosen as research objects for this study:

a) the molecules of the studied compounds should have electron–donor–acceptor, strongly polar end groups;

b) the molecules of the selected compounds must have long alkyl chains to reveal the role of lateral interactions and steric factors in the mechanism of induction of the smectic phase [1];

c) in binary systems, compounds must be unlimitedly mutually soluble;

d) the selected objects should be of interest in terms of practical application.

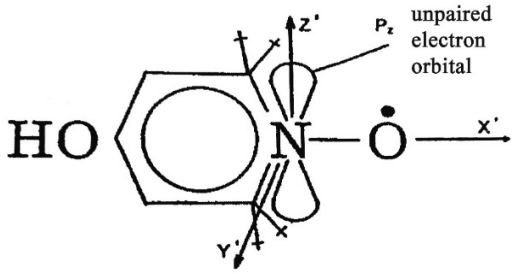

Fig. 1. Structural Formula of Nitroxyl Radical

The mobility (rotatory diffusion) and ordering of molecules were investigated by electron spin resonance (ESR) technique with the help of spin probe (Fig.1) in such crystals, as 4–n–buthyl–4–n–heptanoiloxyazoxybenzene {I}; n–cyanophenil ether of n–heptylbenzoic acid {II}; n–cyanophenil ether of n–hexylbenzoic acid {III}, (which possess nematic phase falling in the temperature range of 35–76^{0}C; 44–58^{0}C; and 44–56^{0}C, accordingly) (Fig.2,3). Their systems: {I}/{II} ; {I}/{III} with different concentration of components were also studied with the abovementioned technique. ESR measurements were carried out in the temperature range of –27^{0}C – +70^{0}C, which is far beyond LC→Crystal transition point.

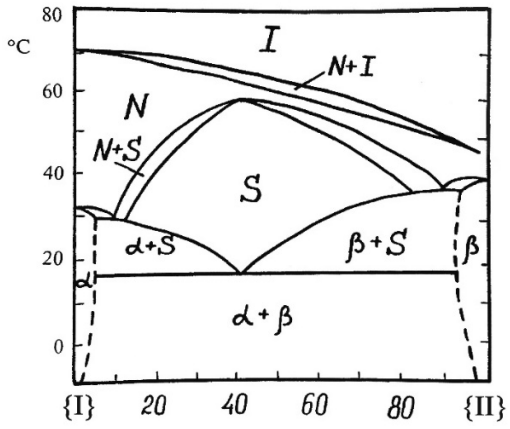

Fig. 2. Phase diagram {II}/{I}

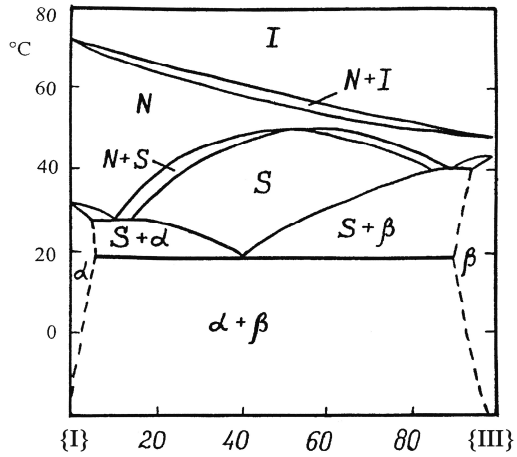

Fig.3. Phase diagram {III}/{I}

The use of a spin probe is based on the analysis of changes in the line widths of the ESR spectra caused by rotational and translational diffusion of radicals. As we know from [2–4], the mobility of a radical depends on the mobility of environmental molecules. Therefore, the radical is a kind of molecular sensor of structural and dynamic information about the local environment. The paramagnetic resonance spectra of nitroxyl radicals are sensitive not only to the molecular movements, but also to the nature of the medium in which they are dissolved. In this connection, the magnetic parameters of the radical are very sensitive functions of the electronic distribution in the molecule, and therefore they are affected by perturbations from the environment. These perturbations become especially strong in polar solvents due to the specific interaction of such solvents with a lone pair of electrons on the oxygen atom of the nitroxyl radical.

ESR measurements were carried out on a radio spectrometer РЭ–1301 in a microwave region of 9 GHz. To avoid the distortion of line shape, the amplitude of the high frequency modulation was set to be several times smaller than the line width, and the microwave power was chosen to be so small that the ESR signal was far from saturation. The magnetic parameters were measured with an accuracy of ±0,4 G. To minimize line broadening, due to the dipole – dipole interaction between the molecules of the spin probe, the concentration of the radical was determined to be as low as ~ 10^{-4}mol / l.

The samples under study were prepared by thoroughly mixing the LC components in the isotropic phase to obtain a homogeneous solution of the system. Uniformly oriented samples were obtained by the application of a sufficiently strong magnetic field ~ 3000 G. During the experiment, the samples were heated by a hot air stream, blowing through a quartz tube passing through the resonator of the spectrometer. At low temperatures (from ambient temperature to –27°C) spectra were recorded by blowing liquid nitrogen vapor through the resonator. The accuracy of temperature measurement was ±0,1°C.

As known, the position and hyperfine splitting of the resonance lines of the spin are associated with the ordering of molecules of investigated objects and their dynamic properties related to the width and shape of these lines. Our analyses of the ESR spectra is based on well–developed theory of spin relaxation [5–7]. According to this theory the width of spectra $T(m)^{-1}$ is defined by the equation [5, 8]:

$$T(m)^{-1} = L + Bm + Cm^2 \quad (1)$$

where, $m = -1,0,+1$ –is nuclear quantum number characterizing the hyperfine splitting component; parameters L, B, C depend on the magnitude of magnetic anisotropy and the rate of molecular reorientation.

To simplify the analysis of ESR spectra, it is assumed that the rotational diffusion tensor is axially symmetric. The laboratory coordinate system (X, Y, Z) is chosen so that the Z – is the axis of symmetry and is directed by director. X, Y– axes are in the plane perpendicular to the Z– axis. The main values of the hyperfine splitting constant tensor: $A_{xx} = A_{yy} = A_{\perp}$, $A_{zz} = A_{\parallel}$.

$A_{\perp}$ – is the value of the hyperfine splitting constant of the experimental spectrum when magnetic field is normal to the Z axis; $A_{\parallel}$ – is the value of the hyperfine splitting constant of the experimental spectrum when magnetic field is directed along the Z axis. The molecular coordinate system (X′, Y′, Z′,) relates to radical fragment as shown on Fig.1. In this coordinate system $\hat{A}$ and $\hat{g}$ tensors can be considered diagonal [9]. $A_{x'x'}$ = 31 G, $A_{y'y'}$ = 5,2 G, $A_{z'z'}$ = 5,2 G – are the main values of the hyperfine splitting constant of radical in the molecular coordinate system.

For further calculations it is necessary to establish the orientation of Z– axis on the molecular coordinate system (X′, Y′, Z′,). The idea of solving this problem is to compare the theoretically calculated ratio B/C with the experimentally derived (based on the analysis of line width) value $(B/C)_{exp}$. The B/C calculation results and their corresponding $(B/C)_{exp}$ experimental values are shown in Table1. $(B/C)_{exp}$. is observed to best coincide with the corresponding calculated value for the case when the Z–axis of the rotational diffusion tensor coincides with the Y′– axis of the molecular coordinate system. Small deviations between these quantities, apparently, are associated with various fluctuations, leading to a non–strict coincidence of Z– and Y′– axes .Thus, the radical in the LC medium is oriented in such way that the Y′– axis of the molecular coordinate system becomes parallel to the Z– axis of the laboratory coordinate system.

Table 1. Calculation results of the B/C for the binary systems with different orientations of the rotational diffusion tensor in the molecular coordinate system

Mol%	**°C**	**$(B/C)_{exp}$**	**$(B/C)_{cal}$ Z=X′**	**$(B/C)_{cal}$ Z=Y′**	**$(B/C)_{cal}$ Z=Z′**
100%{I}	35	0,29	0,54	0,29	0,24
	40	1,75	1,04	1,18	2,33
	48	1,13	1,10	1,40	2,49
	60	0,28	0,95	0,35	0,30
85%{II}/15%{I}	35	1,00	1,93	1,09	——
	40	0,39	0,48	0,43	——
	45	1,14	1,02	1,19	——
	55	4,25	0,48	4,12	——
70%{II}/30%{I}	30	0,40	0,50	0,42	0,34

	50	0,34	0,35	0,32	0,36
	60	1,97	1,15	1,81	—
50%{II}/50%{I}	35	0,53	0,51	0,53	0,64
	50	0,61	0,56	0,63	0,64
	60	0,50	0,43	0,64	0,63
25%{II}/75%{I}	35	0,39	—	0,35	0,43
	45	0,58	—	0,53	0,63
	60	1,21	—	1,19	2,40
100%{II}	35	0,43	0,37	0,42	0,34
	40	1,13	1,05	0,11	2,40
	50	5,23	1,07	5,33	3,03
	60	0,49	0,51	0,44	0,64

The degree of ordering S and the angle θ between Z'– axis and the direction of magnetic field, were calculated using the following expressions [10]:

$$S = (< A > -A)/[(A_{z'z'} - A_{x'x'})cos^2\,\theta + A_{x'x'} - A] \quad (2)$$

$$cos^2\,\theta = \frac{[(A_{x'x'}-A)(<g>-g)-(g_{x'x'}-g)(<A>-A)]}{[(g_{z'z'}-g_{x'x'})(<A>-A)-(<g>-g)(A_{z'z'}-A_{x'x'})]} \quad (3)$$

where $A = \frac{1}{3}(A_{x'x'} + A_{y'y'} + A_{z'z'})$, $g = \frac{1}{3}(g_{x'x'} + g_{y'y'} + g_{z'z'})$, $< A > and < g >$ – are experimental values of the hyperfine interaction constants and g–factor in a liquid crystal medium.

As follows from Table 2, at a given temperature in the nematic phase the degree of ordering in {I} is greater than that in {II} and {III}. At the same temperature in the nematic phase the degree of ordering in {I}/{II} and {I}/{III} systems is greater than that in pure {II} and {III}. In the range of temperatures when the systems {I}/{II} and {I}/{III} are in the smectic phase their degree of ordering is less than that in pure {II} and {III}.

Table 2. Calculated values of the ordering parameter S.

Mol %	**ºC**	**S**
100%{II}	50	0,56
100%{III}	50	0,54
85%{II}/{I}	45	0,58
70%{II}/30%{I}	40	0,45
70%{II}/30%{I}	50	0,61
70%{III}/30%{I}	40	0,50
70%{III}/30%{I}	50	0,59
50%{II}/50%{I}	40	0,38
50%{II}/50%{I}	60	0,45
50%{III}/50%{I}	40	0,41
50%{III}/50%{I}	60	0,46
25%{II}/75%{I}	40	0,11
25%{II}/75%{I}	50	0,16
25%{III}/75%{I}	40	0,14
25%{III}/75%{I}	50	0,18
100%{I}	50	0,68

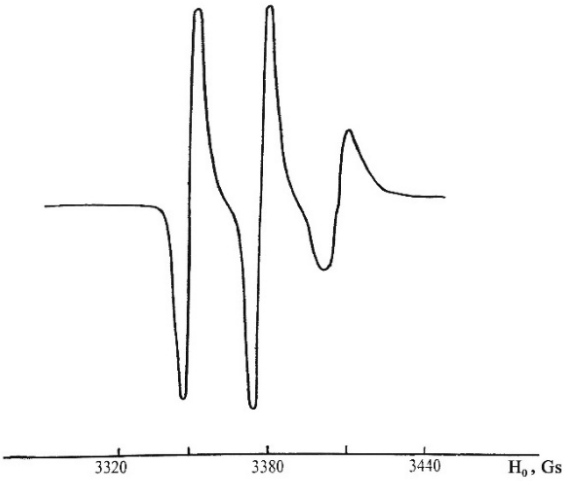

Fig.4. ESR spectrum of {I} at +19°C

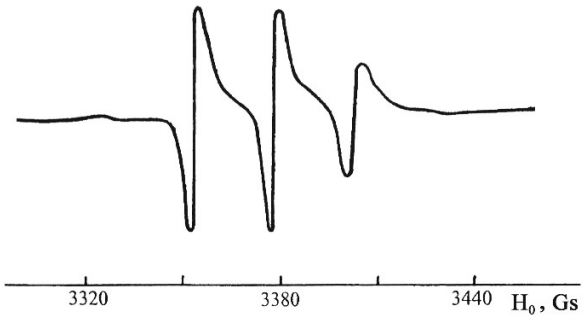

Fig.5. ESR spectrum of {II} at +21°C

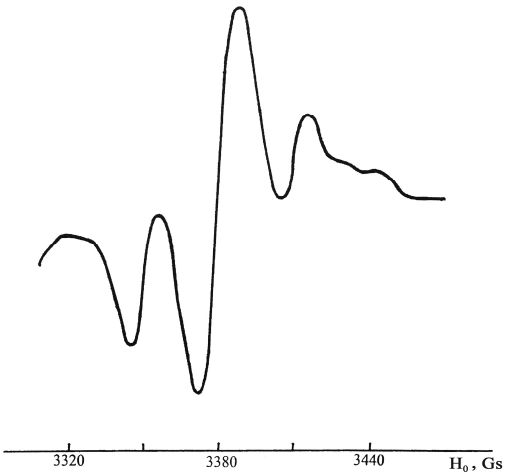

Fig.6. ESR spectrum of {III} at +18°C

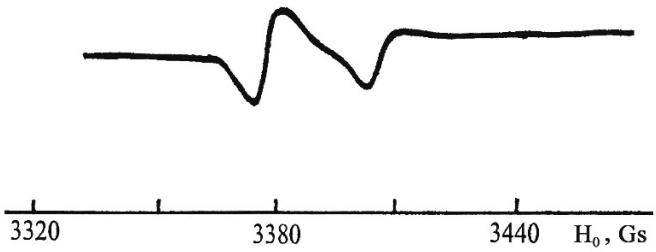

Fig.7. ESR spectrum of {I} at +2°C

ESR spectra of the mentioned systems in the liquid state represents a well–resolved triplet (Fig.4,5,6). The analyses of ESR spectra shape and width showed that the rotatory diffusion correlation time was $10^{-11} < \tau_c < 10^{-9}$ sec in the liquid state. It was determined that the τ_c changes in the same way as the rotational anisotropy, depending on the system.

Remarkable reduction in the rotatory diffusion rate parallel to the decreasing temperature was observed in the abovementioned {I}, {II}, {III} LCs. The ESR spectra component, corresponding to *m=–1,* almost completely disappeared at the LCs' freezing temperature (Fig.7, 8, 9).

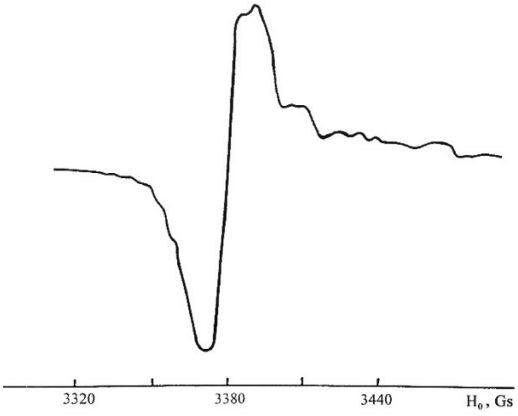

Fig.8. ESR spectrum of {II} at +6°C

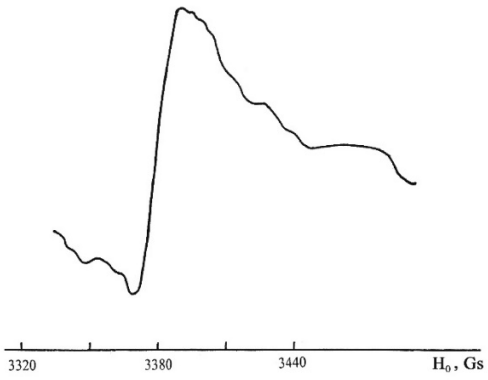

Fig.9. ESR spectrum of {III} at –13°C

At the same time, this rate was found to be considerably changed when {I} was added to {II} or {III}. In these systems the ESR spectra component, corresponding to *m=–1,* was clearly observed during freezing. In frozen systems, high molecular mobility of – $\tau_c = 10^{-9}$ sec was found to be preserved up to t= -20^0C (Fig. 11). Such a high mobility of molecules far beyond the LC→Crystal transition point indicates that in the solid phase these systems are either in the gas crystalline or glassy state, where the anisotropic rotation around the long axes of the molecules is preserved.

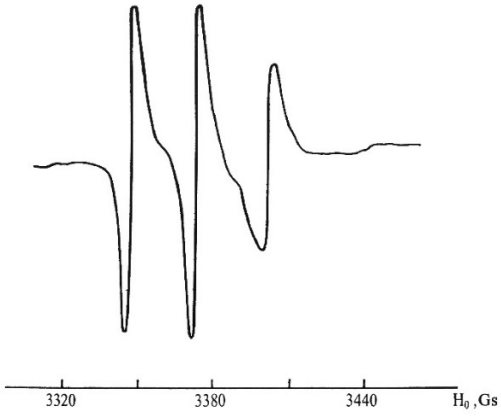

Fig.10. ESR spectrum of 54%{I}/46%{II} at +19°C

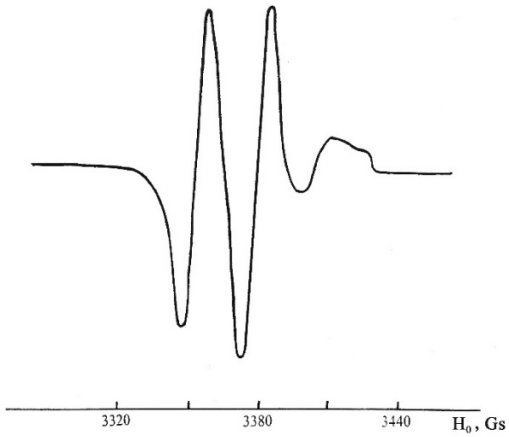

Fig.11. ESR spectrum of 54%{I}/46%{II} at – 19°C

The mechanism of de–association and the formation of new associates presented in [11] makes the understanding of the "longevity" of the rotational degrees of freedom in the {II}/{I} system possible. This "longevity" is caused by the structural features of component molecules that lead to an increase in system polarity. The change in the splitting constant depending on the concentration of {I} (splitting constant increases with the increase of the number of the {I} molecules in system {II}/{I}[11]) serves as a confirmation of the increase in the system polarity. Changes in the activation energy for rotational motion can reflect the changes in the dynamic molecular structure experienced by the probe molecule as the LC undergoes phase transitions. According to [12, 13], the pair interaction energy in {II}{II} is greater than in {II}{I}. Indeed, the de–associative effect of {I} leads to the fact that the paired associates of {II} molecules are destroyed, and the activation energy of rotation in this system is significantly reduced before the new mixed associates are formed. These are equilibrium processes depending on the concentration of various types of the components of a LC system. This substantially complicates the pattern of the relationship between the splitting constant of the ESR spectra and the factors affecting it.

References.

1. L.S. Bezhanova, Z.V. Bagdasaryan, M.L. Baburyan. Proceedings of NAS of Armenia., 42, № 1, 43 (2007).
2. K. Matsuura, Y. Kotake, K. Kuwata. Mol. Cryst. Liq. Cryst., 140, 327 (1986).
3. Ч. Сликтер. Основы теории магнитного резонанса. М., Мир, 1981.
4. S.A. Goldman, G.V. Bruno, J.H. Freed. J. Chem. Phys. 59, 6, 3071 (1973).
5. C.F. Polnaszek, J.H. Freed. J. Phys. Chem. 79, 21, 2283 (1975).
6. Метод спиновых меток. Под ред. Берлинера. М., Мир, 1979.
7. Shigeru Mita, Sheichi Kondo. Mol. Cryst. Liq. Cryst. 140, 153 (1986).
8. S.A. Goldman, G.V. Bruno, C.F. Polnaszek, J.H. Freed. J. Chem. Phys. 56, 2, 716 (1972).

9. D. Bordeaux, et al. Organic Magnetic Resonance. 5, 47 (1973).
10. G.R. Luchurst, M. Setaka, C. Zanoni. Molecular Phys. 28, 1, 49 (1994).
11. А.Ц. Саркисян, Л.С. Бежанова. Журн. физической химии. 69, 2504 (1989).
12. S.M. Yayloyan, L.S. Bezhanova, E.B. Abrahamyan. Ferroelectrics. 245, 147 (2000).
13. А.Ц. Саркисян, С.М. Яйлоян, Л.С.Бежанова. Журн. структурной химии. 31, 6, 42 (1990).

Researches of Acoustic Properties of Some Lakes and Reservoirs of the RA

A.H. Mkrtchyan*, A.R. Mkrtchyan, A.K. Atanesyan, G.A. Harutyunyan, S.A. Mkhitaryan, Kh.V. Kotanjyan, S.A. Mirakyan, V.N. Agabekyan, V.V. Nalbandyan, H.R. Muradyan, E.A. Mkrtchyan, E.G. Baghdasaryan, G.G. Tokhmaxyan, S.M. Petrosyan, A.A. Papazyan, E.S. Shadyan

Institute of Applied Problems of Physics NAS RA
25 Hr. Nersissian Str., Yerevan, Republic of Armenia, 0014

***Abstract**: The work is dedicated to the studies of the acoustic properties of some lakes and reservoirs located in the territory of the Republic of Armenia (RA). The acoustic properties of multilayer structures and reservoirs and the influence of the location and shape of the layers on these properties are investigated. The resonant frequencies of reservoirs with various configurations and the coefficients of transmission of acoustic waves through layered structures with different orders of arrangements of layers are found. The parameters of the reverberation patterns are determined depending on the size and form of the reservoir and the nature of the underlying stratums of the earth. The experiments on recording of signals from artificial and natural sources were carried out on Sevan and Parz Lich lakes. In order to record these acoustic vibrations unique acoustic devices have been developed. In parallel, measurements were made by using the SV–5 vertical seismograph. The characteristic background noise and the resonant frequencies of Sevan and Parz Lich lakes were determined. The time and amplitude spectra from different sources of acoustic vibrations were recorded. Analyzes of the obtained data are submitting that lakes and water cavities in areas with a certain geological structure can be used as super sound acoustic antennas allowing to record weak signals in the frequency range from 0.01 Hz to 200 Hz and to determine the type and range of the source of these signals. Currently, the works are ongoing in the field of more detailed studies of the influence of the configuration of water basins on their acoustic properties and the possibilities of suppression reduction of the natural noise in the low–frequency range.*

1. Introduction

One of actual problems of modern science and technology is identifications of influence of super weak distortions on the processes proceeding in medium on the assumption of coherent interaction. In this area of investigations on development and creation of registration systems of the acoustic waves propagating in stratified medium with rather small amplitude are of special interest. Since 1980 at Institute of applied problems of physics of NAS RA scientific and technical researches in this area are conducted. Under the leadership of the academician of NAS RA of A.R. Mkrtchyan new approach to solve this problem by utilizing some methods of AcustaPhysics was formed. During the investigation unique experimental and theoretical results were obtained. Theoretical approach and bases of the technique of the experiment for the solution of this problem are given in papers [1–7]

*E – mail: *amktychyan@sci.am*

2. Experimental setup

Various types of seismic receivers and hydrophones are utilized for registration of super weak low–frequency acoustic waves in water environments and caves. However they have the number of deficiency, such as the dependence of sensitivity of hydrophones on temperature, small frequency range, absence of reconfiguration of characteristic frequency, small term of operation, small sensitivity, etc.

For the exception of deficiencies in the IAPP of NAS RA unique acoustic detectors operating on the basis of the phenomenon of modulation of Messbauer radiation under the influence of external acoustic fields were developed.

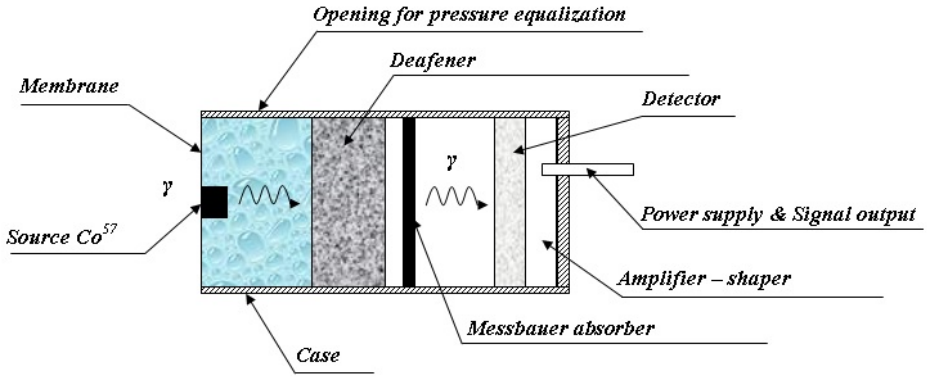

Fig. 1. Schematic view of modulated Messbauer radiation phenomenon based detector.

The schematic view of the Messbauer acoustic detector is presented on Figure 1. The Messbauer acoustic detector consists of the following principal components: a membrane – 1 on which the gamma of quanta Messbauer source Co^{57} – 2 is fixed, rigidly fixed Messbauer absorber – a foil from stainless steel – 3 and the detector of gamma quanta – 4.

The principle of operation of the detector can be explained as follows: variation of the energy of gamma quanta as a result of acoustic vibrations influence on the condition of gamma–resonant absorption and, therefore, variation of the intensity of the quanta radiations registered by the detector.

Gamma the quanta emitted by the Messbauer source fall on the Messbauer absorber and are absorbed by the Messbauer nucleus. The gamma quanta which passed through the absorber are registered with the gamma quanta detector. The intensity the gamma quanta emitted by motionless source and absorbed by the motionless absorber are constant. The influences of acoustic wave on the membrane are originated vibrations with characteristic frequencies and the gamma quanta source fixed on it is vibrating. Due to the Doppler effect the energy of the gamma quanta fell on the absorber is changed. The resulting output of the Messbauer acoustic detector after preliminary amplification and discrimination is directed to specially designed communications unit, which is connected with the computer where obtained experimental data are saved and analyzed.

By means of registration of the temporal dependence of the variation of the intensity of gamma quanta the main characteristics of acoustic waves causing this variations can be determined:

$$N(t) = N_0(1 - \frac{\beta/2}{(\Delta x + \frac{V_0 \sin \omega t}{\lambda\Gamma/2})^2 + 1})$$

where N(t) is the number of resonant gamma quanta depending on time t, N0 is the number of gamma quanta out of the resonance, V0 is the maximum speed of the absorber movement, Δx – is the energy shift between the resonance emission and absorption, β – the effective thickness of the absorber.

The developed by us Messbauer acoustic detector allows to register acoustic waves in the frequency range up to 10^4 Hz, with sensitivity on vibrational speed – $10^{-6} \div 10^{-5}$ cm/sec., in the dynamic range of 80 dB. Characteristic frequency of the Messbauer acoustic detector is tunable.

The amplitude–frequency characteristic of the Messbauer detector defined during the researches is presented in Figure 2.

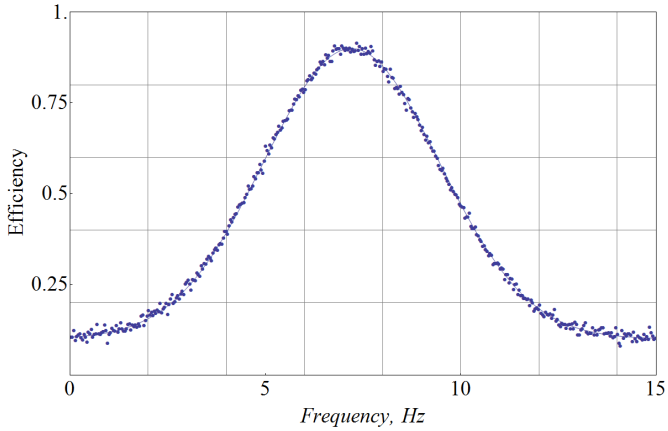

Fig. 2. The amplitude–frequency characteristic of the Messbauer detector.

The experimental setup also included temporary gamma acoustic spectrometer – GAS which is developed on the basis of the microprocessor with signal discrete processing, providing registration of weak non–periodic and periodic acoustic waves. The spectrometer registered signals in real time and at connection with the computer can operate in the mode of accumulation and information processing. Automatic control of the registration system GAS provides three–channel registration of periodic and non–periodic acoustic vibrations in three directions at the same time that gives the chance to utilize the spectrometer as a vector sensor, for the purpose of measurement of three–dimensional component of the vibration parameters that is very important in the acoustics and hydrophysics researches.

For carrying out underwater measurements in IAPP NAS RA sensitive sonar systems registering the acoustic waves propagating in liquid mediums are developed and created. As main elements of the hydrophones radially polarized piesoceramic spheres from barium titanium are utilized. Such design of the receiver in comparison with flat and package piezo – converters allows to increase sensitivity at the expense of coefficient of electromechanical transformation. These detectors have good phase identity and stability.

For calibration of utilized acoustic sensors underwater and land low–frequency radiators with controlled output power were developed and created.

On the basis of results of laboratory researches and the carried–out theoretical calculations necessary optimal conditions for conducting experimental studies in field conditions were revealed. It should be noted that for conducting experimental field studies the following experimental conditions were provided:

1. The reservoir must have a certain configuration and must be located where geological layers under its bottom met conditions of accumulation and amplification of acoustic energy,
2. Underwater devices for measurement of amplitude, form and duration of an acoustic response of the resonant system must operate independently at certain depth,
3. For comparative analysis of the obtained results land measurements with vertical and horizontal seismic sensors and underwater measurements with developed registration systems in parallel must be carried out.

Taking into account upper mentioned conditions and the fact that the resonant systems of corresponding theoretical models must have accumulating and amplifying characteristic of acoustic waves propagating through the multi stratum system containing heterogeneity of certain geometrical forms some natural and artificial reservoirs located in territories of Armenia were chosen. Thus, for carrying out experimental field researches to register weak and super weak acoustic vibrations Lakes Sevan, Parz–lich, etc. were chosen.

The Lake Sevan chosen as the seismic hydroacoustic antenna is water basin of 1150 km^2 surface with maximum depth of 72 m, located at height ~ 1900 m above sea level. Bottom stratums of the lake have schistous structure consisting of basalt, clay and volcanic rocks. The measurements were carried out in the deep–water part of the lake.

3. The results of experimental investigations

Experimental investigations to solve the main objectives and to confirm our proposition on utilization of certain water reservoirs and caves as supersensitive antennas of acoustic vibrations were conducted according to the following scheme (Figure 3).

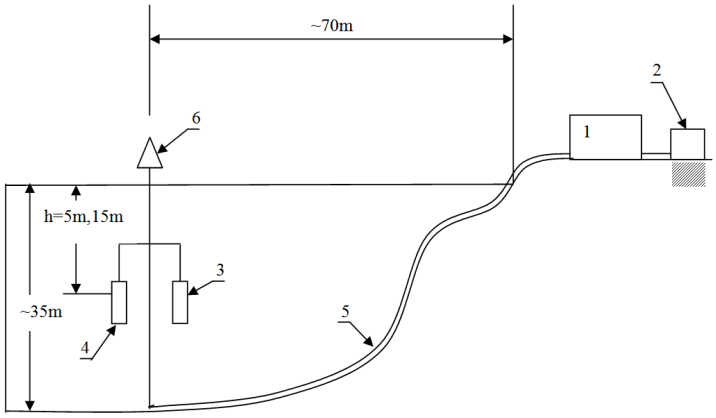

Fig. 3. The scheme of the experimental setup: 1 – center of obtained data collations; 2 – seismic sensor; 3 – Messbauer acoustic detector; 4 – hydrophone; 5 – feed cable; 6 – buoy.

Seismic sensors SM–3 (2) for registration of horizontal and vertical components of vibration process were placed on the shore of the Lake Sevan on the concrete pedestal having

surface area of 52×52 cm2. Sensors are attached by the protected cable with multichannel recording unit and with the personal computer.

Hydrophones (4) were placed in the lake in suspension and are kept by buoy (6) under water in vertical position. Such installation of hydrophones provides homogeneous contact with the surrounding medium and free from the strayes originated by the surface waves.

The Messbauer acoustic detector (3) is placed in the lake together with hydrophones and by means of special cable enclosed under water is connected to GAS and to personal computer which provides saving, processing and interpretation of registered temporary and modulated Messbauer spectra of hydro acoustic signals.

Simultaneously registration of acoustic vibrations by means of the seismic detectors located on the shore of the lake and under water at depths of 5 and 15 meters by means of hydrophones and the modulation Messbauer sensor were conducted.

During the experimental investigations the main characteristics of the utilized detectors of acoustic vibrations were defined and are presented in Table 1.

Table 1
The main characteristics of the utilized acoustic sensors

Type of sensor	**Frequency range**	**Dynamic range**	**Characteristic frequency**
Hydrophones	0.1÷1 KHz	70 dB	10Hz, 100Hz, 250Hz, e.t.c.
Seismic sensor	0.5÷0.03 KHz	60 dB	100Hz
Messbauer acoustic detector	0.0÷10 KHz	80 dB	7,5Hz*

* The characteristic frequency of the Messbauer acoustic detector tunable.

To determine the characteristic frequency of the resonant antenna system – the Lake Sevan, measurements in the presence of artificially excited hydroacoustic vibrations of different forms, amplitude and frequency were conducted. Measurements were conducted for the frequency range of 0.1 ÷ 30 Hz under identical conditions of excitation. In the frequency spectrums registered by the hydrophone increase in the relation of signal to noise around 7.5 Hz (Figure 4) is observed. This frequency matches the calculated characteristic frequency of the Lake Sevan. In this range the maxima corresponding to frequencies of artificially excited hydroacoustic vibrations from the underwater acoustic radiator with frequency of 15 Hz and the land radiator with frequency of 30 Hz are also observed.

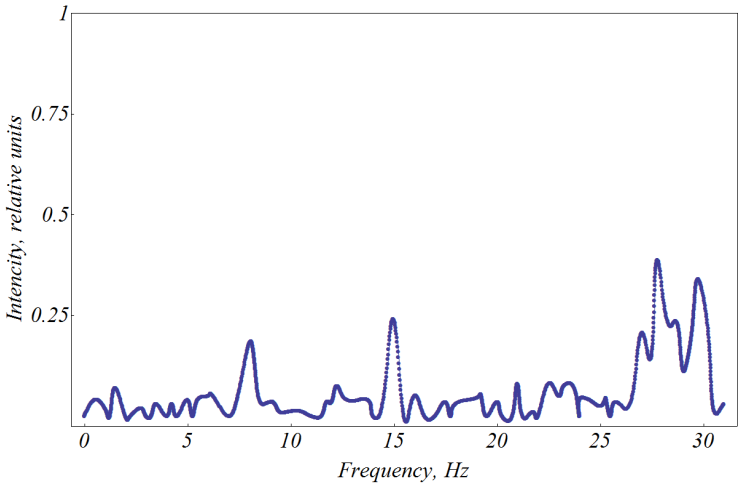

Fig. 4. The characteristic frequency distribution spectra of the noise of the Lake Sevan registered by the hydrophone.

The temporal spectra of acoustic vibrations from the underwater acoustic radiator of different frequency registered by the hydrophone are given in Figure 5. From the drawing it is visible that at registration in the temporary mode on ranges sinusoidal forms of artificially excited acoustic vibrations are allocated.

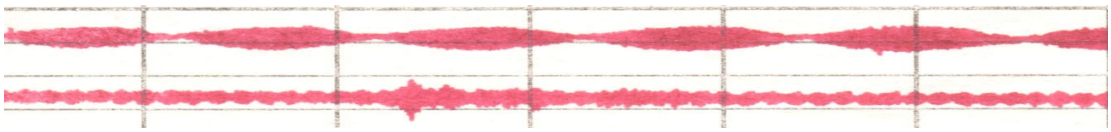

Fig. 5 The temporal spectra from artificial source initiating of acoustic vibrations of a sinusoidal form of different frequencies.

It should be noted that in the frequency distribution spectra registered by seismic sensors located on the shore maximums corresponding to the characteristic frequency of the Lake Sevan and the underwater calibrating radiator was not observed (Figure 6). This sensor registered only the presence of the land calibration radiator and other artificial sources of acoustic low–frequency vibrations. Apparently from comparison of this spectra with the similar specters received by means of hydrophones and Messbauer acoustic detectors in the lower frequency range there are no maxima around the frequencies of 7.5 Hz and 15 Hz. This circumstance, first, can be explained with the technical parameters of the sensor determined during the experimental studies and specified in Table 1, secondly, it means that the water reservoir entirely is a resonant antenna system for registration of super week acoustic signals.

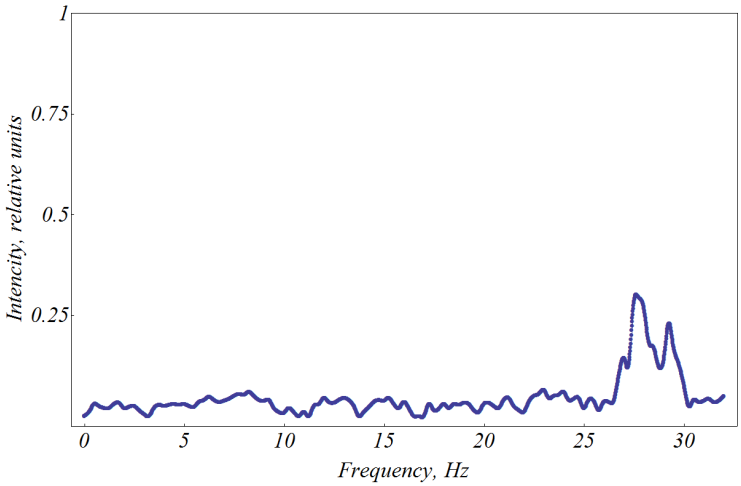

Fig. 6. The characteristic frequency distribution spectra of registered by the seismic sensor located on the shore of the Lake Sevan.

In all frequency distributions specters registered by Messbauer acoustic detectors and hydrophones maxima in the range about 7.5 Hz corresponding to the characteristic frequency of the Lake Sevan and the calibration maxima caused by the excited artificial sources of acoustic vibrations of different frequency, amplitude and form are presented.

One of the features registered during the experimental studies is the phenomenon of reverberation of acoustic signals in the resonant antenna system – the Lake Sevan. Due to utilization of artificial underwater and surface sources of acoustic vibrations of certain temporal and frequency characteristic in the registered temporary and modulation specters repeated excitations of primary vibration frequency and lowered amplitude is observed. The temporal specter registered by the hydrophone with observed phenomenon is visually presented in Figure 7.

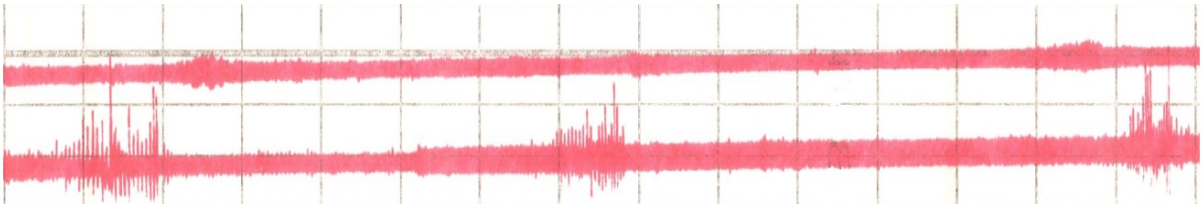

Fig. 7. The temporary spectra registered by hydrophone including the phenomenon of reverberation of acoustic vibration.

Researches on registration of frequency–amplitude characteristics of noise and determination of characteristic frequency of the Lake Parz–Lich were also conducted. These researches showed that the characteristic frequency of the Lake Parz–Lich is 18.2 Hz, and the level of noises in different frequency ranges 1.5–1.7 times are less, than on the Lake Sevan. During the experimental investigations which are carried out on the Lake Parz–Lich, the reverberation phenomena were not observed.

The analysis of characteristics of the frequency amplitude spectrums of noises of Lakes Sevan and Parz–Leitch based on the measurements of acoustic vibrations by Messbauer acoustic detectors, hydrophones and seismic sensor shows that frequency range is separated into three

main ranges. In the first range: 0 ÷ 5 Hz, generally noises from the surface of the lakes carried in main contribution to frequency distribution spectra of the lakes. In the range of 5 ÷ of 20 Hz generally the responses corresponding to microseismic and resonance characteristics of the spreading stratums and lakes are observed. In higher than 20 Hz frequency range in frequency distribution specters maximums which were caused by existence of artificial sources of acoustic vibrations are observed.

In the first frequency range registered specters almost do not changed. In the second range there irregular separate peaks at various frequencies which can be explained with variation of seismic, biological, structural and resonance characteristics of the area of registration were observed. In the upper range both irregular and regular variations are observed.

By the aim to determine the unknown irregular and regular sources of low–frequency vibrations the area of registration was monitored. Analyzing the registered frequency distributions specters it was established that some regular changes in frequency and temporary specters match frequency of trains passing near the area of registration, the frequency and the amplitude changes due to the characteristics of the trains.

The temporary characteristic specter of the acoustic vibrations originated from the cargo train and registered by the Messbauer acoustic detector is given in Figure 8.a, and the temporary characteristic specter of the same cargo train at the same time registered by the hydrophone is given in Figure 8.b.

During the conducted researches on definition of unknown irregular sources of acoustic vibrations temporary specters from the compressor (Figure 9.a), the moving truck (Figure 9.b) and the floating boat (Figure 9.c) were registered.

On separate specters sharply allocated signals with frequency about 10 Hz are observed (Figure 10). These signals as showed further researches were corresponding to supersonic airplanes upon transition of the sound barrier. In registered specters also the maximums corresponding to flights of passenger airplanes on the horizon over the lake are observed. Different intensity of signals from supersonic airplanes with frequency ~ 10 Hz are explained by the different height and distance at which there is transition of the sound barrier.

a)

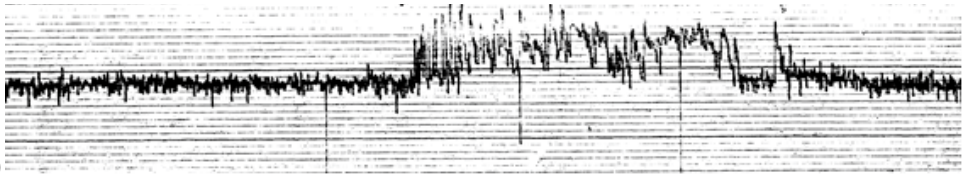

b)

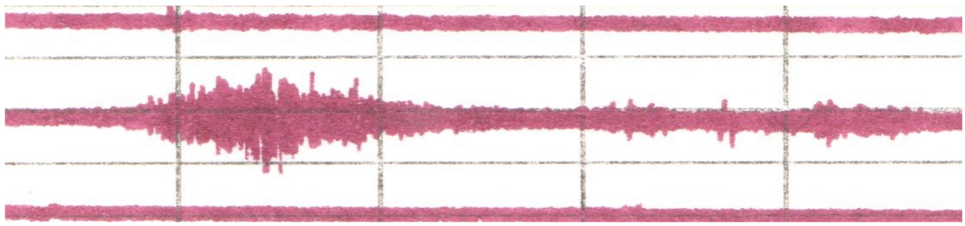

Fig. 8. The temporal frequency spectra of the cargo train registered by the Messbauer acoustic detector (a) and hydrophone (b).

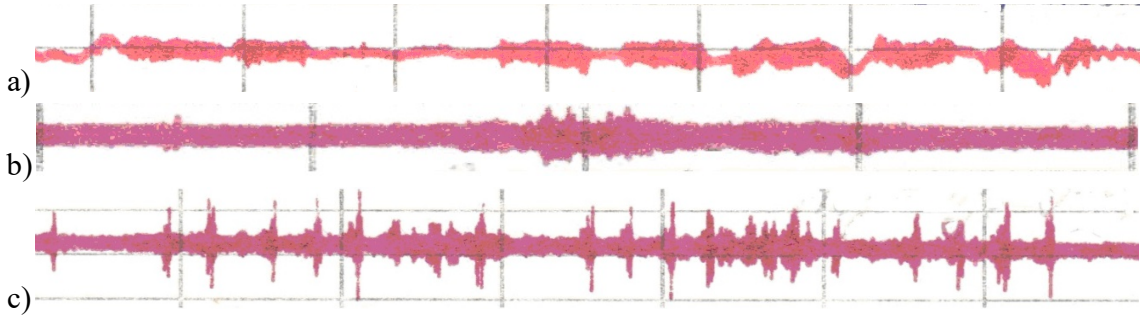

Fig. 9. The temporary specters of the compressor (a), truck (b) and boat (c) registered by the hydrophone.

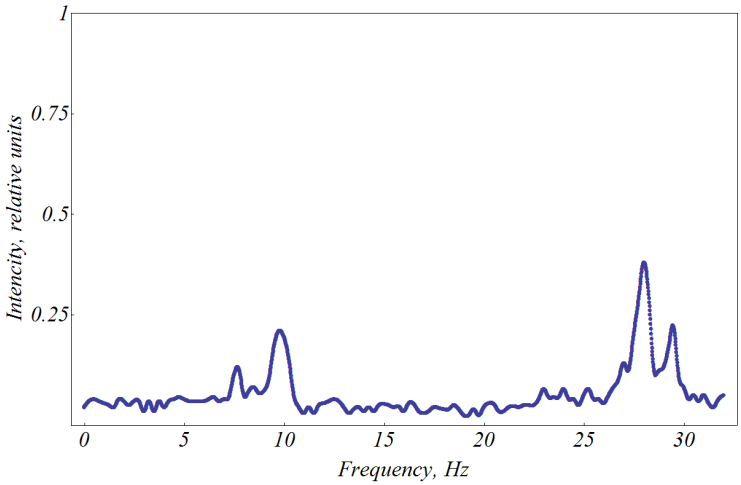

Fig. 10. The characteristic frequency distribution specter of upon transition by airplane of a sound barrier registered by the Messbauer detector.

We also have conducted experiments on registration of hydro acoustic waves originated from the artificial sources located at distances ~ 10 km and ~ 20 km from the area of registration. Artificial sources were located at depth of 20 m and 50 m. The frequency distribution specter of registered by Messbauer acoustic detectors is given in Figure 11. It is also possible to separate the specter into three ranges where maxima corresponding to the characteristic frequency of the Lake Sevan, the maximums of calibration radiators at 15 Hz and 30 Hz, and the maximums corresponding to acoustic vibrations from artificial sources are allocated. Time slots between the beginnings the first and second strips are made ~ by 5 sec., and between the beginnings the first and third strips – ~ 8 sec. The front two ranges can be interpreted as longitudinal (P) and transverse (S) component of the wave, propagating through the lower basalt stratum with speeds V_P =4000 m/sec and V_S = 3100 m/s respectively, and the third range as the longitudinal component of the wave passing through the top clay stratum with speed V_p = 2000 m/sec (the transverse component of the wave in clay stratum is strongly absorbed).

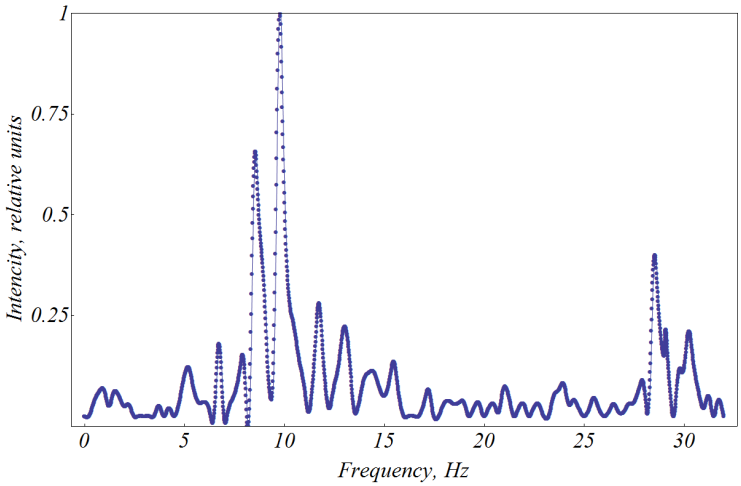

Fig. 11. The frequency distribution spectra from artificial source registered in the Lake Sevan.

Acoustic signals from the artificial sources were registered also on the Lake Parz–Lich. Unlike Sevan, on the specters the third range is absent, and the time slice between introductions of two ranges makes ~ 6 sec. The observed propagated acoustic wave speed corresponding to the first and second spectral ranges were V_1 = 4000m/sec. and V_2 = 3100m/sec. These speeds correspond to the longitudinal and transverse component of the waves passing through basalt stratum. The absence of the third range in the specter can be explained with absence of the clay stratum under the Lake Parz–Lich that it is confirmed also by geological data. Reverberation effect on the Lake Parz–Lich also was not observed.

The similar specters were observed at registration by hydrophones.

The obtained results of seismic and hydroacoustic signal from the artificial sources registered by seismic sensors, hydrophones and Messbauer detector showed that the ratio signal/noise for the seismic sensor is 2.5 times less, than for the hydrophone, and for the last is 2.5 times less in comparison with the Messbauer detector that is explained by higher sensitivity of Messbauer method of registration.

4. Conclusion

The results of experimental studies confirm the possibilities of utilization of lakes, water reservoirs and cavities in areas with certain geological structure as sensitive receivers and accumulating systems for registration of super week acoustic vibrations. The developed new acoustic detectors can be utilized for registration of acoustic vibrations excited from natural and artificial sources.

References.

1. Mkrtchyan A.R., Aslanyan H.A., Kocharyan L.A., Mkrtchyan A.H., Kotanjyan Kh.V., Baghdasaryan E.G., Harutyunyan G.R., Barseghyan N.A.”Lakes and waterfilled cavities as sensitive antennas and memory devices for acoustic vibrations of infrasonic frequencies” – International Symposium “Monitoring and Discrimination of Underground Nuclear Explosions and Earthquakes”, Moscow in November, 17–21, 1997.

2. A.R. Mkrtchyan, A.H. Mkrtchyan, A.S. Baghdasaryan, A.K. Atanesyan, V.V. Nalbandyan, T.G. Dovlatyan, V.N. Agabekyan, H.R. Muradyan, E.A. Mkrtchyan, S.A. Mirakyan, H.T. Hovhannesyan. Influence of Acoustic Fields on Main Parameters of Resonance Systems. Proceedings of the International Conference on Electron, Positron, Neutron and X–ray Scattering under External Influences. Yerevan–Meghri 2011, Armenia, ISBN 978–99941–2–710–8, p.149, 2012.
3. Мкртчян А.Г., Мкртчян А.Р., Котанджян Х.В., Асланян А.А., Арутюнян Э.М., Арутюнян А.С., Айвазян Г.А., Мурадян О.Р., Агабекян В.Н., Миракян С.А. О возможности определения параметров сейсмо–акустических волн методом обратных задач. Фундаментальные Исследования, No 8, с. 51–54, 2014.
4. А.Г. Мкртчян, А.Р. Мкртчян, А.С. Багдасарян, В.К. Сарьян, Х.В. Котанджян, А.А. Асланян, Г.А. Айвазян, О.Р. Мурадян, В.Н. Агабекян, С.А. Миракян. Определение параметров акустических колебаний методом обратных задач. Нелинейный Мир, No 6, Т.12, с. 42–47, 2014.
5. А.Г. Мкртчян, А.Р. Мкртчян, А.С. Багдасарян, В.К. Сарьян, Х.В. Котанджян, А.А. Асланян, О.Р. Мурадян, С.А. Миракян. Накопления акустических волн при распространении в слоистых средах. Нелинейный Мир, No 8, Т.12, с. 16–22, 2014.
6. S.A. Mirakyan. Propagation of acoustic waves through elastic stratified medium with heterogeneity in the form of rectangular reservoir. Armenian Journal of Physics, 2014, vol. 7, issue 2, pp. 102–105.
7. А.Р. Мкртчян, А.Г. Мкртчян, Э.М. Арутюнян, С.А. Миракян. Детектор акустических колебаний. Авторское свидетельство № 2864 А, 2014.
8. А.Р. Мкртчян, А.Г. Мкртчян, Э.М. Арутюнян, С.А. Миракян. Метод регистрации параметров акустических колебаний. Авторское свидетельство №2863 А, 2014.

Detector of Charged Particles Based on Synthesized New Composite Mediums (Si) $_{I}$ (Csj) $_{II}$ (Ag) $_{III}$

A.H. Mkrtchyan*, A.R. Mkrtchyan, V.V. Nalbandyan, A.S. Hakopyan, I.A. Babayan, A.A. Papazyan, E.S. Shadyan, A.A. Nalbandyan

Institute of Applied Problems of Physics NAS RA
25 Hr. Nersissian Str., Yerevan, Republic of Armenia, 0014

Abstract: *Experimental researches in the field of development of new generation of detectors for registration of the elementary charged particles based on the physical phenomena births, drift and multiplication of delta electrons, originated due to interaction of the charged particles with the synthesized composite mediums of different density in the presence of external accelerating field, were conducted. To carry out of experimental researches on the matrix of high ordered silicon composite mediums* ***(Si)$_{I}$(CsJ)$_{II}$(Ag)$_{III}$*** *of different thickness and relative density have been synthesized. On the basis of the synthesized mediums laboratory samples of registering systems of the charged fundamental particles have been developed and created. By the aim to explain the physical processes for charged elementary particles with some correctives the theoretical model developed for gamma quanta has been applied [8, 9]. As shown in the paper, the developed approach provided good coordination with the obtained experimental results. The preliminary analysis of the obtained experimental results confirms expediency of utilization of the phenomenon of the secondary electron emission, as operating basis of the new generation of detectors.*

1. Introduction

In previous years' improvement of the methods of registration of the elementary charged particles was restricted to difficulties of the basic character which do not allow to achieve the velocity of account more than 10^8 particles per second and the dead time necessary for restoration of the registration ability of the detector less 10^{-9} second [1–4]. All these difficulties are caused by the properties of the physical phenomena based on which appropriate registering systems have been developed. Therefore investigations on development of essentially new methods of registration based on other physical phenomena, have an actual importance. From this point of view practical interest represents investigation of the phenomena of the secondary electron emission [5].

A series of laboratory samples of detectors of gamma quanta, with supplied electronic and software, operating on the basis of the phenomena birth, drift and multiplication of delta electrons in porous mediums were developed and created by our group. Detectors were included in the experimental setups for conducting various experimental researches in order to detect gamma quanta in the energies range 1÷600keV and have passed corresponding approbation, having shown unique registering properties. The results of experimental investigations have confirmed the possibility of utilization of the synthesized porous layers as basic media for gamma quantum registration systems with high performance in a wide range of energies [6–10]. Investigations of the physical phenomena of birth, drift and multiplication of delta electrons in the synthesized mediums has shown that under certain conditions with application of an exterior

***E – mail:** amktychyan@sci.am*

accelerating electric field it is possible to control the secondary electron emission coefficient. It has experimentally been shown that the cross section of delta electrons birth with the characteristic time of the order 10^{-10}sec. and localization area round the point of passage of charged particle 10^{-3}cm, depends on value of applied accelerating electric field.

2. Experimental setup

By the aim to elicit the possibilities of utilization of the phenomena of the birth, drift and multiplication of delta electrons as basis of functioning of registering systems of the charged particles composite medium $(Si)_I(CsJ)_{II}(Ag)_{III}$ of different relative density and ordering degrees were synthesized. For synthesizing these environments a special vacuum experimental setup was developed. During the process of synthesis of working layers from porous medium various methods of vacuum evaporation of corresponding materials under certain conditions (pressure, speed of rotation of the substrate etc.) in atmosphere of dry inert gases or hydrogen were applied. Composite porous mediums were synthesized on the matrix of high ordered silicon with usage of alkaline–haloids compound CsJ and with supplement of silver in various relative proportions. Depending on the value of residual pressure in the vacuum chamber porous composite mediums with relative density from 0,3 % to 10 % were synthesized.

The detectors used in experimental researches consist of two grids of plane–parallel cathode electrodes the space between which is filled by the synthesized porous material. In the central plane of the cathodes the grid of anode electrode is located. The detector by operating principle is similar to the gas–discharge chamber with that difference that instead of gas as working substance the synthesized porous mediums were utilized. Now not all physical processes originating at interaction of the elementary charged particles with porous mediums can be described theoretically. Nevertheless, already now it is possible to deduce some aprioristic parities helping understanding of physical bases of operating principle of created detectors and allowing to optimize their parameters.

To carrying out the experimental researches universal vacuum installation in which the tested detectors were placed was developed and created. By applying electric voltage on the grid of electrodes of the detectors an accelerating electric field was originated. The yielded output impulses proceeding from the anode wire electrodes were registered with specially developed electronic device. On all path of experimental setup the vacuum of an order 10^{-6}torr was ensured. During the researches sources of alpha particles with energy 5MeV and electrons with energy 1MeV were used.

The schematic view of the experimental setup is given in Figure 1.

The bunch of charged particles, passing through systems of collimators (K) and magnets (M) placed in the vacuum chamber, falls on registering system with a working porous layer (RS). Due to interaction with a porous layer the charged particles stimulated surface ionization and yielded primary delta electrons, which were accelerating in porous of the porous layer under the influence of external electric field originated by applying electric voltage on contacts GA and GK. The born delta electron after acceleration interacted with the porous medium and yielded in the working layer new delta electron. This process repeated continually and leaded to avalanche reproduction of the delta electrons, which is accompanied with origination of corresponding pulse currents depending on energy delta electrons. Under the standard electric scheme the pulse current was transformed to voltage and on the output of registering system the analogue pulse

signal with duration ~10^{-9}sec is formed. The analogue pulse signal from registering system was directed to the developed high–speed SHF–HF shaper–converter, and then to the input of the analogue–digital converter, which is attached to the personal computer. The obtained data were processed and accumulated in the computer with specially developed software.

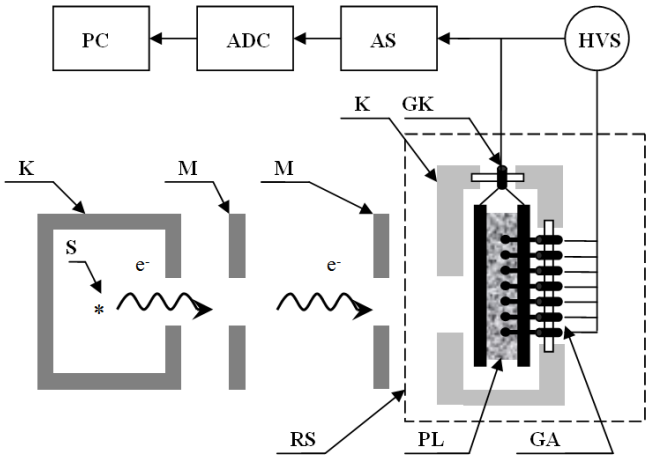

Fig. 1. The schematic view of experimental setup: S – source of the charged particles; K – collimator; M – magnetic system; RC – registering system; PL – porous layer; GA – grid of anodes; GK – grid of cathode; HVS – high voltage source; AS – amplifier–shaper; ADC – analogue–digital converter; PS – personal computer.

3. Experimental results and their discussion

All researches were conducted on experimental setups developed and created in IAPP NAS RA. Experimental researches were conducted under the scheme presented in paragraph 2.

3.1. Experiments on registration of alpha particles

Registration of alpha particles with energy of 5 MeV was carried out by utilization of detector with working composite porous materials $(Si)_I(CsJ)_{II}(Ag)_{III}$ with relative density from 0,5 % to 5 %. As have shown theoretical calculations, ionization losses of energy of alpha particles in substance of the detector of an order of 1,5 MeV. In Figure 2 values of registration efficiencies η_α depending on submitted working voltage U for the detector with relative density of medium of 2 % are presented. Similar pictures of dependences registration efficiencies also were obtained for other samples of detectors. Apparently from the Figure 2, with the increase of submitted accelerating electric voltage (U) efficiency of registration monotonously increases. At value of accelerating electric voltage (U) 780B efficiency of registration reaches almost 95 %. In the range of values of accelerating electric voltage from 780B to 1200B the efficiency of registration fluctuates within 95–100 %. The increase in value of submitted accelerating electric voltage from above 1200B leads to breakdowns in substance of the detector owing to what, the alpha particle, which trajectory pass through this area, are not registered that leads to reduction of the value of efficiency of registration of the detector.

Thus, utilization of the given type of detectors of the alpha particle allows to detect alpha particles with energy 5 Mev with efficiency of registration η_α up to 98 %, hence they can register with the same efficiency all other charged particles, which ionization losses of energy in

substance of the detector not less 1,5 MeV. To achieve the efficiency of registration of 100 % it is necessary to synthesize porous mediums with less smaller values of ionization losses of energy of the charged particles.

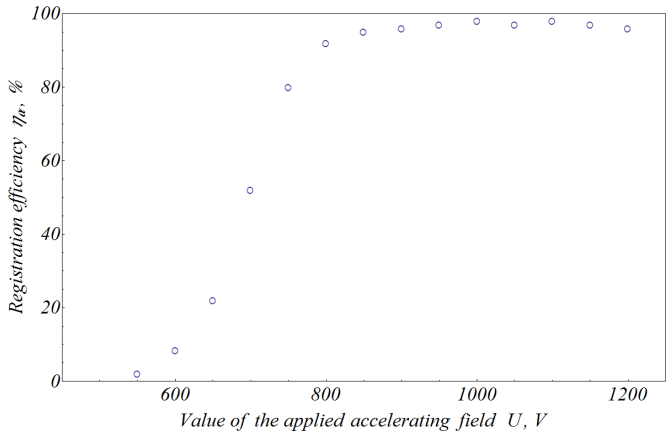

Fig. 2. Dependence of efficiency registration of alpha particles on value of the applied accelerating field.

3.2. Experiments on registration of electron

According to the formula of Bette– Blokh, ionization losses of electrons have a minimum in the field of distribution of energy Ee=0,9–1,1 MeV. Hence, electrons with energy 1MeV can be registered with 100 % efficiency, i.e. almost all charged particles in the given range of energy also can be registered with identical efficiency. In Fig. 3 results of investigation of efficiency of registration of electrons with energy 1 MeV with various developed by us laboratory samples of detectors are presented, the only difference between them in the thickness of working substance. Other parameters of the detectors were the same, as well as at registration of alpha particles. Squares, mugs and triangles designate the curves, measured efficiency of registration of the detectors with thickness of 200mkm, 250 mkm and 500 mkm, accordingly. At comparison of the curves of the dependence of efficiency of registration of alpha particles (Fig. 2) with the curves of the dependences of efficiency of registration of electrons (Fig. 3) it is possible to observe shift on the axis of value of working voltage of the detector. This shift is caused due to difference of ionization energy losses in substance between the alpha particles and electrons. Thereof, for reception of identical number of delta electrons in substance, it is necessary to increase the value of accelerating electric field. Due to the shift on the value of accelerating electric field, detectors get good selective ability, from fig. 3 it is visible that the relation η_e/η_α is an order of 3 % at U=850V, i.e. with the detector of the given type it is possible to carry out accurate registration of high ionized components of the radiation on the background of gamma and relativistic particles. From the figure 3 also it is visible that almost 100 %–s' registration of electrons becomes possible only at the thickness of the working layer of the detector in 500mkm. As show the calculations, ionization energy losses of electrons with minimum ionizing ability in the detector with the thickness of 500 mkm are almost 3 keV, hence, the lower energy range for almost 100 %–s' registration of the light charged elementary particles has value of order of 3 keV.

Approximately the same pictures of the dependence of the efficiency of registration of electrons were obtained for other developed detectors.

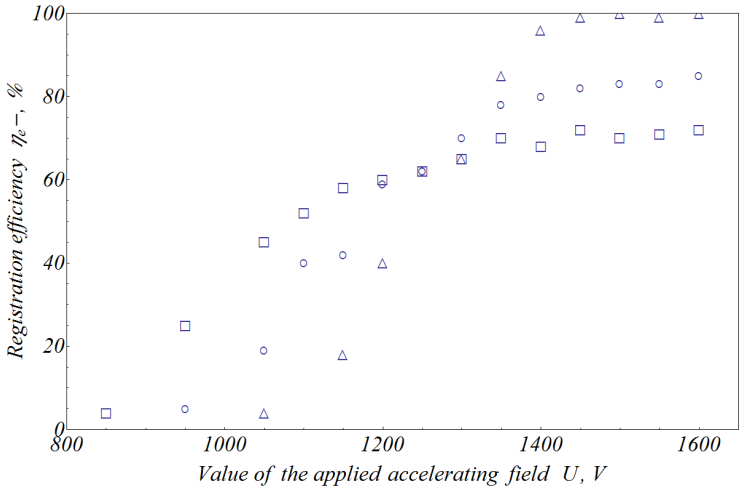

Fig. 3. Dependence of efficiency of registration of electrons on the value of applied electric field for detectors with different thickness of working substance (□ – 200μ, o – 250μ, Δ – 500μ).

4. Conclusion

The experimental and theoretical investigations have shown that utilization of the phenomena of the birth, drift and multiplication of the delta electrons in the synthesized composite porous mediums can provide possibility to create a new generation of detectors of alpha particles and electrons with surpassing in all parameters to existing analogous.

Further we are planning to carry out investigations on synthesis of new composite mediums with different ordering degree and relative density that will allow to develop new systems of registration of elementary particles with the improved characteristics.

References.

1. H. Bubert, H. Jenett. Surface and Thin Film Analysis: Principles, Instrumentation, Applications. Darmstadt, Wiley–VCH Verlag GmbH, 2002.
2. А.И. Абрамов, Ю.А. Казанский, Е.С. Матусевич. Основы экспериментальных методов ядерной физики. М., Энергоиздат, 1985.
3. Ю.К. Акимов, А.И. Калинин и др. Полупроводниковые детекторы ядерных частиц и их применение. М., Атомиздат, 1967.
4. Г. Е. Пикус. Основы теории полупроводниковых детекторов. М., Наука, 1965.
5. И.М.Бронштейн ,Б.С.Фрайман . Вторичная электронная эмиссия. Издательство: М.Наука 1969. 408 с.
6. A.H. Mkrtchyan, R.H. Ghajoyan, et. al. Proc. of the ISTC Int. Seminar ”Conversion Potential of Armenia and ISTC Programs”, October 2–7, Yerevan, Armenia, 163 (2000).
7. A.H.Mkrtchyan, R.H.Ghajoyan, Kh.S.Mehrabyan, G.R.Harutyunyan, H.M.Hovhanesyan, A.Gh.Balyan, G.A.Ayvazyan “Development of New Porous Materials and Creation of New Generation of Detectors of Ionizing Radiation Based on Them” Proc. of the 5th Int. Symp. on Radiation from Relativistic Electrons in Periodic Structures, September 10–14 , Lake Aya, Altai Mountains, Russia, 38 (2001).

8. А.Р. Мкртчян, А.Г. Мкртчян. Рентгеночувствительные пористые пленки. Патент РА, P20030103 (2004).
9. А.Г. Мкртчян, Г.А. Айвазян, В.В. Налбандян, М.М. Мирзоян, А.Н. Саргсян, А.А. Аршакян "Координаточувствительный быстродействующий детектор гамма–квантов на основе созданных пористых материалов" Известия НАН Армении, Физика, т.40, №3, с.200–208 (2005).
10. A.H. Mkrtchyan, A.S. Bagdasaryan, A.S. Ayvazyan, T.G. Dovlatyan, V.V. Nalbandyan, H.R. Muradyan, A.H. Aslanyan, S.A. Mirakyan, Detectors of Ionizing Radiation on the Basis of Porous Layers Doped with Aluminum Oxides, Proceedings, International Conference On Electrons, Positrons, Neutrons and X–Rays Scattering Under External Influences, Yerevan–Meghri, Armenia, p.159–161(2009).

Detector of Thermal Neutrons Based on Synthesised New Composite Mediums $(Si)_I (Lif)_{II}(Csj)_{III}(Ag)_{IV}$

A.H. Mkrtchyan*, A.R. Mkrtchyan, V.V. Nalbandyan, S.A. Mkhitaryan, G.A. Ayvazyan, A.A. Papazyan, E.S. Shadyan

Institute of Applied Problems of Physics NAS RA
25 Hr. Nersissian Str., Yerevan, Republic of Armenia, 0014

Abstract: *The present paper is devoted to investigations in the field of development of new detectors of thermal neutrons. This research is based on the investigations of the phenomenon of birth, drift and multiplication of delta electrons originated due to interaction of thermal neutrons with the synthesized new composite mediums* $(Si)_I(LiF)_{II}(CsJ)_{III}(Ag)_{IV}$ *under the influence of external accelerating electric field. These investigations are continuation of the cycle of researches [1–5] in which the possibility of utilization of the above mentioned phenomena as operating bases of more effective detectors of elementary particles were explored. Experimental data of the conducted investigations and the results of comparative analysis with theoretical calculations are presented.*

1. Introduction

At the present time investigations to improve the methods of registration of thermal neutrons are conducting. However more important are investigations on development of essentially new methods of registration. In this respect major practical interest is represented by the phenomena of birth, drift and multiplication of delta electrons in porous mediums due to interaction with elementary particles under the influence of external electric field. Investigations of these phenomena have shown that under certain conditions it is possible to control the cross section of these phenomena. On the basis of these physical phenomena detectors of gamma quanta with fine temporary–spatial properties and high energy resolution were developed [1–5].

The efficiency of registration of neutrons mainly depends from three factors: probability of interaction of neutron with substance of the radiator, probability of exit of the formed fission products from substance of the radiator and efficiency of registration of these yields. Registration of fission products usually does not represent major work. Depending on energy of neutrons, methods of their recording essentially differ. Till now there are no highly effective methods of registration of fast neutrons and consequently their registration occurs only after moderation of neutrons to thermal energies. In this field of energy, porous composite mediums reveal essentially new possibilities for highly effective registration.

For registration of thermal neutrons usually utilize either capture reactions, or fission reactions which with very high cross section occurs on some nucleus–radiators of neutrons. As a radiator the substances containing nucleus of helium (He), lithium (Li), boron (B) are most suitable and consequently response yields mainly are α – particles and protons. The thickness of radiator simultaneously should satisfy two requirements: to be potentially thick and to allow the formed charged particles exit substance of the radiator. In view of last requirement for each type of radiator, there is a critical thickness and magnification of thickness of the radiator at quantity

*E – mail: *amktychyan@sci.am*

major, than critical though increments probability of uptake of neutrons, but is not reflected in efficiency of registration. However, if the radiator is porous and an accelerating electric field is applied then the requirement for bounden exit of charged particles from substance of the porous radiator becomes inessential as effective drift of electrons of ionization can be achieved and secondary electronic emission will result. Thus depth of the exit of electrons is not restricted the porous radiator has no critical thickness.

Exothermic reactions (n, p) and (n, α) are most convenient for registration of slow neutrons by capture reactions, which occur with high cross section on some light nuclides:

$$n + {}^{3}He \rightarrow p + {}^{3}H + Q \approx 0,78MeV$$
$$n + {}^{6}Li \rightarrow {}^{4}He + {}^{3}H + Q \approx 4,78MeV \qquad (1a,1b,1в)$$
$$n + {}^{10}B \rightarrow {}^{4}He + {}^{7}Li + Q \approx 2,78MeV$$

where Q – energy of reaction. Till energies of neutrons of ten KeV the cross section of these reaction σ is proportional $E_n^{-0.5}$, where E_n is kinetic energy of neutron. Energy of capturing Q is proportioned between the formed charged particles, which in inverse proportion to their masses. For example, in reaction (1б) $E_{3H}/E_{4He} \sim M_{4He}/M_{3H}$. It must be mentioned, that even at very small energy of the neutron, the originated charged particles, possessing energy of reaction Q, form considerable ionization effect. So, in the same reaction (1б) $E_{3H} \approx 2,7$MeV, $E_{4He} \approx 2$Mev. In this is consisting conveniences of exothermic reactions for registration of neutrons. Taking account above mentioned facts among alkaline– haloids only suitable are compounds containing atoms of Li (LiF, LiCl, LiBr, LiI). Among these compounds good secondary electron emission properties have compound LiF.

On figure 1 dependence of absorption efficiency of thermal neutrons with energy E_n=0.025eV from the thickness of LiF and LiJ is given. With magnification of energy to E_n=10KeV absorption efficiency falls as $1/\sqrt{E}$.

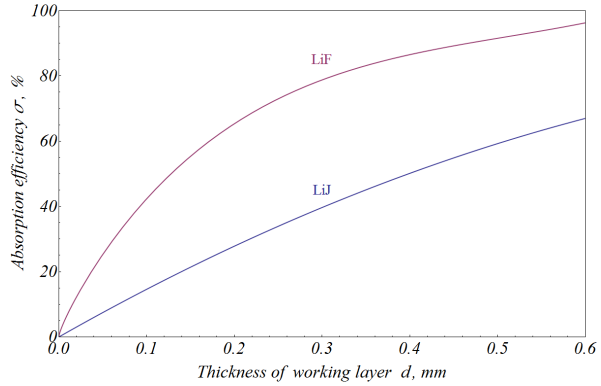

Fig. 1. Dependence of absorption efficiency of thermal neutrons on the thickness of operating porous layers LiJ and LiF

2. Experimental setup

For conducting the experimental investigation the laboratory sample of detectors of the thermal neutrons operating on the basis of the phenomenon of birth, drift and multiplication of secondary electrons in synthesized porous composite mediums $(Si)_I$ **$(LiF)_{II}$**$(CsJ)_{III}(Ag)_{IV}$ has been developed. Providing certain requirements (pressure, velocity of rotation of substrate etc.) and utilizing of different methods of vacuum deposition composite mediums $(Si)_I$ **$(LiF)_{II}$** $(CsJ)_{III}$ $(Ag)_{IV}$ with relative density of 0,2 %–10 % and different percentage correspondence of chemical combinations have been synthesized.

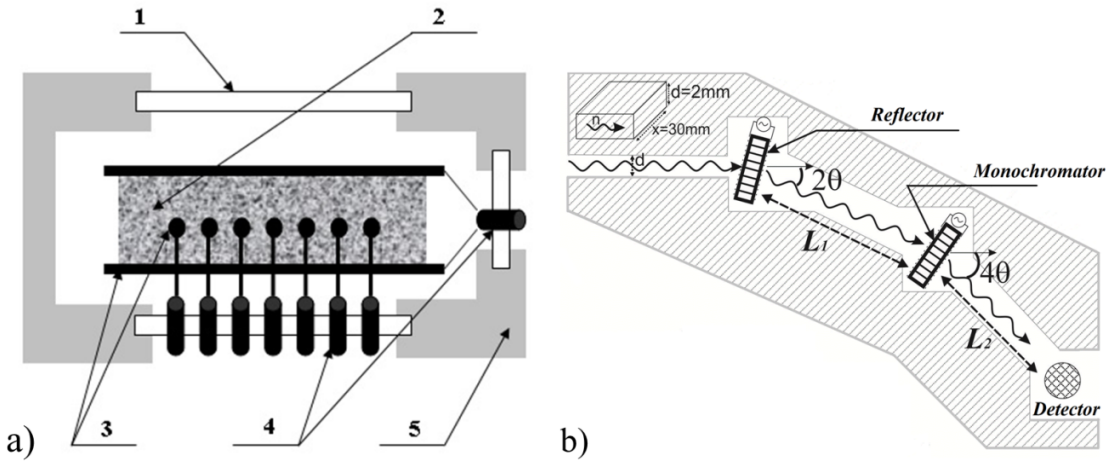

Fig. 2. a) Schematic view of the detector of thermal neutron and
b) schematic view of the experimental setup

In figure 2a the schematic view of the detector from a porous medium (2) placed in special vacuum chamber from stainless steel (5) with the vacuum tight window (1) from special material is given. By applying voltage on grid electrodes (4) and (3) the necessary accelerating electric field is created. Originated impulses which have proceeded from anodic wire electrodes, are registered by expressly developed electronic units.

On the construction, the developed registering systems can be compared to the proportional chamber with those odds that instead of gas as operating medium the synthesized medium serves. However on the performance characteristics and principles of operation they strongly differ that testifies to absolutely different processes occurring in gases and in multilayered composite mediums.

For carrying out the experimental researches a special experimental setup has been developed and created. The experimental setup schematic view is given in Figure 2b.

Utilization of new types of neutron monochromators gives the chance to determine with high accuracy the energy of thermal neutrons and to make calibration of the detector.

Passing through the system of collimation and monochromators, the neutron beam fell on the developed detector. By means of expressly developed electronic device the registered data are transmitted to accumulation and processing system.

3. Experimental results

To measure the efficiency of registration of neutrons, on either side of the cathodic electrodes of the detector, collateral to them, apart from them 5000μ the additional electrodes which are under a high voltage of the negative polarity in relation to the cathodic electrodes have been located. The space between additional and cathodic electrodes has been charged by substance of the radiator from LiF with relative density of 10 %, and in the central part composite medium $(Si)_I$**$(LiF)_{II}$**$(CsJ)_{III}(Ag)_{IV}$ different relative density. At passage of neutrons through the detector perpendicularly to the cathodic electrodes the quantity of substance of the radiator taking into account relative density was 10^3μ. Meanwhile ≈100 % efficiency of registration was provided. On figure 3 the detector count characteristic at registration of neutrons with energy E_n =0,025eV depending on the voltage U applied on radiator is given. Operating voltage corresponded to 100 %–s' efficiency of registration of the secondary electrons injected from the radiator. From the Figure 3 it is visible that with magnification of accelerating electric field U the count rate of the detector is incremented and in the rage of the value U=4000V reaches plateau. Above U=4500V breakdowns occurred in the radiator.

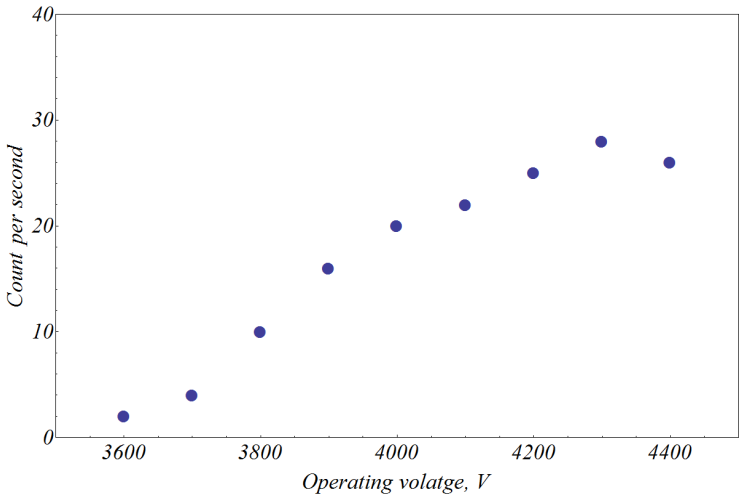

Fig. 3. The detector's count rate characteristic dependence on operating voltage

The behavior of the curve in the range of values up to Up=4000V is caused by magnification of number of secondary electrons n_e, injected from the radiator. When the median number of the injected electrons n_e reached quantities of registration with 100 %–s' efficiency, its further growth is not reflected any more in efficiency of recording that leads to plateau occurrence on the curve. Due to fluctuation n_e, value $\overline{n}_e$ at which 100 %–s' efficiency of registration is reached, is set by a relation: $\eta_e = 1 - e^{-\overline{n}_e}$ whence follows that $\overline{n}_e \approx 5$.

The plateau presence in count rate characteristics of the detector testifies about ≈100 %–s' efficiency of registration of neutrons. It also proves to be true calculations of geometry of measuring and passport data of performances of the neutron source.

4. Conclusion

Preliminary experimental and theoretical investigations have shown that utilization phenomenon of birth, drift and multiplication of secondary electrons in the new porous mediums synthesized by us can yield jolt in sphere of development of neutron detectors as new generation which surpass all existing similar detectors in the all explored parameters. Necessity of conducted of the further investigations in this field are advisable and actual.

References.

1. A.H. Mkrtchyan, R.H. Ghajoyan, et. al. Proc. of the ISTC Int. Seminar "Conversion Potential of Armenia and ISTC Programs", October 2–7, Yerevan, Armenia, 163 (2000).
2. A.H.Mkrtchyan, R.H.Ghajoyan, Kh.S.Mehrabyan, G.R.Harutyunyan, H.M.Hovhanesyan, A.Gh.Balyan, G.A.Ayvazyan "Development of New Porous Materials and Creation of New Generation of Detectors of Ionizing Radiation Based on Them" Proc. of the 5th Int. Symp. on Radiation from Relativistic Electrons in Periodic Structures, September 10–14 , Lake Aya, Altai Mountains, Russia, 38 (2001).
3. А.Р. Мкртчян, А.Г. Мкртчян. Рентгеночувствительные пористые пленки. Патент РА, P20030103 (2004).
4. А.Г. Мкртчян, Г.А. Айвазян, В.В. Налбандян, М.М. Мирзоян, А.Н. Саргсян, А.А. Аршакян "Координаточувствительный быстродействующий детектор гамма–квантов на основе созданных пористых материалов" Известия НАН Армении, Физика, т.40, №3, с.200–208 (2005).
5. A.H. Mkrtchyan, A.S. Bagdasaryan, A.S. Ayvazyan, T.G. Dovlatyan, V.V. Nalbandyan, H.R. Muradyan, A.H. Aslanyan, S.A. Mirakyan, Detectors of Ionizing Radiation on the Basis of Porous Layers Doped with Aluminum Oxides, Proceedings, International Conference On Electrons, Positrons, Neutrons and X–Rays Scattering Under External Influences, Yerevan–Meghri, Armenia, p.159–161(2009).

Neutron Diffraction Study of Phase Stresses Evolution in Two Phase Polycrystalline Al/Sic Composite During Elastoplastic Deformation

Andrzej Baczmański[1*], Elżbieta Gadalińska[2] , Sebastian Wroński[1], Przemysław Kot[1], Marcin Wroński[1], Mirosław Wróbel[3], Christian Scheffzük[4,5], Gizo Bokuchava[4], Krzysztof Wierzbanowski[1]

[1]AGH–University of Science and Technology,
WFiIS, al. Mickiewicza 30, 30–059 Kraków, Poland
[2]Institute of Aviation, al. Krakowska 110/114, 02–256 Warszawa, Poland
[3]AGH–University of Science and Technology,
WIMiIP, al. Mickiewicza 30, 30–059 Kraków, Poland
[4]Frank Laboratory of Neutron Physics, Joint Institute for Nuclear Research, Joliot–Curie st. 6, 141 980 Dubna, Russian Federation
[5]Karlsruhe Institute of Technology, AGW, Adenauerring 20b, 76131 Karlsruhe, — Germany

Keywords: neutron diffraction; lattice strains; elastic–plastic self–consistent model; metal matrix composites, phase stresses.

Abstract: The stress partitioning between phases, phase stress relaxation as well as origins of Al/SiC_p composite strengthening are studied in the present work. In this aim, the measurements of lattice strains by neutron diffraction were performed in situ during tensile test up to sample fracture. The experimental results were compared with the results of elastic–plastic self–consistent model. It was found that thermal origin phase stresses relax in the beginning of plastic deformation of Al/SiC_p composite. The evolution of lattice strains in both phases can be correctly simulated by the elastic–plastic self–consistent model only if the relaxation of initial stresses is taken into account. A major role in the strengthening of the studied composite plays a location of stresses in the SiC_p reinforcement, however the hardness of Al metal matrix is also important.

1. Introduction

Metal Matrix Composites (MMC) are an interesting alternative to classical alloys. Their superior mechanical properties – in comparison to classical alloys – are their unique stiffness, high specific strength and/or ductility, as well as improved wear resistance. The strengthening mechanism of the MMC is obtained by: the addition of reinforcement which possess definitely superior mechanical properties than the matrix and by locking dislocation movement which depends on the mechanical properties, geometry and space distribution of the constituents [1].

The Al/SiC_p composite studied in this work consists of the Al2124 aluminium alloy matrix with silicon carbide particles reinforcement. Aluminium is a material of relatively low density and high ductility, but the limitation for its application is caused by relatively low

[*]**E – mail:** *andrzej.baczmanski@fis.agh.edu.pl*

strength, hardness, stiffness and tribological properties [2,3]. However, strength and hardness of aluminium can be improved by alloying and heat treatment leading to precipitation or age hardening by the phases precipitated in a solid state reaction, as is in the case of the classical Al–Cu or Al–Cu–Mg alloys, or by the strengthening by particles insoluble during the powder compaction technology, as in the case of the composites reinforced by silicon carbide particles.

In the present work the mechanical behaviour of the Al/SiC_p composite was studied using neutron diffraction. The advantage of diffraction methods is that the mechanical behaviour of different phases of polycrystalline material can be independently studied during sample loading [cf. 4 – 10]. This method enables measuring of the lattice strains/stresses selectively for Al–matrix and SiC_p – reinforcement constituents, only for the crystallites contributing to the recorded diffraction peaks [cf. 11 – 14]. The results of neutron experiment are usually analysed and interpreted using elastic–plastic models.

The elastic–plastic behaviour of Al/SiC_p composites have already been studied using the Finite Element Method (FEM) [15–18] and the influence of the SiC_p reinforcement on the overall elastic–plastic properties including stress relaxation during reinforcement fraction [17] and decohesion processes [18] were predicted. The Eshelby type models [19] were also applied to calculate the stress in the ellipsoidal reinforcement inclusion and in the metal matrix [20–24]. The results of the Elastic–Plastic Self–Consistent (EPSC) model were sucesfully compared with diffraction measurements in which the lattice strains in both phases were determined during the bending test [24]. It was shown that the se EPSC model correctly predicts the behaviour of the particle reinforced MMC and the stress partitioning between phases in the case of relatively low content of the reinforcement. Both the diffraction method as well as the self–consistent model provide statistical information concerning the mean strains/stresses for groups of crystallites and phases, but the spatial heterogeneities of these quantities in the matrix, around the reinforcement particles are not visible in a diffraction experiment performed for a large sample volume.

The lattice strains in both phases of Al/SiC_p composite were already measured in situ during heat treatment [25], during elastic–plastic loading [14, 24] and evolution of residual stresses was determined after thermal or mechanical treatments [13, 26]. A significant influence on stress partitioning between phases was also determined using diffraction during damage process [27, 28]. The interpretation of the diffraction data using Eshelby type models (including self–consistent method) showed that important mismatch stresses are induced during composite cooling due to the difference in thermal expansion coefficient of the phases [29]. These stresses can be significantly modified by plastic deformation [30] or combination of thermal and mechanical treatments [31] long before damage of the material. The release/modification of the residual phase stresses is of vital importance due to their influence on fatigue cracking process in MMC [32].

The aim of this work was the study of mechanical behaviour of both components of Al/SiC_p composite using neutron diffraction in situ during tensile test. The interpretation of the experimental results was done by comparing the measured lattice strains and overall mechanical composite behaviour with the prediction of a self–consistent model. The focus of the present investigation was put mainly on the evolution of phase stresses during external loading of the sample, including process of stress relaxation. The neutron diffraction measurements analysed with help of EPSC model were used to determine a value of tensile sample strain for which

hydrostatic thermal stresses were released. Finally, the mechanical properties of the matrix and reinforcement and their influence on the strengthening of the composite were determined.

2. Experiment and model prediction

2.1. Materials

Materials tested in this work are the Al2124 alloys (Table 1) either unreinforced or reinforced with SiC particles. The Al/SiC_p composite produced by powder metallurgy route was provided by Materion Aerospace Metal Composites, Farnborough, Hampshire, UK. This technique is based on blending and compaction of mixed aluminium and SiC powders. The amount of the reinforcement particles in the composite is 17.8% by volume and the particle average size is 0.7 μm.

Table 1. Chemical composition of the Al2124 alloy (mass fraction, %).

Cu	Mg	Mn	Ti	Zn	Cr	Fe	Si	Al
4.18	1.46	0.52	0.15	0.25	0.1	0.3	0.2	balance

Two sorts of the material with different heat treatments were studied. The first one was subjected to the T6 heat treatment (i.e. solution treatment at 491 °C for 6 h and then cold water quenching to produce a supersaturated solid solution, and finally artificial aging for 4 h at 191 °C. This treatment resulted in the hardening of the Al2124 alloy by semi–coherent Cu–Al–Mg precipitates [33]. The second sort of the composite was subjected to the T1 heat treatment, consisting in the natural aging with a calm air cooling directly after 6 h annealing at 491 °C. In this work, the composite specimens subjected to the heat treatments T6 and T1 are marked respectively Al/SiC_p–T6 and Al/SiC_p–T1, while the unreinforced aluminium alloy sample subjected to T6 treatment is labelled as Al2124–T6.

In Fig. 1, the SEM image of the examined Al/SiC_p specimen is presented. A significant dispersion of the particles size around the nominal value 0.7 μm and their not perfectly uniform spatial distribution can be observed. However, in the case of the large relative gauge volume in the diffraction experiment, a macroscopically homogeneous material was assumed in this study.

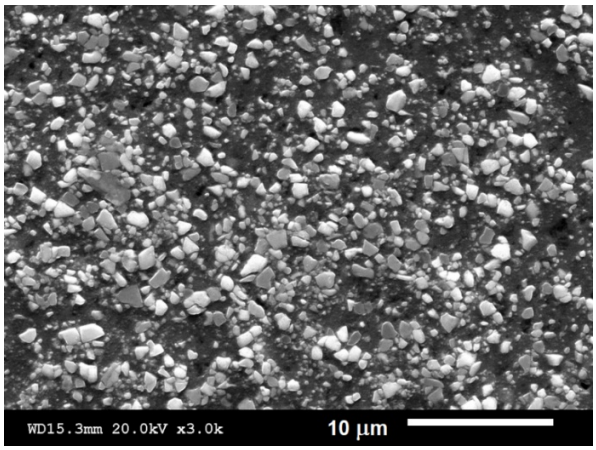

Fig. 1. The microstructure of the Al/SiC_p composite – SEM image. Some particles of SiC were separated from the Al2124 matrix during surface preparation by etching

The crystal structure and crystallographic texture of the composite phases were determined on the Panalytical Empyrean diffractometer using Cu K alpha X–ray radiation. The Rietveld analysis of the experimental results showed that the 6H polytype with hexagonal structure is dominant (content of ca. 80%) in the investigated SiC powder, while the aluminium alloy Al2124 has a face centred cubic structure. No significant crystallographic texture was found in both phases of the composite.

2.2. Neutron diffraction measurements

The lattice strains in the studied materials were measured using a time of flight (TOF) neutron diffraction method on the EPSILON–MDS and FSD diffractometers [34, 35] installed at the IBR–2 pulsed reactor in the JINR in Dubna (Russia). On the FSD diffractometer the evolution of crystal structure and coefficient of thermal expansion in the temperature range 20ºC–500 ºC were investigated for the SiC powder and the Al2124 alloy [36]. The main experiments were performed on the EPSILON–MDS diffractometer (at ambient temperature) using two configurations presented in Fig. 2. The first configuration (Fig. 2a) with two detectors *L2* and *L8* (other detectors were shaded by the tensile rig) was applied during the in situ tensile test for the dog–bone shaped samples having a square cross section 4 mm x 4 mm and a gauge length of 15 mm.

The applied loads were measured in situ by load cell and the macroscopic strain was determined ex situ by an extensometer connected to an identical sample subjected to the same loads. To obtain satisfactory counting statistics, the diffraction measurements through the whole cross section of the sample were done using the wide incident beam with an aperture of 10 mm. The diffraction measurements were performed for constant grip positions (corresponding to given sample strains), after stabilisation of the applied load, which decreased over a period of about ½ hour. Both composite samples (Al/SiC_p–T1 and Al/SiC_p–T6) fractured very close to macroscopic strain of E_{11} = 3% and in such a case the last diffraction measurement was done on one part of the broken sample. Consequently, the last measurement of unreinforced alloy Al2124–T6 was also performed after the sample unloading at E_{11} = 3%.

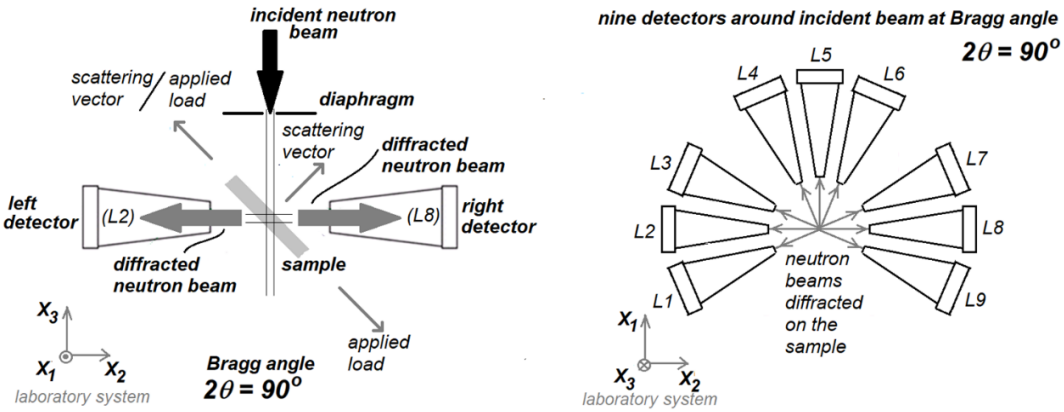

a) **b)**

Fig. 2. A schematic view of the experimental setup at the EPSILON–MDS diffractometer

The relative lattice strains in direction of the load $\langle \varepsilon_{11} \rangle_{\{hkl\}}$ and in the transverse direction $\langle \varepsilon_{22} \rangle_{\{hkl\}}$ were calculated using Eq. 1:

$$\langle \varepsilon_{11} \rangle_{\{hkl\}} = \frac{\langle d_{LD} \rangle^{\Sigma}_{\{hkl\}} - \langle d_{LD} \rangle^{0}_{\{hkl\}}}{\langle d_{LD} \rangle^{0}_{\{hkl\}}} \text{ and } \langle \varepsilon_{22} \rangle_{\{hkl\}} = \frac{\langle d_{TD} \rangle^{\Sigma}_{\{hkl\}} - \langle d_{TD} \rangle^{0}_{\{hkl\}}}{\langle d_{TD} \rangle^{0}_{\{hkl\}}} \quad (1)$$

where $\langle d \rangle^{\Sigma}_{\{hkl\}}$ and $\langle d \rangle^{0}_{\{hkl\}}$ are the interplanar spacings determined for the loaded (for given applied stress Σ_{11}) and non–loaded sample (initial, i.e. for $\Sigma_{11} = 0$); the $<\ldots>_{\{hkl\}}$ brackets denote an average over the diffracting grains volume for given reflection *hkl*. Indices LD and TD mean that the interplanar spacing were measured in the direction of the applied load and in the transverse direction, respectively.

Additionally, the ex situ diffraction measurements were performed for the initial as well deformed/fractured samples using the second configuration with nine detector banks arranged around the sample at the EPSILON–MDS diffractometer (*L1 – L9*) as shown in Fig. 2b [34]. In this case the tensile machine was removed and the measurements were performed for two sample positions, the first at the orientation shown in Fig. 2 and the next after rotation by 90º around the sample long axis. In principle, the measurements of the interplanar spacings for the 18 orientations enable determining of the stress tensor for each phase if the strain free parameters are known.

2.3. Elastic-plastic self-consistent model

In this work, the prediction of stresses evolution during elastic and elastic–plastic processes was done using the EPSC model proposed by Lipinski and Berveiller [37, 38] and applied to two phase materials by Baczmanski et al. [7, 24]. This model is based on the interaction of the grains with the surrounding matrix described by Eshelby tensor [19]. The model predictions were performed for a set of 2000 spherical grains representing 17.8% volume fraction of SiC reinforcement (356 grains) and 82.2% of the Al matrix (1644 grains). Because of weak crystallographic textures, the orientations of grain lattice were randomly generated and corresponding single crystal elastic constants were assigned to the grains of both phases (cf. Table 2). The spherical inclusions and zero residual stresses were assumed for the particles of SiC reinforcement and for the Al2124 matrix. The elastic–plastic deformation with slip systems <110> {111} were assumed for aluminium, while only elastic deformation was assumed for SiC grains. In the case of the tensile tests, calculations were performed for various values of the critical resolved shear stress (CRSS, τ_c) and the hardening parameter (H) of the Al2124 matrix [37,38,7,24] (assuming linear and isotropic work hardening process for small deformations considered in this work). The optimal values of τ_c and H were determined by comparing the experimental and theoretical lattice strain evolutions for all the measured reflections, as well as macroscopic dependence of overall stress vs. sample strain. The same procedure of experimental data analysis was carried out for the Al2124–T6 alloy, but in this case the single phase polycrystalline aggregate consisting of 2000 aluminum grains was considered.

Table 2. Single crystal elastic constants and coefficient of thermal expansion for SiC and Al2124 alloy at room temperature.

Material	Single crystal elastic constants (GPa) [37, 38]					CTE (10^{-6} K^{-1}) [37,39]
	c_{11}^{SiC}	c_{12}^{SiC}	c_{13}^{SiC}	c_{33}^{SiC}	c_{44}^{SiC}	
6H SiC	501	111	52	553	163	22.9 – 24.7
Al	105.8	60.4	60.4	28.3	28.3	4.0 – 4.9

3. Results

3.1. Macroscopic behaviour of the Al/SiC$_p$ composite and Al2124 alloy

Firstly, the dependence of the applied stress vs. sample strain was analysed in order to choose the best model parameters. In Fig. 3a the macroscopic plots obtained in the tensile test for the Al2124–T6 alloy and Al/SiC$_p$–T6 composite are compared with the prediction of the EPSC model. The values of $\boldsymbol{\tau_c}$ and H for slip system <110> {111} were adjusted in order to fit the theoretical macroscopic stress–strain plot to the experimental one obtained for the Al2124–T6 alloy. A very good convergence of the model and experimental plots both in the elastic and plastic ranges of deformation was obtained for the elastic constants given in Table 2 and plastic slip system parameters shown in Table 3. Next, the properties of the unreinforced Al2124–T6 alloy were assumed for the matrix of the Al/SiC$_p$–T6 composite (cf. the T6 treatment in Table 3), and the tensile test was predicted for this composite, using elastic constant of the 6H–SiC polytype given in Table 2. It was found that the EPSC model correctly predicts elastic and plastic deformation of the studied composite at a macroscopic scale (Fig. 3a), when the CRSS and hardening parameter determined for Al2124–T6 alloy (Table 3) are used for the matrix.

Using the model prediction, the role of SiC$_p$ in the hardening of Al/SiC$_p$ was also studied. To do this, the evolution of von Mises stress calculated for each phase within the Al/SiC$_p$–T6 composite as well as for the Al2124–T6 alloy are shown in Fig. 3b. It was found that this stress changes almost identically in the Al2124–T6 alloy (without reinforcement) and in this alloy being a matrix in the Al/SiC$_p$–T6 composite, i.e. the theoretical curves representing aluminium overlap and agree with the experimental ones obtained for the unreinforced Al2124–T6 alloy. This means that the SiC$_p$ particles do not cause significant hardening of the aluminium matrix. The overall macrostress for the composite is much higher comparing with Al2124–T6 alloy only due to large stress accumulated in elastically deformed SiC$_p$ reinforcement, as shown in Fig. 3b. It should be emphasized, however, that until now no experimental information on the state of stresses in SiC$_p$ is provided, therefore the stress partitioning between the composite phases is shown in section 3.3.

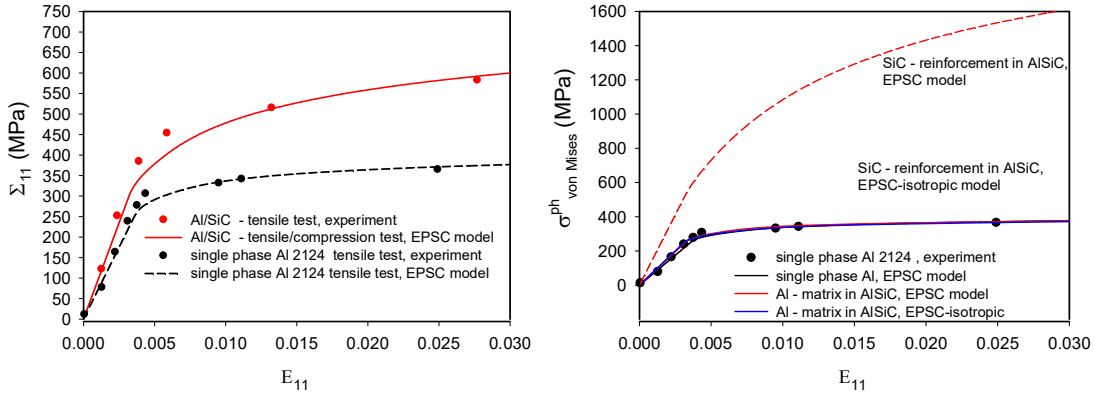

a) b)

Fig. 3. Overall stress vs. sample strain (a) and von Mises stresses in phases (b) in the tensile test performed for the Al2124–T6 alloy without reinforcement and the Al/SiC_p–T6 composite (T6). The experimental results are compared with EPSC prediction for single crystal elastic constants given in Table 2 and plastic parameters presented in Table 3

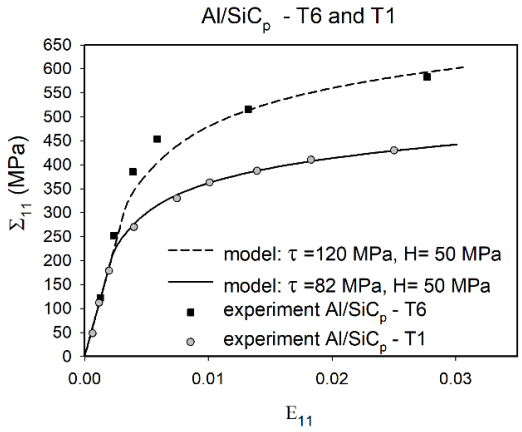

Fig. 4. Macroscopic dependence of macroscopic stress (after stabilisation) vs. macroscopic strain for the Al/SiC_p (T1 and T6) composite subjected to tensile tests. The experimental results are compared with EPSC prediction for single crystal elastic constants given in Table 2 and plastic parameters presented in Table 3

The analysis of the macroscopic stress vs strain dependence was performed also for the Al/SiC_p–T1 composite. It was found that the value of the CRSS determined from the EPSC model adjustment to the macroscopic curves (Fig. 4) is much lower for the T1 treatment in comparison with that for the T6 treatment, while the hardening parameter *H* is similar for both treatments (cf. Table 3). The macroscopic stress vs strain plots (Fig. 4) showed an important influence of the matrix state on the overall mechanical behaviour of the composite, which is much softer after the T1 treatment than after the T6 treatment.

Table 3. Value of critical resolved shear stress τ_c and hardening parameter H determined for studied composites and Al2124 alloy.

Material	**Sample treatment**	**CRSS (τ_c) (MPa)**	**Hardening parameter (H) (MPa)**
Al2124	T6	120	50
Al/SiC_p	T6	120	50
	T1	82	50

3.2. Relaxation of thermally induced stresses

Here, the analysis of phase stresses in the initial and fractured composite specimens is presented (based on results of the ex situ measurement with nine detectors, Fig. 2b). Data analysis was performed with the Kröner–Eshelby model used for calculation of the X–ray elastic constants (XECs) for each phase separately [39]. In the case of 6H–SiC, the diffraction peaks for 006/102, 108/110 and 116/202 reflections were measured, while for the Al2124 matrix – 111, 200, 220, 311 and 220 reflections were taken into account. The stress values were calculated on the basis of experimental data using the least square method in which the tree principal stress components were adjusted, while the shear stresses were neglected due to symmetry of the sheet from which the samples were cut. The measurements at elevated temperatures up to 500ºC (FSD diffractometer) performed for 6H–SiC powder showed that the structure of SiC_p did not change during T1 and T6 heat treatments. Therefore the stress free interplanar spacings were measured for the same powder that was used as the composite reinforcement. However, the accurate value of a stress free lattice parameter (a_0) for the aluminium alloy was not available due to a differences in the precipitation solution process at elevated temperatures occurring in the Al2124 alloy (or powder) and in this alloy creating the Al2124 matrix of the composite [36]. The stress analysis was based on the decomposition of the stress tensor into two parts, containing the hydrostatic component (p) and deviatoric components (q, r, s):

$$\begin{bmatrix} \sigma_{11} & 0 & 0 \\ 0 & \sigma_{22} & 0 \\ 0 & 0 & \sigma_{33} \end{bmatrix} = \begin{bmatrix} p & 0 & 0 \\ 0 & p & 0 \\ 0 & 0 & p \end{bmatrix} + \begin{bmatrix} q & 0 & 0 \\ 0 & r & 0 \\ 0 & 0 & s \end{bmatrix} \quad \text{and} \quad p = (\sigma_{11} + \sigma_{22} + \sigma_{33})/3 \qquad (2)$$

The deviatoric stresses were correctly determined for both phases because they do not depend on the values of the stress free lattice parameters. Also, the value of hydrostatic stress p for SiC_p reinforcement, based on the lattice parameters determined for SiC powder, can be determined. However, the hydrostatic stress in the aluminium matrix subjected to the given heat treatment should be deduced from the mixture law for the case of non–loaded sample:

$$(1-f)\sigma^{Al} + f\sigma^{SiC} = 0 \qquad \text{for non–loaded sample,} \qquad (3a)$$

$$(1-f)\sigma^{Al} + f\sigma^{SiC} = \Sigma \qquad \text{for sample under load with macroscopic stress } \Sigma \qquad (3b)$$

where $f = 0.178$ is a volume fraction of SiC_p and the above law is fulfilled for all stress components as well as for deviatoric and hydrostatic stresses.

In the stress analysis performed for aluminium matrix, an approximated value of a_0 was temporarily assumed. Then, the determined hydrostatic stresses were adjusted by shifting p by the same value simultaneously for the results obtained for the initial and fractured samples in order to fulfil Eq. 3a. This correction corresponds to the adjustment of a_0 value for both states (initial and fractured), subjected previously to the same heat treatment. The so–obtained stresses for all specimens examined during the tensile test and for both phases are presented in Tables 4 and 5, for the Al/SiC_p–T1 and Al/SiC_p–T6 specimens, respectively. It was found that the mean stresses calculated for p values, according to Eq. 2, are approximately equal to zero within the uncertainty range, simultaneously for the initial and deformed samples. This condition is fulfilled for both materials subjected to the treatments T6 and T1 (cf. the first column in Tables 4 and 5). An evolution of the hydrostatic stresses during deformation was also calculated from relative changes of interplanar spacings for the deformed sample with respect to the initial one. Although the latter method does not allow for calculating the absolute values of the hydrostatic stresses, however in the calculations of the relative changes of these stresses (Δp) the values of a_0 are not required. As shown in the second columns of Tables 4 and 5, the Δp values are very close to the differences between the hydrostatic stresses p for the deformed and initial samples (cf. the first columns). Moreover, the mixture law (Eq. 3) applied to the Δp values gives the mean value close to zero (within uncertainty range), i.e. the equilibrium condition is fulfilled. Therefore, it can be concluded that the values of the hydrostatic stresses p and their changes Δp are correctly determined.

Table 4. Stress state in both phases in the initial and deformed Al/SiC (T6) specimen. The mean stresses are calculated according to the mixture law given by Eq. 3.

	Specimen state	$\boldsymbol{p}$ $\boldsymbol{(MPa)}$	$\boldsymbol{\Delta p}$ $\boldsymbol{(MPa)}$	$\boldsymbol{q}$ $\boldsymbol{(MPa)}$	$\boldsymbol{r}$ $\boldsymbol{(MPa)}$	$\boldsymbol{s}$ $\boldsymbol{(MPa)}$
Al2124–T6	Initial	122 ± 18	–96 ± 15	29 ± 17	–37 ± 20	8 ± 18
	Deformed	33 ± 11		–73 ± 21	29 ± 25	44 ±23
SiC	Initial	–614 ± 115	512 ± 26	143 ± 89	–6 ± 93	–136 ± 93
	Deformed	–103 ± 55		306 ± 51	–182 ± 56	–124 ± 57
Mean Eq. 3	Initial	–10 ± 25	13 ± 13	49 ±21	–32 ± 23	–18 ± 22
	Deformed	10 ± 12		–6 ± 20	–9 ± 23	14 ± 21

Table 5. Stress state in both phases in the initial and deformed Al/SiC_p (T1) specimen. The mean stresses are calculated according to the mixture law given by Eq. 3.

	Specimen state	$\boldsymbol{p}$ $\boldsymbol{(MPa)}$	$\boldsymbol{\Delta p}$ $\boldsymbol{(MPa)}$	$\boldsymbol{q}$ $\boldsymbol{(MPa)}$	$\boldsymbol{r}$ $\boldsymbol{(MPa)}$	$\boldsymbol{s}$ $\boldsymbol{(MPa)}$
Al2124–T1	Initial	126 ± 18	–74 ± 15	26 ± 7	–9 ± 7	–18 ± 7
	Deformed	59 ± 11		–75 ± 9	42 ± 9	34 ± 9
SiC	Initial	–647 ± 85	403 ± 27	75 ± 73	44 ± 77	–119 ± 77
	Deformed	–200 ± 49		183 ± 45	–68 ± 51	–115 ± 51
Mean Eq. 3	Initial	–11 ± 21	11 ± 13	35 ± 15	0 ± 15	–37 ± 15
	Deformed	12.5 ± 13		–29 ± 11	22 ± 12	7 ± 12

It was found that the large hydrostatic compressive stress in SiC_p reinforcement and tensile stress in aluminium matrix were generated during T1 or T6 treatment. This effect is caused by a difference in coefficient of thermal expansion (CTE) for the composite components (Table 2), leading to larger volume contraction for aluminium matrix comparing with particles of SiC_p, during the cooling process. On the other hand, small deviatoric stresses in the initial sample are caused by possible temperature gradients in the heat treated sheets as well as plastic deformation during sample machining. Also, it should be stated that the equilibrium condition (Eq. 3) is not strictly fulfilled for the components of deviatoric stresses in the initial samples, probably due the relatively large experimental uncertainties, comparing to small values of these stresses. More pronounced deviatoric stresses, resulting from phase interaction during plastic deformation, were measured after tensile test. The components of the latter stresses in some approximation fulfil equilibrium condition.

Analysing the results presented in Tables 4 and 5, it can concluded that an important decrease in hydrostatic compressive stress occurred in the SiC_p reinforcement corresponding to the relaxation of initially large thermal stress. Also, the decrease in the hydrostatic part of the mean tensile stress in the Al2124 matrix has been observed as a consequence of stress relaxation around the SiC_p inclusions. The process of stress relaxation has been studied post factum for the already fractured sample, but it is interesting to determine when this phenomenon start to occurs. To solve this problem, it is necessary to follow the evolution of the stresses and lattice strains measured in situ during the deformation tests.

3.3. Evolution of lattice strains in the Al/SiC_p composite and Al alloy

The lattice strain evolutions in the Al and SiC_p phases along the direction of applied load $\langle\varepsilon_{11}\rangle_{\{hkl\}}$ and in the perpendicular direction $\langle\varepsilon_{22}\rangle_{\{hkl\}}$ (Eq. 1) were determined in situ using configuration with two detectors shown in Fig. 2 a and compared with EPSC model (Figs. 5–7). Model calculations were performed up to the maximum sample strain before fracture/unloading (i.e. E_{11} = 3%) for the CRSS (τ_c) and hardening parameter (H), determined previously for the studied samples on the basis of the mechanical curves (Table 3). In the case of fractured composite samples the experimental macrostrain was unknown, therefore the experimental lattice strains for broken samples were inserted close to simulated macroscopic strain after unloading.

A very good result of the experiment – model comparison was found for the relative lattice strains (cf. Eq. 1) measured for the Al2124–T6 specimen under the tensile load both in the elastic and elastic–plastic range of deformation up to E_{11} = 3%. The model predicted values of lattice strains are slightly overestimated during the tensile test, but for the unloaded sample the modelling calculations hit the experimental points correctly (Fig. 5). The lattice strain evolution for different *hkl* reflections confirms that the EPSC model correctly predicts the partitioning of stresses between the grains in the Al2124–T6 alloy [42, 43] and well reproduces the anisotropy of plastic deformation for the different groups of grains.

To solve the problem of stress partitioning between phases, the lattice strains measured in situ in the SiC_p and in Al2124 constituents of the composite during the tensile test were analysed. The important influence of the evolution of mean values of lattice strain along loading direction measured for reflections 200, 111, 220, 311 in aluminium and for reflections 006/102, 108/110, 202/116 in SiC are shown in Fig. 6. In this figure, the results for the sample subjected to

the treatments T6 and T1 are shown. The experimentally measured relative lattice strains were determined using Eq. 1 and then the strains caused by initial stresses (cf. Tables 4 and 5) were superimposed. Subsequently, the lattice strains were calculated using the EPSC model with two assumptions, i.e. accounting for the initial stresses given in Tables 4 and 5 or setting zero stresses for both phases.

Analysing Fig. 6, it was found that for the elastic deformation, a good agreement between the experiment and model was obtained taking into account the initial stresses, while for the further elastic–plastic deformation much better accordance was observed with zero initial stress assumption (cf. Fig. 6). Therefore, it can be concluded that the initial phase stresses relax at very small tensile deformation (ca. 0.2– 0.8 %), and consequently do not influence further stress partitioning and mechanical behaviour of the composite phases. The residual lattice strains in both phases are also well predicted by the model, assuming zero initial stresses. This results well agree with previous works showing relaxation and complete exchange of stress state in the Al/SiC_p composite and also in other materials subjected to plastic deformation [11, 13, 30, 31].

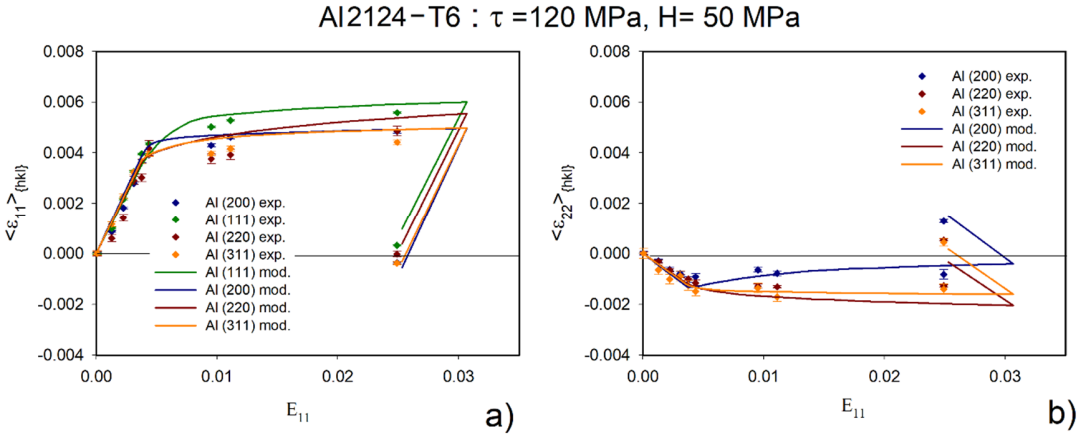

Fig. 5. Lattice strains measured for different reflections *hkl* (points) during tensile test are compared with the EPSC modelling (lines) performed for the parameters given in Tables 2 and 3. The lattice strains in loading direction (a) and perpendicular direction (b) are presented as functions of macrostrain

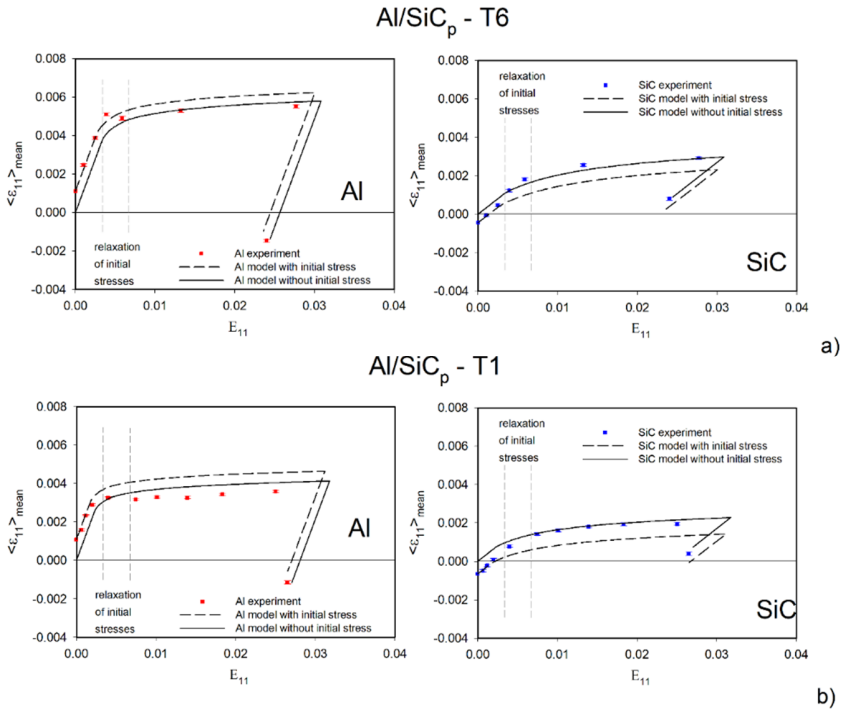

Fig. 6. The experimental and model mean lattice strains along the loading direction $\langle\varepsilon_{11}\rangle_{mean}$ in both phases of Al/SiC–T6 and Al/SiC–T1 samples, calculated as the average over 200, 111, 220, 311 reflections in Al and over 006/102, 108/110, 202/116 reflections in SiC. The model results were computed for parameters given in Tables 2 and 3, starting from initial stresses or assuming zero initial stresses

The new finding of the present work is that the stress relaxation occurs very early i.e. for a small elastic–plastic deformation, close to the yield point of the matrix. Finally, in Fig. 6 the lattice strains for individual reflections *hkl* in both phases of Al/SiC–T6 sample measured along applied load and in the transverse direction are shown. The experimental results agree with the model prediction if in the calculation the initial stresses are taken into account for the beginning of deformation (up to about E_{11} = 0.2% of sample strain), and zero initial stress is assumed for further deformation (above about E_{11} = 0.8% of sample strain). This can be explained due to discussed above relaxation of hydrostatic stress in the beginning of plastic deformation.

4. Conclusions

The diffraction method combined with crystallographic models are an important tool in the study of the mechanical behaviour of polycrystalline materials at the scale of phases or particular grains. In this work a complete study of the mechanical behaviour of the Al/SiC$_p$ composite containing 17.8% of SiC reinforcement with a grain size of 0.7 μm was performed using neutron diffraction and EPSC model. Based on the results of in situ measurements during the tensile test the following conclusions can be formulated:

1) The thermal stresses relax during tensile deformation only at the beginning of plastic strain and a new stress state is created.

2) The strain/stress partitioning between the composite phases during the tensile test can be well predicted by the EPSC model, except for the thermal stress relaxation, which must be introduced into the model at the yield point.
3) Anisotropy of plastic incompatibility stresses occurs during and after plastic deformation, both for the unreinforced and reinforced aluminium alloy and this effect is approximately predicted by EPSC model.
4) Strengthening of the Al/SiC_p composite results mainly from the localisation of high stress in the reinforcement, while the hardening of the matrix by the SiC_p particles is insignificant.
5) Using two different thermal treatments for the initial material, it was shown that the overall strength of the composite depends on the hardness of the Al2124 matrix, which can be increased through appropriate treatment.

Acknowledgements

This work was supported by grant from the Polish National Scientific Centre (NCN) No. UMO–2017/25/B/ST8/00134. The authors wish to thank the Frank Laboratory of Neutron Physics (JINR Dubna, Russia) for providing the neutrons. The neutron experiments were supported by the Polish–JINR Programme 2017 (item 24), and the operation of the EPSILON diffractometer was supported by the Federal Ministry for Education and Research in Germany.

References.

1. K.V.C. Amitesh, Aluminium based Metal Matrix Composites for aerospace application: a literature review, IOSR J. Mech. Civ. Eng. 12 (2015) 31–36.
2. S.B. Prabu, L. Karunamoorthy, S. Kathiresan, and B. Mohan, Influence of stirring speed and stirring time on distribution of particles in cast metal matrix composite, J. Mater. Process. Technol. 171 (2006) 268–273.
3. M.M. Boopathi, K.P. Arulshri, and N. Iyandurai, Evaluation of mechanical properties of aluminium alloy 2024 reinforced with silicon carbide and fly ash hybrid metal matrix composites, Am. J. Appl. Sci. 10 (2013) 219– 229.
4. M.R. Daymond, H.G. Priesmeyer, Elastic–plastic deformation of ferritic steel and cementite studied by neutron diffraction and self–consistent modeling, Acta Mater. 50 (2002) 1613–1623.
5. G. Garcés, K. Máthis, P. Pérez, J. Čapek, P. Adeva, Effect of reinforcing shape on twinning in extruded magnesium matrix composites, Mat. Sci. Eng. A 666 (2016) 48–53.
6. N. Jia, Z.H. Cong, X. Sun, S. Cheng, Z.H. Nie, Y. Ren, P.K. Liaw, Y.D. Wang, An in situ high energy X–ray diffraction study of micromechanical behavior of multiple phases in advanced high–strength steels, Acta Mater. 57 (2009) 3965–3977.
7. A. Baczmański, C. Braham, Elastic–plastic Properties of Duplex Steel Determined Using Neutron Diffraction and Self–Consistent Model, Acta Mater. 52 (2004) 1133–1142.
8. S. Cai, M.R. Daymond, and R.A. Holt, Deformation of high β–phase fraction Zr–Nb alloys at room temperature, Acta Mater. 60 (2012), pp. 3355–3369.

9. A. Baczmański, Y. Zhao, E. Gadalińska, L. Le Joncour, S. Wroński, C. Braham, B. Panicaud, M. François, T. Buslaps, K. Soloducha M., Elastic–plastic deformation and damage process in duplex stainless steels studied using synchrotron and neutron diffractions in comparison with a self–consistent model, International Journal of Plasticity. 81 (2016), 102–122
10. C.J. Davidson, T.R. Finlayson, M. E. Fitzpatrick, J.R. Griffiths, E.C. Oliver and Q. Wang, Observations of the stress developed in Si inclusion following plastic flow in the matrix of an Al–Si–Mg alloy, Phil. Mag. 97 (2017) 1398–1417.
11. M.E. Fitzpatrick, P.J. Withers, A. Baczmański, M.T. Hutchings, R. Levy, M.Ceretti and A. Lodini, Changes in the misfit stresses in an Al/SiCp metal matrix composite under plastic strain, Acta Mater. 50 (2002) 1031–1040.
12. A.J. Allen, M.A.M. Bourke, S. Dawes, M.T. Hutchings, and P.J. Withers, The analysis of internal strains measured by neutron diffraction in Al/SiC metal matrix composites, Acta Metall. Mater. 40 (1992) 2361–2373.
13. M. Dutta , G. Bruno , L. Edwards, M.E. Fitzpatrick, Neutron diffraction measurement of the internal stresses following heat treatment of a plastically deformed Al/SiC particulate metal–matrix composite, Acta Mater. 52 (2004) 3881–3888
14. M.R. Daymond and M.E. Fitzpatrick, Effect of cyclic plasticity on internal stresses in a metal matrix composite, Metall. Mater. Trans. A 37 (2006) 1977–1986.
15. T.W. Clyne, P.J. Withers, An Introduction to Metal Matrix Composites, Cambridge Solid State Science Series, Cambridge, 1993.
16.] J. Segurado, J. Llorca, A numerical approximation to the elastic properties of sphere–reinforced composites, J. Mech. Phys. Solids, 50 (2002) 2107 – 2121.
17. J. Segurado, J. LLorca, A new three–dimensional interface finite element to simulate fracture in composites. Int. J. Solids Struct. 41 (2004) 2977–2993.
18. J.J. Williams, J.Segurado, J.LLorca, N.Chawla, Three dimensional (3D) microstructure–based modeling of interfacial decohesion in particle reinforced metal matrix composites. Mat. Sci. Eng. A 557 (2012) 113–118.
19. J.D. Eshelby, The determination of the elastic field of an ellipsoidal inclusion, and related problems, Proc. R. Soc. London A. 241 (1957), 376–396.
20. A. Roatta and R.E. Bolmaro, An Eshelby inclusion–based model for the study of stresses and plastic strain localization in metal matrix composites. I: General formulation and its application to round particles, Mater. Sci. Eng. A 229 (1997) 182–191.
21. C. Gonzalez, J. LLorca, A self–consistent approach to the elastic–plastic behavior of two–phase materials including damage, J. Mech. Phys. Solids 48 (2000) 675–692.
22. O. Pierard, C. Gonzalez, J. Segurado b, J. LLorca , I. Doghri, Micromechanics of elastic–plastic materials reinforced with ellipsoidal inclusions. Int. J. Solids and Str. 44 (2007) 6945–6962.
23. M. Kursa, K. Kowalczyk–Gajewska, M.J. Lewandowski, H. Petryk, Elastic–plastic properties of metal matrix composites: Validation of meanfield approaches. Eur. J. Mech. A Solids 68 (2018) 53–66.

24. A. Baczmański, R. Levy–Tubiana, M.E. Fitzpatrick and A. Lodini, Elastic–plastic properties of Al/SiCp metal matrix composite studied by self–consistent modelling and neutron diffraction, Acta Mater. 52 (2004) 1565–1577.
25. G. Requena, D, C. Yubero, J. Corrochano, J. Repper, G. Garcés, Stress relaxation during thermal cycling of particle reinforced aluminium matrix composites, Composites: Part A 43 (2012) 1981–1988.
26. P. Fernandez–Castrillo, G. Bruno, G. Gonzalez–Doncel, Neutron and synchrotron radiation diffraction study of the matrix residual stress evolution with plastic deformation in aluminum alloys and composites, Mat. Sci. Eng. A 487 (2008) 26–32.
27. S. Cabeza, T. Mishurova, G. Bruno, G. Garcés, G. Requena, The role of reinforcement orientation on the damage evolution of AlSi12CuMgNi +15% Al2O3 under compression, Scripta Materialia 122 (2016) 115–118.
28. S. Cabeza, T. Mishurova, G. Garcés, I. Sevostianov, G. Requena, and G. Bruno, Stress–induced damage evolution in cast AlSi12CuMgNi alloy with one– and two–ceramic, J. Mater. Sci. 52 (2017) 10198–10216.
29. M.E. Fitzpatrick , M.T. Hutchings , P.J. Withers, The determination of the profile of macrostress and thermal mismatch stress through an A1/SiCp composite plate from the average residual strains measured in each phase, Physica B, 213–214 (1995) 790–792
30. R. Levy–Tubiana, A. Baczmanski, and A. Lodini, Relaxation of thermal mismatch stress due to plastic deformation in an Al/SiCp metal matrix composite, Mater. Sci. Eng. A 341 (2003), 74–86.
31. G. Bruno, M. Ceretti, E. Girardin, A. Giuliani , A. Manescu, Relaxation of residual stress in MMC after combined plastic deformation and heat treatment, Scripta Mat. 51 (2004) 999–1004
32. M.E. Fitzpatrick, M. Dutta, L. Edwards, Determination by neutron diffraction of effect of plasticity on crack tip strains in a metal matrix composite, Mat. Sci. Tech. 14 (1998) 980–6.
33. L.F. Mondolfo, Aluminium Alloys: Structure and Properties, Butter Worths, London/Boston, 1976.
34. K. Walther, A. Frischbutter, Ch. Scheffzük, M. Korobshenko, F. Levchanovski, A. Kirillov, N. Astachova, and S. Murashkevich, EPSILON–MDS – a neutron time–of–flight diffractometer for strain measurements, Solid State Phenomena 105 (2005) 67–70.
35. A.M. Balagurov, G.D. Bokuchava, Kuzmin E.S., Tamonov A.V., Zhuk V.V. Neutron RTOF diffractometer FSD for residual stress investigation, Zeitschrift für Kristallographie, Suppl. Issue No. 23 (2006) 217–222.
36. P. Kot, A. Baczmański, E. Gadalińska, S. Wroński, M. Wroński, M. Wróbel, Ch. Scheffzük, G. Bokuchava, Neutron diffraction study of phase stresses evolution in Al/SiC composite during heat treatment and compression, in preparation for publication in J. Mech. Phys. Solids.
37. P. Lipinski and M. Berveiller, Elastic–plasticity of micro– inhomogeneous metals at large strains. Int. J. Plast. 5 (1989) 149–172.

38. P. Lipinski, M. Berveiller, E. Reubrez, J. Morreale, Transition theories of elastic–plastic deformation of metallic polycrystals, J. Arch. Appl. Mech. 65, (1995) 291–311.
39. L.L. Snead, T. Nozawa, Y.Katoh, T.–S. Byun, S. Kondo, D.A. Petti, Handbook of SiC properties for fuel performance modeling, J. of Nucl. Mater. 371 (2007) 329–377.
40. G. Simmons and H. Wang, Crystal Elastic Constants and Calculated Aggregate Properties: A Handbook. Cambridge, MA/London: The MIT Press; 1971.
41. ASM Handbook, Volume 2: Properties and Selection: Nonferrous Alloys and Special–Purpose Materials ASM Handbook Committee, Properties of Wrought Aluminum and Aluminum Alloys, ASM International, 1990, 62–122.
42. S. Wronski, A. Baczmanski, R. Dakhlaoui, C. Braham, K. Wierzbanowski, E.C. Oliver, Determination of stress field in textured duplex steel using TOF neutron diffraction method. Acta Mater. 55 (2007) 6219–6233.
43. A. Baczmański, N. Hfaiedh, M. François, K. Wierzbanowski, Plastic Incompatibility Stresses, Stored Elastic Energy in Plastically Deformed Copper, Mater. Sci. Eng. A, 501 (2009) 153–165.

Diffraction on an Aperture Located Between Media With Different Refractive Indices

A.R. Mkrtchyan[1], A.A.Lalayan[2*], H.S. Eritsyan[1,2], A.L.Margaryan[1]

[1]Institute of Applied Problems of Physics NAS of the Republic of Armenia
25 Hrachya Nersissian Str., Yerevan, Republic of Armenia, 0014
[2]Yerevan State University, 1 A. Manoogian Str., Yerevan, Republic of Armenia, 0025

Fraunhofer diffraction of a plane electromagnetic wave on an aperture in an opaque screen located between two media with different refractive indices, as well as between vacuum and refractive material medium, in the presence and absence of birefringence is considered. The angular distribution of the intensity of diffracted radiation is determined.

The case of an anisotropic medium is also considered. Some peculiarities of diffraction in this formulation are revealed, in particular, the nonreciprocity phenomenon.

It is shown that the intensity of the diffracting wave, depending on the wavelength, depends on the refractive index of the medium into which electromagnetic radiation penetrates, which leads to the possibility of creating new optical elements, the scope of which, in particular, can be the creation of alternative schemes of the light energy storage devices. An experimental study of the nonreciprocity phenomenon was carried out.

1. Introduction

The diffraction of an electromagnetic wave on an infinite screen with a slit or a round hole is known to be considered in optics in the case when a vacuum is located in front of the screen and also after the screen [1,2]. In material media diffraction phenomenon is usually considered in situations when it is caused not by the limitation of the wave front (diffraction from the edges of slits or openings), but mainly by the periodicity of the inhomogeneities of the medium in which the wave propagates [3–5].

In [6], the Fraunhofer diffraction of a plane wave by an infinite slit was considered, when on both sides of the screen with a slit there is not a vacuum, but a medium with different values of the refractive index (one of which may be a vacuum). It was shown, in particular, that in such a situation there is a nonreciprocity of the passage of an electromagnetic wave through a slit. This phenomenon is of great practical importance in the creation of optical systems that have nonequivalence of mutually opposite directions of transmission of electromagnetic waves [7–8].

In the present work, we consider diffraction by a rectangular slit and circular hole in a metal screen, on both sides of which there are media with different values of the refractive index.

[*]**E – mail:** *alalayan@ysu.am*

2. The intensity of an electromagnetic wave diffracted from air into a dielectric medium through a slit in the screen

Let us consider the normal incidence of an electromagnetic wave on an opaque screen with a slit width **a** (Fig. 1). Then the wave intensity in the interval $\theta \div \theta + d\theta$ is determined by the formula [9] :

$$dI = \frac{I_0}{2\pi} \times \frac{sin^2(ka\theta)}{(ka\theta)^2} d(ka\theta) \tag{1}$$

where I_0 – is the intensity of the incident wave, θ – is the angle of deviation from the direction of the normal to the screen of the diffracted wave and $k = \frac{\omega}{c} n$.

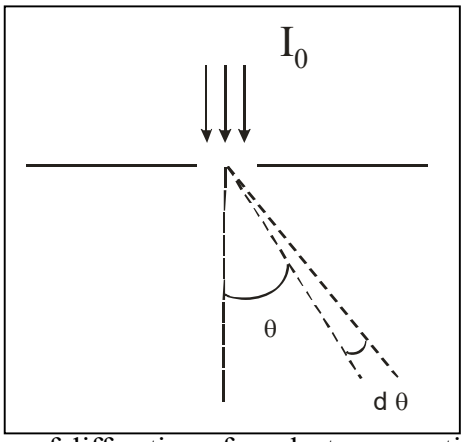

Fig. 1. Scheme of diffraction of an electromagnetic wave on a round hole.

The total intensity I of the diffracted wave is equal to:

$$I = \frac{I_0}{2\pi} \times \int_{-\frac{\pi}{2}}^{\frac{\pi}{2}} \frac{sin^2(ka\theta)}{(ka\theta)^2} d(ka\theta) \tag{2}$$

where $-\frac{\pi}{2}$ and $\frac{\pi}{2}$ are the boundaries of the θ.

In expression (2), the integral is not analytically solved. Figure 2 shows the dependence of I on k, obtained by numerical methods, showing that with increasing k the intensity of the wave behind the slit also increases.

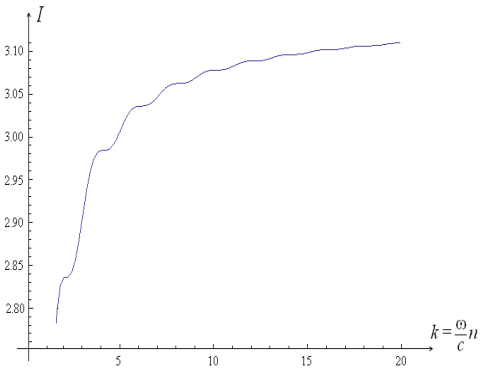

Fig. 2. The dependence of the integral (2) on k at a fixed frequency ω

The increase in intensity with an increase in the refractive index is understandable: for the shorter wavelength, the more intensity passage through a narrow gap (commensurate with λ). Mathematically, an increase in the intensity I with an increase in the refractive index can be understood as a result of a broadening of the integration interval in formula (2) with an increase in the value of the refractive index.

Indeed, Fig. 3 shows the dependence of the function $\frac{\sin^2(\theta)}{\theta^2}$ on θ. The value of the integral over this function is equal to the hatched area.

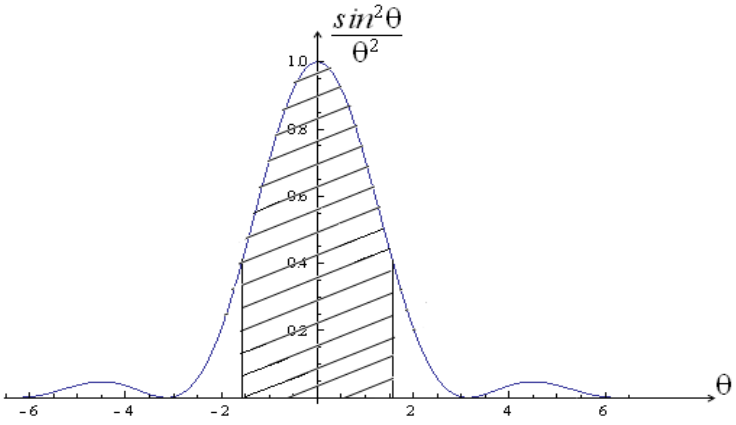

Fig. 3, The dependence of the integrand $\frac{\sin^2(\theta)}{\theta^2}$ on θ

With an increase in the refractive index, the integration limits are equal to $-\frac{\pi}{2}$ and $\frac{\pi}{2}$ and become $-\left(\frac{\omega}{c}na\frac{\pi}{2}\right)$ and $\left(\frac{\omega}{c}na\frac{\pi}{2}\right)$, that is, with an increase in n, the integration region grows, which leads to a change in the value of the integral.

3. The experimental part.

We experimentally investigated the diffraction passage of an electromagnetic wave through a narrow slit cut in a metal plate mounted between two dielectric plates of two different materials with different refractive indices. For the convenience of measurements, an electromagnetic radiation source in the range 40–50 GHz was used. The experimental design is shown in Fig. 4. A metal slit 3 with a width of 5 mm was made of a metal (brass) plate 1 mm thick, plates 2 and 4 of teflon (polytetrafluoroethylene) and plexiglas (polymethylmethacrylate) of the same thickness (equal to 3.5 mm), which have different values of the refractive index were attached to this metal plate from different sides, Directly at the output of such a three–layer structure, a radiation detector 5 was placed. Next, the analog signal from the detector was converted to digital by means of ADC 6 and entered into a computer.

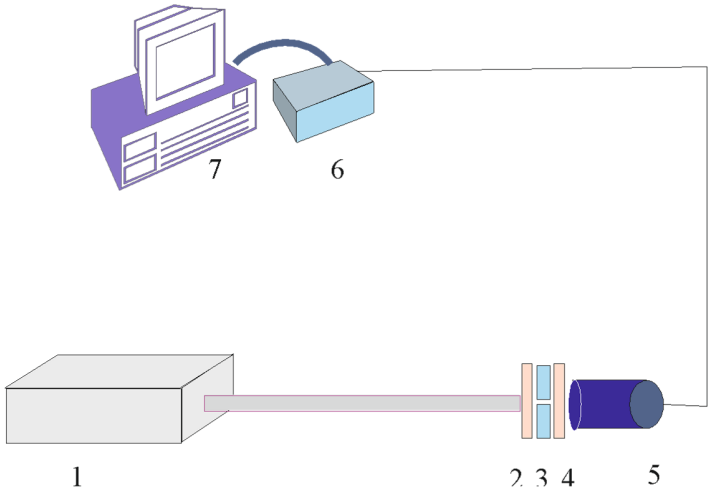

Fig. 4, The scheme of the experimental setup. 1 – electromagnetic radiation generator, 2 and 4 – plates of dielectric material, 3 – metal plate with a rectangular slit, 5 – radiation detector, 6 – ADC, 7 – computer

Note that the range of refractive indices of amorphous polymers is much smaller than that of traditional optical glasses and reaches up to n = 1.70 [7]. Accordingly, the n value for PMMA is 1.51. For polymeric materials, a significant decrease in the refractive index is possible by introducing fluorine atoms into the molecule of the initial monomer. Fluorinated polymers have the lowest refractive indices ($n \leq 1.4$) [8]. In the case of teflon that used in the experiment, n is of the order of 1.35–1.38 [9].

For a slit of 5mm wide, the measurements showed the difference in the amplitude of the transmitted signal depending on arrangement of the teflon and plexiglas plates (Fig. 5).

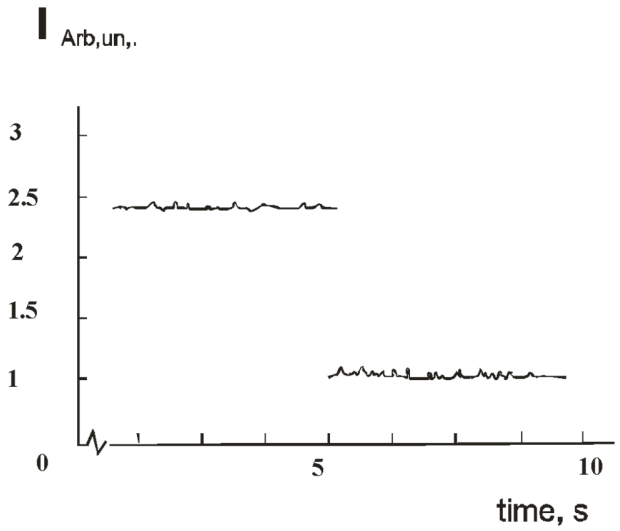

Fig. 5. Dependence of the amplitude of the transmitted signal on the change in the arrangement of teflon and plexiglas plates relative to the slit. **a**: plexiglass–slit–teflon, **b**: teflon–slit–plexiglass, microwave generator frequency was 41 GHz, slit width was 5 mm

As can be seen from the figure, for the case of radiation passing in the teflon–slit–plexiglas system, the amplitude of the recorded signal is 2.5 times different from the amplitude for the reverse sequence of the same dielectric plates, which experimentally confirms the nonreciprocity of the passage of the electromagnetic wave through the gap in the described optical system.

4. Diffraction on the round hole

The calculation of the influence of the refractive index of the medium where diffracted radiation penetrates at the round hole is based on the well–known formula [9]

$$dI = I_0 \frac{J_1^2(ak\theta)}{\theta^2} d\theta \qquad (3)$$

where I_0 is the intensity of the incident wave, θ is the angle of deviation from the direction of the normal to the screen of the diffracted wave, J_1^2 – first–order Bessel function, $d\theta$ – solid angle at which rays propagate in the direction interval $\theta \div \theta + d\theta$

Unlike to the case when there is a vacuum behind the screen, in the case of a material medium, the modulus of the wave vector k changes in formula (3), and accordingly, the value of the refractive index **n** also changes.

Note that in expression (3), the integral is not analytically calculated. Fig. 6 shows the dependence of I on **a** given in the wavelength λ obtained by numerical methods, which demonstrates that with increasing radius of the hole, the wave intensity behind the slit increases, and the shape of this curve depends on the value of the refractive index n.

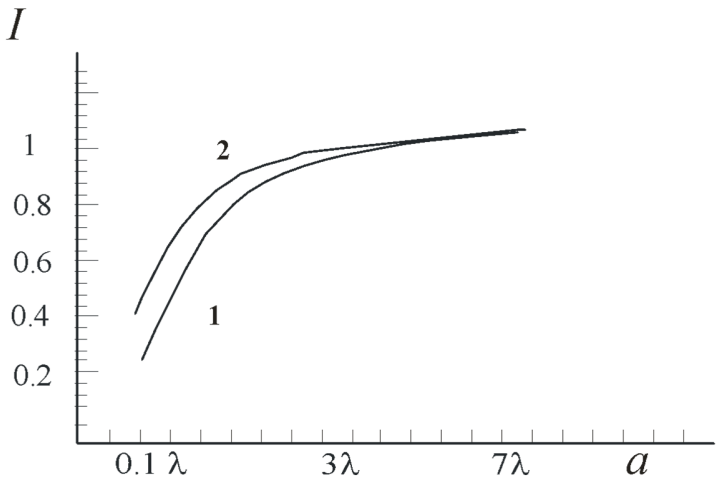

Fig. 6. Dependence of the intensity of the diffracted wave *I* on the radius of the circular hole **a**. Curve 1 corresponds to the case n = 1, curve 2 to the case n =2

From the form of expression (3), one should also expect a change in the angular distribution of the intensity of the diffracted wave with a change in the value of the refractive index. Fig. 7 shows the calculated dependences of the angular distribution of the intensity of the diffracted wave for various values of the refractive index, in the case when the medium behind the hole is an isotropic medium.

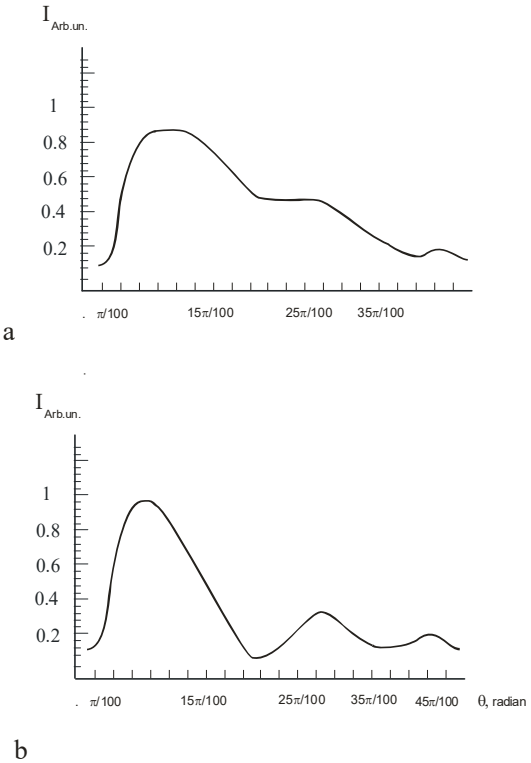

Fig. 7. Angular distribution of the diffracted wave intensity:
for the (a) n = 1 and for the (b) n = 2

As can be seen from the figure, a noticeable change in the angular distribution of the intensity of the diffracted wave is observed with a change in the refractive index. Based on the

obtained result, it can be noted that in the case of placing a demonstration screen behind the hole, it will be possible to observe the well–known diffraction pattern consisting of a set of diffraction rings, however, in contrast to the standard situation of air (vacuum) with n = 1 on both sides of the hole, in the considered case, the distance between the interference rings and the intensity distribution between them will already depend on the value of the refractive index of the medium. As can be seen from the figure, a noticeable change in the angular distribution of the intensity of the diffracted wave is observed with a change in the refractive index.

Another case of diffraction is also of undoubted interest when a uniaxial anisotropic medium with an optical axis parallel to the plane of the screen is placed behind the screen with an aperture. In this case, at small diffraction angles, formula (3) must be written separately for the ordinary and extraordinary waves when the change in the refractive index of the extraordinary wave upon deviation of the diffracted extraordinary ray from the perpendicularity to the optical axis can be neglected.

$$dI_o = I_{oo} \frac{J_1^2(a\frac{\omega}{c} n_o \theta)}{\theta^2} d\theta$$
$$dI_e = I_{oe} \frac{J_1^2(a\frac{\omega}{c} n_e \theta)}{\theta^2} d\theta \quad (4)$$

Thus, in this case, when the demonstration screen is located behind the hole, it will be possible to observe a complex diffraction pattern consisting of two sets of diffraction rings formed separately by ordinary and unusual waves. As a result, detailed photometry of the obtained diffraction pattern makes it possible to analyze the optical anisotropy of various media using a simple optical scheme. Note that the study and analysis of anisotropic media using standard refractometers is a rather complicated technical task.

5. Conclusion

Our assumption on the nonreciprocity of diffraction of an electromagnetic wave by a aperture between two media with different refractive indices is experimentally confirmed. This experiment was carried out for the millimeter range; polytetrafluoroethylene (teflon) and polymethylmethacrylate (plexiglass) were used as dielectric media on different sides of the slit. Numerical calculations also confirm the presence of nonreciprocity in such an optical system. The phenomenon of optical nonreciprocity considered in this work can be used to develop new optical elements, as well as the storage of electromagnetic energy.

In the present work, the phenomenon of diffraction by a round hole in a screen located between two media differing in their refractive indices is also studied. A numerical calculation of the intensity of the diffracted wave in this optical system is carried out. The peculiarities of the diffraction pattern are studied depending on the refractive index of the medium, including the case of a birefringent medium.

References.

1. M. Born, E. Wolf**.** Principles of Optics (4th.ed.). Pergamon Press , (1968).
2. R. Vaganov, B. Katzenelenbaum. Bases of the diffraction theory. Moscow, Nauka, (1982).
3. B.C. Kress, P. Meyrueis. Applied Digital Optics : From Micro–optics to Nanophotonics. John Wiley & Sons, (2009).
4. V.A.Belyakov. Diffraction Optics of complex–Structure Periodic Media. Springer, New York, (1992).
5. О.С. Ерицян. Изв. НАН Армении, Физика, 37, с. 244 (2002).
6. А.А. Лалаян, О.С. Ерицян, О.М. Аракелян, Ш.К. Ерицян. НАН Армении, Физика, т.53, с.50 (2018).
7. И.А. Андронова, Г.Б. Малыкин. УФН, 172, с.849 (2002).
8. С. И. Назаров. Наука и образование. 9. с 479 (2013).
9. Л. Д. Ландау, Е. М. Лифшиц. Теория поля. Наука, Физматгиз., (1967).

Bragg's X–ray Microscope and X–ray Holography Development Perspectives

A.M. Yegiazaryan*, A.K. Atanesyan

Institute of Applied Problems of Physics NAS RA,
25 Hrachya Nersissian Str., Yerevan, Republic of Armenia, 0014

Drawing on the phenomenon of optical Fourier synthesis, Lawrence Bragg in 1929 received a visible image of the atoms of the diopside crystal [1,2,3]. The unit cell of a diopside crystal has a centrosymmetric structure, in the center of which a heavy atom is located.

In the Fraunhofer region of X–ray diffraction on a crystal, an X–ray diffraction pattern of a crystal is recorded.

The spatial distribution of the intensity of the diffracted wave, in this region, is determined by the Fourier transform of the electron density distribution in the crystal cell. Bragg chose a crystal of such a structure that the Fourier transform of the electron density distribution turned out to be a real positive function. Then, under these conditions, the amplitude of the diffracted X–ray wave is uniquely determined by the recorded intensity. This means that when recording the wave intensity, we do not lose information about the phase of the wave.

After registering the diffracted X–ray wave and processing the X–ray topographic picture of the crystal, Bragg proposed a method for obtaining a similar wave in the visible region of radiation. This means that the wave obtained in the visible region of the radiation contains exactly the same amplitude and phase information as the diffracted X–ray wave.

To this end, the author, on an impervious plate for visible light, opens gaps, the geometry of which coincides with the geometry of the location of diffraction peaks. The size of the slit is directly proportional to the peak intensity. After passing through such a plate, visible light acquires such amplitude and phase information as the X–ray diffracted on the crystal. The resulting light wave passes through a collecting lens. The spatial distribution of the wave amplitude after the lens is determined by the Fourier image of the distribution of the amplitude of the wave incident on the lens. In this two–step process, after a double Fourier transform, a three–dimensional image of the atomic cell of the crystal lattice is obtained in the region of visible light. For crystals of any structure, the Bragg X–ray microscope method is incorrect. However, this method proved to be the basis for Denes Gabor at the discovery of Holography in 1948 [4].

Holography is a two–stage method of complete registration and restoration scattered on the subject of a wave. Full wave registration or registration of the amplitude and phase information of the object wave is carried out by the corresponding modulation of the recorded intensity. Such modulation occurs when the interference of the object wave with the reference wave. The recorded interference pattern, after processing, is illuminated with a similar reference wave. When the reference wave is scattered, on the modulation of the intensity of the interference pattern or hologram, the object wave is restored, which creates a three–dimensional image of the object.

* **E – mail:** *artaky_mail@yahoo.com*

Optical holography developed rapidly after the discovery of optical lasers as light sources with high spatial and temporal coherence. The latter is essential for the implementation of the holographic method.

In the X–ray region of the spectrum, there are no quantum generators. However, estimates show that the diffraction collimation of X–ray beams in single–crystal monochromators significantly increases the spatio–temporal coherence parameters of these beams. From this point of view, the actual task of performing X–ray short–wave holography according to the axial registration scheme [5, 6]. The rapid development of optical holography in the eighties led to the development of new areas of applied physics such as holographic interferometry, holographic microscopy, holographic cinema, etc.

X–ray interferometry also developed during this period. X–ray interferometric patterns with high contrast were recorded in single–crystal interferometers [7,8]. The high contrast of these patterns uniquely determines the degree of spatiotemporal coherence of the interfering X–ray beams. Proceeding from this, an interferometric method and corresponding schemes for performing X–ray short–wave holography were proposed in [9, 10, 11].

For example, in a multi–unit interferometric system of single crystals, two beams of X–rays interfere. If the interferogram represents the same stripes of parallel bands, then the interfering beams are plane, monochromatic waves, then the interferogram represents the simplest X–ray short–wave hologram recorded outside the axial holographic pattern.

Suppose that one of the interfering beams, passing through some crystalline inhomogeneity, acquires additional amplitude and phase information, becomes an object wave. The spatial frequencies of the object wave, which lie in the angular transmission region of the single crystal, pass through the next single–crystal block.

Estimates show that from the point of view of acquiring an additional phase, beams passing through the single crystal and air are not distinguished in this angular region. Consequently, the Fourier transform of the inhomogeneity of the electron density of a single crystal determines the complex amplitude of the object wave in the far diffraction region.

An interferogram recorded in this region represents an off–axis shortwave X–ray hologram of a single crystal inhomogeneity. Suppose restoration of a subject wave is made by a plane monochromatic wave of visible light. In the region of visible light, we obtain an objective wave that contains the same amplitude and phase information as an X–ray diffracted on crystalline inhomogeneities. When such an object wave passes through a collecting lens, we obtain a visible, three–dimensional image of the inhomogeneities of the single crystal.

References.

2. Bragg W.L., Zs. Kristallogr., 70, 474, (1929). Оптический метод представления результатов рентгеновского анализа
3. Bragg W.L., Nature, 143, 678, (1939). Новый тип рентгеновского микроскопа
4. Bragg W.L., Nature, 149, 470, (1942). Рентгеновский микроскоп
5. Gabor D., Nature, 161, 777, (1948). Новый принцип микроскопии
6. Егиазарян А. М., Ростомян А. Г., Безирганян П. А., ДАН Арм. ССР, т. 66, №4, 228, (1978) О пространственной когерентности излучения
7. Егиазарян А. М., Безирганян П. А., Изв АН Арм. ССР, Физика, 15, 35 (1980) О возможности записи рентгеновской коротковолновой голограммы

8. Bonse U., Hart M., Z. füz phus.,190, 455 (1966) Moiré Patters of Atomic Planes obtained by X–ray Interferometry
9. Petrascheck D., Folk R., Phys. Stat. Sol., (a) 36, 147, (1976) Theory of a Symmetric LLL Interferometer with Arbitrary Absorption.
10. Егиазарян А. М., Труни К. Г., Мкртчян А. Р., Рентгеновская интерферометрическая коротковолновая голография дифракционной фокусировкой. Письма в ЖЭТФ, (1998), т. 68, №9, с. 681 – 684
11. Егиазарян А. М., Новые перспективы развития рентгеновской коротковолновой голографии. Письма в ЖЭТФ, т. 24, №10, с. 55 – 59, (1998)
12. Безирганян П. А., Егиазарян А. М., Способ записи рентгеновской коротковолновой голограммы А.С.N1082174, (1987)

Noise Reduction Methods in Laboratory X–ray Microtomography

V.E. Asadchikov[1*], A.V. Buzmakov[1], A.S. Ingacheva[1,2], Yu.S. Krivonosov[1], D.A. Zolotov[1], M.V. Chukalina[1,2,3]

[1] Shubnikov Institute of Crystallography of Federal Scientific Research Centre "Crystallography and Photonics" of Russian Academy of Sciences
59 Leninskii pr., Moscow, Russian Federation, 119333
[2]Institute for Information Transmission Problems of Russian Academy of Sciences (Kharkevich Institute)
19 Bolshoy Karetny per., build.1, Moscow, Russian Federation,127051
[3]Smart Engines
9 60–letiya Oktyabrya Ave., Moscow, Russian Federation, 117312

Abstract: Laboratory X–ray microtomography is a convenient method of studying the three–dimensional structure of objects of different types. Modern laboratory microtomographs allow us to carry out measurements with submicron resolution. The laboratory sources of X–ray radiation used in such microtomographs have low intensity, so the recorded tomographic projections are noisy. This often leads to the situation when the reconstructed tomographic images are also noisy and artefacts may appear on them (objects of a characteristic shape, which are absent in the real object). In this work, we describe the methods of noise suppression in tomographic reconstructions at all stages of data processing: reducing noise in the original projection images; inclusion of regularizing members in the tomographic reconstruction procedure; filtering of reconstructed data. The reduction of noise and artefacts on tomographic data allows not only to reconstruct the internal structure of the objects under study but also to make a step towards temporal resolution and spectral tomography on laboratory sources.

1. Introduction.

Laboratory X–ray microtomography [1] is used to study the three–dimensional structure of the objects in a nondestructive way. Modern microtomographs allow us to carry out measurements with the resolution up to 1 nanometer [2, 3]. The spatial resolution of the tomographic method can be increased in various ways, for example, using a submicron probe in scanning schemes or applying optical schemes with magnification. However, an increase in spatial resolution inevitably leads to a decrease in the number of quanta collected by a detector cell per unit of time. At the same time, increasing the exposure time is not always possible, since the dose deposited in the sample increases proportionally. This can lead to degradation of the sample until its destruction. The conclusion suggests itself that it is necessary to develop the methods of working with tomographic data that are able to work in conditions of a poor signal–to–noise ratio [4, 5]. In this work, we present the methods of noise suppression in tomographic reconstructions at all stages of data processing: reducing noise in the original projection images; inclusion of regularizing members in the tomographic reconstruction procedure; filtering of reconstructed data.

How to work with tomographic projections.

[*]**E – mail:** *asad@crys.ras.ru, asad@ns.crys.ras.ru*

Since all reconstruction methods are based on assumptions about the ideal hardware of the tomograph and the ideal implementation of the measurement scheme, any deviations from these assumptions introduce artifacts into the result of reconstruction. Let's describe the model of the experiment, which we use further to analyze the sources of error. The source and detector are stationary. The specimen under study is mounted on the holder. The sample holder is reinforced on the goniometer, allowing circular rotation of the sample with a given accuracy.

As was demonstrated [6] the source is not stable during the tomographic measurement. Measurement time can range from a few minutes to a few days. If the instability is not compensated, it can lead to slur (motion aberration) of different areas on the reconstructed image. The approach to correct the effect of thermal instability of the spot position is described [7].

Different detector cells have different quantum output. Miss calibration of the shells produces the rings on the reconstructed image (Fig. 1) due to vertical lines on the sinograms (Fig.2). In Fig.1 (left image) unfiltered sinogram was used to reconstruct the sample. Coaxial circles are well pronounced. There are different approaches to filter the lines. In [8] it was proposed to use one–dimensional low–pass filtering of the sums in Fourier space. The sum of all grey values of each column of a sinogram is calculated before the filtering. The filtering in sinogram space is evaluated in [9, 10].

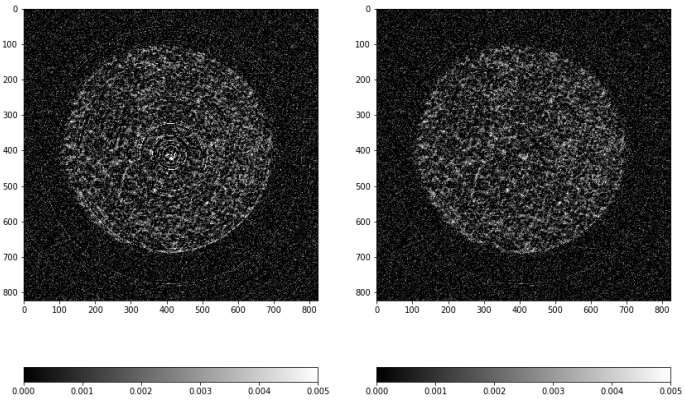

Fig.1. Left: Reconstruction without orthotropic artifacts removing. Right: Reconstruction after sinogram filtering.

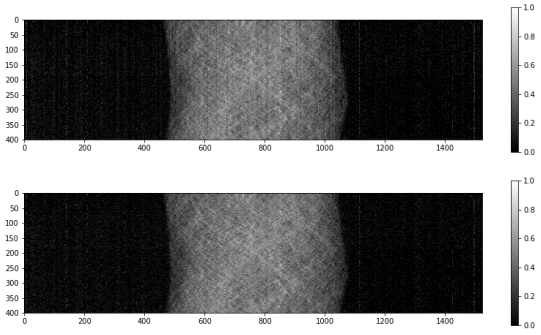

Fig.2. Up: Sinogram with orthotropic artifacts of image registration. Down: Result after filtering.

The tilt of the rotation axis, which causes the measurement geometry of all but the center layer of the object to be disturbed, is the next problem. One of the approaches to solving the problem of 'aligning' geometry on the basis of the analysis of neighboring projections is presented in [11, 12].

2. Regularization–based reconstruction to reduce the noise influence

After all corrections of the measurement results (tomographic projections), they transfer to the reconstruction. There are different approaches to reconstruct the images. The most frequently the integral approaches based on the inverse Radon transform are used. However, they produce not acceptable results in the presence of a high level of noise. To decrease the noise influence on the reconstruction result the tomography inverse task is presented as a linear system of equations and it is solved by a non–linear optimization algorithm. In Fig.3 the result of the phantom reconstruction from the sinogram with high–level noise by algebraic approach is presented. To compare the reconstruction performed by different approaches, we present the cross–section of the phantom at the same Fig.3 on the right. Gray color corresponds to reconstruction by algebraic method and black one corresponds to Filtered Back Projection reconstruction.

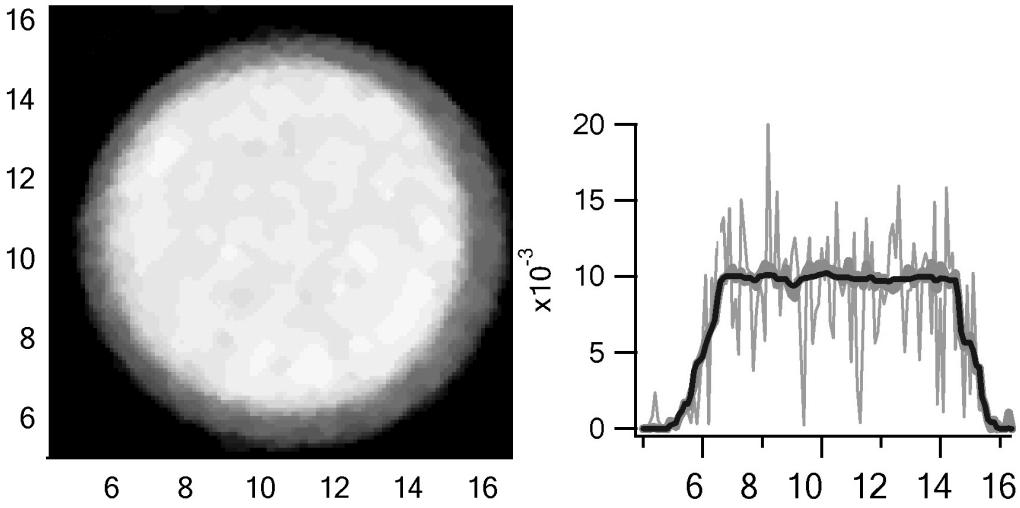

Fig. 3. Left: Reconstruction of the phantom from the sinogram with high level noise.Right: Cross–section of the phantom.

The optimizing expression in algebraic approach is a linear combination of two parts. The first one is a quadratic discrepancy in the tomographic projections space. The second term is a regularization part. In Fig.4 one tomographic projection of baby tooth with Pb inclusion inside from the set, collected in the “Crystallography and Photonics” Federal Researcher Centre of the Russian Academy of Science [13], is presented.

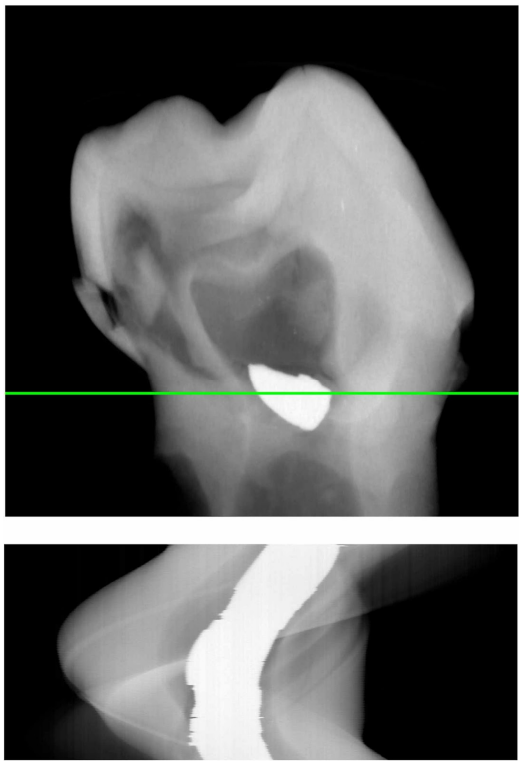

Fig.4. Tomographic projection and sinogram (corresponds to the green line on the projection) of the baby tooth.

An X–ray tube with Mo anode as a radiation source and a vacuum gauge for intensity stability reasons we used. The projections were collected with a XIMEA–xiRay 11 Mpix detector. The measurement parameters are – the tube was 40 kV voltage, 20 mA current and 5 s acquisition time per frame. The object–source distance was 1.2 m and the object–detector distance was 0.05 m. No filters were used. Every rotational scan consisted of 400 projections with an angular constant step size of 0.5 deg. The detector pixel resolution was 9 μm. In Fig.5 we present the reconstruction of the cross–section from the sinogram presented in Fig.4. On the left the cross section reconstructed by the Filtered Back projection method is presented. Pb inclusion has very white border that does not correspond to the real case. The algebraic method was used to reconstruct the central and right images.

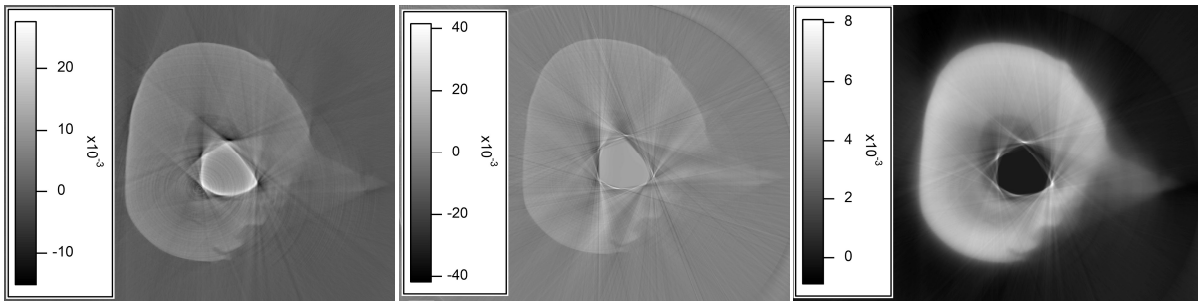

Fig.5. Cross–section reconstruction by FBP (left) and SIRT with different coefficients in linear combination.

3. Conclusion.

We presented an overview of methods for noise suppression in tomographic reconstructions at all stages of data processing: noise reduction in the original projection images; usage the additional regularizing terms in the optimized expression on reconstruction step; filtering of reconstructed data. However, to suppress the noise completely is not possible. The filtering back–projection procedure applied to the image of the residual error built in the sinogram space will allow you to select the most dubious areas on the restored image [14]. It is a way to delegate to the end customers (for example, to the doctors) 2 images: final reconstruction result (like Fig. 6b) and the reconstruction from residual error (like Fig. 6b) as a criterion of the truthfulness of the reconstruction result.

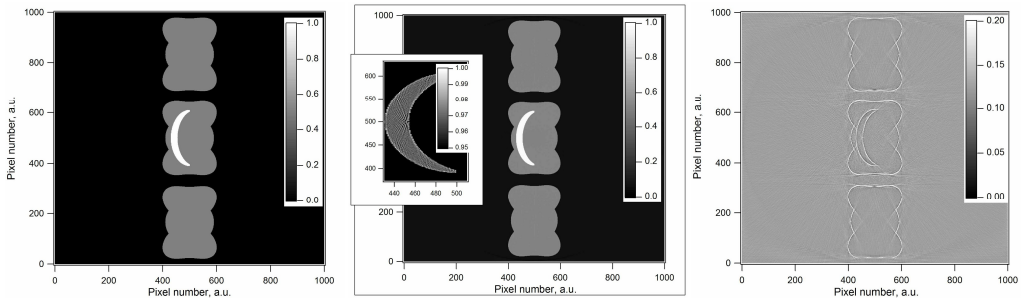

Fig.6. a – Phantom, b– reconstruction result, c– reconstruction from residual error.

The presence of an image containing the distribution of the remaining error reduces the odds of wrong decision when a doctor diagnoses or rejects products formed during a multi–step manufacturing procedure.

This work was supported by the Russian Foundation for Basic Research, project No. 19–01–00790 (reconstruction algorithms development) and project No. 18–29–26036 (tomography measurements) and by the Ministry of Science and Higher Education within the State assignment FSRC «Crystallography and Photonics» RAS (tomography reconstruction calculations)

References.

1. A. V. Buzmakov, V. E. Asadchikov, D. A. Zolotov, B. S. Roshchin, Yu. M. Dymshits, V. A. Shishkov, M. V. Chukalina, A. S. Ingacheva, D. E. Ichalova, Yu. S. Krivonosov, I. G. Dyachkova, M. Balzer, M. Castele, S. Chilingaryan, A. Kopmann. Laboratory Microtomographs: Design and Data Processing Algorithms. Crystallography Reports, Volume 63, Issue 6, pp 1057–1061, November 2018.
2. Christopher T. G. Smith, Christopher A. Mills, Silvia Pani, Rhys Rhodes, Josh J. Bailey, Samuel J. Cooper, Tanveerkhan S. Pathan, Vlad Stolojan, Daniel J. L. Brett, Paul R. Shearingdand S. Ravi P. Silva. X–ray micro–computed tomography as a non–destructive tool for imaging the uptake of metalnanoparticles by graphene–based 3D carbonstructures. Nanoscale, Royal Society of Cemistry, 2019,11, 14734–14741, 19 Jul 2019.
3. E. Longo, A. Bravin, F. Brun, I. Bukreeva, A. Cedola, O. De La Rochefoucauld, M. Fratini, X. Le Guevel, L. Massimi, L. Sancey, O. Tillement, P. Zeitoun. 3D imaging of theranostic nanoparticles in mice organs by means of x–ray phase contrast

tomography. Proceedings Volume 10573, SPIE Medical Imaging 2018: Physics of Medical Imaging; 2018, 105734I.
4. A. Buzmakov, V. Asadchikov, D. Zolotov, M. Chukalina Optimization of micro–tomographic experiment and reconstruction parameters at low signal–to–noise ratio. 12th Biennial Conference on High–Resolution X–Ray Diffraction and Imaging XTOP–2014. Villard–de–Lans, France. 2014. P.87.
5. C. H. McCollough, L. Yu, J. M. Kofler, Sh. Leng, Yi Zhang, Zh. Li, R. E. Carter, Degradation of CT Low–Contrast Spatial Resolution Due to the Use of Iterative Reconstruction and Reduced Dose LevelsRadiology: Volume 276: Number 2—August 2015. P.499–506.
6. A. Fukuda, K. Matsubara, I. Miyati T. Long–term stability of beam quality and output of conventional X–ray units. Radiol Phys Technol. 2015 Jan;8(1):26–9. doi: 10.1007/s12194–014–0282–1.
7. A. S. Ingacheva, A. B. Buzmakov. Methods of Preprocessing Tomographic Images Taking into Account the Thermal Instability of the X–ray Tube. Optoelectronics, Instrumentation and Data Processing, March 2019, Volume 55, Issue 2, pp 138–147.
8. M. Boin and A. Haibela. Compensation of ring artefacts in synchrotron tomographic images. Optics Express Vol. 14, Issue 25, pp. 12071–12075 (2006) https://doi.org/10.1364/OE.14.012071.
9. N.T. Vo, R. C. Atwood, M. Drakopoulos. Superior techniques for eliminating ring artifacts in X–ray micro–tomography. Optics Express Vol. 26, Issue 22, pp. 28396–28412 (2018) •https://doi.org/10.1364/OE.26.028396
10. E.E. Berlovskaya, A.V. Buzmakov, A.S. Ingacheva, A.M. Makurenkov, D.P. Nikolaev, I.A. Ozheredov, M. V. Chukalina, A. P. Shkurinov. A.P.Suppression algorithm for the orthotropic artifacts in images registered in X–ray and terahertz band. Information Processes. 19(2), 2019, pp. 200–207 (In Russian).
11. T. Sanders, M. Prange, C. Akatay, P. Binev. Physically motivated global alignment method for electron tomography. Adv Struct Chem Imag 1, 4 (2015) doi:10.1186/s40679–015–0005–7.
12. K. Jun, S. Yoon. Alignment Solution for CT Image Reconstruction using Fixed Point and Virtual Rotation Axis. Scientific Reports, 2018, 7:41218, DOI: 10.1038/srep41218.
13. A. Buzmakov, M. Chukalina, D. Nikolaev, V. Gulimova, S. Saveliev, E. Tereschenko, A. Seregin, R. Senin, D. Zolotov, V. Prun, G. Shaefer and V. Asadchikov. Monochromatic computed microtomography using laboratory and synchrotron sources and X–ray fluorescence analysis for comprehensive analysis of structural changes in bones. Journal of Applied Crystallography 48(3), 2015, pp 693–701.
14. Marina Chukalina, Dmitry Nikolaev, Anastasia Ingacheva, Alexey Buzmakov, Ivan Yakimchuk, and Victor Asadchikov "To image analysis in computed tomography", Proc. SPIE 10341, Ninth International Conference on Machine Vision (ICMV 2016), 103411B (17 March 2017); https://doi.org/10.1117/12.2268616

The Study of MF Electromagnetic Waves Radiation Caused by the Effects of Solar Radiation on Spacecraft

A.R. Aramyan*

Institute of Applied Problems of Physics NAS RA
25 Hr. Nersissian Str., Yerevan, Republic of Armenia, 0014

Abstract: This work proposed research of the emission of electrons born from the outside of spacecraft under the influence of solar radiation. The results can be used to combat harmful noises, which can lead to the failure of devices. On the other hand, these results can be used to create new devices for studying solar activity.

1. Preliminary results

The work goal is to study the radiation of electron caused by solar rays in the Earth's magnetic field.

The work done in this field last year's [1–4] give justification to assert that the radiation of electron's electromagnetic waves caused in the Earth atmosphere in Earth magnetic field is quite interesting and could have wide applied interest. It is of specific interest MF electromagnetic waves registered by DEMETR spacecraft, which is caused due to solar rays. The purpose of the work is to study this problem, discover the reasons of causes and reveal the possibility of influence of this effect on electronic equipment.

The object of the study is the radiation of 1–2 MHz frequency registered by French spacecraft DEMETR. The radiation frequency changes depending on the geographical latitude from 1.2MHz to 1MHz and again to 1.2MHz (see Fig.1a,b.). Near the poles where the magnetic field is relatively strong the radiation frequency is bigger than on the equator where the magnetic field is weak. As can be seen from Fig.1a,b such radiation appears only on the sunny side. In the shadow side, such radiation is absent. This indicates that such radiation is associated only with the sun.

According to the preliminary estimated the frequencies of these radiations rather well coincide with the frequency of electron radiation (cyclotron radiation). The preliminary evaluations have been done with the following formula.

$$\nu_e = \frac{eH}{2\pi m_e c} \tag{1}$$

where ν_e – cyclotron frequency, e and m_e –accordingly electron charge and mass, H – the Earth magnetic field in the given point and c– the light speed.

*E – mail: *aramyan.artur@gmail.com*

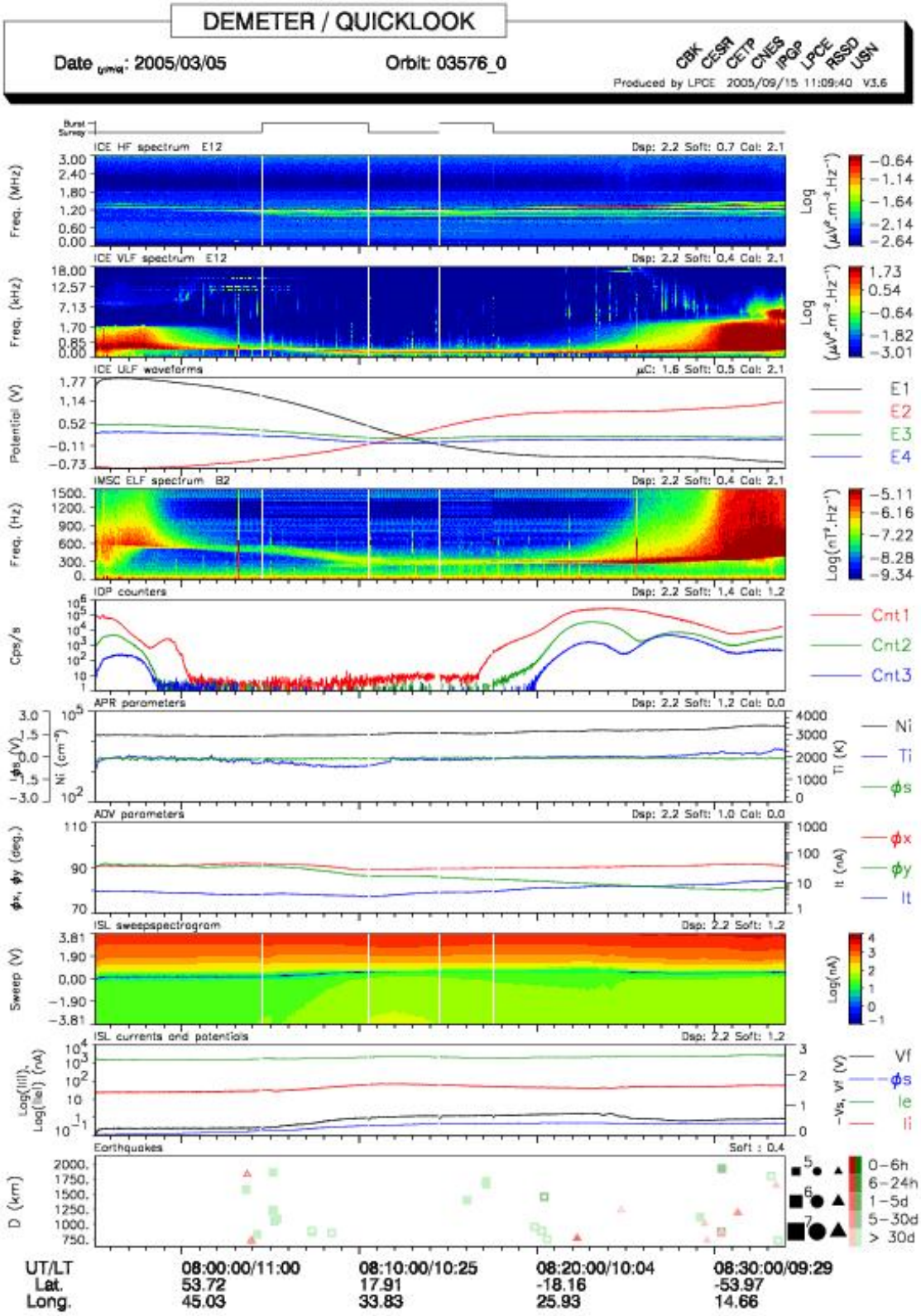
DEMETER / QUICKLOOK
Date (y/m/d): 2005/03/05
Orbit: 03576_0
CBK CESR CETP CNES IPGP LPCE RSSD USN
Produced by LPCE 2005/09/15 11:09:40 V3.6
Burst
Survey
ICE HF spectrum E12
Dsp: 2.2 Soft: 0.7 Cal: 2.1
Freq. (MHz)
3.00
2.40
1.80
1.20
0.60
0.00
Log (μV².m⁻².Hz⁻¹)
-0.64
-1.14
-1.64
-2.14
-2.64
ICE VLF spectrum E12
Dsp: 2.2 Soft: 0.4 Cal: 2.1
Freq. (kHz)
18.00
12.57
7.13
1.70
0.85
0.00
Log (μV².m⁻².Hz⁻¹)
1.73
0.54
-0.64
-1.82
-3.01
ICE ULF waveforms
μC: 1.6 Soft: 0.5 Cal: 2.1
Potential (V)
1.77
1.14
0.52
-0.11
-0.73
E1
E2
E3
E4
IMSC ELF spectrum B2
Dsp: 2.2 Soft: 0.4 Cal: 2.1
Freq. (Hz)
1500.
1200.
900.
600.
300.
0.
Log(nT².Hz⁻¹)
-5.11
-6.16
-7.22
-8.28
-9.34
IDP counters
Dsp: 2.2 Soft: 1.4 Cal: 1.2
Cps/s
Cnt1
Cnt2
Cnt3
APR parameters
Dsp: 2.2 Soft: 1.2 Cal: 0.0
Vs (V)
Ni (cm⁻³)
Ti (K)
Ni
Ti
ϕs
ADV parameters
Dsp: 2.2 Soft: 1.0 Cal: 0.0
ϕx, ϕy (deg.)
It (nA)
ϕx
ϕy
It
ISL sweepspectrogram
Dsp: 2.2 Soft: 1.2
Sweep (V)
3.81
1.90
0.00
-1.90
-3.81
Log(nA)
ISL currents and potentials
Dsp: 2.2 Soft: 1.2
Log(|Ii|), Log(|Ie|) (nA)
-Vs, Vf (V)
Vf
ϕs
Ie
Ii
Earthquakes
Soft : 0.4
D (km)
2000.
1750.
1500.
1250.
1000.
750.
0-6h
6-24h
1-5d
5-30d
> 30d
UT/LT
Lat.
Long.
08:00:00/11:00
53.72
45.03
08:10:00/10:25
17.91
33.83
08:20:00/10:04
-18.16
25.93
08:30:00/09:29
-53.97
14.66

a

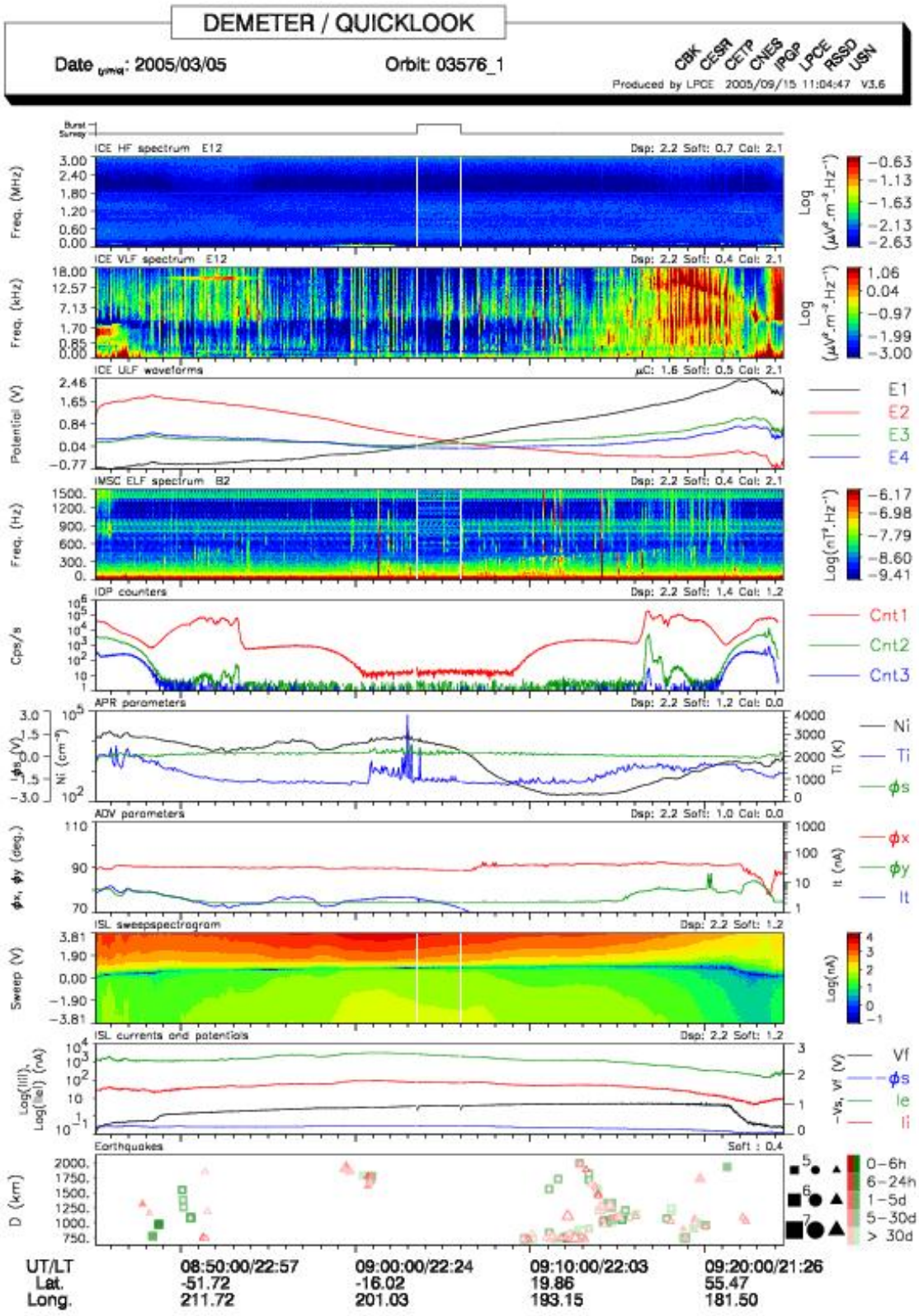

b

Fig.1. The measurement of results from a spacecraft “DEMETR”
a) measurement from the sunny side, b) measurement from the shadow side

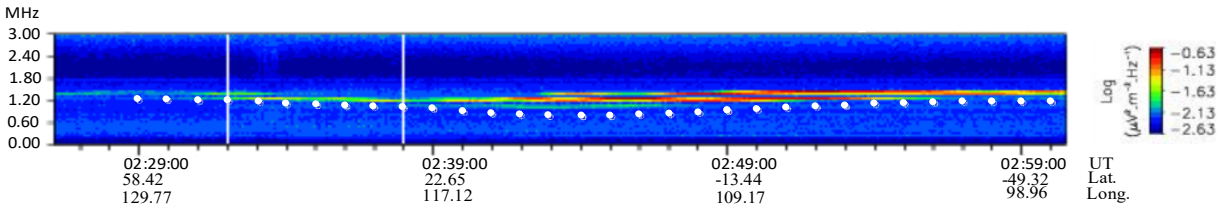

Fig.2. The spectrogram registered by French spacecraft DEMETR. As it is seen, the radiation frequency changes depending on the geographical latitude. White dotes are indicated with the cyclotron radiation frequencies calculated by DEMETR spacecraft measured value of the magnetic field.

On Fig.2 the spectrogram registered by French spacecraft DEMETR. As it is seen, the radiation frequency changes depending on the geographical latitude. White dotes are indicated with the cyclotron radiation frequencies calculated by (1) accordance with DEMETR spacecraft measured value of the magnetic field. As can seen from Fig.2, there are quality matches.

References.

1. A. R. Aramyan, G. R. Aramyan, K. P. Haroyan, G. A. Galechyan, A. A. Vardanyan, G.A.Danielyan, H.B.Nersisyan, S.G.Bilén, “A Study of Acoustic Waves Generated by the Shock Waveof an Antihail Gun”, *Acoustical Physics*,vol. 57, no. 3, pp. 432–436, March. 2011.
2. A.R.Aramyan, S.A. Aramyan, S.G.Bilén, 2013 The 31st International Conference on Phenomena in Ionized Gases, (Granada Spain 14–19 July 2013) pp 494–497, 2013.
3. A.R.Aramyan, S. A.AramyanS.A., S.G.Bilén, L.Sh.Grigoryan, H.F.Khachatryan, “Radiation of Ultra Low Frequency Electromagnetic Waves from Atmosphere underthe Influence of Strong ShockWaves”, *Chin. Phys. Lett*., vol. 32, no. 3, pp. 034101–1—034101–3, March 2015.
4. A.H. Mkrtchyan, L. Sh. Grigoryan, H. F. Khachatryan, S. G. Bilén, M. Parrot, A. V. Sargsyan, and A. R. Aramyan, Shock Wave Generated Megahertz Radiation of Atmosphere, *IEEE Transactions on Plasma Science*, v. 47, N1, 2019, pp.118–120.

Cavity Magnetron Spectra

A.S. Abrahamyan*

Institute of Applied Problems of Physics NAS of the Republic of Armenia,
25 Hrachya Nersissian Str., Yerevan, Republic of Armenia, 0014

Abstract: *It was experimentally investigated in the visible radiation range from the inner cavity of a cylindrical magnetron. Helium acoustoplasma in the absence of a magnetic field was used. Helium pressure in the discharge chamber was 0.1 torr. To create an acoustoplasma, the magnetron was fed with a modulated current, which contained a constant and a variable component. DC component of discharge current was 100mA. The depth of current modulation M is the ratio of the amplitude of the variable component to the value of the constant component varied from zero to unity. As the modulation depth increases from M = 0 to M = 0.5, the intensity of the spectral lines increases. At M ≈ 1, the intensity of the spectral lines drops sharply. A significant fraction of the energy in the visible part of the spectrum is concentrated in the lines of molecular helium, which is formed in the discharge. The experimentally obtained spectra are presented.*

1. Introduction

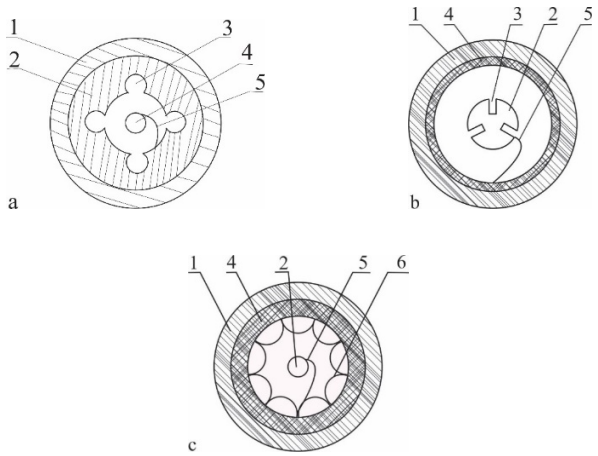

Fig. 1. a) Conventional magnetron for generating electromagnetic waves, b) Inverted magnetron for generating elecrtomagnetic waves, c) Magnetron for sputtering. 1 – magnet, 2 – anode, 3 – resonator, 4 – cathode, 5 – trajectory of slow electrons that accelerates in an electric field and reaches the anode, 6 – trajectory of fast electrons

A conventional magnetron is shown in Fig. 1a. The electric field is applied in the plane of the figure, the magnetic field is orthogonal to the plane of the figure. An electron emerging from the cathode in a magnetic field spirals toward the anode. Due to the resonators, the electric field in the anode–cathode gap is modulated and therefore the spiral path is distorted.

The design of a reversed magnetron is known when the cathode is located around a circle, and in the center there is an anode with a system of resonators (Fig. 1b).

For sputtering systems, it is advisable to use a magnetron with a reverse inclusion (Fig. 1c). Those, in the center is an anode, usually a cylindrical rod, and around it at a certain distance

***E – mail:** arbel11@mail.ru*

is a cathode in the form of a cylinder, ring, cone or other shape. The magnetic field is again orthogonal to the plane of the figure. Electric field is in the plane of the figure. In the case of using magnetrons for sputtering, a resonator system is not necessary, since the generation of electromagnetic radiation is parasitic for the sputtering process.

For sputtering, magnetron systems are used in which the cathode material is sprayed. In this case, a region is formed between the cathode and the anode where electrons ionize the buffer gas and the cathode material vapors, some of the ions from this region bombard the cathode with high energy, and new atoms, electrons and ions are knocked out of the cathode. Some ions and neutral atoms leave the anode–cathode region and are deposited directly on the substrate, or form clusters. Slow electrons accelerated in an electric field in the region of the anode–cathode again ionize part of the neutral atoms.

The magnitude of the electric and magnetic fields is selected so that fast electrons 6 emitted from the cathode 4 are wrapped in a magnetic field and again bombard the cathode, knocking out new electrons, neutrals and ions. Slow electrons 5 gain energy when the anode–cathode moves in an electric field. But because of the magnetic field, they move along spiral paths and along the way, almost all of the accumulated energy is wasted on ionizing the buffer gas and vapor of the cathode material, which fill the space between the cathode and anode.

The result is an effective ion source of the sprayed material, which flies orthogonal to the plane of the picture. By varying the potential of the substrate, the deposition rate can be changed. At an accelerating potential, the ionic component can bombard the substrate with such energy that instead of sputtering, the surface will be cleaned and not only the cathode, but also the substrate will be sprayed.

In the case of using a cylindrical anode and cathode, the region between the anode and cathode is a cavity. Because of this, the magnetron was called cavity.

2. Experimental setup

In the work, radiation in the visible region of the spectrum from such a magnetron cavity was studied. A copper cylindrical cathode and an aluminum cylindrical anode with a copper coating were used. Helium was used as a buffer gas.

The operation of such a magnetron in the DC power mode and in the acoustoplasma mode, when the discharge current has a direct and variable component, i.e. modulated discharge [1–4].

The acoustoplasma mode can also be obtained by supplying the discharge with direct current due to pulsations of the space charge in the gap between the anode and cathode in case of violation of quasi–neutrality.

The radiation from the magnetron cavity was fed through the fiber to the ISP–51 spectrograph, which was converted into a computer spectrograph and showed the spectrum under study on a computer display.

3. Results and discussion

Figure 2 shows one of the obtained spectra.

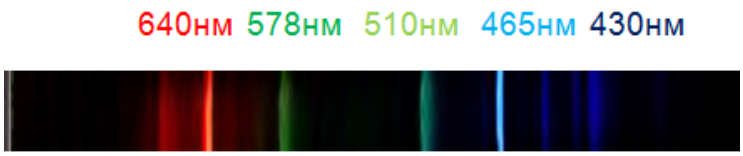

Fig. 2. Spectrum from the cavity of a working magnetron

Green lines are the lines of self–reversed transitions of copper 510 and 578 nm (the lines of the copper laser). True, pulsed copper lasers operate at the trailing edge of nanosecond pulses, and in our case, the modulation frequency is 1 kHz. The remaining copper lines are very weak, or not observed at all.

Strong blue (465nm), red–orange (640nm) and one of the red lines belong to the molecular helium He_2, which is formed in the discharge.

The remaining lines are not identified and may belong to atomic helium and magnetron construction materials [5]. The spectral lines for copper are taken from [6].

It can be seen that molecular helium lines dominate in the spectrum, i.e. in the discharge, almost all helium is in a molecular state.

Figure 3 shows the change in the spectra with a change in the acoustoplasma operating mode.

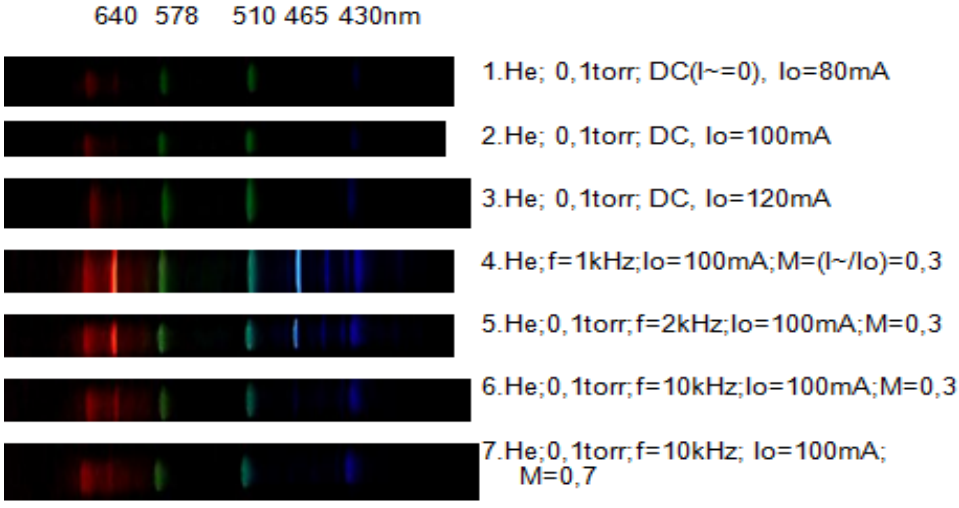

Fig. 3. Changes in the spectra in the acoustoplasma mode

It can be seen from Fig. 3 that, when the magnetron discharge is supplied with direct current, the spectral lines of copper are very weak, and the spectral lines of He_2 are practically invisible.

When operating in the acoustoplasma mode, the strongest spectral lines of copper and He_2 are obtained at a modulation frequency of 1 kHz. Further, with an increase in the modulation frequency, the intensity of the spectral lines decreases.

Figure 4 shows the intensities of the spectral lines (in relative units) for different frequencies and depths of modulation of the discharge current. The spectra presented correspond to spectrograms 2, 4, 5, 6 of Fig. 3.

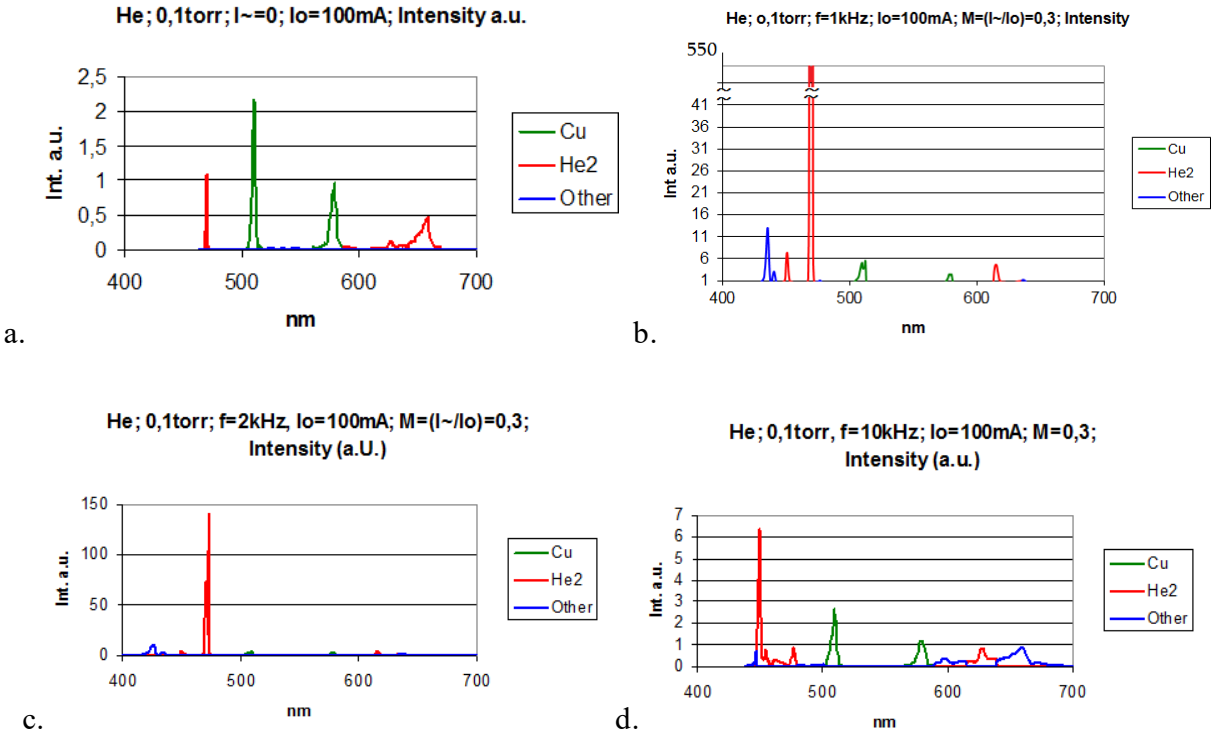

Fig. 4. Intensity of spectral lines for different frequencies and depth of modulation of the discharge current, for spectrogram of Fig. 3: a) for spectrogram 2 direct current supply, b) acoustoplasma mode for spectrogram 4, c) for spectrogram 5, d) for spectrogram 6

A comparison of Figs. 4a and 4b shows that the He_2 465 nm line in the acoustoplasma mode at a modulation frequency of 1kHz is 550 times stronger than the same line, but when the magnetron is supplied with direct current, the 510 nm copper line increases only 2 times.

Figure 5 shows the possibility of tuning the blue spectral line of molecular helium in the wavelength range 450–467 nm with a change in the modulation frequency.

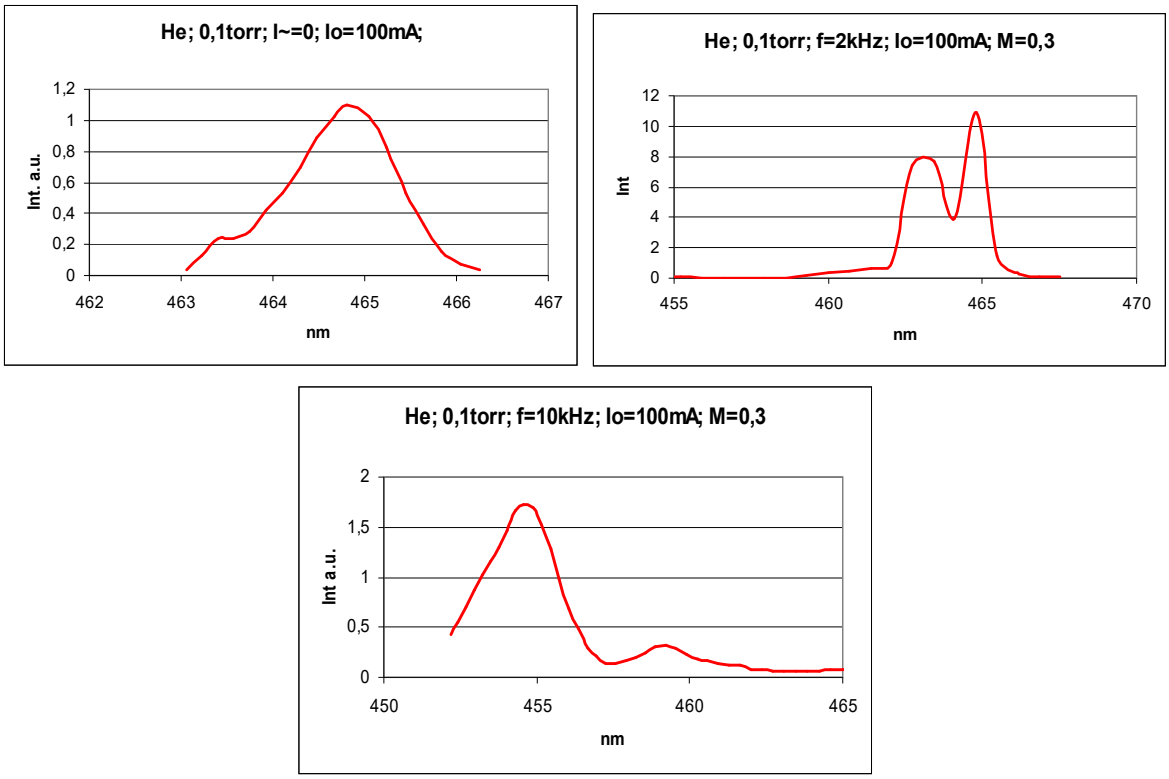

Fig. 5. Changing of the spectral line in the acoustoplasma mode

4. Conclusion

The spectrum of the helium discharge in the magnetron cavity, in the gap between the anode and cathode, is investigated. The anode and cathode are copper. The design of a reversed magnetron was used, i.e. a cylindrical tubular cathode inside which is located a rod anode.

1. We studied the mode of supply of a magnetron with direct current and the acoustoplasma mode.
2. In the emission spectrum from the magnetron cavity is dominated by lines of molecular helium (blue 465 nm and red–orange 640 nm) and copper lines (510 and 578 nm).
3. Copper lines are characteristic of a copper laser. However, in a laser, they are generated only at the trailing edge of nanosecond pulses. In this setup, operating in the acoustoplasma mode, the modulation frequency of the discharge current was 0.1–10 kHz.
4. A sharp increase in the intensity of spectral lines in the acoustoplasma mode was obtained experimentally in comparison with the spectrum of a direct current discharge. For molecular helium, the line intensity of 640 nm in the acoustoplasma mode can be 550 times stronger than for a direct current discharge.
5. The possibility of tuning the 465 nm line with a change in the modulation frequency of the discharge current is shown.

References

1. Galechyan G.A., Mkrtchyan A.R. Acoustoplasma. Apaga, Yerevan, p.338, 2005. (In Russian).
2. Mkrtchyan A.R., Mkrtchyan A.H., Abrahamyan A.S. Acoustoplasma is a new state of plasmas. VII Intern.Conf.Plasma Physics and Plasma Technology, PPPT–7, Minsk, Belarus, 17–21 Sept.2012, Proc., v.1, pp.3–5, 2012.
3. Mkrtchyan A.R., Abrahamyan A.S. Creation of new generation magnetrons based on acoustoplasmic states for surface cleaning and deposition on substrates. *The First Russian Crystallographic Congress*, Moscow, 2016, p.177. In Russian.
4. Mkrtchyan A.H., Mkrtchyan A.R., Abrahamyan A.S., Nalbandyan V.V. Acoustoplasma sputtering method in vacuum. Patent Armenia, no.3086A.
5. Pearse R.W.B and Gaydon A.G. The Identification of Molekular Spectra. London, Chapman & Hall Ltd, 221p. 1941, or (4th edn., London, Chapman & Hall, 1976.)
6. V.M. Batenin, V.V. Buchanov, M.A. Kazaryan, I.I. Klimovski, E.I. Molodih. Lasers based on self–limited transitions of metal atoms. Nauchnaia kniga, Moscow, p.544, 1998. (In Russian).

The Interaction of the Discharge Modules

A.S. Abrahamyan*, K.V. Hakobyan, Q.G. Sahakyan

Institute of Applied Problems of Physics NAS of the Republic of Armenia,
25 Hrachya Nersissian Str., Yerevan, Republic of Armenia, 0014

Abstract: *When compiling a long discharge tube from separate series–connected discharge modules, the question of the stability of such a multimodule tube becomes relevant. In this case, it is important to investigate when the instability arise in one of the modules how it will affect the other ones. This is especially important when acoustoplasmic supply power is connected to at least one of the modules. In this case, we create periodic instability in time and space, which will lead to acoustopolasma mode of the operation. The experiment was conducted with a discharge tube composed of two series–connected modules that were in a common optical resonator. One of the modules was connected to a constant current and the other one to a modulated variable current, which contain constant and variable components and worked in acoustoplasma mode. The depth of current modulation that occurs in a DC–powered module due to the influence of a modulated current is measured. It is experimentally shown that the choice of the value of the constant components of the discharge current in each module and the modulation frequency of the variable components of the discharge current in acoustoplasma module one can manage the degree of influence of acoustoplasmic module to the DC power module.*

1. Introduction

Laser radiation power can be increased in three ways:

1. An increase in the discharge cross section;
2. Parallel connection of discharge tubes;
3. By increasing the length of the discharge tube or by connecting the discharge tubes in series.

With an increase in the discharge cross section, conventional electric discharge power is not possible due to contraction of the discharge; therefore, large–diameter electron beam pumping or ultraviolet preionization is used. We will not consider this option.

*E – mail: arbel11@mail.ru

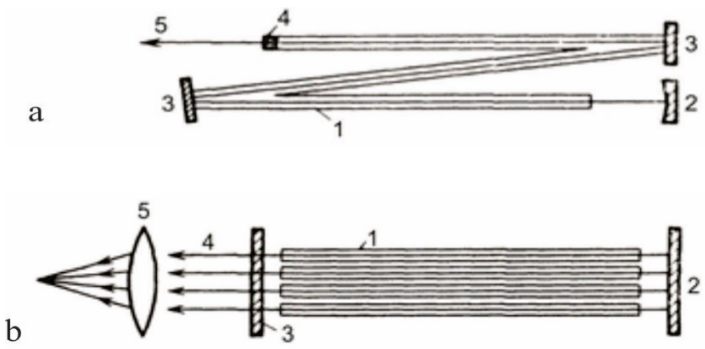

Fig.1. Diagrams of multisectional (modular) tube lasers with diffusion cooling [1]; a – serial connection of modules, 1 – discharge tubes, 2 – deaf mirror, 3 – rotary mirrors, 4 – translucent output mirror, 5 – output beam; b – parallel connection of the discharge tubes into the optical resonator, 1 – discharge tubes, 2 – deaf mirror, 3 – translucent output mirror, 4 – output rays, 5 – focusing lens

The literature describes the construction of serial connection of discharge tubes [1]. To reduce the length of the discharge tube, it is folded, as shown in Fig. 1a. The length of individual tubes is about 1 m and each tube is powered by a separate power supply. Another way to increase the total laser power is to parallelly incorporate the discharge tubes into a common cavity as shown in Fig.1b. Parallel beams from different laser tubes are focused by a large–diameter lens. For example, the TL–6 multibeam CO_2 laser had 124 tubes and a radiation power of 6 kW [1].

Another way to combine the beams of different lasers in parallel is shown in Fig. 2.

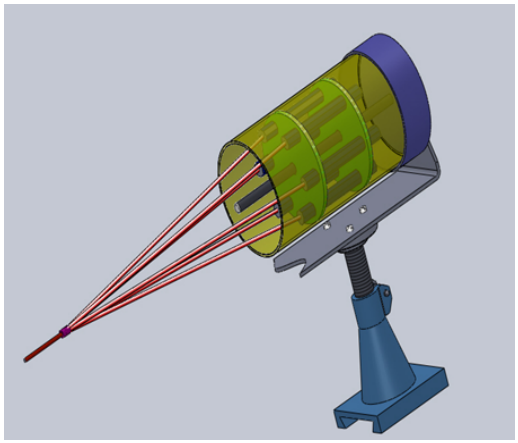

Fig.2. Parallel connection of lasers with individual resonators and power supplies

2. Experimental setup

Figure 3 shows a laser circuit with a series connection of modules and a common resonator [2].

Each of the discharge modules 3 with its own water cooling jacket had its own electrodes 5 and a power supply 6. The modules were interconnected by bellows 2. Mirrors 1 and 4 created an optical resonator common to all modules. A translucent mirror 1 with an adjustment mechanism was hermetically attached to the first discharge module through a bellows 2, a blind mirror 4 was glued to the end of the last discharge module. The appearance of the manufactured

modular laser is shown in Fig.4a. The appearance of the bellows assembly of the modules is shown in Fig.4b.

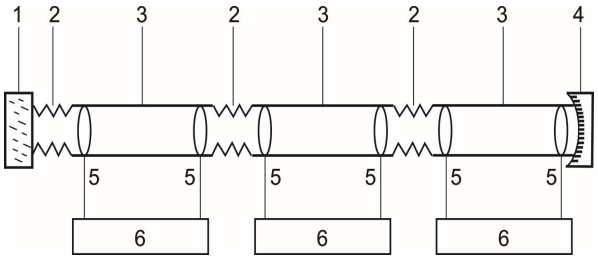

Fig.3. Laser circuit with series switching of modules and a common resonator; 1 – semitransparent flat mirror with an alignment mechanism, 2 – bellows, 3 – bit tubes, 4 – deaf spherical mirror, 5 – electrodes, 6 – power supplies

a.  b. 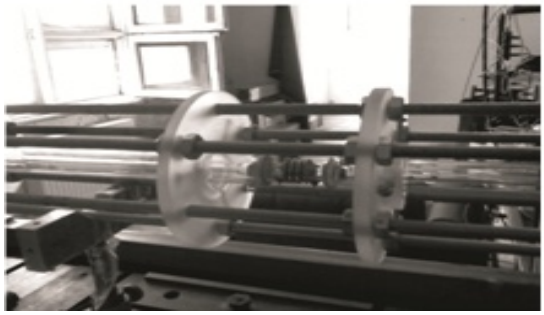

Fig. 4. The appearance of a modular laser. a) general view, b) module bellows assembly

When compiling a long discharge tube from separate series–connected or parallel–connected modules, the issue of the stability of such a multi–module tube becomes relevant. The question arises how the instability that accidentally occurred in one of the modules will affect the other modules. This is especially important with the acoustoplasma power mode of at least one of the modules. In this case, we ourselves create instabilities that are periodic in time and space, which lead to the acoustosplasma mode of operation [3, 4]. The experiment was carried out with a discharge tube composed of two series–connected modules (Fig. 5), which were located in a common optical resonator. One of the modules was powered by direct current, and the other was fed by modulated alternating current, which contained constant and variable components and worked in the acoustoplasma mode [5].

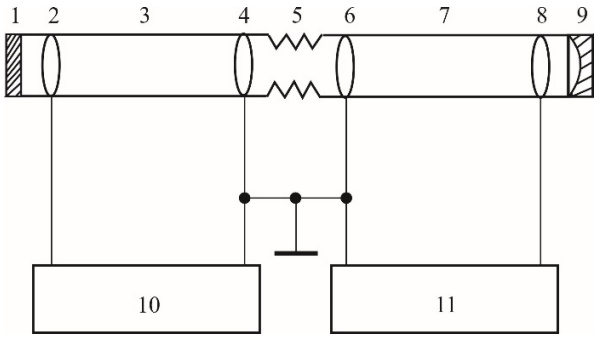

Fig.5. Scheme with sequential inclusion of two modules. 1–flat translucent mirror, 2–anode tube module with DC power, 3–module with DC power, 4–cathode, 5–bellows, 6–cathode, 7–module with acoustoplasma power mode, 8–anode, 9– blind mirror, 10–DC power supply, 11–module power supply with acoustoplasma mode

The effect of the module with acoustoplasma mode on the module powered by a direct current source was measured. This effect led to the fact that in the module powered by a direct current source there was a modulation of the supply voltage.

3. Results and discussion

Fig. 6 shows the dynamic characteristic of the influence of a module with acoustoplasma power on a module with DC power. The abscissa axis represents the current voltage value between the anode and cathode in the tube with an acoustoplasma power mode, with voltage modulation according to a law be alike to sinusoidal. The ordinate represents, respectively, at the same time, the current voltage value between the anode and cathode in the module powered by a direct current source. If there was no interaction, then they would have a straight line parallel to the abscissa axis.

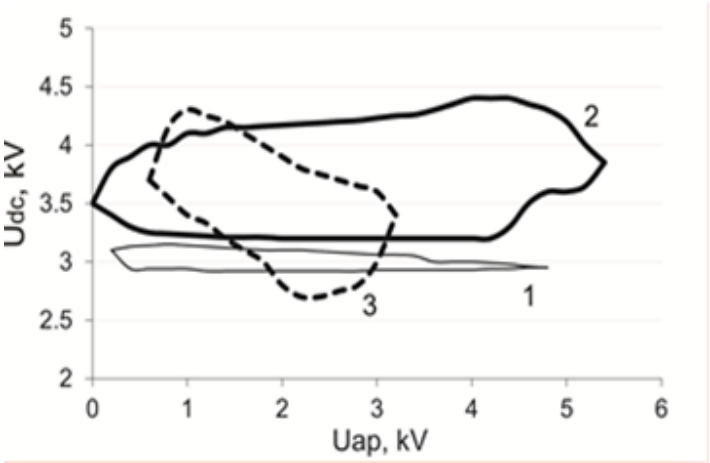

Fig.6. Dynamic characteristics of the interaction of modules. 1 – f = 1kHz, I_{dc} = 10mA; 2 – f = 1kHz, I_{dc} = 6mA; 3 – f = 5kHz, I_{dc} = 6mA

Since both modules have both constant and variable components of the supply voltage, the curves are above the zero point.

When assessing voltage modulation it is convenient to introduce the concept of modulation depth M, i.e. the ratio of the amplitude of the variable component to the value of the constant component.

It can be seen from Fig. 6 that for the first case, at a modulation frequency of f = 1 kHz and a depth of voltage modulation in the acoustoplasma module $M_{ap1} \approx 1$ for a module powered by a direct current source due to the appearance of induced modulation $M_{dc1} \approx 0.03$. For the second case, at f = 1kHz, $M_{ap1} \approx 1$ and less direct current we obtain $M_{dc1} \approx 0.15$. For the third case, at $M_{ap1} \approx 0.75$ $M_{dc1} \approx 0.3$. Thus, by choosing the magnitude of the constant component of the discharge current or voltage in each of the modules and the modulation frequency of the variable component of the discharge current in the module with acoustoplasma power, one can control the degree of influence of the acoustoplasma module on the module with direct current power.

It is especially important to note the first mode of Fig. 6. In this mode, the acoustoplasma module has almost no influence on the DC–powered module, despite the fact that the discharge tubes are connected by a common volume.

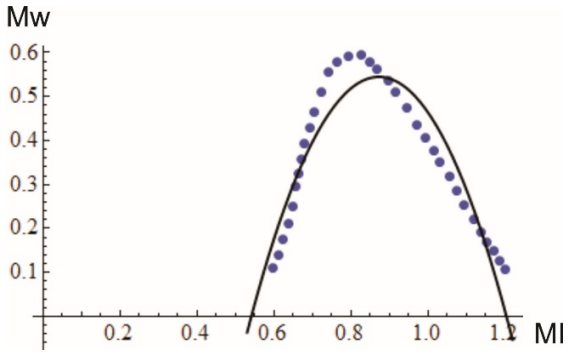

Fig.7. Dependence of the modulation depth of the laser radiation power M_W on the modulation depth of the shot current M_I

Figure 7 shows the dependence of the modulation depth of the power M_W of the acoustoplasma CO_2 laser radiation on the modulation depth of the discharge current M_I at a modulation frequency of 0.1 kHz. It can be seen from Fig. 7 that the depth of modulation of the laser radiation power nonlinearly depends on the modulation depth of the discharge current and has a threshold character. With a current modulation depth $M_I < 0.5$, the power modulation M_W is close to zero, i.e. there is almost no modulation of radiation power. With a depth of modulation of the discharge current $M_I = 0.8$, the depth of modulation of the power reaches a maximum value of $M_W = 0.6$. At the maximum depth of current modulation $M_I = 1.2$, there is almost no modulation of radiation power again. This, at first glance, paradoxical result is explained by the fact that with such a large modulation depth, the acoustoplasma mode is destroyed and at the same time a large number of harmonics are present in the discharge tube in the variable component of the discharge current, as a result, the radiation power is averaged.

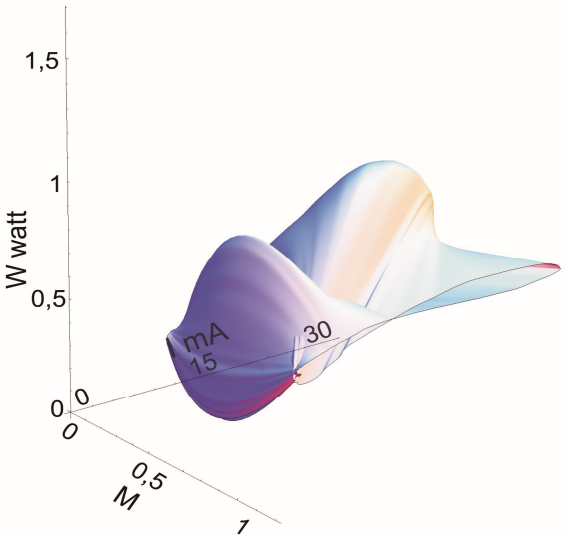

Fig.8. Three–dimensional surface of the dependence of the laser radiation power in the acoustoplasma mode (when modulating the discharge current at a frequency of 0.1kHz) on the modulation depth and the current value of the discharge current

Figure 8 shows a 3–D dependence of the instantaneous laser radiation power on the modulation depth and the current value of the discharge current (instantaneous during the modulation period). The X axis shows the depth of modulation of the discharge current, the Y axis represents the instantaneous value of the discharge current during the modulation period, and the Z axis represents the laser radiation instantaneous power. A laser mixture of CO_2: N_2: He = 1: 1: 8 was used.

It is clearly seen from Fig.8 that, at a large depth of modulation of the current, the laser radiation power very weakly depends on the instantaneous value of the discharge current during the modulation period.

Fig.9 shows the manufactured discharge modules. Four tandem modules have a rigid connection (glass junction or long tube). Outside, water shirts are visible, separate for each module. The electrode leads from each module come out in the gaps between the water jackets.

From such modules, it is possible to assemble both tandem tubes (connecting the modules using bellows) and parallel circuits, where each such tube is a separate laser.

Fig.9. Discharge modules

4. Conclusion

1. The effect of modules on each other in a two–module serial design with a common vacuum volume was studied, one of the modules was supplied with direct current, and the other worked in the acoustoplasma mode (it had direct and alternating components of the discharge current).

2. It is shown that the interaction of the modules depends on the frequency of the current modulation in the module with acoustoplasma power. You can select such a frequency that the module with modulation of the discharge current has almost no influence on the module with DC power.

3. By choosing the optimal depth of modulation of the discharge current, especially when overmodulating ($M_I > 1$), the output optical power of the laser is practically not modulated. Those, in this mode, the mutual influence of the modules in optical power will be minimal.

References.

1. Raizer Yu.P. Physics of gas discharge. Nauka, Moscow, 537p., 1987. (In Russian).
2. Hakobyan K.V. The acoustoplasma CO_2 laser parameters controle by acoustic fields. PhD Thesis, Yerevan, 2011.
3. Galechyan G.A., Mkrtchyan A.R. Acoustoplasma. Apaga, Yerevan, p.338, 2005. (In Russian).
4. Mkrtchyan A.R., Mkrtchyan A.H., Abrahamyan A.S. Acoustoplasma is a new state of plasmas. VII Intern.Conf.Plasma Physics and Plasma Technology, PPPT–7, Minsk, Belarus, 17–21 Sept.2012, Proc., v.1, pp.3–5, 2012.
5. Abrahamyan A.S., Hakobyan K.V., Sahakyan Q.G. Interaction of modules in discharge tube. Journal of Contemporary Physics (Armenian Academy of Sciences), v.46, issue 4, pp. 262–266, 2011 (In Russian. Взаимное влияние модулей в газоразрядной трубке. Изв.НАН РА Физика, 2011, т.46, N4, с.262–266).

Generation of Monodisperse Particles

S. H. Harutyunyan, L. E. Khachikyan, G. A. Harutyunyan

Institute of Applied Problems of Physics NAS RA
25 Hr. Nersissian Str., Yerevan, Republic of Armenia, 0014

Abstract: A laboratory device for generation of monodisperse particles (droplet and solid particles) of variable size and generation frequency is presented. The solid particles are formed by drying of droplets of different solutions in the glass tube. Experimental investigation has been performed in order to create periodical structures using these micro crystals. For focusing and "trapping" thermophoretic force affect on particles trajectory is applied.

1. Introduction

Monodisperse aerosol particles (droplets and solid particles with the narrow size distribution) with a known size and chemical composition are used in different applications such as instrument calibration, fundamental aerosol research applications, creation of artificial periodic structures (known as photonic crystals). Different methods for generating of monodisperse droplets are known [1]. The generation of droplets is based on the phenomenon of formation of satellite droplets in capillary breakup [5] of vibrating meniscus in the space between two identical capillary nozzles. The solid particles are formed as a result of drying of initial droplets of water solvable crystals (NaCl, LiIO3) in the glass tube with the controllable conditions of evaporation process and crystal particle formation. The droplets and particle were sized by using both direct microscope measuring and the diffraction patterns obtained by the superposition of diffraction patterns from the large number of single particles of uniform size chaotically distributed on the glass plate. The size range of droplets is 10 to 100 mcm in diameters and 2 to 25 mcm for solid particles (solid particle size depends on solution concentration). Experimental investigation has been performed in order to create periodical structure using these micro crystals. For focusing and "trapping" the particles thermophoretic force affect on particle trajectory is applied.

2. Generation of monodisperse droplets

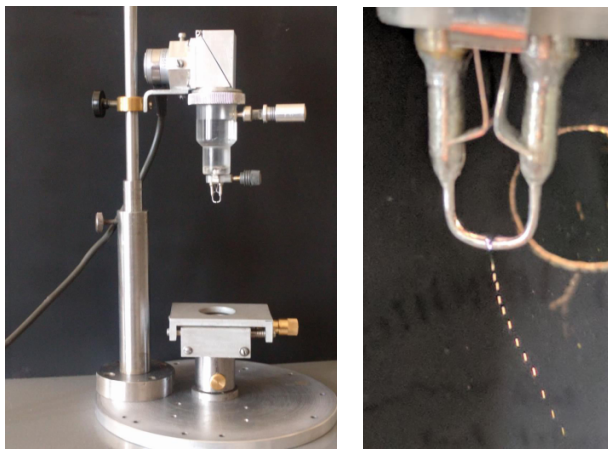

Fig. 1. Generator of monodisperse droplets

The principle of droplets generation is shown schematically in Fig.2 Generator includes a reservoir 1 for the liquid, an atomizer 3 and a source 2 of mechanical vibrations. The atomizer is made in the form of two L–shaped capillary nozzles 3 disposed towards each other in a small variable distance. The generator is also equipped with an elastic membrane 4 mounted above the surface of the liquid and connected to the source of mechanical vibrations 2. The output ends of the capillary tubes 3 are cut off at an angle θ.

The source of mechanical vibrations 2 by means of the elastic membrane 4 creates periodically changing pressure on the surface of the liquid, which leads to the periodic coalescence and breakup of the menisci formed at the output ends of the capillary tubes 3. (Fig. 2. a,b,c,d,e). With the reverse flow of liquid through the capillary tubes 3 the meniscus decreases and a filament is formed (Fig.2.d) which breaks up in the zones of instability .The liquid filament (satellite droplet) due to the surface forces takes a spherical form and falls at a certain initial velocity depending on the cutting angle. The droplet size dependence on the distance between atomizer nozzles for capillary diameter D=600mcm and generation frequency f=15 is shown in the graph in Fig.3.

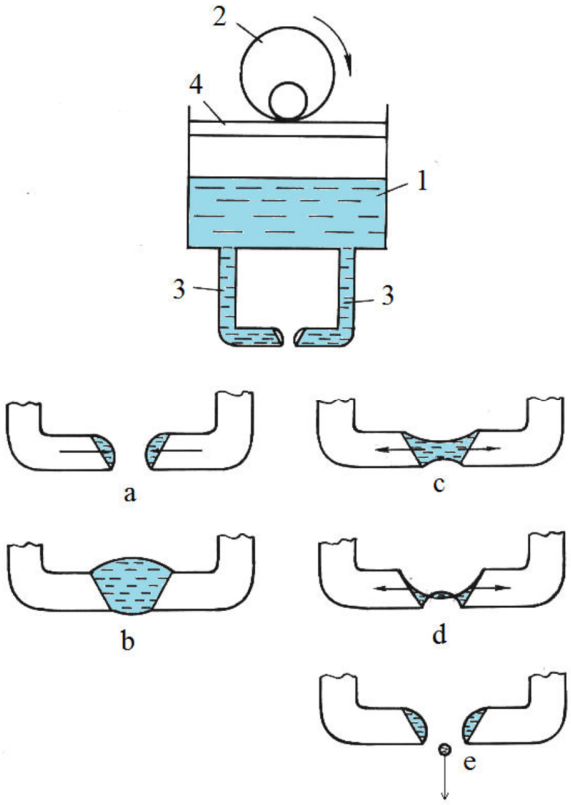

Fig.2. Principle of droplets generation

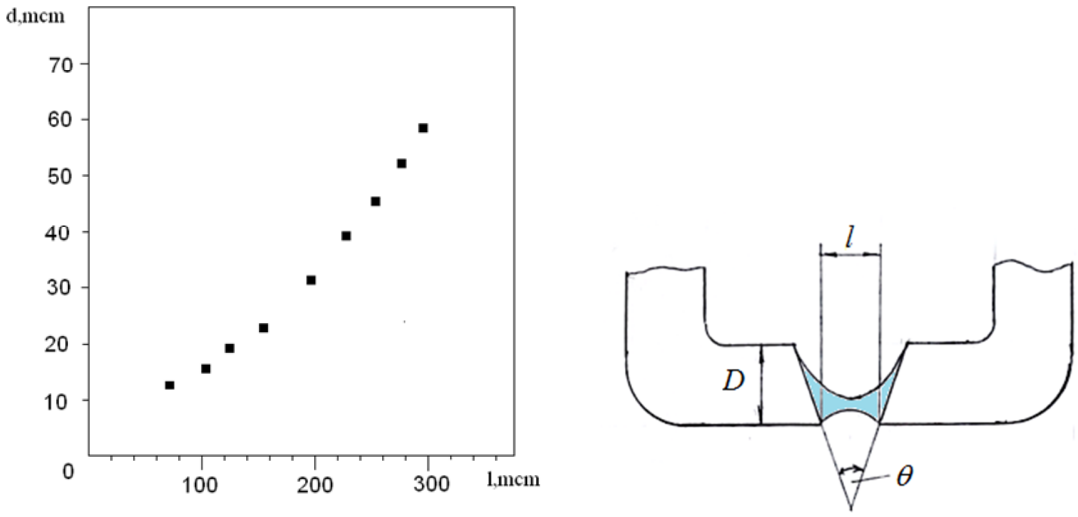

Fig.3. The droplet size (d) dependence on the distance (L) between atomizer nozzles

3. Solid particles

To obtain solid particles (micro crystals), various solutions ofwater–soluble crystals (NaCl, LiIO3, KDP, etc.) are used.

Crystallization of the generated droplets is carried out usingthe dry technology by evaporation [2] of the initial droplets in the crystallization chamber (a glass tube with controllable conditions of relative humidity and temperature inside).

The process of sold particles formation from the initial droplets is schematically shown in Fig .3. (a–e)

Inside the glass tube the particles move vertically with the sedimentation velocity. Simultaneously the evaporation of the solvent (water) takes place until the saturation of droplet solution is achieved after which the process of formation of crystal particle begins. Due to the droplet motion the evaporation intensity becomes higher in the front zone of droplet since the relative humidity is lower here that means that the concentration of solution is higher in this zone and the nucleation starts (most probably) just in the front zone of the droplet and the crystal particle grows [6] in the shape illustrated In Fig.4.e.The photographs of crystal particles of NaCl and LiJO3 are shown in Fig4 a,b.

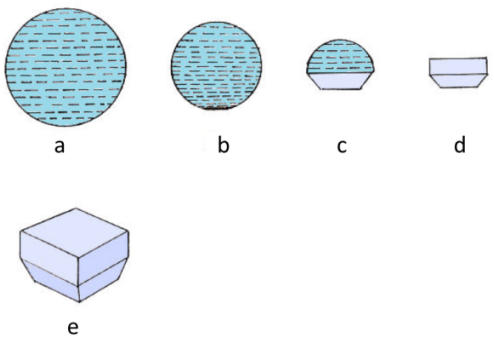

Fig.4. Schematic of solid particle (NaCl) formation

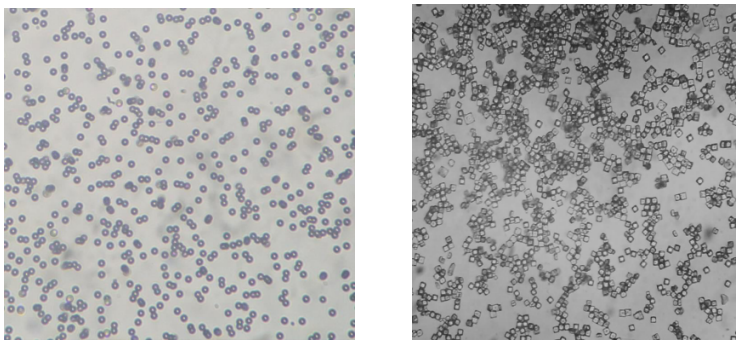

a b

Fig.5 a,b Photographs of crystal particles NaCl and LiJO3

4. Particle size measuring

The diffraction pattern observed on the screen (Fig. 6) is the result of a superposition of diffraction from the large number of individual obstacles (micro crystals) chaotically spread on the glass plate. The nature of the intensity distribution in each ring depends on the diameter of the beam, the size of the micro crystals, and their bulk shape.

Since the laser beam has a negligible small angle of divergence, we can assume that the plate is illuminated by a practically parallel beam of light.

If a large number N of micro crystals enters the beam region, the intensity of diffracted light is N times greater than the intensity created by a single particle. Since the diameter of the laser beam is very small, all particles that are in this region give very close–up diffraction patterns on the screen, a system of alternating wide light and dark concentric rings.

In the case of Fraunhofer diffraction the calculation formula for determining the particle size *d* can be written as

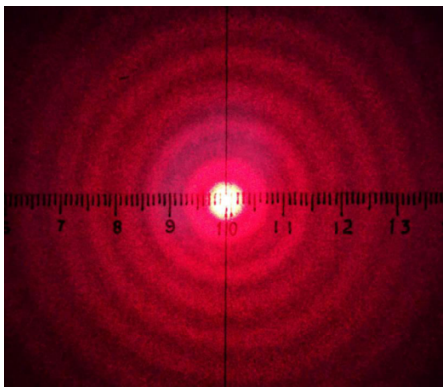

Fig.6. Diffraction pattern

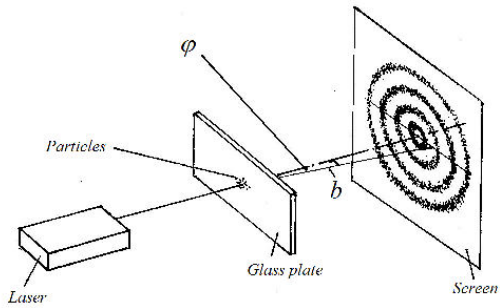

Fig.7. Particle size determining scheme

$$d = \frac{k_i \lambda}{\cos[\mathrm{arctg}(\frac{D_i}{2b})]}$$

where Di notes the diameter of i–th ring, b is the distance between sample and screen, λ– light wavelength, *k* takes the values 1.22; 2.22; 3.24 – for odd dark rings (i = 1,3,5) and 1,64; 2.70; 3.72 – for even light rings (i = 2,4,6), respectively.

5. Periodic structures

In order to create periodic distribution of particles on the substrate, masks with different size and periods of holes were used (Fig. 8) Masks are mounted directly on the surface of the glass plate, and particles (micro crystals) passing through the holes are distributed on the substrate along the corresponding micro–holes. However, the role of the mask is not limited only to the function of mechanical separation of particles. They are also used to create a temperature gradient inside the micro holes (by heating), and the particle falling into the hole region, under the influence of thermophoretic forces [3] moves to the central region of the cell. The mask is heated by a diode laser beam. Photographs (Fig. 9 and Fig. 10) show the results of applying of the mask. Laser beam diffraction pattern from this structure is shown in Fig.11.

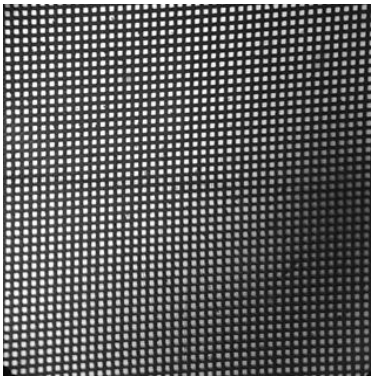

Fig.8.

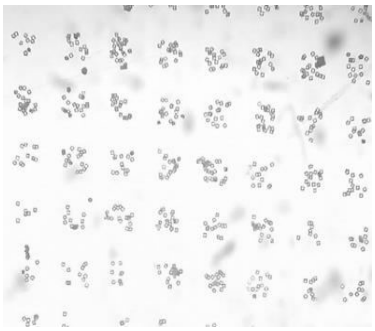

Fig.9.

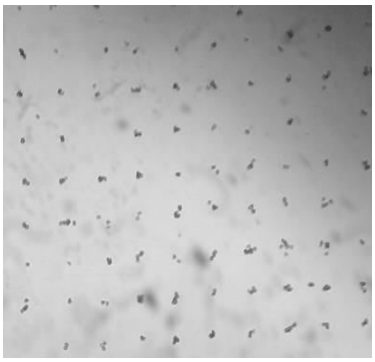

Fig.10.

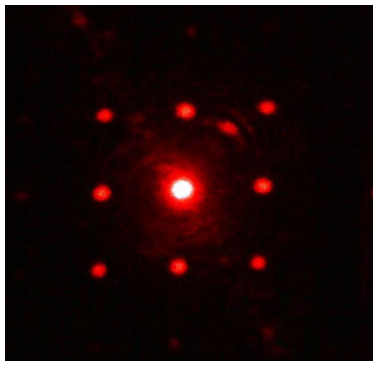

Fig.11. Difraction pattern from the periodic structure in Fig.10

Acknowledgment.

The authors of the present work would like to thank for A.K. Atanesyan and the staff of the laboratory of crystal growth IAPP NAS RA, for assistance.

References.

1. Shin–ichi Shimasaki1and shoji taniguchi1 formation of uniformly–sized droplets from capillary jet by electromagnetic force Seventh International Conference on CFD in the Minerals and Process IndustriesCSIRO, Melbourne, Australia
2. R Hołyst1, M Litniewski, D Jakubczyk, K Kolwas, M Kolwas, K Kowalski, S Migacz, S Palesa and M Zientara.Evaporation of freely suspended single droplets: experimental, theoretical and computational simulationsRep. Prog. Phys. 76 (2013) 034601 (19pp)
3. Kathleen De Bleecker and Annemie Bogaerts Role of the thermophoretic force on the transport of nanoparticles in dusty silane plasmas PHYSICAL REVIEW E 71, 066405 s2005d
4. Benjamin Y.H.Liu, Francisko J.Romay, William D.Dick, Keung–Shan Woo, Mihai Chiruta. A Wide–Range Particle Spectrometer for Aerosol Measurement from 0.010 μm to 10μm. Aerosol and Quality Research, 10;125 139,2010.
5. Gunter Brenn, Krassimir Danov. The formation of satellite droplets by unstable binary drop collisions. Physics of Fluids. September 2001.
6. A.A. Hovhannesyan, G.K.Grigoryan and A.K.Atanesyan. Growth of profiled single crystals of lithium iodate using a shaper from polimer nanoparticles, Journal of Contemporary Physics (Armenian Academy of Sciences) 2008, Volume 43, Number 5, Pages 251–253.

X–ray Study of the Lyotropic Mesomoophism pf Sodium Dioctyl Sulfosuccinate–Water System

A.G. Sargsyan[1*], S.M. Jomardyan[1], S.M. Grigoryan[1], M.A.Ghukasyan[1], A.A. Shahinyan[2]

[1]Institute of Applied Problems of Physics NAS RA
25 Hr. Nersissian Str., Yerevan, Republic of Armenia, 0014
[2] International Scientific Educational Center of the National Academy of Armenia
24d M. Baghramyan ave., Yerevan, Armenia 0019

Abstract: *In the work, the structural changes of the lamellar liquid–crystal phase of the sodium dioctyl sulfosuccinate (Aerozol–OT(AOT))–water system were studied by the method of X–ray analysis. The concentration of AOT in the system was from 23 to 98%. It was established that in this concentration range, the lamellar "smooth" phase is realized. The characteristic parameters and structural features of this phase are revealed.*

Keywords: x–ray analysis, lyotropic liquid crystal, mesomorphism, models of biomembranes, lamellar phase.

1. Introduction

Numerous studies show that lyotropic liquid crystals are typical representatives of biological phospholipid membranes, and the use of the latter as models of biomembrane organization has been proven.

Our task is to consider membranes as liquid crystal systems and to clarify mesomorphism in these systems.

To solve the main task of this work in terms of analyzing the structural rearrangements that underlie the shifts from the amorphous–crystalline properties of model membranes, the method of X–ray diffraction at small angles was used.

1.1. Experiment

X–ray structural studies to explore the dynamic behavior of molecules in liquid crystal systems require predetermined solutions of a number of technical and methodological problems. Sampling was carried out on the SURS–60 and URS–2 X–ray installations with cameras of the type KRON, RKSO intended for shooting on flat film, which were modified to study small angles at distances of samples from films in the range 0.05–0.1 m. The converted camera provide an opportunity to get reflexes in the range of angles from 1 to 45^0. Schematic images of the camera are shown in Picture 1

[*]**E – mail:** *ansarishkhan@yahoo.com*

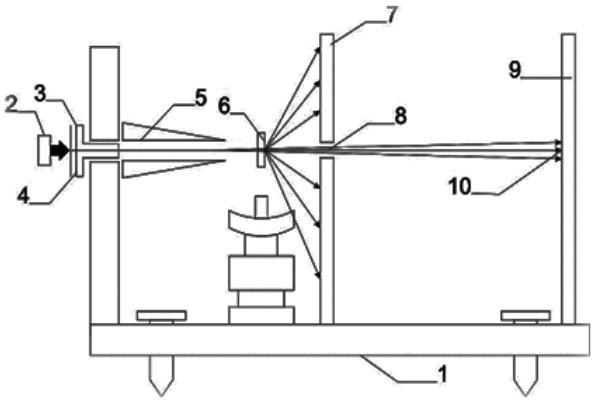

Fig. 1. Schematic images of the camera

X–rays coming out of the focus of the X–ray tube 2 pass through the nickel filter 3, diffraction 4 and collimator 5 and fall onto sample 6. The diameter of the aperture opening is $1x10^{-4}$m, the length of the collimator $8x10^{-2}$m, the diameter of its opening at $1x10^{-4}$m. Such collimation provides fairly good accuracy.

Diffracted at large angles, the rays are recorded on an X–ray film placed in the cassette 7. The latter has an opening 8 in the middle through which the transmitted rays are fixed on the film placed in the cassette 9. The primary beam is absorbed by the absorber 10. The modified camera makes it possible to record reflexes within the angles 1 – 45°(the small angle part is 1 – 5°).

Tubes of the types BSV–24, BSV–11 with an anticatode from Cu, producing radiation in the region of relatively long waves were used. The Kα lines of copper were distinguished using nickel filters with a thickness of 0.015 mm. Anode voltage is 40kv, anode current is 20ma. The exposure time was chosen 4 hours. It was used films type RTG–B company of Primax Berlin Germany. Quartz thin–walled capillaries (made in Germany) with a wall thickness of 0.01 mm and a diameter of 0.4–1mm were used to prepare the sample. Absorption of rays and the appearance of the background on radiographs when using these capillaries is almost absent.

The X–ray diffraction method that we redesigned will allow us to obtain information on the size, shape, and compactness of the colloidal formations.

2. Samples

The structures of mesophases obtained on the basis of Aerosol–OT (AOT) and water are studied in this paper.

Production description – production name –Dioctylsulfosuccinatesodiumsalt, formula – $C_{20}H_{37}NaO_7S$, molecular weight of formula – 444.56 g / mole, color – white, appearance–hard, analysis (according to USP) – purity 97.0 – 103.0%, water (according to Karl Fischer) – 2%, manufactured by,, Sigma–Aldrich,, USA, website – www.sigmaaldrich.com.

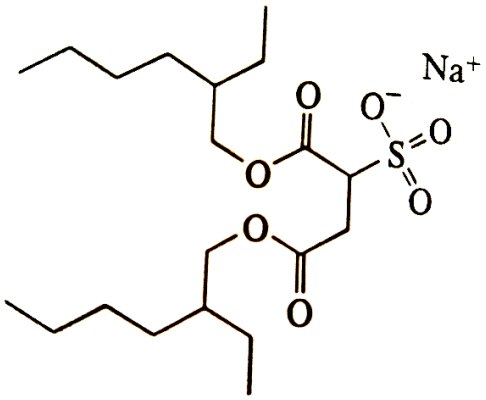

Fig.2. The structural formula of the AOT molecule.

Quartz capillaries with a wall thickness of 1x 10^{-5}m and a diameter of 0.4 x10^{-3} to 1x 10^{-3}m were used to prepare the samples.

X–ray diffraction samples were prepared according to the following method: heat treatment was carried out – the specimen was kept at a temperature of 353K before taking radiographs for half an hour, after which an isotropic melt of the corresponding concentration was introduced into the capillary, sealed on both sides and cooled to room temperature. The finished sample was examined immediately after processing, as well as at certain intervals. Studies were conducted in the temperature range of 293 – 300K.

The orientation of the samples in the absence of water was carried out using mechanical stretching. Radiographs of the stretched "anhydrous" specimens, made in the form of cylinders, with a diameter of 0.4 – 1mm, were taken without a capillary. Orientations of concentrated aqueous solutions were carried out by drawing the solution into the capillary.

3. Results

On X–raygrams, the reflexes were obtained, having the form of homogeneous circles, indicating the presence in the sample of randomly arranged relative to each other domains, within which the AOT molecules are arranged in order, forming liquid crystal mesophases. Samples were taken with concentrations from 23 to 93% and "dry" solutions, which were obtained with open–length aging. In the latter samples, only reflexes of hydrated water remained. "Dry" samples were taken without a capillary.

Interplanar distances and relative intensities at various concentrations of AOT–water solutions are given in Table 1[6].

Table 1. Interplanar distances and relative intensities of the AOT–water system

N	AOT concentrations in %	Св/С	Interplanar distances d_w Å	Relative intensities
1	26	2.9	58	4
2	31	2.2	50	5
3	38	1.6	51.4 ; 22	9
4	42	1.4	38.2 ; 23	9
5	48	1.1	38.5 ; 22	6 ; 5
6	50	1	35 ; 21	7 ; 5
7	59	0.7	30 ; 28 ; 15.6	6 ; 4; 2
8	60	0.66	24.7	8
9	64	0.56	24.6 ; 21	5 ; 7
10	70	0.43	25 ; 22	6 ; 8
11	75	0.33	22	8
12	84	0.19	21.5 ; 4.6 ; 3.6	9 ; 5 ; 3
13	91	0.09	22 ; 4.6 ; 3.9 ; 3.6	9 ; 5 ; 3 ; 4
14	94,7	0.05	21 ; 4.6 ; 3.9 ; 3.6	10 ; 5 ; 2 ; 5

In the presence of a forced mechanical orientation – (by pulling the sample into the capillary), there is a mutual orientation of the domains. The X–raygram of samples of the oriented domains is shown in Fig. 3.

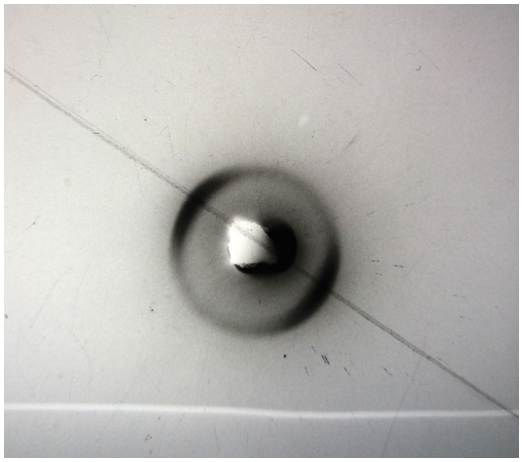

Fig. 3. X–raygram of the orientated sample with 75% AOT concentration.

With prolonged exposure of the samples, without changing the concentration, the circles on the X–raygram become grainy (Fig. 4).

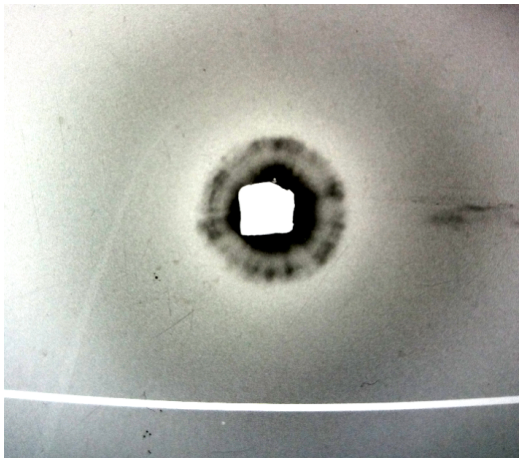

Fig. 4. The X–raygram of AOT–water sample with 75% concentration of AOT.

On X–raygrams of the concentrated samples, thin reflections at large angles are revealed. In the circumference, which characterizes the lamellar phase, intensity blobs appear in the form of a six–gram (Fig. 5).

Fig. 5. The X–raygram of the concentrated sample of AOT– water.

4. Discussion

AOT molecules possess high amphiphilic properties, as a result of which they form micelle solutions and liquid crystal mesophases. Due to the amphiphilicity of AOT molecules, their lyotropic mesomorphism is manifested. The peculiarities of their behavior in the aquatic environment are determined by the balance of hydrophilic and hydrophobic interactions, which ensure, on one side, the maximum contact of polar groups of molecules with water, and on the other – the contact of hydrocarbon sections mainly with each other. At low concentrations, AOT in water forms micellar solutions and, beginning with 23%, lyotropic liquid–crystal “smooth” phases are formed with intradomain lamellar structures, i.e. there is an alternation of parallel layers of AOT mono– (L_2) and bimolecular (L_1) thickness and water layers [2,4]. In lyotropic

mesophases, at higher concentrations of AOT, the structure stability and the presence of long–range order are detected. With the help of X–ray diffraction, the ordering of the long–range order and the dimensions of the diffracting cell of LCC [5] are determined. On X–raygrams revealed reflexes, having the form of homogeneous circles. They indicate the presence in the samples of domains randomly located relative to each other, within which the AOT molecules are arranged in an ordered manner. Besides these lines there are two fuzzy diffuse halos, characteristic of "liquid" paraffins and water.

The presence of halos on X–raygrams indicates that there are areas with unoriented molecules in the sample and hydrocarbon tails are in the "liquid" state. Under certain external influences, orientation order may be lost in lamellae. Even in the orientational state, due to the presence of rotational and oscillatory motions around the axis of the molecule, identical carbon atoms located in different molecules can be located in different planes passing through the axis of the AOT molecule at any given moment. Since a large number of molecules are involved in the appearance of a reflex during X–ray, the "average" or "statistical" molecule will have a look of cylinder (Fig. 2). The X–ray reflexes due to the dynamic state of the AOT molecules in the lamellae are poorer compared to the case when carbon atoms located in different molecules, have a certain spatial arrangement. The latter state is average between the crystalline and gel state, i.e. represents "coagel". AOT "coagel" is found starting from an AOT concentration of 84%. High–angle, thin reflexes that show up at large angles indicate an orderly packing of AOT molecules at the AOT–water interface. Based on the obtained X–raygrams, we construct the dependence of the interplanar distance d on the ratio of water concentration (C_w) to AOT concentration (C) (Fig. 6).

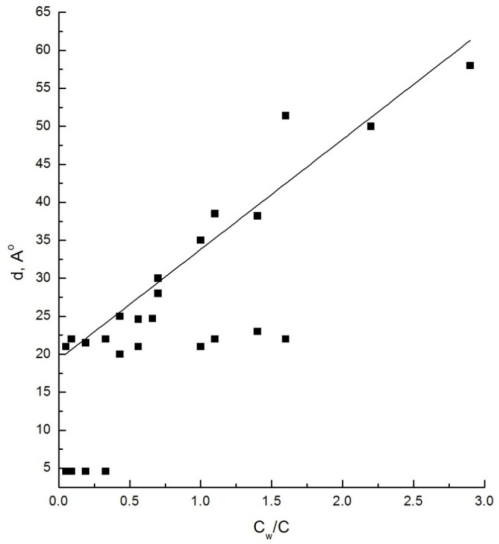

Fig. 6, Dependence between distance d and C_w /C.

As can be seen from the figure, with an increase in the concentration of water, a linear increase in d from C_w / C occurs. At an AOT concentration of less than 23%, only diffuse halo of water is present on X–raygrams. As the concentration increases, a second diffuse halo appears, which is characteristic of "liquid" paraffins. With an increase in the concentration of AOT, the reflexes become thin and clear. An analysis of the registration data revealed that a "smooth" lamellar phase appears in the AOT–water sample over time. Extrapolation of direct from C_w/C to zero water content, according to the data in Fig.6, the lamella thickness is determined: $d_l = 17.5$Å. This value corresponds to the length of a monomolecular lamella. The difference $d - d_l = d_w$ is the minimum thickness of the interlamellar water layer, that is the amount of water bound to the lamella surface. This value is 4.5Å (Fig.6.). As can be seen from the figure, at high AOT concentrations, the interplanar distances remain unchanged. When $C_w/C \leq 0.3$, it does not depend on the concentration of water. This indicates that "bound" water (hydrated water) remains in the interlamellar space. At the same time, the "coagel" phase is realized in the system, as evidenced on X–raygrams by the appearing reflexes at large angles.

According to the method developed by Luzati, one can determine the changes in the interplanar distances (d) from concentration of amphiphilic substance [4]. For the lamellar phase, this formula has the form:

$$d=d_l(1+pC_w/p_wC) \quad (1)$$

where $d = d_l+d_w$, d_w and d_l respectively the thickness of the water layer and lamella. p, p_w density of lamellae and water, C and C_w concentration of AOT and water. Equation (1) makes it possible to determine the density of a lamella without hydrated water, which is a measure of the structural organization of the hydrophobic core of the lamella. From the slope of the straight line d from C_w/C for the density of the AOT lamellae, obtained at C_w/C =0.3, $p = 0.938p_w = 1.0323$g/cm; at $C_w/C = 0.25$ $p = 1.276p_w = 1.404$;

Since a measure of the compactness of the location of AOT molecules in a lamella, in addition to density, is also the specific surface S, i.e. the size of the area on the surface of the lamella, coming to the polar group of one AOT molecule, then, having determined the values of the density and thickness of the lamella, we obtain values for 75% of the solution S=88Å^2, and for 80% of the solution $S = 64.5$Å^2.

The presence of homogeneous circles in X–raygrams proves a chaotic location of domains in the sample. But in X–raygrams also present cresent–like circles (Fig. 3). This takes place at presence of forced mechanical stretching and extrusion of the sample in capillary. It may be assumed that an orientation of domains and consequently lamells as well takes place. The angle of inclination of molecules axis can be determined directly from analyzing the intensity distribution relative to equator (for the equator direction it is taken the direction parallel to the plane of lamella multilayer plane) in X–raygram diffraction image (6) from orientated samples according to intensity bunches (sycles) in Fig.3, that corresponds to results 38^o (1).

While long keeping the samples in AOT–water system, the orientation of domains takes place. This proves by the grainity of circles in the X–raygrams (Fig.4). For more concentrated solutions the circles become intermittent. In X–raygrams of concentrated samples during further long drying while containing only hydrated water in a "dry" sample it was revealed an ordered hexagon, which enables to assume about the reorientation of lamellas parallel to the walls of the capillary (Fig. 5). In the "coagel" state of a complex two–deminsional hehagonal packing of AOT

moleculae, it must correspond to the following Brague distancs ratio: 1:√3/2:1/2…., that is weakly seen in X–raygram – 4,5; 3,8; 2,25 Å ….

Thus in the Aerosol OT–water system when water concentration more than 23%, “smooth” liquid–crystal mesophasa with lamella single–molecular thickness is realized. The molecules in lamellas are bent at angle 38° to the surface of separation lipid–water phase. In the system the liquid–crystal “gel” phase is realized that when lipid concentration is high is turned into the “coagel” phase. In the AOT sample when only hydrate water is present the “coagel” state is realized.

References.

1. Dorest D.L., //Biochem. et Biophis. Acta, Biomembranes, 1987, v.203, N2, p.319–332.
2. Folgner P.L., Thompson T.E., Barenholz D.Y., Lichtenberg D. Plastisity of biological membranes. //Biochemistry, 1983, v.22, p. 1670– 1674.
3. Hitchcock P.B., Mason R. //J. Mol.Biol. 1975, 94,p.297–299.
4. Luzzati V., Chapman D. X–ray Diffraction studies of lipid–water Systems in Biological Membranes //N.Y. 1968, –71p.
5. Rand R.P., Sengupta S. //Biochem. et Biophis. acta, 1972, v.255, p.484–492.
6. Tonford Charles. Mucelle shape and size. – J. of Physical Chemistry, 197,No.21, v.76, 1072, p.3020–3061.

The Study of Lyotropic Mesomorphism of A System of Sodium Pentadecyl Sulfonate–Polyethylene Glycol –Water under the Influence of Temperature

A.G. Sargsyan[1*], S.M. Jomardyan[1], S.M. Grigoryan[1], M.A.Ghukasyan[1], A.A. Shahinyan[2]

[1]Institute of Applied Problems of Physics NAS RA
25 Hr. Nersissian Str., Yerevan, Republic of Armenia, 0014
[2] International Scientific Educational Center of the National Academy of Armenia
24d M. Baghramyan ave., Yerevan, Armenia 0019

***Abstract**: The method of X–ray analysis was used to study the structural changes of a multicomponent liquid crystal of sodium pentadecyl sulfonate–polyethylene glycol–water in the lamellar liquid crystal phase under the influence of temperature. Studies were carried out at concentrations in the system from 23 to 98% at different contents of polyethylene glycol. The concentration interval of the lamellar "smooth" phase is established. The characteristic parameters and structural features of this phase and the influence of temperature on them in the range from 293–353 K are revealed.*

Keywords: radiography, multicomponent liquid crystal, lyotropic liquid crystal, biomembrane models, lamellar phase.

1.Introduction

The formation and stability of lyotropic liquid crystals (LLC) is due to the balance of hydrophilic–hydrophobic interactions in a system of molecules [1, 2]. Just this determines the ability to control the structure and properties of LLC through the influence of non–mesogenic additives that can effectively change the interaction forces between the matrix molecules and the included components, therefore, there should be significant differences in the nature of the effects of various non–mesogenic substances on the structure of LLC . From this point of view, it is of interest to study multicomponent models of biomembranes based on lyotropic liquid crystals.

Under certain conditions, biomembrane lipid suspensions can form aggregates of various structures, that is lipids have the property of polymorphism. Polymorphic transformations were also found in biological membranes [3–11]. Structural thermal rearrangements in eukaryotic membranes containing relatively many cholesterol or membrane proteins found by various physicochemical methods indicate that they are the result of structural rearrangements affecting the lipid and protein components of membranes [12] The question arises whether structural rearrangements are caused observed in the region of 283–303K, crystallization of membrane lipids or polymorphic transformations of a gel–liquid crystal.

Each of the biomembrane models was studied in order to understand and explain some of the facts observed in the study of membranes. But not one of them is able to explain satisfactorily all the data accumulated by science.

[*]**E – mail:** *ansarishkhan@yahoo.com*

Thus, the question of the nature of the occurring thermal and lyotropic rearrangements remains open.

In this work, we studied the effect of temperature on a model system of biomembranes containing macromolecular non–mesogenic additives and mesomorphic transformations depending on their characteristic parameters.

Since LLC is determined by the equilibrium of hydrophilic hydrophobic interactions of molecules, it can be assumed that the introduction of a new component into the system effects the structure of LLC through the impacked on the balance of hydrophilic and lipophilic interactions. In this case, LLC can act as a matrix for the orientation of molecules that do not have the ability to independently form a liquid crystal phase. To this aim, the influence of temperature on the system of sodium pentadecyl sulfonate (PDSN) –polyethylene glycol (PEG) –water capable of effectively changing the interaction forces between the molecules of the matrix and the macromolecule at different temperatures was studied.

The choice of PEG as a macromolecular additive is due to its widespread use in light industry, in the food industry, in the cosmetics industry, and is used to restore and preserve wet wood, in archaeological finds, and to model underwater eruptions. Based on PEG, lubricants, cutting fluids, and solvents are produced. PEG is also used for the manufacture of biomembranes, water–soluble films, and drugs. With the help of PEG, the Italian neurosurgeon Sergio Canavero expects to connect the nerve cells responsible for transmitting vital impulses from the brain to organs and limbs. PEG is also capable of repairing a damaged membrane, facilitating the fusion of two damaged cells into one large nerve cell.

Thus, a set of methods, including a key component – PEG was used in practice. However, more work remains to be done to make its application reliable and to ensure confidence in the correct selection of many variables that are important for a successful outcome.

2. Experiment

To study LLC, it is necessary to consider the phases of not individual molecules, but of structural elements, which are supramolecular formations. The nature of the symmetry of the structural element is determined by the symmetry of the arrangement of the molecules that form it – the bilayer, cylinder, sphere. Polymorphic transformations relate to objects consisting of many structural elements [13, 14].

Our task is to create experimental conditions for studying the structural elements of both molecular and supramolecular formations, for which requires a preliminary solution of a number of technical and methodological problems.

The following requirements are imposed on the experiment: X–ray collimation, slit width, small–diameter holes, focusing, exposure, sample size and preparation, X–ray radiation wavelength, data recording methods, effects arising from small–angle X–ray scattering, diffuse scattering, results obtained and their discussion. Samples were taken on URS–60 and URS–2 X–ray installations with KRON and RKSO cameras intended for shooting on a flat film and modified for studying simultaneous scattering at large and small angles of reflexes in the range of angles from 30 to 850 at sample–film distances 0.05–0.3 m. A schematic image of the camera is shown in Fig. 1.

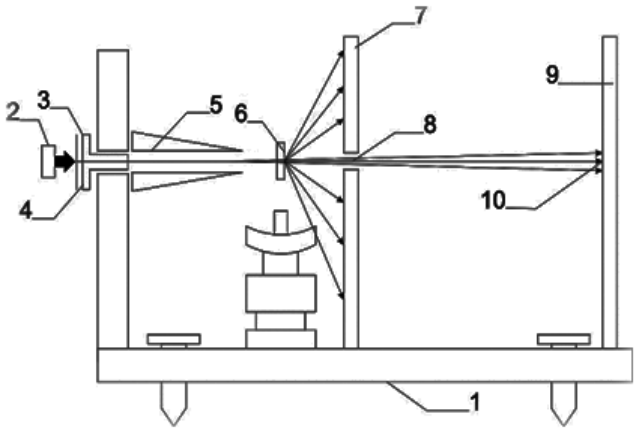

Fig. 1 Schematic picture of the camera

X–rays coming out of the focus of the X–ray tube 2 pass through a nickel filter 3, the diaphragm 4 and the collimator 5 and fall onto the sample 6. The diameter of the aperture is $1x10^{-4}$ m, the length of the collimator is $8x10^{-4}$ m, the diameter of its hole at the exit is $0.8x10^{-4}$m The improvement in the beam collimation consisted in the optimal reduction of the width of the slit placed in the beam path. The main advantage of small–hole collimation is the absence of distortion in the X–ray diffraction patterns when studying oriented samples. The main disadvantage is associated with a rather long exposure time necessary for obtaining undistorted paintings. Such collimation provides a fairly good accuracy.

Diffracted at large angles, the rays are recorded on an x–ray film placed in the cassette 7. The latter has a hole in the middle 8 through which the transmitted rays are fixed on the film placed on the cassette 9. The primary beam is absorbed by the absorber 10. The modified camera makes it possible to register reflections within the angles 1–45° (the small–angle part is 1–5°).

We used tubes of the BSV–24, BSV–25, and BSV–11 types with a Cu cathode that emits radiation in the region of relatively long waves. Copper Kα lines were extracted using nickel filters 1.5×10^{-5} m thick. The voltage at the anode is 40kV, the anode current is 20mA. The exposure time was selected 4 hours. Films of the RTG–B type from Primax Berlin Germany were used. To prepare the sample, quartz thin–walled capillaries (manufactured by Germany) with a wall thickness of $1x10^{-5}$m and a diameter of $0.4x10^{-3}$m to $1x10^{-3}$m were used. Absorption of rays and the appearance of the background on radiographs when using these capillaries are practically absent.

The reconstructed method of x–ray diffraction allows us to obtain information about the size, shape, compactness of the location of colloidal formations.

3. Samples

The structures of simplified three–component models of liquid crystal systems, obtained on the basis of highly concentrated aqueous solutions of the surfactant PDSN – ($C_{15}H_{31}SO_3Na$) and PEG, are studied.

The mid–range PDS product of Veb Leuna contains the following impurities:

The main substance ……..	n / m	98%
Sodium chloride ……..	n / a	1.4%
Sodium sulfate ……	n / a	0.1%

Neutral oils …… .n / a 0.1%
Water ……n / a 0.2%
Sodium hydroxide ……n / a 0.1%
Iron …….. n / a 0.5%

At room temperature, the studied sample has the appearance of a dull white paste containing 6% hydrated water. The spatial structure of the PDSN molecule can be represented as shown in Figure 2.

Fig. 2. Schematic structure of the PDSN molecule and its arrangement in the lamella

PEG with a molecular weight of 2000g/mol was used as a high molecular weight additive. PEG with a mass of up to 2000g/mol – highly–shaped flakes or cream–colored powder. The structural formula has the following form:

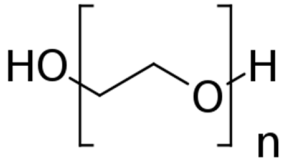

$HO-\left(CH_2-CH_2-O\right)_n-H$, rational formula – $C_{2n}H_{4n+2}O_{n+1}$, density 1,1 – 1,2g/cm^3.

For the preparation of samples, quartz capillaries with a wall thickness of 1x 10^{-5} m and a diameter of 0,4x10^{-3}m to 1x10^{-3}m were used.

Samples for X–ray diffraction were prepared by the following method: heat treatment was carried out – until the X–ray diffraction patterns were taken, the sample was kept at a 353K temperature for half an hour, after which an isotropic melt of the corresponding concentration was introduced into the capillary, hermetically closed on both sides and cooled to room temperature.The finished sample was examined immediately after processing, as well as at certain intervals. The studies were carried out in the temperature range fr om 293 to 353 K.

The orientation of the samples in the absence of water was carried out using mechanical tension. X–ray diffraction patterns of stretched “anhydrous” samples made in the form of cylinders with a diameter of 0.4–1 mm were taken without a capillary. Orientations of concentrated aqueous solutions were carried out by drawing the solution into the capillary.

4. Results

The studies were carried out at a PEG content of 9% in the PDSN–PEG system in the "smooth" phase. The control image of an 86% sample of the PDSN–water system revealed the lamellar structure of PDSN molecules of a monomolecular layer 27.5 Å thick. On radiogram revealed a reflex in the form of a uniform circle. When a 67% sample of the PDSN–PEG–water system is added to the PEG system in an radiogram with a PEG content of 9%, the reflex becomes clear and slightly grainy. By evaporation of the sample up to 86% at room temperature, the reflex in the radiogram remains clear and oriented, sickle–shaped with an inclination angle of 42°. When the sample is heated to 308K, the tilt angle increases to 68°, at a temperature of 313K – 80° and at 318K – 90°. Further heating to 333K leads to the disappearance of the sickle–shaped reflex. Pictures of samples at temperatures of 343 and 353K give clear and uniform circles on the radiogram.

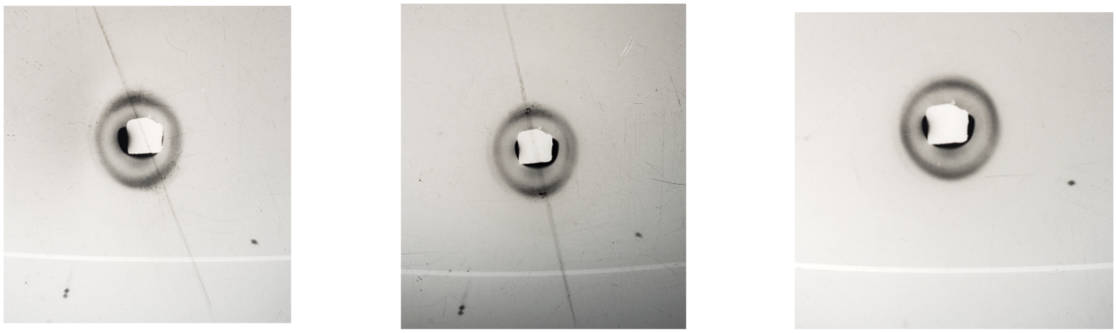

Fig. 3. The radiogram of 86% samples of the PDSN–PEG–water system with the content 9% PEG at temperatures of 308, 313, 353K.

A sample heated to a temperature of 353 K was cooled to room temperature. In this case, monocrystallism and reflexes appear at large angles.

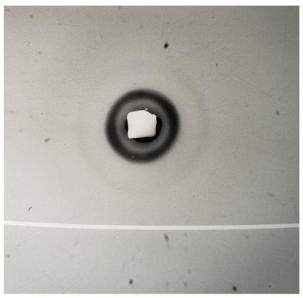

Fig.4. The radiogram of an 86% sample of the PDSN–PEG–water system, when PEG 9%, heated to 353K and cooled to room temperature.

The texture is also preserved after two days of taken radiogram. When reheating the same sample to 353K, on the the radiogram only traces of monocrystallinity remain, but a clearly defined circle preserved.

With an increase in the concentration of PEG to 36% in the PDSN–PEG–water system at room temperature, a characteristic circle with an interplanar distance of 24.7 Å appears on the x–ray in a 54% sample. With increasing temperature, the interplanar spacing decreases. The results are shown in table 1

Table 1. Temperature dependence of the 54% PDSN–PEG–water system

Temperature in K	Interplanar distance in Å
295	27.5
308	27
313	24.7
318	24
333	23.8
343	23.5
353	22.5

On the radiograms of a 70% sample at a PEG content of 36% at room temperature show a crescent circle. The latter is formed when the concentrated solution is drawn into the capillary. With a further increase in concentration, the intensity of reflexes characteristic of the lamellar structure increases and thin weak reflexes appear at large angles. When the sample is completely dry, when it contains only hydrated water, a number of distinct reflexes are revealed at large angles. Interplanar distances and relative intensities of the "dry" sample are shown in table 2.

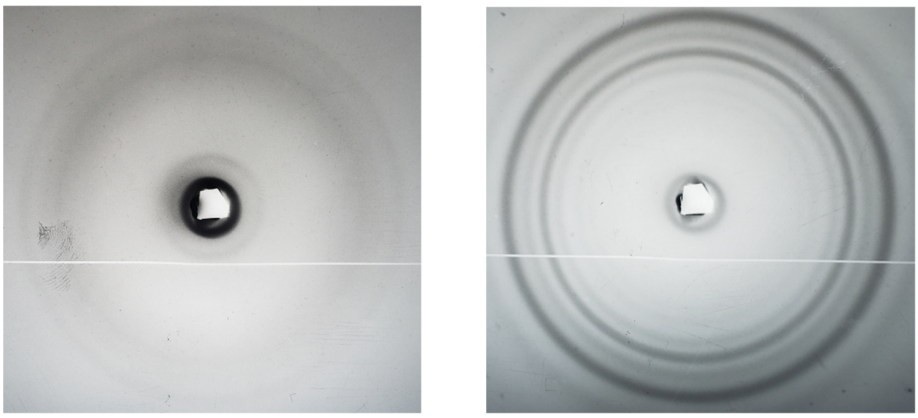

a b

Fig.5. The radiograms of samples of the PDSN–PEG–water system, with a PEG content of 36% a) a concentration of 86%, b) a "dry" sample with a content of hydrated water.

Table 2. Interplanar distances and relative intensities of a highly concentrated sample of the PDSN–PEG–water system at a PEG content of 36%.

N	Interplanar distance in Å	Relative intensity
1	27.4	10
2	6.6	1
3	6.2	2
4	5.3	3
5	4.8	9
6	4.3	5
7	3.96	8
8	3.5	4

Studies were also conducted to determine the effect of temperature on highly concentrated PDSN–PEG–water systems with a PEG content of 36%. Samples were taken at temperatures of 308, 313, 318, 333, 343, 353K. Under the influence of temperature, the intensity of reflections at large angles gradually decreased, and at a temperature of 343K, they completely disappeared. But at the same time, the reflex with an interplanar distance of 27.4 Å was split into two thin, clearly defined reflexes with interplanar distances of 27.4 Å and 24.7 Å. The latter was also revealed at a temperature of 353K.

5. Discussion

To decipher the obtained X–ray diffraction patterns, we schematically represent the possible intra–domain structures of the lyotropic liquid crystal “smooth” phase (Fig. 6).

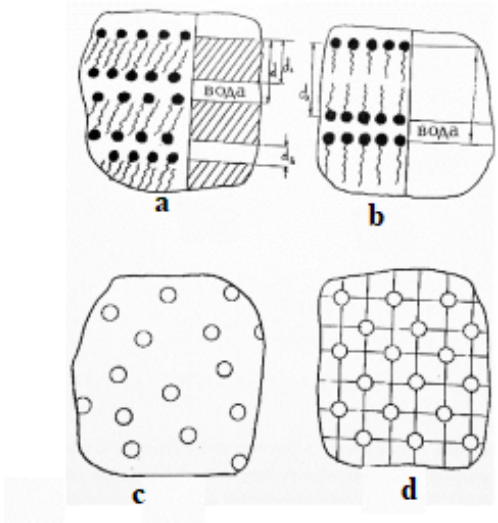

Fig.6. Arrangement of molecules in the “smooth” phase: a–lamellae of monomolecular thickness; b–lamella of bimolecular thickness; c– chaotic arrangement of the heads of the molecules; d–rectangular centered packing of heads.

We found that in the “smooth” phase, in the absence a little water content, an intradomain lamellar structure is realized, there is an alternation of PDSN parallel layers of

monopolymer and bimolecular thicknesses and water layers. In lamellae, surfactant active molecules can orient themselves at an angle to the lamella–water interface or perpendicular to it. Remaining oriented, the molecules in the lamellae can be located randomly relative to each other or in a certain order. The trans structure of the hydrocarbon skeleton of the PDSN molecule is shown in Fig. 2.

When 9% PEG is added to the system in the "smooth" phase, the reflex appears more distinct, slightly granular, characteristic of a layered structure with alternating layers of PDSN and water. It can be assumed that PEG is located in the water layer and leads to the strengthening of the layers. With an increase in the concentration of the sample — by evaporation, the interplanar spacing decreases, and starting from a concentration of 60% it equals 27.4Å and does not change with further evaporation. But with a further increase in concentration, the reflex with an interplanar distance of 27.4 Å becomes sickleshaped. This indicates that the PDSN molecules in the layers are inclined to the lamella–water interface. It can be assumed that this is the effect of PEG, which, located in the water layer of "bound" water, compresses the lamella, tilting the molecules. In a 86% sample at room temperature, the PDSN molecules are tilted at an angle of 42^{o} to the interface.

By heating the sample, the tilt angle increases and already at 318K equals 90^{o}. This can be explained by the fact that an increase in temperature leads to partial loosening of the structure and a decrease in the thickness of "bound" water: since the interplanar distance remains unchanged – equal to 27.4Å. A further increase in temperature to 353K does not change the structural parameters. This states that the PEG shields the lamellar structure of the PDSN, ensuring its strength and stability with respect to water and temperature.

After cooling to room temperature in a heated sample, the "smooth" phase is retained in the sample but the crystallinity of the system increases. The PDSN molecules, remaining perpendicular to the surfactant PDSN – water interface, are compressed, and their heads are oriented on the surface. Clumps of surfactant PDSN molecules are detected in the system, forming monocrystals. It can be assumed that the domains in the system are located randomly relative to each other, but in the domains there is a partial crystallization of the system. A mixed phase "gel" – "coagel" is formed. The resulting phase does not change over time. Upon repeated heating of the same sample to 353K, crystallinity decreases, but the formed phase is preserved.

With a further increase in the concentration of the system at room temperature, the molecules in the layers orient themselves in a "dry" image, where only hydrated water is contained, the heads of the molecules on the surface of the surfactant–water are distributed in an orderly manner, as evidenced by reflexes at large angles in X–ray diffraction patterns. The interplanar distances and relative intensities of highly concentrated samples of the PDSN–PEG–water system at a PEG content of 36% are shown in table 2.

The effect of temperature on highly concentrated systems leads to a decrease in the crystallization of the system. The intensity of reflexes at large angles gradually decreases and at a temperature of 343K they completely disappear. This is because hydrocarbon chains become "liquid". The ordering of the molecular heads on the lipid–water phase interface also disappears. But two types of ordering coexist in the system: lamellae of monomolecular thickness with interplanar spacings of 27.4 Å and 24.7 Å. This can be explained by the fact that at high concentrations in the system, the possibility of PEG penetrating into the aggregate is limited and an inhomogeneity is formed. In lamellae with an interplanar distance of 24.7 Å, PEG, penetrating

the interlamellar water layer, compresses the layers, leading to compaction, and in lamellas with an interplanar distance of 27.4 Å, the effect of PEG is not very pronounced.

Thus, the study found that the effect of PEG on the liquid crystal structure of models of biomembranes based on PDSN–water leads to the compaction of the system, penetrating into interlamellar water layers, spreads on the surfaces of the heads, compresses the layers by tilting the hydrocarbon chains at an angle to the lipid–water interface . The influence of temperature reduces the compactness of the system, but the liquid crystal mesophase is retained.

An increase in the PEG content leads to a phase transition from the “gel” to the “collagen”. Under the influence of temperature, the reverse process takes place: the “coagel” turns into a “gel” phase. The liquid crystal “smooth” phase is retained in the system with the coexistence of different types of lamellae. The influence of temperature leaves a residual effect on the system, but the liquid crystal phase is retained. Thus, PEG, being introduced into the liquid crystal structure of biomembrane models, provides its strength and stability with respect to water and temperature.

References.

1. Ekwall F., Mandel L., Fontell K. Solubilization in micells and mesophases and the transition from normal to reversed structures.//In the book: Proceedings of the 11 Int. Liquid Crist. Cont.–Kent, 1968, p.325–381.
2. Ekwall F., Fontell K., Mandel L. Some isotropic mesophases in Systems containing amphiphilie compounds.//Acta chemica Scandinavica, 1968, N22, p.3209–3223.
3. *Vasilenko*, I. A., *Evstigneeva*, R. P. Structural studies of polymer films.// Izv. USSR Academy of Sciences, ser. Biol., 1984, N4, p. 550–560. (in Russian)
4. Vasilenko I.A., Chupin V.V., Tarakhovsky Y.S., Obraztsov V.V., Borovyagin V.L., Evstigneeva R.P. Studies of biological membranes. / Dokl. USSR Academy of Sciences, 1980, v. 252, No. 5, p. 1258–1260. (in Russian)
5. Cullis P.R., De Kruijff B. Polymorphic of lipid membranes.//Biochem. etbiophysacta, 1979, v.559, p.399–420.
6. Cullis P.R., De Kruijff B., Hope M.J., Verkleij A.J., Wayar R., Farren S.B., Tilcock C.P.S., Madden T.D., Bally M.B. Membrane fluidity in Biology. / YI Conception of membrane Structure, ed. Aloia R.C.N.Y.: Acad. Press, 1983, p. 39–82.
7. Cullis P.R., Hope M.,J., Tilcock C.P.S. Phospholipid membranes. //Chem. And Phys. Lipids. 1986, v.40, p. 69–75.
8. Gounaris K., Brain P.R., Quinn P.J., Williams N.P. A direct analysis of lamellar X–ray diffraction from hydrated oriented multilayers of fully functional sarcoplasmic reticulum. // FEBS Lett, 1983, v.153, p.47–52.
9. Borovjagin V.L., Sabelnikov A.G., Tarakhovsky Y.S., Vasilenko I.A. Storage and steroid–induced release from rat leucocytes of a phospholipose inhibitor. //J. Membrane Biol., 1987, v.100, p.229–242.
10. Borovjagin V.L., Vasilenko I.A. Formation of graphitizing carbons from the liquid. // Anat.Roc. 1981, v.193, N3, p.32A.
11. Verkleij A.J. Properties of lipid bilayer membranes deformation of membrane thicknesess. //J. Biochem. et Biophys. Acta, 1984, v.779, p.43–84.

12. 12. Shaginyan A.A., Sargsyan A.G., Garibyan L.M., Minasyants M.Kh., Oganesyan S.S. X–ray study of the influence of a number of physiologically active compounds on the structure of the PAV–water system / All–Union Conference on Colloid Chemistry and Phys. Chem. Mechanics, Tashkent, 1983, p. 156–157. (in Russian)
13. Chupin V.V., Bovin A.N., Vasilenko I.A., Evstigneeva R.P. Polymorphic transformations of unannounced aqueous dispersions of phosphatidylethanolamines with a simple and complex ether bond. // Bioorgan. Chemistry, 1981, T. 6, N5,p. 773–778. (in Russian)
14. Shahinyan A. A., Hakobyan P. K., Arsenyan L. H., Poghosyan A. H. "The Study of Lyotropic Liquid Crystal Structure Using the Molecular Dynamics Simulation Method"// *Molecular Crystals and Liquid Crystals,* **2012**, 561: 155–169

Parallel X–ray Beams with Controllable Quantity and Distances under the External Acoustic Fields in Quartz Crystals

T.R. Muradyan, E.H. Bagdasaryan, S.M. Petrosyan, H.H. Samsonyan, V.R. Kocharyan

Institute of Applied Problems of Physics NAS RA
25 Hr. Nersissian Str., Yerevan, Republic of Armenia, 0014

Abstract: The possibility of obtaining parallel X–ray beams and controlling their quantity and distances in a wide range has been experimentally considered. To implement this experiment, a three–crystal scheme was assembled. The first crystal is set to monochromatize an X–ray beam, which provides high resolution. The second quartz crystal with AT – cut is used to obtain parallel X–ray beams with different distances and quantities using the effect of bulk acoustic waves with different frequencies. And the third quartz crystal with asymmetric reflection is used to control the distances of parallel beams in a wide range (from 50 μm to 1 mm). Thus it is shown that, using such a three–crystal scheme, it is possible to obtain any number of parallel X–ray beams and control their distances in wide ranges.

Keywords: X–ray radiation, quartz single crystal, volume acoustic waves.

1. Introduction

The requirement for creation of more sensitive and universal research methods in different fields of science and technique stimulates the development of new methods for obtaining monochromatic beams of X–rays with parameters controlled in space and time, as, e. g., the angular divergence, spatial distribution and monochromaticity. X–ray diffractometry in the presence of external influences is one of such methods. For instance, the presence of external acoustic fields or temperature gradient in crystal monochromators enables one to control the parameters of diffracted X–rays in space and time [1–3]. The possibilities of controlling the parameters of reflected X–rays from different atomic planes $(10\bar{1}1)$ of single quartz crystal with different bends in the presence of volume acoustic waves up to 10 MHz have studied in [4–10]. The phenomenon of the full transfer of X–rays from the transition direction to the reflection direction in quartz single crystal in the Laue geometry under the influence of ultrasonic oscillations was first observed in [4]. Since the dependence of the intensity of the reflected X–ray radiation on the parameters of the external acoustic fields or temperature gradient it possible to obtain controllable X–ray beams both in time and space, numerous studies were subsequently carried out to study the various characteristics (angular divergence, spatial distribution, energy dispersion) of the reflected X–rays [5–7]. In [8, 9], the diffraction of X–ray radiation on various reflecting atomic planes of a quartz single crystal with an AT cut in the Laue geometry was experimentally studied when volume acoustic waves were excited in the crystal. Certain reflecting atomic planes are curved and have periodicity along the thickness of the crystal, which is equal to $n \times \lambda / 2$, where n is an odd number and corresponds to the order of the resonant frequency, and λ is the wavelength of acoustic waves. It is shown that volume acoustic waves lead to spatial modulation of diffracted beams, that is, bands appear in the frontal section, which

perpendicular to the diffraction vector. The number of bands depends on the order of the harmonic of the excited acoustic field. The intensity of the emerging bands depends on the amplitude of the acoustic waves excited in the crystal. It was shown in [10] that a spatially modulated beam formed from the quartz single crystal with an AT cut of excited acoustic waves can be completely pumped in the direction of reflection at a certain value of the temperature gradient applied to the second crystal while preserving the spatial distribution of the beam.

In this work, the possibility of controlling the distances of the obtained parallel X–ray beams in a wide range has been experimentally considered.

2. Experiment

In experiment the spectrum of X–rays produced from Mo БСВ–29 X–ray tube under voltage of 30 kV and 10 mA anode current was used. The size of the focal spot of the source is 0.2×10 mm^2. The three–crystal scheme was used to control the distances of the obtained parallel X–ray beams in a wide range (Fig. 1). The first quartz crystal was located in a reflective position of atomic planes $(10\bar{1}1)$ Bragg geometry for monochromatization of X–ray radiation with an energy of 17.48 keV (MoKα1), which provides high resolution. The second quartz crystal with AT – cut was located in a reflective position of atomic planes $(10\bar{1}1)$ Laue geometry for the obtained of parallel X–ray beams with different distances and quantities using the effect of bulk acoustic waves with different frequencies. Acoustic vibrations with frequencies of 2.979, 4.890, 6.933 and 8.836 MHz were excited to the second quartz crystal, and X–ray parallel beams were recorded using photographic film (Ph1). And the third quartz crystal with X – cut was located in a reflective position of atomic planes $(11\bar{2}0)$ Bragg geometry with asymmetric reflection is used to control the distances of parallel beams in a wide range (from 50 μm to 1 mm). After third crystal the X–ray parallel beams were recorded using photographic film (Ph2).

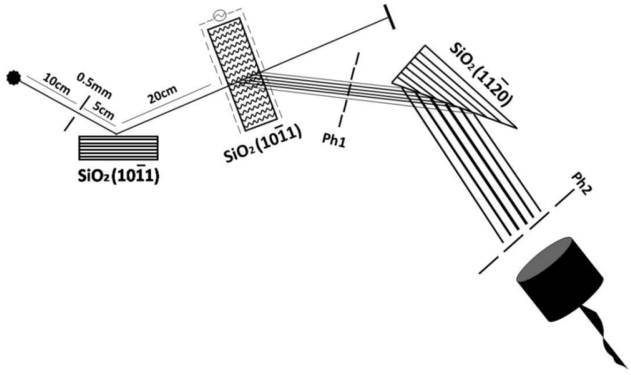

Fig.1 Experimental scheme

The experiments showed that the intensity of the reflected beam increases with the increase of the amplitude of the electromagnetic field applied to the second crystal with a resonant frequency (Fig.2).

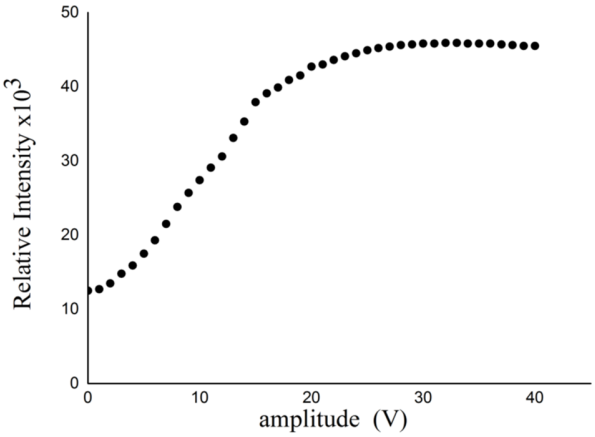

Fig. 2. The intensity of the reflected beam depending of the amplitude of the electromagnetic field applied to the crystal with a resonant frequency of 4.89MHz

Increasing amplitude of the electromagnetic field, applied to the crystal with a resonant frequency, means that the amplitude of the acoustic wave exciting in the crystal increases. Acoustic wave leads to the curvature of the reflecting atomic planes $(10\bar{1}1)$ of the crystal. The experiments showed that starting at a certain value of the amplitude of the acoustic waves (the curvature of the reflecting atomic planes) at the nodes of the standing wave, the Bragg condition is violated. However, from antinodes the intense reflected X–rays are formed. As a result, the reflected X–ray beam splits, and narrow beams are visible in the cross section of the reflected beam (Fig.3), the number of which is equal to the number of antinodes of the standing acoustic wave.

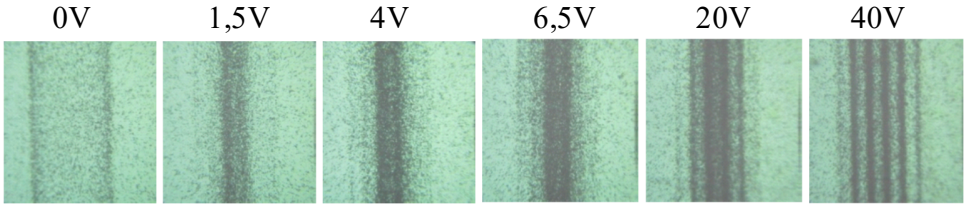

Fig. 3 The formation of narrow x–ray beams from a crystal under the excitation of the standing acoustic wave at a fifth–order resonant frequency.

Experiments show that with an increase in the order of the resonant frequency, the number of narrow X–ray beams also increases (Fig.4).

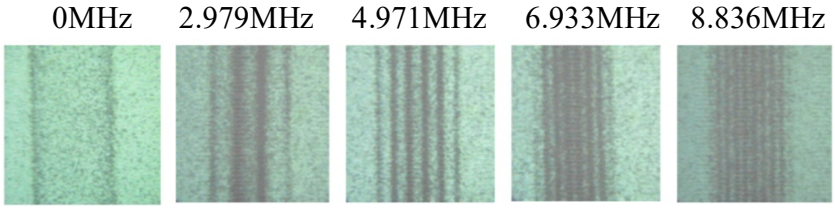

Fig.4. Narrow X–ray beams formed from a crystal under excitation of a standing acoustic wave with the different order of resonant frequency

The formation of parallel X–ray beams in the frontal section from the second “splitter” crystal, falling on an asymmetric crystal, is reflected and their distance increases more than 20 times (Fig.5).

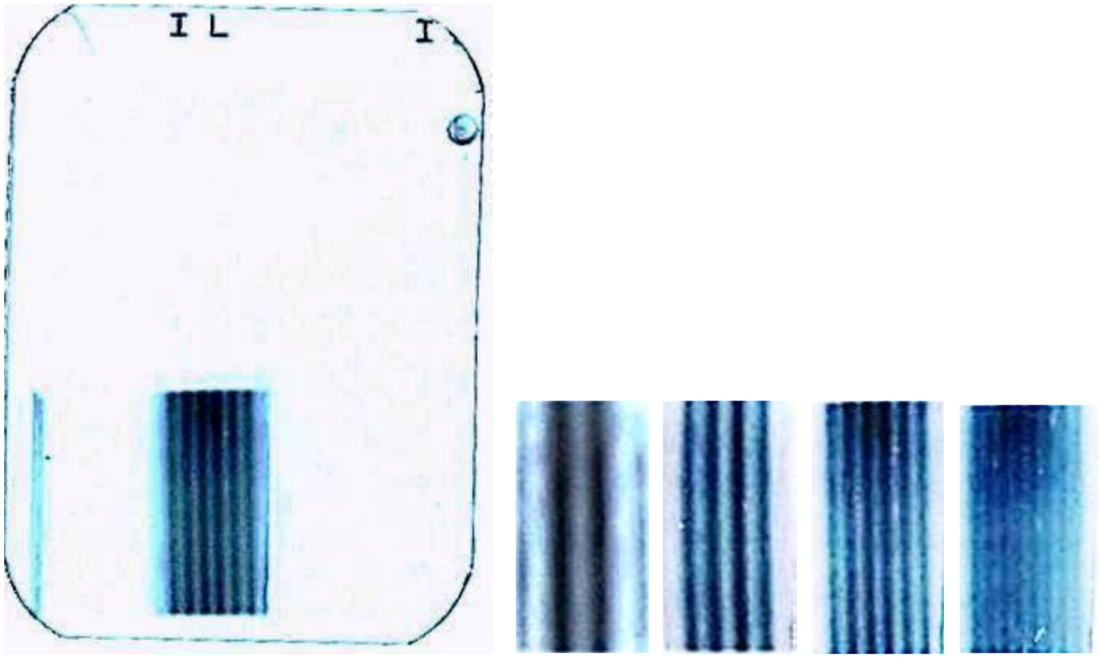

Fig.5. Parallel x–ray beams after an asymmetric crystal

3. Conclusion

Thus it is shown that, using such a three–crystal scheme, it is possible to obtain any number of parallel X–ray beams and control their distances in wide ranges.

This work was supported by the RA MES State Committee of Science and Russian Foundation for Basic Research (RF) in the frames of the joint research project SCS 18RF–142 and RFBR 18–52–05024 Arm_a accordingly.

References.

1. Mkrtchyan, A.R., Gabrielyan, R.G., Aslanyan, A.A., Mkrtchyan, A.G., and Kotanjyan, Kh.V., Izvestiya Akademii Nauk ArmSSR, Fizika, 1986, vol. 21, p. 297.
2. Kocharian, V., Mkrtchyan, A., Gogolev, A., Khlopuzyan, S., and Grigoryan, P., Advanced Materials Research, 2015, vol.1084, p.107.
3. Hayrapetyan, K.T., Noreyan, S.N., and Margaryan, V.V., J. Contemp. Phys. (Armenian Ac. Sci.), 2017, vol. 52, p. 38.
4. A.R. Mkrtchyan, M.A. Navasardyan, R.G. Gabrielyan // JETP Lett., 1983, vol. 9, issue 11, pp. 1181.
5. A.R. Mkrtchyan, R.G. Gabrielyan, A.A. Aslanyan // J. Contemp. Phys. (Armenian Ac. Sci.), 1986, vol. 21, p. 297.
6. A.R. Mkrtchyan, A.G. Mkrtchyan, V.R. Kocharyan, A.E. Movsisyan, S.B. Dabagov, A.P. Potilicin // J. Contemp. Phys. (Armenian Ac. Sci.), 2013, vol. 48, p. 212.
7. V.R. Kocharyan, R.Sh. Aleksanyan, K.G. Truny // J. Contemp. Phys. (Armenian Ac. Sci.), 2010, vol. 45, p. 290.
8. T.R. Muradyan, R.V. Amiraghyan, S.H. Khlopuzyan, A.R. Wagner, V.R. Kocharyan. J. Contemp. Phys. (Armenian Ac. Sci.), 2015, vol. 50, p. 204.
9. Mirzoyan, V.G., Yeghiazaryan, A.A., Baghdasaryan, E.H., and Mirzoyan, P.V., J. Contemp. Phys. (Armenian Ac. Sci.), 2007, vol. 42, p. 235.
10. T.R. Muradyan. Armenian Journal of Physics, 2017, vol. 10, issue 3, pp.104–107

X–Ray Diffraction Method of Investigation of Imperfections in Crystals Based on Interpretation of Sectional Topogram

H. R. Drmeyan*, H. G. Margaryan

Institute of Applied Problems of Physics NAS RA
25 Hr. Nersissian Str., Yerevan, Republic of Armenia, 0014

Abstrakt: *To increase the resolution of X–ray diffraction methods, a new method is proposed in the work, which is theoretically proven and with which thin structures of diffraction images are experimentally observed. The X–ray interference pattern obtained by X–ray diffraction in a system consisting of a two–crystal system with a narrow gap and a thick absorbing crystal was studied. The theoretical period of the interbranch scattered bands obtained from this system is calculated. It is shown that the presence of a thick plate makes it possible to increase the period of the bands by about 5 to 10 times. For the first time, two dynamic effects were simultaneously observed: on one topogram, interbranch scattering bands and moire patterns formed in a two–crystal system were observed.*
Keywords: fine structures of X–ray interference patterns, two–crystal system, interbranch band scattering.

1. Introduction

X–ray diffraction methods, which are widely used in detecting structural imperfections in crystalline materials, have limited capabilities due to insufficient resolution, in particular, it is impossible to detect the fine structure of X–ray diffraction patterns or section topograms. The unambiguous interpretation of X–ray topographic images of crystal imperfections is sometimes greatly complicated, on the one hand, due to the overlapping of various dynamic and kinematic effects and their superimposition on imperfections, on the other.

It is known [1–5] that the image of defects depends on the thickness of the crystal, on the divergence and spectral composition of the primary incident beams, on the orientation of the reflecting families of planes relative to the defect, on the location of the defect in the crystal — on the input, output surface, or in the bulk of the crystal and on the degree deformation of the surface layer. The image of imperfections also essentially depends on whether the scattering of x–rays by these defects is kinematic or dynamic. Sometimes an inhomogeneous intensity distribution (splitting into separate components) appears in the diffracted beam, which can be a manifestation of both crystal defects and dynamic scattering effects in perfect crystals.

A number of works [6–9] have been devoted to X–ray studies of the influence of these factors on the intensity of scattering of X–rays in crystals, and it would seem that all questions of the influence of these factors on the scattering intensity of X–rays have been thoroughly investigated and clarified. However, new experimental data, such as sectional topograms obtained from a two–block crystalline system with a narrow air gap and from a thick absorbing ideal crystal in the reflection position, show that it is necessary to conduct special studies to elucidate the nature of the influence of the above factors on the intensity of X–ray scattering. Therefore, a further more detailed study of these issues is important both for the development of

* **E – mail:** *drm–henrik@mail.ru*

X–ray diagnostic studies and for the unambiguous interpretation of X–ray diffraction patterns using the interpretation of a section topogram, which the present work is devoted to.

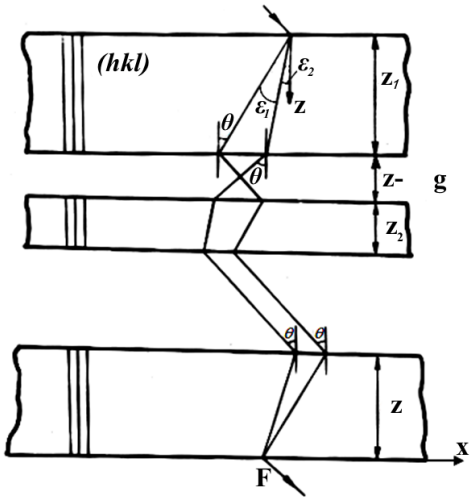

Fig. 1. A system consisting of a two–unit interferometer and a magnifying crystal

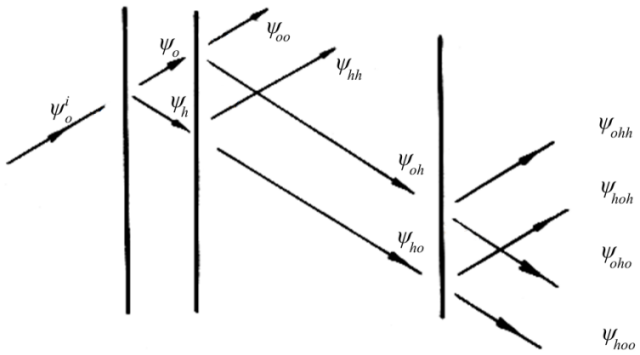

Fig. 2. The components of the amplitude of the incident wave after diffraction in the first, second blocks and in the magnifier block

Obviously, the higher the resolution of the X–ray diffraction methods, the greater the visibility of the fine structure of the X–ray diffraction patterns, therefore, the more information received from these patterns is about the structural imperfections of crystalline materials.

We, in order to increase the resolution of X–ray diffraction methods, propose a new method, which is theoretically proven, and with the help of which we experimentally observed displacement lines, moire bands, pendulum bands and other fine structures of diffraction images that are not observed by conventional methods. So, it is known [10] that, during X–ray diffraction in crystals, a strong angular increase in the beam occurs, which is expressed by the formula:

$$M = \frac{d\eta}{d\varepsilon} = \frac{K\cos\theta_B}{R\cos\varepsilon} \tag{1}$$

where $d\varepsilon$ – is the angle of convergence of the incident beam, $d\eta$ –is the angle of divergence of the incident beam in the crystal, θ_B –is the Bragg angle, R –is the radius of the dispersion surface, K –is the wave number $(K = 1/\lambda)$.

As can be seen from (1), a crystal is a powerful magnifier: when $M_0K_{\alpha_1}$ emitting and $(2\bar{2}0)$ reflecting silicon, M has an order of magnitude 10^2. This effect of angular magnification can be used to obtain linear magnification, which makes it possible to increase the resolution of X–ray diffraction patterns, which is the aim of the present work. This goal is achieved by the fact that a beam containing information about structural defects of the studied sample or moire patterns obtained from a two or three–block interferometer is passed through an ideal thick crystal in the reflection position.

Thus, the aim of this work is to study the imperfections of crystalline substances on the basis of revealing the fine structure of X–ray diffraction patterns during dynamic X–ray scattering, using the interpretation of the obtained sectional topograms.

2. Theoretical Analysis

Let a spatially inhomogeneous wave packet with amplitude Ψ_0^i fall on a crystalline system consisting of a two–block system with a narrow gap and a thick absorbing crystal (Fig. 1). The third block (thick block) is located so far from the first two that the beams diffracted in the first two do not overlap each other on the input surface of this block, i.e. the third block plays the role of a magnifier.

After diffraction in the first crystal, the incident beam is decomposed into two components: the transmitted wave with amplitude After diffraction in the first crystal, the incident beam is decomposed into two components: the transmitted wave with amplitude Ψ_0 and diffracted with amplitude Ψ_h (Fig.2). After diffraction in a two–block system with a narrow gap (after the second block), the beam decomposes into four components with amplitudes Ψ_{h0}, Ψ_{hh}, Ψ_{0h} and Ψ_{00} (Fig.2).

Let us consider the diffraction of waves with amplitudes Ψ_{h0} and Ψ_{0h} in the third thick plate (the beams Ψ_{hh} and Ψ_{00} do not differ from the considered ones in the nature of interference). In the third thick plate, the beams Ψ_{h0} and Ψ_{0h} form four beams, with Ψ_{h00} and Ψ_{0h0} interfering in the direction of reflection, and Ψ_{h0h} and Ψ_{0hh} in the direction of incidence. To find the distribution of interference fringes, we need to know the phase value Φ_q of the interfering beams, which are determined by the expression:

$$\Psi_q = |\Psi_q| \exp(i\Phi_q)$$

These phases can be easily found from the Takagi equation [11], using the stationary phase method [12,13] and omitting the terms corresponding to strongly absorbed wave modes. In the symmetric Laue case for the phases of the bundles Ψ_{h0h} and Ψ_{0hh} we obtain the following expressions:

$$\begin{aligned} \Phi_{ohh} &= -\frac{\pi}{\Delta_0}\left(Z + Z_1 + Z_2\right)\left(I - P_1^2\right)^{1/2} + \frac{3}{4}\pi \\ \Phi_{hoh} &= -\frac{\pi}{\Delta_0}\left(Z + Z_1 + Z_2\right)(I - P_2^2)^{1/2} + \frac{3}{4}\pi \end{aligned} \tag{2}$$

where Δ_0 – is the real part of the extinction length, Z – is the thickness of the thick plate, Z_1 and Z_2– are the thicknesses of the first and second crystals of the two–crystal system, the parameters $P_1 = tg\varepsilon_1 / tg\theta$, $P_2 = tg\varepsilon_2 / tg\theta$ characterize the directions of energy fluxes, and θ – is the Bragg angle.

The Ψ_{h00} and Ψ_{0h0} bundles will not be considered, because by the nature of the interference, they are similar with the bundles Ψ_{0hh} and Ψ_{h0h}.

From (2) for the phase difference $\Delta\Phi = \Phi_{ohh} - \Phi_{hoh}$ we obtain

$$\Delta\Phi \approx \frac{\pi}{\Delta_0}\left(Z + Z_1 + Z_2\right)\frac{PdP}{(I - P^2)^{1/2}}$$

where $P=(P_1+P_2)/2$ and $dP=P_2-P_1$ calculated for the case of strong absorption, i.e. calculations are made for the central part of the topogram. Interfering rays, which make up the angles ε_1 and ε_2 with the normal of the input surface, satisfy the condition:

$$Z+Z_1+Z_2=\frac{2Z_g}{dP}=\frac{2Z_g tg\theta}{tg\varepsilon_2-tg\varepsilon_1} \tag{3}$$

where Z_g – is the width of the air gap (non–diffracting zone).

Combining the last expression with the condition of the maxima of the interference bands $\Delta\Phi=2\pi n$, where $n=1,2,3....$ you can get the coordinates of the surfaces (bands) of maximum intensity:

$$X_n=\pm\frac{n\cdot\Delta_o\cdot tg\theta}{Z_g[1+(n\Delta_0/Z_g)^2]^{1/2}}(Z+Z_1+Z_2).$$

The direction of the X coordinate axis is shown in Fig. 1. In the central part of the topogram, without making a big mistake, we can assume that $(n\Delta_0/Z_g)^4<<1$, then for the period value of these bands we get:

$$\Lambda=\frac{(Z+Z_1+Z_2)\Delta_0 tg\theta}{Z_g}\left[1-\frac{3}{2}n^2\left(\frac{\Delta_0}{Z_g}\right)^3-\frac{3}{2}n\left(\frac{\Delta_0}{Z_g}\right)^3-\frac{1}{2}\left(\frac{\Delta_0}{Z_g}\right)^3\right] \tag{4}$$

Since $Z_g<<Z_1$ and $Z_g<<Z_2$, we get a family of parallel planes perpendicular to the scattering plane, the intersection of which with the photographic plate is a family of straight lines [14–17], and the general character of the decay of the period of the bands with an increase in their order n can be noted.

When operating without a thick crystal, displacement bands are obtained with a period

$$\Lambda'=\frac{(Z_1+Z_2)\Delta_0 tg\theta}{Z_g}\left[1-\frac{3}{2}n^2\left(\frac{\Delta_0}{Z_g}\right)^3-\frac{3}{2}n\left(\frac{\Delta_0}{Z_g}\right)^3-\frac{1}{2}\left(\frac{\Delta_0}{Z_g}\right)^3\right] \tag{5}$$

Comparing the values of periods (4) and (5), we can conclude that the presence of a magnifying crystal makes it possible to obtain interference fringes with the following linear increase coefficient in the direction of the diffraction vector:

$$D=1+\frac{Z}{Z_1+Z_2} \tag{6}$$

This increase is interference in nature and, as can be seen, depends on the thickness of the thick plate. When choosing a rather large value of Z, one can achieve an increase of up to 10 or more times and observe experimentally interference fringes with a large period and resolution. However, an excessive increase in the thickness of a thick plate is impractical because with increasing thickness, absorption increases and the intensity of reflected beams decreases.

3. Experimental Part

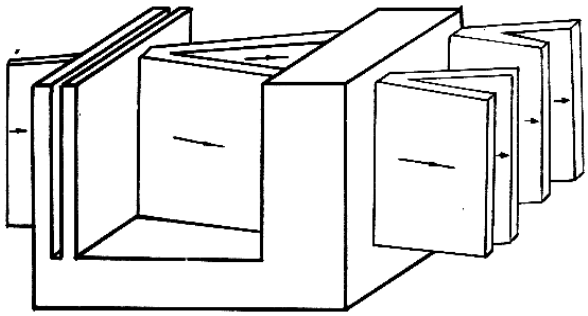

Fig. 3. A system consisting of two thin, closely spaced blocks and a magnifying block

To confirm the validity of the above reasoning, experimental studies were carried out using a highly perfect single–crystal two–block system with a narrow air gap and from a thick absorbing ideal crystal in the reflection position (Fig.3).

Thickness of thin blocks of a two–crystal system $Z_1 = 420\mu m,\ Z_2 = 1315\mu m,$ a thick perfect crystal $Z = 5550\mu m,$ width of a non–diffracting zone $Z_g = 290\mu m,$ radiation $M_0K_{\alpha_1}$, reflection $(2\bar{2}0)$, width of a collimated beam $80\mu m$.

The system shown in fig. 3 is schematically shown in fig. 4, where a narrow X–ray beam, passing through a collimator with a diaphragm, falls on a two–block system consisting of crystals 1 and 2. The diffracted beam falls on a perfect thick crystal 3, which is in the reflection position, and the transmitted beam is delayed by the screen 4. The diffracted beam containing moire patterns, passes through a thick crystal, which without changing the character of moire, increases this moire pattern. In fig. 4a shows a moire pattern formed by a dual–crystal system.

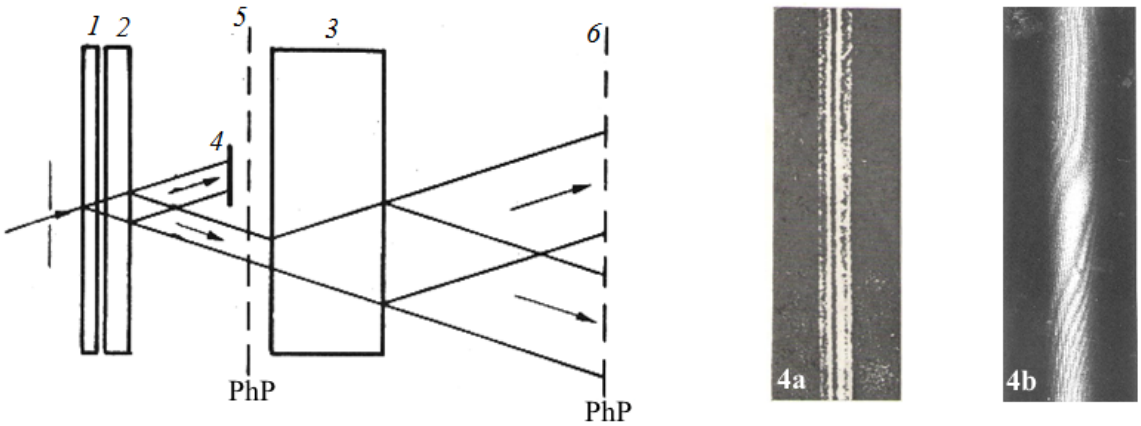

Fig. 4. An increase in X–ray moire patterns obtained using a dual–crystal system. 4a moire pattern formed by a dual–crystal system; 4b — moiré pattern 4a after enlargement

This image was obtained on a photographic plate 5 placed between the second and third blocks (Fig. 4). In fig. 4b shows the same moire pattern on film 6, located after the third block. As can be seen from these figures, after the second block, the moire on the film is almost invisible, and only after the third block, i.e. after enlargement, moire stripes are clearly visible.

4. Results and its Discussion

In a similar way, one can obtain an increase in interference patterns obtained from interferometers of an arbitrary type, and also increase the resolution of X–ray topographic methods.

This effect can be applied in areas of physical research, such as X–ray diffraction of microdefects, X–ray spectroscopy, X–ray interferometry, precision X–ray diffraction analysis, and also for studies of the fine structure of interference patterns.

It may seem that the interference patterns observed after the magnifier (an ideal thick crystal) did not exist before it and formed in it, that is, the last crystal does not play the role of the magnifier, but participates in the formation of these patterns. The fact that the last thick crystal only increases the linear dimensions of the diffraction pattern and does not introduce any additional information into the interference pattern can be verified on the basis of the following theoretical considerations (reasoning) and experimental facts:

1) The magnifying crystal is thick and ideal, therefore, the field having a large absorption coefficient completely disappears, and inside the crystal the distribution of the field having a period equal to the interplanar distance of the reflecting planes is not stored outside the crystal. Further, since the magnifier crystal is perfect and defects are not observed on its topogram, it follows from what was said in this section that the magnifier crystal does not change the nature of the intensity distribution in the beam passing through it.
2) It can be seen from Figs. 4a and 4b that, after thin plates, the interference pattern is not observed (Fig. 4a), but after a thick crystal it is observed (Fig. 4b), and the primary moire pattern (Fig. 4a) and its enlarged pattern (Fig. 4b) differ only in dimensions in the scattering plane.
3) We can verify that this interference pattern is not created by a thick crystal, but by the superposition of waves on the second crystal obtained in the first thin crystal as a result of splitting of the primary wave. Indeed, if one of these thin plates is removed or the distance between them is increased, then the interference pattern observed after the thick crystal disappears. Consequently, the interference pattern observed after the thick crystal arose in the subsystem of two thin crystals and became visible after magnification.

5. Conclusion

The results of our research form the basis for stating the following:

1. The crystal–magnifier does not introduce new information into the interference pattern, but only increases its angular dimensions in the scattering plane.
2. The magnifier crystal does not change the nature of the intensity distribution in the beam passing through it.
3. The crystal–magnifier reduces the overall intensity without changing the interference pattern.
4. An increase in D depends on the relative thicknesses of the magnifier Z and the total thickness of the thin plates $(Z_1 + Z_2)$: with an increase in Z and a decrease in the sum of $(Z_1 + Z_2)$, this parameter increases.

5. With an increase in the sum $(Z_1 + Z_2)$, the magnification in the thick crystal D decreases and tends to unity, i.e., the thick crystal ceases to play the role of a magnifier. But, as expression (6) shows, for large Z_1 and Z_2, the interference pattern is increased by these plates themselves and the need for an additional magnifier disappears.

References.

1. Tolan M., Vacca G., Sinha S.K. et al., J. Phys. D., V.28, P. A231, (1995)
2. Абоян А.О., Тез. докл. РСНЭ–99, Москва: ИК РАН, с.172. (1999)
3. Caderstrom B., Cahn R., N. Danielsson et al., Nature, V.404. pp 951–955, (2000)
4. Aristov V., Grigoriev M., Kuznetsov S. et al., Appl. Phys. Lett., V.77., pp 4058–4063, (2000)
5. Бушуев В.А., Имамов Р.М., Мухамеджанов Э.Х., Орешко А.П., Кристаллография, Т. 46, №6, с.991–997, (2001)
6. Drmeyan H.R., Melkonyan A.H. and Knyazyan Z.H., Journal of surface Investigation X–ray, Synchrotron and Neutron Technigues, Vol.11, №5, pp 1089–1095, (2017)
7. Дрмеян Г.Р., Поверхность. Рентгеновское, синхротронные и нейтронные исследования, №4, с.103–106, (2018)
8. Kocharyan V.R., Movsisyan A.E. and Grogolev A.S., Journal of Contemporary Physics (Armenian Akademy of Sciances), Vol.53, №3, pp 263–269, (2018)
9. Takeda T., Momose A., Yu Q., Wu J., Hirano K., Itaia Y., J.Synchr. Rad. V.7, pp 280–286, (2000)
10. Authier A., Acta geologica et geografhica Universitatis Comenianac. Geologica, 14, 37 (1968).
11. Takadi S. Acta Cryst, 15, 1311 (1962), J. Phys. Soc. Japan 26, 1239 (1969).
12. Борн М., Вольф Э. «Основы оптики». Изд–во “Наука’’, М. (1970)
13. Свешников А.Г., Тихонов А.Н., “Теория функции комплексной переменной”, М. Наука. 304 стр. (1967)
14. Authier A., Miln A.D., Sauvage M., Phys. Stat. Sol., V. 26, pp 469–484, (1968)
15. Hart M., Milne A.D., Acta Cryst., A26, pp. 223–229, (1970)
16. Hashizume H., Ishida H., Kohra K., Phys. Stat. sol. (a), 12, 453, (1972)
17. Tanemura S., Lang A.R., Naturforsch Z., V. 28a, pp. 668–676, (1973)

Advanced Ferroelectric $LiNb_{(1-x)}Ta_xO_3$ Crystal: Crystal Growth, Crystal Structure, Physical Properties

D.V. Roshchupkin[1*], E.V. Emelin[1], O.A. Plotitcyna[1], R.R. Fahrtdinov[1], D.V. Irzhak[1], V.K. Karandashev[1], T.V. Orlova[1], B.S. Redkin[2], H. Fritze[3], Yu. Suhak[3]

[1] Institute of Microelectronics Technology and High–Purity Materials of Russian Academy of Sciences
Chernogolovka, 6 Academician Osipyan str., Moscow District, Russian Federation, 142432
[2] Institute of Solid – State Physics Russian Academy of Sciences,
Chernogolovka, 2 Academician Osipyan str., Moscow District, Russian Federation, 142432
[3]Clausthal University of Technology, Institute of Energy Research and Physical Technologies
Leibnizstraße 4, Clausthal–Zellerfeld, Germany, D–38678

Abstrakt: *The process of promising ferroelectric $LiNb_{(1-x)}Ta_xO_3$ crystals growing by Czochralski method is studied. For the first time $LiNb_{0.88}Ta_{0\text{o}12}O_3$ crystals were grown. The composition of the crystals was determined by the method of ion mass spectrometry with inductively coupled plasma. Curie temperature T_C=1102 °C was measured by the method of differential scanning calorimetry. The parameters of the crystal unit cell were measured using high–resolution X–ray diffraction. The crystal unit cell parameters a and c occupy an intermediate position between the corresponding values in $LiNbO_3$ and $LiTaO_3$ crystals. The use of scanning electron microscopy and high–resolution X–ray diffraction allowed to measure the velocity of surface acoustic waves.*

1. Introduction

Ferroelectric $LiNbO_3$ and $LiTaO_3$ crystals are widely used in acoustoelectronics and acoustooptics due to the high values of the piezoelectric modules. These crystals were first grown by the Czochralski method in the mid–sixties of the last century. Crystals have the same structure and belong to the class of symmetry 3m, but have a significant difference in melting point and Curie temperatures. So in crystals $LiNbO_3$ and $LiTaO_3$ the Curie temperature T_C makes 1190 °C and 650 °C, and melting temperature T_m makes 1240 °C and 1650 °C, accordingly.

$LiNbO_3$ crystal has the higher values of piezoelectric modules, while the $LiTaO_3$ crystal has the good temperature stability, but lower values of piezoelectric modules. Therefore, in the middle of the 70's there was an idea to grow $LiNb_{(1-x)}Ta_xO_3$ crystals, which would combine the best properties of $LiNbO_3$ and $LiTaO_3$ crystals (high values of piezoelectric modules and good temperature stability). In this direction, a large number of studies have been carried out, but so far attempts to grow $LiNb_{(1-x)}Ta_xO_3$ crystals have been fruitless [1–3]. The growth processes of $LiNbO_3$ and $LiTaO_3$ crystals differ only in temperatures in the process of the crystals growth at the same speed of rotation and pulling the crystals out of the melt. The use of the parameters of $LiNbO_3$ and $LiTaO_3$ crystal growth process did not allow to grow $LiNb_{(1-x)}Ta_xO_3$ crystals. In [4] it was shown that the use of the conventional Czochralski method does not allow to grow $LiNb_{(1-}$

[*]**E – mail:** *rochtch@iptm.ru*

$_{x)}Ta_xO_3$ crystals because of the wide separation between the solid and liquid phase lines in the phase diagram of the $LiNbO_3$–$LiTaO_3$ system (Fig. 1).

All attempts to grow $LiNb_{(1-x)}Ta_xO_3$ crystals ended to grow crystals with a large number of pores. It has been demonstrated in [2] that for growing $LiNb_{(1-x)}Ta_xO_3$ crystals by the Czochralski method it is necessary to reduce the rate of pulling the crystal out of the melt. Decrease in crystal speed allowed to grow a small crystal of $LiNb_{0.9}Ta_{0.1}O_3$ composition without pores. The small size of the crystal did not allow to investigate the physical properties of the crystal.

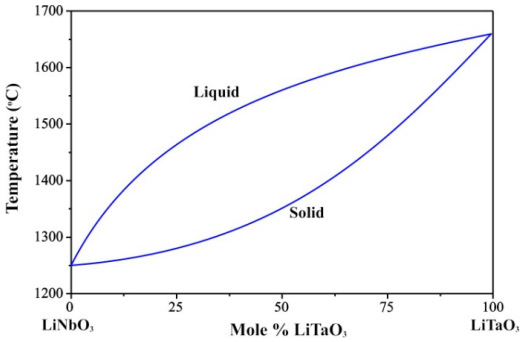

Fig. 1. phase diagram of the $LiNbO_3$–$LiTaO_3$ system [4].

This paper presents the results on the successful growth of the $LiNb_{(1-x)}Ta_xO_3$ crystals by the Czochralski method and the study of their structural and physical properties.

2. $LiNb_{(1-x)}Ta_xO_3$ crystal growth by Czochralski method

The study of $LiNb_{(1-x)}Ta_xO_3$ crystal growth process by Czochralski method was performed on a NIKA–3M growth machine. For growing $LiNb_{(1-x)}Ta_xO_3$ solid solution the recrystallization method was used, i.e. at the initial stage congruent $LiNbO_3$ and $LiTaO_3$ crystals were grown. Then the corresponding proportions of $LiNbO_3$ and $LiTaO_3$ crystals were used to grow $LiNb_{0.88}Ta_{0.12}O_3$ crystals. The crystals were grown along axis *Z*. The use of standard parameters of $LiNbO_3$ and $LiTaO_3$ conventional crystal growth process allows to grow crystals with a large number of pores (Fig. 2).

Fig. 2. $LiNb_{0.88}Ta_{0.12}O_3$ crystal grown by conventional Czochralski method.

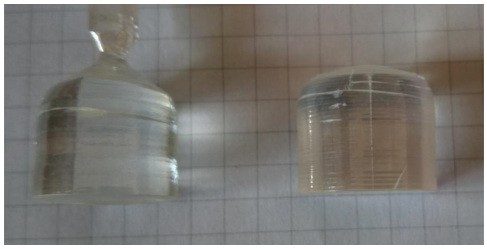

Fig. 3. $LiNb_{0.88}Ta_{0.12}O_3$ crystal grown by Czochralski method with a very low pulling rate.

Reduction of the crystal pulling rate from the melt by 4 times (~0.5 mm/h) allowed to grow crystals with a diameter of 2 cm (Fig. 2). Several crystals of $LiNb_{0.88}Ta_{0.12}O_3$ solid solution were grown, which allowed to carry out a complex study of this material.

3. Investigation of crystal composition, Curie temperature and crystal lattice parameters

Inductively coupled plasma atomic spectrometry was used to study the composition of the grown crystals. This method allowed us to determine the composition of the grown crystal in mass percentages: Li – 3.0±0.1 mass %, Nb – 48.2±0.5 mass %, Ta – 13.4±0.2 mass %. Conversion of mass % into atomic % allowed to determine the composition of the grown crystal: $LiNb_{0.88}Ta_{0.12}O_3$. The composition of the grown crystal was studied at the top, in the middle and at the bottom of the grown crystal and showed the same results.

Differential Scanning Calorimetry has been used to measure the temperature of the Curie, i.e. to determine the temperature of the ferroelectric–paraelectric phase transition. Fig. 4 shows the curve of heat flow versus heating temperature of the grown crystal $LiNb_{0.88}Ta_{0.12}O_3$. The fracture of the heat flow curve is observed at the temperature of 1102 °C. This fracture corresponds to the Curie temperature T_C=1102 °C of these crystals. The measured temperature above Curie temperature of $LiTaO_3$ crystal, but below Curie temperature of $LiNbO_3$ crystal.

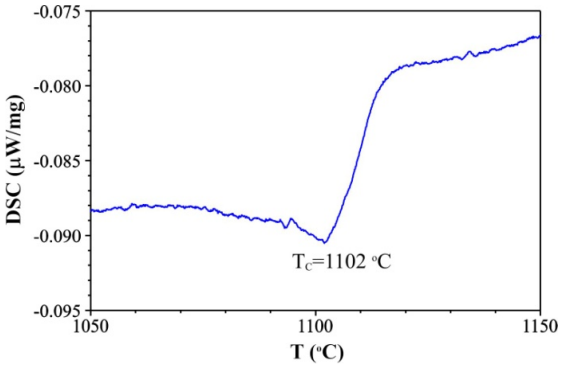

Fig. 4. Change of heat flow versus the crystal heating temperature.

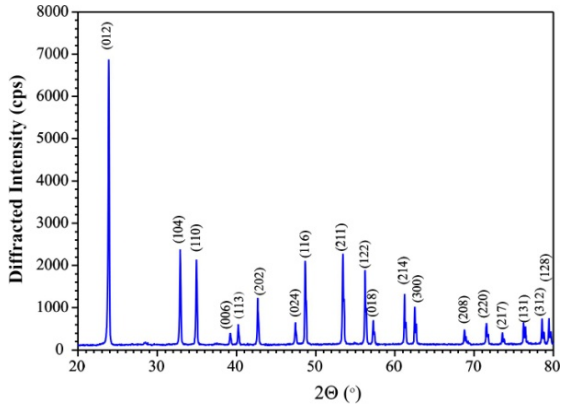

Fig. 5. XRD spectra of a $LiNb_{0.88}Ta_{0.12}O_3$ crystal.

High–resolution X–ray diffraction was used to study the structure of the grown crystal using the 4–circles Bruker D8 DISCOVER X–ray diffractometer. The powder diffraction method in the scheme of a double–crystal X–ray diffractometer was used to measure the XRD spectrum of $LiNb_{0.88}Ta_{0.12}O_3$ crystal (Fig. 5). The elementary crystal unit cell parameters were calculatyed from measured interplanar spacings. The comparison of parameters of the elementary crystal unit cells in $LiNbO_3$, $LiNb_{0.88}Ta_{0.12}O_3$ and $LiTaO_3$ crystals presents in Table 1. It is seen from Table 1 that parameters of the elementary crystal cells *a* and *c* in $LiNb_{0.88}Ta_{0.12}O_3$ crystal occupy an intermediate position between corresponding values in $LiNbO_3$ and $LiTaO_3$ crystals.

Table 1. Parameters of the elementary crystal unit cell

N	Crystal	*a* (Å)	*c* (Å)
1.	$LiNbO_3$	5.1502	13.8653
2.	$LiNb_{0.88}Ta_{0.12}O_3$	5.1510	13.8164
3.	$LiTaO_3$	5.2135	13.7694

4. Acoustic properties of a $LiNb_{0.88}Ta_{0.12}O_3$ crystal

To study the acoustic properties the grown crystal was preliminarily subjected to the monodomenization process, because the ferroelectric domain structure is formed in the process of growth of congruent ferroelectric crystal. During the process of monodomenization, the crystal is heated to Curie temperature, an external electric field is applied to crystal along the polar axis *Z*, and after crystal is slowly cooled down in the conditions of external electric field application to the crystal. After the monodomenization process, the substrates of the *YZ*–cut were cut out of the crystal. These substrates are the most used cuts in acoustoelectronics for surface acoustic wave (SAW) devices.

The SAW delay time lines with the structures of interdigital transducer (IDT) were designed on the crystal surface for surface acoustic wave excitation with wavelengths of Λ=60 μm and Λ=4 μm. The process of the SAW excitation and propagation on the crystal surface was studied using different experimental methods. The process of the SAW propagation with wavelength of Λ=60 μm was studied using measurement of amplitude–frequency response and scanning electron microscopy.

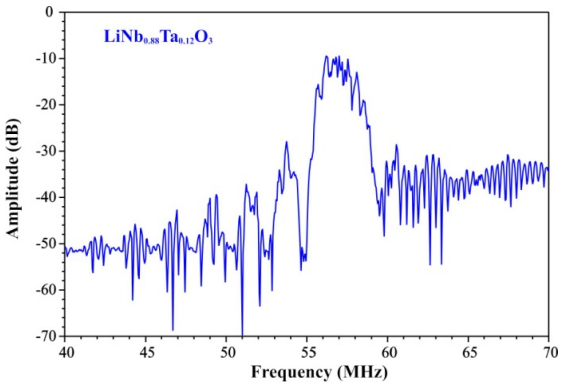

Fig. 6. Amplitude–frequency response of the SAW delay time line with SAW wavelength of Λ=60

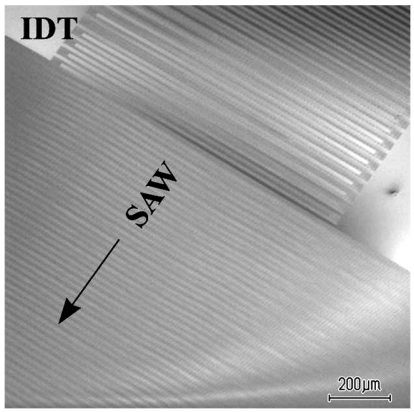

Fig. 7. SEM microphotograph of the SAW propagation in the *YZ*–cut of a $LiNb_{0.88}Ta_{0.12}O_3$ crystal. Λ=60 μm, f_0=57.33 MHz, *V*=3440 m/s.

Fig. 6 display the amplitude–frequency response of the delay line based on the *YZ*–cut of a $LiNb_{0.88}Ta_{0.12}O_3$ crystal. The resonance excitation frequency of the SAW is crystal is f_0=57.33 MHz at the SAW wavelength of Λ=60 μm, which corresponds to the SAW velocity of V=Λ× f_0=3440 m/s. The process of the SAW propagation on the surface of the *YZ*–cut of a $LiNb_{0.88}Ta_{0.12}O_3$ crystal was visualized by scanning electron microscopy method [5]. This method in the low–energy secondary electrons emission mode allows to visualize the acoustic

wave fields on the surface of piezoelectric crystals, as the low–energy secondary electrons with energy of ~1 eV are sensitive to the electric field that accompanies the SAW propagation in piezo– and ferroelectric crystals. Fig. 7 shows the microphotograph of the SAW with wavelength of Λ=60 μm on the surface of the *YZ*–cut of a $LiNb_{0.88}Ta_{0.12}O_3$ crystal. The SAW propagates along polar axis *Z* with a velocity of *V*=3440 m/s.

YZ–cut of a $LiNb_{0.88}Ta_{0.12}O_3$ crystal modulated by SAW with wavelength of Λ=4 μm was studied at synchrotron radiation source BESSY II in the scheme of X–ray double axis diffractometer schematically shown in Fig. 8 [6]. The energy of X–ray radiation *E*=10 keV was selected by a double Si(111)–monochromator. X–ray radiation was collimated by primary and secondary slits of 1 mm and 50 μm, respectively. X–ray radiation diffracts on an acoustically modulated crystal. SAW propagates in crystal and causes the sinusoidal modulation of the crystal lattice, which acts as a diffraction grating. X–ray radiation diffracts on the acoustically modulated crystal, which leads to the appearance of diffraction satellites on the rocking curve on the both sides of the Bragg peak. The angular divergence between the diffraction satellites is determined by the wavelength of the SAW, and the number of the diffraction satellites and their intensity are determined by the amplitude of the SAW. In the first approximation, the amplitude of the SAW can be determined as $h \sim md/2\pi$, where *m* is the number of the diffraction satellites on the rocking curve, *d* is the interplanar spacing. Diffracted X–ray radiation was recorded by standard scintillation detector NaI.

To study the diffraction process, the reflection from the planes (300) in the acoustically modulated *YZ*–cut of a $LiNb_{0.88}Ta_{0.12}O_3$ crystal was used. At the SAW wavelength of Λ=4 μm, the resonant excitation frequency of SAW was f_0=860 MHz, which corresponds to the SAW velocity of *V*=3440 m/s. Fig. 9 shows the rocking curve of acoustically modulated crystal, on which a large number of diffraction satellites can be observed. The rocking curve was measured at amplitude of the input high–frequency signal on an IDT of *U*=10 V. Taking into account the interplanar spacing *d*=1.487 Å for reflection (300) and the number of diffraction satellites on the rocking curve *m*=19, we obtain the value of the SAW amplitude of *h*~4.5 Å.

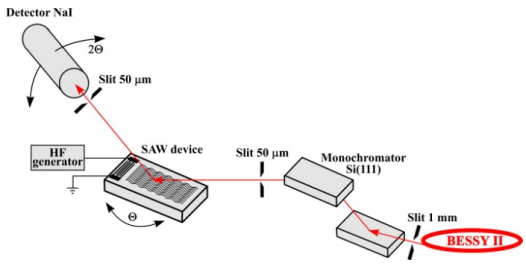

Fig. 8. X–ray double axis diffractometer at synchrotron radiation source BESSY II.

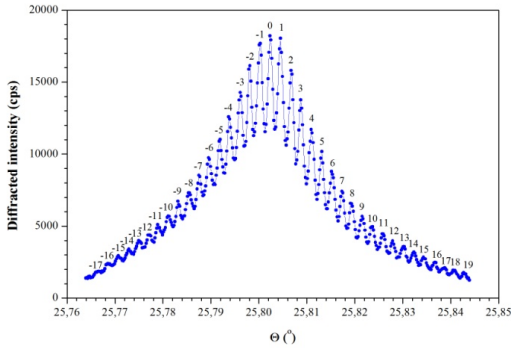

Fig. 9. Rocking curve of a $LiNb_{0.88}Ta_{0.12}O_3$ crystal modulated by SAW with wavelength of Λ=4 μm. SAW amplitude h~4.5 Å, reflection (300).

The investigations by scanning electron microscopy and X–ray diffraction methods allowed to determine the SAW velocity in the *YZ*–cut of $LiNb_{0.88}Ta_{0.12}O_3$ crystal. Table 2 presents comparison of SAW velocities in $LiNbO_3$, $LiNb_{0.88}Ta_{0.12}O_3$ and $LiTaO_3$ crystals. Table 2 shows that the SAWt velocity in the YZ–cut of a $LiNb_{0.88}Ta_{0.12}O_3$ crystal occupies an intermediate position between the corresponding values of the SAW velocity in the $LiNbO_3$ and $LiTaO_3$ crystals.

Table 1. SAW velocity in *YZ*–cut

N	Crystal	*V* (m/s)
1.	$LiNbO_3$	3488
2.	$LiNb_{0.88}Ta_{0.12}O_3$	3440
3.	$LiTaO_3$	3250

5. Conclusion

For the first time the solid solution of ferroelectric $LiNb_{0.88}Ta_{0.12}O_3$ crystals were grown by the Czochralski method. The measured temperature of the ferroelectric phase transition in the crystal was T_C=1102 °C. X–ray powder diffraction method was used to measure the parameters of the elementary crystal unit cell, which were *a*=5.1510 Å and *c*=13.8164 Å. Methods of X–ray high–resolution X–ray diffraction and scanning electron microscopy allowed to determine the SAW velocity in the *YZ*–cut of $LiNb_{0.88}Ta_{0.12}O_3$ crystal, which was *V*=3440 m/s.

Acknowledgements

The work was done according to the joint project of RFBR (grant #19–52–12044) and DFG (grant # FR1301/32–1).

References.

1. T. Fukuda, H. Hirano, Solid–solution $LiTa_xNb_{1-x}O_3$ single crystal growth by Czochralski and edge–defined film–fed growth technique, *J. Crystal Growth*, Vol. 35, 1976, pp. 127–132.
2. F. Shimura, Y. Fujino, Crystal growth and fundamental properties of $LiNb_{1-y}Ta_yO_3$, *J. Crystal Growth*, Vol. 38, 1977, pp. 293–302.
3. A. Bartasyte, A. M. Glazer, F. Wondre, D. Prabhakaran, P. A. Thomas, S. Huband, D. S. Keeble and S. Margueron, Growth of $LiNb_{1-x}Ta_xO_3$ solid solution crystals, *Mater. Chem. Phys.*, Vol. 134, 2012, pp. 728–735.
4. G. E. Peterson, P. M. Bridenbaugh, & P. Green, NMR Study of Ferroelectric $LiNbO_3$ and $LiTaO_3$. I, *J. Chem. Phys.,* Vol. 46, 1967, pp. 4009–4014.
5. D. V. Roshchupkin, M. Brunel, Scanning electron microscopy observation of surface acoustic wave propagation in the $LiNbO_3$ crystals with regular domain structures, *IEEE Transaction on Ultrasonics, Ferroelectrics, and Frequency Control*, Vol. 41, 1994, pp. 512–517.
6. R. Tucoulou, F. de Bergevin, O. Mathon, D. Roshchupkin, X–ray Bragg diffraction of $LiNbO_3$ crystals excited by surface acoustic waves, *Physical Review B*, Vol. 64**,** 2001, pp. 134108(9).

A Wave Packet Evolution in the Field of an One–Dimensional Potential

A.Zh. Khachatrian[2*], Zh. R. Panosyan[2*], Zh. B. Khachatryan[1]

[1] *Institute of Applied Problems of Physics NAS RA*
25 Hr. Nersissian Str., Yerevan, Republic of Armenia, 0014
[2]*National Polytechnic University of Armenia*
105 Teryan St., Yrevan, Republic of Armenia, 0009

Abstact: In the framework of this work a general theory for description of a wave packet evolution in the field of an one–dimensional potential is developed. Based on the method of counter propagating waves it is shown the evolving wave can be presented as a sum of three terms. The first item corresponds to the wave motion on the positive direction and the second one describes the wave motion on the negative direction. The last third item defines the interference between the counter propagating waves. It is proofed that when the center of the carrier energy of the wave packet equals to the resonant tunneling energy then the motions of counter propagating waves separately take place.

In this work we consider a time evolution of a wave process in the field of the one–dimensional potential. It is well known that any process of matter waves is described by means of the time dependent Schrödinger equation [1];

$$i\hbar\frac{\partial\Phi(x,t)}{\partial t}=\hat{H}\Phi(x,t) \tag{1}$$

where $\hat{H}$ is the system Hamiltonian, which for an one–dimensional potential has the form of:

$$\hat{H}=-\frac{\hbar^2}{2m}\frac{\partial^2}{\partial x^2}+U(x) \tag{2}$$

where $U(x)$ – potential energy. Due to the present of the first derivation of time the initial condition for equation (1) is given by mean of a one function:

$$\Phi(x,0)=\Phi_0(x) \tag{3}$$

Below we consider the wave packets constricted on the base of so called contra propagating waves which are the solutions of the one dimensional Schrödinger equation;

$$\Phi(x,t)=\int_{k_0-\Delta k}^{k_0+\Delta k}v(k)\left[a(x,k)e^{ikx}+b(x,k)e^{-ikx}\right]\exp\left(-\frac{ik^2\hbar}{2m}t\right)dk \tag{4}$$

where the functions $a(x,k)$ and $b(x,k)$ are the solutions of the following set of differential equations [2]:

$$\frac{da(x,k)}{dx}=-\frac{iu(x)}{2k}a(x,k)-\frac{iu(x)}{2k}b(x,k)\exp\{-i2kx\} \tag{5}$$

$$\frac{db(x,k)}{dx}=\frac{iu(x)}{2k}b(x,k)+\frac{iu(x)}{2k}a(x,k)\exp\{i2kx\} \tag{6}$$

[*]**E – mail:** ashot.khachatrian@gmail.com

It can be checked that the function

$$\psi(x,k) = a(x,k)e^{ikx} + b(x,k)e^{-ikx} \tag{7}$$

is the solution of the stationary Schrödinger equation;

$$\frac{d^2\psi(x,k)}{dx^2} + \left(k^2 - u(x)\right)\psi(x,k) = 0 \tag{8}$$

where

$$k = \sqrt{2mE}/\hbar,\ u(x) = 2mU(x)/\hbar^2 \tag{9}$$

It is important to note that in Eq. (7) the wave function $\psi(x,k)$ is given as the sum of two depend functions. It means that separately the function $a(x,k)\exp\{ikx\}$ or the function $b(x,k)\exp\{-ikx\}$ is not the solution of the stationary Schrödinger equation. The solution is their sum only. In accordance with the above mentioned in general case the wave propagation in the positive direction $a(x,k)\exp\{ikx\}$ generates the wave propagation in the negative direction $b(x,k)\exp\{-ikx\}$. The converse is also true, i.e. the wave $b(x,k)\exp\{-ikx\}$ provokes the wave propagating in the positive direction. We also note that the derivative of the wave function written by means of amplitude functions $a(x,k)$ and $b(x,k)$ has the form:

$$\frac{d\psi(x,k)}{dx} = ik\left[a(x,k)e^{ikx} - b(x,k)e^{-ikx}\right] \tag{10}$$

The functions $a(x,k)$ and $b(x,k)$ have to satisfy to asymptotic conditions:

$$a(-\infty \leftarrow x,k) = a_0, \quad b(x \to +\infty,k) = b_0 \tag{11}$$

where a_0, b_0 are constants, which represent the problem statement and define the normalization of the wave function of the continues spectrum [3];

$$\int_{-\infty}^{+\infty} \psi(x,k)\psi^*(x,k')dx = 2\pi(a_0a_0^* + b_0b_0^*)\delta(k-k') \tag{12}$$

Note, that if $a_0 = 1$, $b_0 = 0$, when the wave function is the wave function of the left scattering problem ($\psi(x,k) = \psi_l(x,k)$), which has the asymptotic behavior form of

$$\psi_l(x,k) = \frac{1}{\sqrt{2\pi}}\begin{cases} e^{ikx} + R(k)\,\mathrm{e}^{-ikx}, x \to -\infty, \\ T(k)\,\mathrm{e}^{ikx}, x \to +\infty, \end{cases} \tag{13}$$

where $T(k)$, $R(k)$ are the transmission and reflection amplitudes of the left scattering problem. It is easy to see that

$$a(x \to +\infty,k) \equiv a_l(x \to +\infty,k) = T(k),\ b(-\infty \leftarrow x,k) \equiv b_l(-\infty \leftarrow x,k) = R(k) \tag{14}$$

If the constants a_0, b_0 are chosen a $a_0 = 0$, $b_0 = 1$, when the function $\psi(x,k)$ is the wave function of the right scattering problem ($\psi(x,k) = \psi_r(x,k)$);

$$\psi_r(x,k) = \frac{1}{\sqrt{2\pi}}\begin{cases} S(k)\,\mathrm{e}^{-ikx}, x \to -\infty \\ e^{-ikx} + P(k)\,\mathrm{e}^{ikx}, x \to +\infty \end{cases} \tag{15}$$

where $S(k)$, $P(k)$ are the transmission and reflection amplitudes of the right scattering problem and

$$a(x \to +\infty,k) \equiv a_r(x \to +\infty,k) = P(k),\ b(-\infty \leftarrow x,k) \equiv b_r(-\infty \leftarrow x,k) = S(k) \tag{16}$$

The following relations between the scattering amplitudes of the left and right scattering problems exist [4]:

$$T(k) = S(k)\ ,\ R(k) = -P^*(k)T(k)/T^*(k) \tag{17}$$

and $T(k)T^*(k) + R(k)R^*(k) = 1$, $S(k)S^*(k) + P(k)P^*(k) = 1$.

Let us present the amplitude functions $a(x,k)$, $b(x,k)$ and the spectral functions $\nu(k)$ (see (4)) in the form of

$$a(x,k) = |a(x,k)|\exp[\mathrm{i}\mathrm{f}_a(x,k)],\ \ b(x,k) = |b(x,k)|\exp[\mathrm{i}\mathrm{f}_b(x,k)],\ \nu(k) = |\nu(k)|\exp[\mathrm{i}\mathrm{f}_\nu(k)]. \tag{18}$$

where $|a(x,k)|$, $|b(x,k)|$, $|\nu(k)|$ and $\mathrm{f}_a(x,k)$, $\mathrm{f}_b(x,k)$, $\mathrm{f}_\nu(k)$ are modules and phases of corresponding functions. Considering $\Delta k << k_0$ the expressions (18) can be written:

$$a(x,k) = a(x,k_0)\exp\left[\left(\frac{\partial \ln|a(x,k_0)|}{\partial k} + i\frac{\partial \ln \mathrm{f}_a(x,k_0)}{\partial k}\right)(k-k_0)\right] \tag{19}$$

$$b(x,k) = b(x,k_0)\exp\left[\left(\frac{\partial \ln|b(x,k_0)|}{\partial k} + i\frac{\partial \ln \mathrm{f}_b(x,k_0)}{\partial k}\right)(k-k_0)\right] \tag{20}$$

$$\nu(k) = \nu(k_0)\exp\left[\left(\frac{\partial \ln|\nu(k_0)|}{\partial k} + i\frac{\partial \ln \mathrm{f}_\nu(k_0)}{\partial k}\right)(k-k_0)\right] \tag{21}$$

Rerating $k^2 = \left(k_0 + (k-k_0)\right)^2 \approx k_0^2 + 2k_0(k-k_0)$ the exponential time factor of Eq. (4) can be considered as:

$$\exp\left(-\frac{ik^2\hbar}{2m}t\right) = \exp\left(-\frac{ik_0^2\hbar}{2m}t - \frac{ik_0(k-k_0)\hbar}{m}t\right) \tag{22}$$

Using (19) – (22) for the wave packet (4) one can get:

$$\Phi(x,t) = 2\nu(k_0)\Delta k\left(a(x,k_0)\frac{\sin\xi_a(x,t)}{\xi_a(x,t)}\mathrm{e}^{ik_0(x-u_{ph}t)} + b(x,k_0)\frac{\sin\xi_b(x,t)}{\xi_b(x,t)}\mathrm{e}^{-ik_0(x+u_{ph}t)}\right) \tag{23}$$

where

$$\xi_a(x,t) = \left(x/u_g + \tau_a(x,k_0) - i\bar{\tau}_a(x,k_0) - t\right)u_g\Delta k \tag{24}$$

$$\xi_b(x,k_0) = \left(x/u_g + \tau_b(x,k_0) - i\bar{\tau}_b(x,k_0) + t\right)u_g\Delta k \tag{25}$$

and

$$\tau_a(x,k_0) = \frac{1}{u_g}\frac{\partial \ln\left(\mathrm{f}_a(x,k_0)\mathrm{f}_\nu(k_0)\right)}{\partial k},\ \bar{\tau}_a(x,k_0) = \frac{1}{u_g}\frac{\partial \ln|a(x,k_0)\nu(k_0)|}{\partial k} \tag{26}$$

$$\tau_b(x,k_0) = \frac{1}{u_g}\frac{\partial \ln\left(\mathrm{f}_b(x,k_0)\mathrm{f}_\nu(k_0)\right)}{\partial k},\ \bar{\tau}_b(x,k_0) = \frac{1}{u_g}\frac{\partial \ln|b(x,k_0)\nu(k_0)|}{\partial k} \tag{27}$$

In Eqs. (24) – (27) u_{ph}, u_g are the phase and group velocities:

$$u_{ph} = \frac{1}{\hbar}\frac{E(k_0)}{k_0} = \frac{\hbar k_0}{2m}\ ,\ u_g = \frac{1}{\hbar}\frac{dE(k_0)}{dk} = \frac{\hbar k_0}{m} \tag{28}$$

As it can be seen from Eq. (23), the wave function is the sum of two terms, the first of them describes the wave motion from left to right, and the second from right to left. Both terms

are products of three functions, namely, the amplitude function with a value on the carrier wave number k_0, a rapidly oscillating function and also concentration functions of the form:

$$\sin\xi / \xi \tag{29}$$

It is known, that this function takes its greatest value at $\xi = 0$. If we formally imagine that in the both terms of Eq. (23) the concentration functions are equal to unity, then it is easy to see that up to the factor $2v(k_0)\Delta k$ the wave packet function (23) in its form repeats the wave function of the continuous spectrum for the value of the wave number k_0;

$$\psi(x,k_0)\exp\left(-\frac{ik_0^2\hbar}{2m}t\right) = a(x,k_0)\,\mathrm{e}^{ik_0(x-u_{ph})t} + b(x,k_0)\,\mathrm{e}^{-ik_0(x+u_{ph})t}$$

It should be noted that, in contrast to the concentration function of wave packets composed of the base of de Broglie waves where the variable ξ takes only real values, for the wave packet (23) it can also take complex values (see (24), (25)).

$$\frac{\sin(\xi_1 + i\xi_2)}{\xi_1 + i\xi_2} \tag{30}$$

where ξ_1, ξ_2 are real quantities.

Using (23) for the square module one can write:

$$\left|\Phi(x,t)\right|^2 = \left|\Phi_a(x,t)\right|^2 + \left|\Phi_b(x,t)\right|^2 + \left|\Phi_{ab}(x,t)\right|^2 \tag{31}$$

The first item corresponds to the wave motion on the positive direction:

$$\left|\Phi_a(x,t)\right|^2 = 4v^2(k_0)\Delta k^2 \left|a(x,k_0)\right|^2 \frac{\sin\xi_a(x,t)\sin\xi_a^*(x,t)}{\xi_a(x,t)\xi_a^*(x,t)} \tag{32}$$

The second one describes the wave motion on the negative direction:

$$\left|\Phi_b(x,t)\right|^2 = 4v^2(k_0)\Delta k^2 \left|b(x,k_0)\right|^2 \frac{\sin\xi_b(x,t)\sin\xi_b^*(x,t)}{\xi_b(x,t)\xi_b^*(x,t)} \tag{33}$$

And the last third item defines the interference between the counter propagating waves:

$$\left|\Phi_{ab}(x,t)\right|^2 = 8v^2(k_0)\Delta k^2\,\mathrm{Re}\left[a(x,k_0)b^*(x,k_0)\frac{\sin\xi_a(x,t)\sin\xi_b^*(x,t)}{\xi_a(x,t)\sin\xi_b^*(x,t)}\mathrm{e}^{i2k_0x}\right] \tag{34}$$

Note, that calling $\left|\Phi_{ab}(x,t)\right|^2$ as the interference term one should mention that here the overlap between the interconnected or generating each other wave motions takes place.

Below we will investigate the functions $\left|\Phi_a(x,t)\right|^2$, $\left|\Phi_b(x,t)\right|^2$ and $\left|\Phi_{ab}(x,t)\right|^2$ on the problem of maximum. It means that for any fixed value of x we define the time moment, when these functions take the maximum values. One can show that in a point x the functions $\left|\Phi_a(x,t)\right|^2$ and $\left|\Phi_b(x,t)\right|^2$ achieve their mean maximums for the following time moments:

$$t_a = x/u_g + \tau_a(x,k_0) \tag{35}$$

$$t_b = x/u_g + \tau_b(x,k_0) \tag{36}$$

What is about the maximum od the function $\left|\Phi_{ab}(x,t)\right|^2$ it contains the product of two concentration functions. It means that this function can observably differ from zero if $\xi_a(x,t)=\xi_b(x,t)$ only. The last equality leads to the conditions:

$$t_a = t_b \text{ or } \tau_a(x,k_0)=\tau_b(x,k_0) \tag{37}$$

Now we consider the situation when the spectral center of the packet center k_0 equals to value of the wave number corresponding to the resonant tunneling. It means that

$$\left|T(k_0)\right|=1 \text{ and } R(k_0)=P(k_0)=0 \tag{38}$$

In accordance with the scattering matrix method [4, 5]

$$\begin{pmatrix} a(x\to\infty,k) \\ b(x\to-\infty,k) \end{pmatrix} = \begin{pmatrix} T(k) & P(k) \\ R(k) & T(k) \end{pmatrix} \begin{pmatrix} a(x\to-\infty,k) \\ b(x\to+\infty,k) \end{pmatrix} \tag{39}$$

For the resonance tunneling (see (38)) from Eq. (39) one can find:

$$\left|a(x\to\infty,k_0)\right|=\left|a(x\to-\infty,k_0)\right| \text{ and } \left|b(x\to\infty,k_0)\right|=\left|b(x\to-\infty,k_0)\right| \tag{40}$$

As it follows from this result the propagation of the wave packet from a one–dimensional potential takes place without reflecting.

References.

1. D. Bom. Quantum mechanics. Prentice–Hall, NY, 1952.
2. D. M. Sedrakian, A. Zh. Khachatrian, *Phys. Lett.*, **A 265** (2000).
3. A. Zh. Khachatrian, Al. G. Aleksanyan, N. A. Aleksanyan International Journal of Scientific & Engineering Research, **9**, (2013).
4. V. I. Arnold, Supplementary Chapters on the Theory of Ordinary. Nauka, Moscow, 1978.
5. A. Zh. Khachatrian. Armenian Journal of Physics, **3**, (2010).

On Role of Energy Transmission in Mechanisms of Nonradiative Energy Relaxation in Massiv of Quantum Dots

Al.G. Aleksanyan*

Institute of Applied Problems of Physics NAS RA
25 Hr. Nersissian Str., Yerevan, Republic of Armenia, 0014

On the basis of dipole–dipole interaction the role of energy transmission in mechanisms of nonradiative energy relaxation in quantum dots is considered.

The use of QD arrays, including vertically coupled (VCQD), as the active region of an injection semiconductor laser, made it possible to create lasers with unique characteristics (high temperature stability of the threshold current density, high value of the excess inversion parameter, giant specific amplification factors, etc.)

One of the main parameters determining the gain is the relaxation time to the ground state of the QD. Experimental estimates of the rate of inter–level relaxation have shown that relaxation to the ground state of QDs occurs faster if the energy distance between the ground and excited states is equal to an integer number of LO phonons. At the same time, the fact of the presence of effective relaxation was also found for nonresonant charge carriers; moreover, the relaxation rate increases in structures with SCIT.

Nonradiative interlevel transitions in QDs, most likely, are mainly determined by the interaction of two types. The first is the electron–phonon interaction leading to energy transfer between different states in a separate QD. The second is the interaction between active QDs, leading to the transfer of energy between different points. Indeed, with an increase in the concentration of quantum dots, which is always desirable to increase the gain, we believe that the role of energy transfer in the mechanisms of energy relaxation in quantum dots will increase.

Thus, all this predetermines the problem of revealing the role of the transfer of excitation energy in effective relaxation for non resonance (partial frequencies differ, but are within the spectral lines of interacting QDs) of charge carriers.

Because a two–level quantum system with a finite upper–level lifetime can be likened to a classical oscillator with damping [1], then to evaluate the energy transfer process, we take as the initial one the model of two coupled QD oscillators described by the following system of differential equations [2]

$$\left.\begin{aligned} \ddot{z}_1 + 2\gamma_1 \dot{z}_1 + \omega_{01}^2 z_1 = \chi_{21} z_2 \,, \\ \ddot{z}_2 + 2\gamma_2 \dot{z}_2 + \omega_{02}^2 z_2 = \chi_{12} z_1 \,, \end{aligned}\right\} \qquad (1)$$

where $2\gamma_1$ and $2\gamma_2$ are the relaxation rates of the oscillators, χ_{12} and χ_{21} is the connection between them. For the problem under consideration, the most interesting case is when the excited state of the QD oscillator, let it be the second, quickly relaxes, i.e., the resonance conditions are precisely satisfied for this QD. In the framework of the adopted model, this means that for the

* **E – mail:** *alalbert@inbox.ru*

attenuation included in (1), $\gamma_2 >> \gamma_1$ is satisfied. The solution of system (1) is well studied in the theory of oscillations and shows that the presence of a connection between the oscillators increases the attenuation of the first oscillator, with the following relation

$$\gamma_{ef} = \gamma_1 + \frac{\chi^2}{4\omega^2\gamma_2} \quad \frac{\gamma_2^2}{\Delta^2 + \gamma_2^2} \tag{2}$$

where $\Delta=\omega_{01}-\omega_{02}$, $\chi^2=\chi_{12}\chi_{21}$.

Further, to determine the right–hand side of equations (1), which include the amplitudes of the corresponding QD oscillators, we will take into account the quantum nature of the QD.

If the z axis is chosen in the direction connecting the centers of the vertical] stacked QDs, then the matrix elements of the interaction energy will have the form

$$<n_1^{/},n_2^{/}|V|n_1,n_2>=\frac{e^2}{\varepsilon R^3}\left(<n_1^{/}|x_1|n_1><n_2^{/}|x_2|n_2>+<n_1^{/}|y_1|n_1><n_2^{/}|y_2|n_2>-2<n_1^{/}|z_1|n_1><n_2^{/}|z_2|n_2>\right) \tag{3}$$

where the R–distance between the QDs, n_1 and n_2 are sets of quantum numbers characterizing the stationary states of non–interacting QDs, ε– the dielectric constant of the matrix medium, $<|z_1|>$ and $<|z_2|>$ similar terms are the matrix elements of the first and second QDs.

To calculate the matrix elements of the dipole moment, we choose a QD with a limiting potential in the form of an impermeable flattened ellipse. In this case, in the adiabatic approximation, the wave functions corresponding to the lower part of the spectrum have the form

$$\Psi_{mN}(x,y,z) = U_c(r)\,(\sqrt{\pi}\Omega_0 b(\rho) 2^{N-1} N!\,\rho_0)^{-1/2} \exp\left(-\frac{\rho^2}{2\rho_0^2}\right)\ H_N\left(\frac{\rho}{\rho_0}\right) \sin\frac{\pi(m+1)[z+b(\rho)/2]}{b(\rho)} \tag{4}$$

where $b(\rho)=2b_0\sqrt{1-\rho^2/a_0^2}$, $\rho<<a_0$, $\rho^2=x^2+y^2$, $\rho_0=\sqrt{\frac{2a_0b_0}{\pi(m+1)}}$, a_0 and b_0 –are the semiaxes of the ellipsoid, H_N is the Nth order Hermite polynomial, $U_c(r)$ is the modulating factor of the Bloch function, Ω_0 is the unit cell volume of the QD material, m and N are quantum numbers for the fast and slow subsystems, respectively.

Using the orthogonality properties of wave functions (4), we obtain

$$< n_i^{/}|z_i|n_i > = \frac{\hbar}{m^* b_i \omega_{mm^{/}}} \quad \frac{4(m^{/}+1)(m+1)}{(m^{/}-m)(m^{/}+m+2)} \quad \delta_{m^{/}-m,\,2k\pm1}\,\delta_{NN^{/}} \tag{5}$$

$$< n^{/}|\rho_i|n >= \frac{\hbar}{m^*\rho_0\omega_{NN^{/}}}\left[\sqrt{N+1}\,\delta_{N^{/},N+1} + \sqrt{N}\,\delta_{N^{/},N-1}\right]\delta_{mm^{/}} \tag{6}$$

where m^* –is the effective mass of the charge carrier, $i = 1,2$.

Note that when calculating the integrals (5) and (6), we assumed that $b\approx 2b_0$. From (5) it is seen that inter–level transitions in the fast subsystem can occur with a fixed quantum number of the slow subsystem.

Further, considering transitions between the ground $(m=0, N=0)$ and excited $(m=1, N=0)$ states with allowance for (5), for (3) we have

$$< 0,0\,;1,0\left|\mathrm{V}\right|0,1\,;0,0> = -\frac{6{,}3\mathrm{e}^2 b_1 b_2}{\pi^2 \varepsilon R^3} \tag{7}$$

Since the right–hand sides of (1) $\chi_{21}\cdot z_2 = \frac{F_{21}}{m^*}$, $\chi_{12}\cdot z_1 = \frac{F_{12}}{m^*}$, F_{12} and F_{21} the forces and acting on the side of each oscillator on the other, are found from (7), then for χ^2 we have

$$\chi^2 \approx \frac{40\mathrm{e}^4}{\pi^4 \mathrm{m}^* \varepsilon^2 \mathrm{R}^6} \tag{8}$$

Substituting (8) into (2), for the selected QD model, we find the effective relaxation rate.

Note that the influence of the shape of the limiting potential is likely to affect the numerical value of the coefficient in (8). So, for example, for spherical–shaped QDs, when considering transitions between the ground $|1,0,0>$ and excited $|2,1,0>$ states, only $<|z|>$ matrix elements are preserved. Naturally, the calculation of the integrals in (3), with other envelope functions, will only lead to a change in the value of the numerical coefficient.

In conclusion, we note that along with the dipole – dipole mechanism in the VCQD, tunneling exchange of charge carriers is also possible. In this case, the first QD is in the ground state, and the second in the excited state for which resonance conditions are already satisfied.

References.

1. L.Allen, J.H.Eberly. Optical Resonance and Two–Level Atoms. New–York, Dover Publications, Inc (1987).
2. В.В. Мигулин и др. Основы теории колебаний, М., Наука 1978г.

Transition Radiation of Electron Bunches on Acoustic Superlattices

A.R. Mkrtchyan, V.V. Parazian*, A.A. Saharian

Institute of Applied Problems of Physics NAS RA
25 Hr. Nersissian Str., Yerevan, Republic of Armenia, 0014

Abstract: We investigate the transition radiation from a bunch intersecting a dielectric plate excited by acoustic waves. The latter generate a super lattice the characteristics of which are controlled by tuning the amplitude and the wavelength of the acoustic field. Within the framework of quasiclassical approximation, a formula is given for the spectral and angular distributions of the radiation intensity in the forward direction in the general case of distribution function of electrons in the bunch. The coherence effects are discussed for several special cases of the longitudinal distribution function. It is shown that the presence of the acoustic filed gives rise to new peaks in both the spectral and angular distributions of the radiated energy. The heights and the widths of these peaks are controlled by the thickness of the plate and by the parameters describing the acoustic super lattice.

Work of A.A.R. was supported by the RA Science Committee, in the frames of the research project №18T–1C395. A.A.S. was supported by the RA Science Committee, in the frames of the research project №18T–1C397.

1. Introduction

Transition radiation is produced when a relativistic particle traverses an inhomogeneous medium. Such radiation has a number of remarkable properties and at present it has found many important applications. In particular, transition radiation can be fruitfully exploited for energy detection or mass identification of high energy particles. The detectors based on the transition radiation have been used and are currently being used in a wide range of accelerator based experiments and in astroparticle and cosmic ray experiments. The intensity of the transition radiation can be increased considerably by using the interference effects in periodic structures (for a review see [1]–[5]). The corresponding emission, called resonant transition radiation, results from constructive interferences between the waves emitted by each element of the periodic structure. In experiments, incident electrons cross stacks of thin foils and the transition radiation is formed at the interfaces between the material and vacuum. For the generation of high frequency transition radiation periodical structures with a small period is needed and the fabrication of this kind of radiator is a difficult task. In addition, irregularities in the spacing between the foils can rapidly destroy the constructive interference. In Ref. [6] it was suggested to generate the periodic radiator for the X–ray transition radiation by using acoustic waves. The parameters of this type of radiator are easily controlled by tuning the wavelength and the amplitude of the acoustic wave. The radiation from a charged particle for a semi–infinite laminated medium has been recently considered in [7]. The optical transition radiation in an

*E – mail: *vparazian@gmail.com*

ultrasonic super lattice excited in a finite thickness plate is considered in [8] under normal incidence of a relativistic electron and in [9] the results are generalized for the oblique incidence. It is shown that the acoustic waves generate new resonance peaks in the spectral and angular distributions. The heights and the location of these peaks can be controlled by choosing the parameters of the acoustic wave. In the papers given above the transition radiation from a single particle is considered. From the point of view of the experimental observation it is an important step to investigate the radiation from particle beams. Here we consider the forward transition radiation generated by a monoenergetic electron bunch in a dielectric plate in presence of ultrasonic waves.

2. Electromagnetic field and the radiation intensity

Consider the transition radiation emerging in the forward direction when a monoenergetic bunch

of N particles moves at constant velocity $\vec{v} = v\vec{n}_z$ along the z –axis, enters normally into a plate whose surfaces coincide with planes $z = -l$ and $z = 0$. We assume that longitudinal ultrasonic vibrations are excited in the plate along the normal to its surface (along the axis z), that form a super lattice. The dielectric permittivity inside the plate we shall take in the form

$$\varepsilon(z) = \varepsilon_0 + \Delta\varepsilon \cos\left(k_s z + \omega_s t + \varphi\right) \tag{1}$$

for $-l \le z \le 0$. In (1), ω_s, k_s are the cyclic frequency and the wave number of the ultrasound, φ is the initial phase. Under the condition $\nu_s l / v \ll 1$, with $\nu_s = \omega_s / (2\pi)$, during the transit time of the electron the dielectric constant in the super lattice is not notably changed. For relativistic electrons and for the plate thickness $l \le 1cm$ this leads to the constraint $\nu_s \ll 10^{11} Hz$. In the discussion below we shall assume that the plate is immersed in a homogeneous medium with dielectric permittivity ε_1 .

Here we are interested in the radiation with frequencies ω satisfying the condition $\omega \gg k_s c$. The presence of small parameter $k_s c / \omega$ allows one to use the quasi–classical approximation for the evaluation of the radiation field. The current density will be taken in the form

$$\vec{j} = ev \sum_{j=1}^{N} \delta\left(x - X_j\right)\delta\left(y - Y_j\right)\delta\left(z - Z_j\right)\vec{n}_z \tag{2}$$

In the Lorentz gauge, the vector potential of the electromagnetic field for j –th particle can be written as $\vec{A}_j = A^{(j)}\vec{n}_z$. This condition determines the radiation polarization. The magnetic field intensity is perpendicular to the plane containing $\vec{n}_z$ and the photon wave vector. For the j –th particle in the bunch one has $Z_{(j)}(t) = -l + v\left(t - t_0^{(j)}\right)$. Assuming that $|\Delta\varepsilon| \ll 1$, the Fourier transform of the vector–potential in the region $z > 0$ is presented as

$$A\left(\vec{k}_\perp,\omega,z\right)=\frac{iee^{ik_3^{(1)}z}}{2\pi^2 ck_3^{(1)}}\sum_{j=1}^{N}e^{-i\omega Z_j/v-ik_xX_j-ik_yY_j}\left[\frac{e^{i\phi^{(j)}-il\left(\omega/v-k_3^{(1)}\right)}-1}{2i\left(\omega/v-k_3^{(1)}\right)}+e^{ia_1\sin\varphi^{(j)}}\sqrt{\frac{k_3^{(1)}\varepsilon_1}{k_3^{(0)}\varepsilon_0}}\right.$$
$$\left.\times\sum_{m=-\infty}^{+\infty}J_m\left(a_1\right)e^{-im\varphi^{(j)}-il\left(\omega/v-k_{3m}^{(0)}\right)/2}\frac{\sin\left(l\left(\omega/v-k_{3m}^{(0)}\right)/2\right)}{\omega/v-k_{3m}^{(0)}}\right] \tag{3}$$

where and in what follows $\vec{k}_\perp=\left(k_1,k_2\right)$, $Z_j=Z_j\left(0\right)$, $J_m\left(x\right)$ is the Bessel function of the first kind, $k_{3m}^{(1)}=k_3^{(0)}+mk_s$, and

$$k_3^{(i)}=\sqrt{\omega^2\varepsilon_i/c^2-k_\perp^2},\ i=0,1,\ \varphi^{(j)}=\varphi-\left(Z_j+l\right)\omega_s.v,$$
$$\phi^{(j)}=\left(k_3^{(0)}-k_3^{(1)}\right)/l+2a_1\sin\left(k_sl/2\right)\cos\left(\varphi^{(j)}-k_sl/2\right),\ \mathrm{a}_1=\omega^2\Delta\varepsilon/\left(2c^2k_sk_3^{(0)}\right) \tag{4}$$

The spectral–angular density of the radiation intensity during the electron transit time in the forward direction $\left(z\gg l\right)$, averaged over the phase φ, is given by the formula

$$I_N\left(\omega,\theta,\phi\right)=2\pi\varepsilon_1^{3/2}\frac{\omega^4}{c^3}\sin^3\theta\cos^2\theta\int_0^{2\pi}d\varphi\left|A\left(\bar{k}_\perp,\omega,z\right)\right|^2 \tag{5}$$

where θ is the angle between the z–axis and the wave vector of the radiation,

$$k_x=\left(\omega/c\right)\sqrt{\varepsilon_1}\sin\theta\cos\phi,\ k_y=\left(\omega/c\right)\sqrt{\varepsilon_1}\sin\theta\sin\phi \tag{6}$$

with φ being the azimuthal angle for the radiation direction. By taking into account the expression (3), we get

$$I_N\left(\omega,\theta,\phi\right)=\frac{e^2\beta_1^2\sin^3\theta}{2\pi^2c\sqrt{\varepsilon_1}}\sum_{j,j'=1}^{N}e^{-2iq_{jj'}\omega/\omega_s-ik_xX_{jj'}-k_yY_{jj'}}\left\{U\sum_{m,m'=-\infty}^{+\infty}B_m\left(\theta,\varphi\right)\right.$$
$$\times\left[UB_{m'}\left(\theta,\omega\right)J_{m-m'}\left(2a_1\sin q_{jj'}\right)e^{i(m'-m)(k_sl-\pi)/2}e^{i(m'+m)q_{jj'}}\right.$$
$$+\frac{J_{m-m'}\left(a_1\right)}{1-\beta_1\cos\theta}J_{m'}\left(b_1\right)e^{2im'q_{jj'}}\sin\left[\left(k_3^{(0)}-\omega/v\right)l/2+\left(m'-m\right)k_sl/2+m'\pi/2\right] \tag{7}$$
$$\left.\left.U\sum_{m=-\infty}^{+\infty}\frac{W_mB_m^2\left(\theta,\omega\right)}{1-\beta_1\cos\theta}+\frac{1+J_m\left(2b_1\sin q_{jj'}\right)-2\cos\left[\left(k_3^{(0)}-\omega/v\right)l\right]J_0\left(b_1\right)}{4\left(1-\beta_1\cos\theta\right)^2}\right\}\right.$$

where $\beta_1=v\sqrt{\varepsilon_i}/c$, $U_{jj'}=U_j-U_{j'}$, $q_{jj'}=\left(Z_j-Z_{j'}\right)\omega_s/2v$, $b_1=2a_1\sin\left(k_sl/2\right)$, and

$$B_m\left(\theta,\omega\right)=J\left(a_1\right)\frac{\sin\left(l\omega W_m/2v\right)}{W_m},\ W_m=W+mv\frac{k_s}{\omega},\ W=1-\beta_1\sqrt{\frac{\varepsilon_0}{\varepsilon_1}-\sin^2\theta} \tag{8}$$

Now one has $k_3^{(0)}=\left(\omega/c\right)\sqrt{\varepsilon_0-\varepsilon_1\sin^2\theta}$,

$$a_1=\frac{\omega\Delta\varepsilon}{2ck_s\sqrt{\varepsilon_0-\varepsilon_1\sin^2\theta}},\ U=\left(\frac{\varepsilon_1\cos\theta/\varepsilon_0}{\sqrt{\varepsilon_0/\varepsilon_1-\sin^2\theta}}\right)^{1/2} \tag{9}$$

For $N=1$ the expression (7) reduces to the one derived in [8].

3. Averaging over the coordinates of particles

For the radiation intensity averaged over the coordinates of particles in the bunch we get

$$I_N(\omega,\theta,\phi) = NI_1(\omega,\theta) + N(N-1)I_c(\omega,\theta,\phi) \tag{10}$$

where the contribution of the coherent effects is given by the second term on the right–hand side with

$$I_c(\omega,\theta,\phi) = \frac{1}{2}\int d^3R_j \int d^3R_{j'} I_{jj'}(\omega,\theta,\phi) f(R_j) f(R_{j'}),\ j' \neq j \tag{11}$$

(Note that the formula (10) is valid for various types of radiation processes, including the transition radiation, the diffraction radiation and the synchrotron radiation (see [10]).) We assume that the distribution function is normalized in accordance with $\int d^3R_j f(R_j) = 1$. In (11), $I_{jj'}(\omega,\theta)$ is given by the expression (7) if we remove the summation sign and $R_j = (X_j, Y_j, Z_j)$. Assuming that $f(R_j) = f_x(X_j) f_y(Y_j) f(Z_j)$, with the functions $f_u(U_j)$ separately normalized to 1, and introducing the notation $F_u(\tau) = \left|\int_{-\infty}^{+\infty} ds f_u(s) e^{i\tau s}\right|^2$ with $u = x, y, z$, we find

$$\begin{aligned} I_c(\omega,\theta,\phi) = {} & \frac{e^2\beta_1^2 \sin^3\theta}{2\pi^2 c\sqrt{\varepsilon_1}} F_x(k_x) F_y(k_y) \Bigg\{ 2U \sum_{m,m'=-\infty}^{+\infty} B_m(\theta,\omega)\Big[UB_{m'}(\theta,\omega) F_{mm'}(\omega,\theta) \\ & \cos\left(lk_s \frac{m-m'}{2}\right) - \frac{J_{m'}(a_1) J_{m'+m}(b_1)}{1-\beta_1\cos\theta} \sin\left(\frac{l\omega}{2v} W_{m'} + \pi\frac{m'-m}{2}\right) F_{m+m'}(\omega)\Big] \\ & - U \sum_{m=-\infty}^{+\infty} \frac{W_m B_m^2(\theta,\omega)}{1-\beta_1\cos\theta} F_z(\omega/v) + \frac{\left[1 - 2\cos(l\omega W/v) J_0(b_1)\right] F_z(\omega/v) + 2F(\theta,\omega)}{4(1-\beta_1\cos\theta)^2} \Bigg\} \end{aligned} \tag{12}$$

In (12) the following notations are introduced:

$$\begin{aligned} & F_{mm'}(\omega,\theta) = \int_0^{+\infty} d\tau G(\tau) J_{m'-m}\left(2a_1 \sin\left(\frac{\tau\omega_s}{2v}\right)\right) \cos\left(\left(\omega_s \frac{m'+m}{2} - \omega\right)\frac{\tau}{v} - \pi\frac{m-m'}{2}\right) \\ & G(\tau) = \int_{-\infty}^{+\infty} du f_z(u-\tau) f_z(u),\ F_m(\omega) = \int_0^{+\infty} d\tau G(\tau) \cos\left((2m\omega_s - \omega)\right) \\ & F(\omega,\theta) = \int_0^{+\infty} d\tau G(\tau) \cos(\omega\tau/v) J_0\left(2b_1 \sin(\tau\omega_s/2v)\right) \end{aligned} \tag{13}$$

Note that we can write $F_z(u)$ in terms of the function $G(\tau)$: $F_z(u) = 2\int_0^{+\infty} d\tau G(\tau)\cos(u\tau)$.

Note that the dominant contribution in the integrals for the form–factors in (13) comes from the region of the integration $\tau \le L_z$, where L_z is the longitudinal size of the bunch. Now one has $\tau\omega_s / v \le 2\pi(L_z/\lambda_s)(v_s/v)$, where λ_s and v_s are the wavelength and the velocity for the acoustic wave. If $L_z \le \lambda_s$ one has $\tau\omega_s / v \ll 1$ for relativistic electrons. In this case the form–factor $F_{mm'}(\omega,\theta)$ is small for $m \neq m'$ and the main contribution in the corresponding part in (12) comes from the term $m = m'$ with $F_{mm}(\omega,\theta) \approx F_{m/2}(\omega)$. We also have $F(\omega,\theta) \approx F_z(\omega/v)/2$. If

in addition, m is not too large, so $m\omega_s \ll \omega$, we see that $F_m(\omega) \approx F_z(\omega/v)/2$. In this case the summation over m' in the second term in the square brackets of (12) is done explicitly by using the addition theorem for the Bessel function and one finds

$$I_c(\omega,\theta,\phi) \approx F_x(k_x) F_y(k_y) F_z(\omega/v) I_1(\omega,\theta,\phi) \tag{14}$$

Hence, under the conditions $L_z \le \lambda_s$ and $m\omega_s \ll \omega$ the influence of the bunch structure is separated in the form of the form–factor $F_x(k_x) F_y(k_y) F_z(\omega/v)$.

The general formula (12) is further simplified for large values of the plate thickness. Introducing the quantity $I_c^{\infty}(\omega,\theta) = \lim_{l\to\infty} I_c(\omega,\theta)/l$, from (12) we get

$$I_c^{\infty}(\omega,\theta,\phi) = F_x(k_x) F_y(k_y) \frac{e^2\beta_1\omega}{2\pi c^2} \frac{\varepsilon_1 \sin^3\theta\cos\theta}{\varepsilon_0\sqrt{\varepsilon_0/\varepsilon_1 - \sin^2\theta}} \sum_{m=-\infty}^{+\infty} C_m(\omega) J_m^2(a_1)\delta(W_m) \tag{15}$$

with $\delta(x)$ being the Dirac delta function and $C_m(\omega) = F_{mm}(\omega,\theta)$. This expression for the radiation intensity is valid under the condition $l \gg 2\pi v/\nu$, where $\nu = \omega/(2\pi)$. Note that one has $\nu \gg \nu_s$ and this condition does not contradict the condition l _ v/νs (see the paragraph after formula (1)) we have assumed before. In (15), the term with $m = 0$, which we denote by $I_{c,0}^{\infty}(\omega,\theta,\phi)$, describes the radiation which propagates along the direction $\theta_0 = \arcsin\left(\sqrt{\varepsilon_0/\varepsilon_1}\sin\theta_{Ch}\right)$, $\theta_{Ch} = \arccos(1/\beta_0)$ is the Cherenkov angle in the medium with permittivity ε_0. This term corresponds to the Cherenkov radiation in the plate which propagates in the region $z > 0$ after the refraction at $z = 0$. Integrating over θ we find

$$I_{c,0}^{\infty}(\omega,\theta) = \int_0^{\pi} d\theta I_{c,0}^{\infty}(\omega,\theta,\phi) = \frac{e^2\omega}{\pi c^2} F_x(k_x) F_y(k_y) C_0(\omega)\left(1-\beta_0^2\right) J_0^2(a_1) \tag{16}$$

where now $a_1 = \omega v \Delta\varepsilon/\left(2c^2 k_s\right)$ and in the expressions (6) one has $\theta = \theta_0$.

Now we consider the terms with $m \ne 0$. For a given m, the frequency for the radiation propagating along the direction θ is given by the relation $\omega = mvk_s/W$, where $m > 0$ for $W > 0$ and $m < 0$ for $W < 0$. After the integration over ω, for $I_{c,m\ne 0}^{\infty}(\theta,\phi) = \int d\omega I_c^{\infty}(\omega,\theta,\phi)$ we find

$$I_{c,m\ne 0}^{\infty}(\theta,\phi) = \frac{e^2\beta_1^3 k_s^2 \sin^3\theta\cos\theta}{2\pi\varepsilon_0\sqrt{\varepsilon_0/\varepsilon_1 - \sin^2\theta}\,|W|^3} \sum_{mW>0} F_x(k_x) F_y(k_y) C_m(mvk_s/W) m^2 J_m^2(a_1) \tag{17}$$

where in the expressions (6) the substitution $\omega = mvk_s/W$ should be made.

4. Example of a micro bunched beam

As an example of a micro bunched beam we consider a beam with Gaussian distribution functions in x and y with modulated Gaussian distribution in the longitudinal direction:

$$f_u(\tau) = \frac{e^{-\tau^2/\left(2\sigma_u^2\right)}}{\sqrt{2\pi}\sigma_u},\ u = x, y,\ f_z(z) = \frac{e^{-z^2/\left(2\sigma_z^2\right)}}{\sqrt{2\pi}\sigma_z} \sum_{n=-\infty}^{\infty} d_n e^{ink_r z} \tag{18}$$

where k_r is beam modulation wave number and $d_{-n} = d_n^*$, $d_0 = 1$. For these functions one has

$$F_u\left(k_u\right)=e^{-\sigma_u^2k_u^2},\ u=x,y,\ F_z\left(u\right)=\left|\sum_{n=-\infty}^{\infty}d_ne^{-\sigma_z^2\left(nk_r+u\right)^2/2}\right|^2 \tag{19}$$

For the function $G\left(\tau\right)$ one gets the expression

$$G\left(\tau\right)=\frac{e^{-\tau^2/\left(4\sigma_z^2\right)}}{2\sqrt{\pi}\sigma_z}h\left(k_r\sigma_z,\tau/\left(2\sigma_z\right)\right),\ h\left(x,u\right)=\sum_{n,n'=-\infty}^{\infty}d_nd_{n'}e^{-\left(n+n'\right)^2x^2/4}\cos\left[\left(n-n'\right)xu\right] \tag{20}$$

With the use of (20), the expression for the function $F_m\left(\omega\right)$ takes the form:

$$F_m\left(\omega\right)=\frac{1}{2}e^{-\left(2m\omega_s-\omega\right)^2\frac{\sigma_z^2}{v^2}}\sum_{n,n'=-\infty}^{\infty}d_nd_{n'}e^{-\left(n^2+n'^2\right)k_r^2\frac{\sigma_z^2}{2}}\cos\left[\left(n-n'\right)\left(2m\omega_s-\omega\right)k_r\frac{\sigma_z^2}{v}\right] \tag{21}$$

In the simple case $d_n=0,\ n=\pm2,\pm3,\ldots$, defining $d_1=d_be^{i\beta}$, the distribution function is given by

$$f_z\left(z\right)=\frac{e^{-z^2/\left(2\sigma_z^2\right)}}{\sqrt{2\pi}\sigma_z}\left[1+2d_b\cos\left(k_rz\right)+\beta\right] \tag{22}$$

For the function $h\left(x,u\right)$ we find

$$h\left(x,u\right)=1+2d_b^2\cos\left(2xu\right)+4d_be^{-x^2/4}\cos\beta\cos\left(xu\right)+2d_b^2e^{-x^2}\cos\left(2\beta\right) \tag{23}$$

For the numerical example we consider large values of the plate thickness. For the angular density of the number of quanta radiated at a given frequency $\omega_m=mvk_s/W$, per unit trajectory of the particle, one has

$$N_{N,m}\left(\theta,\phi\right)=NN_{1,m}\left(\theta,\phi\right)+N\left(N-1\right)N_{c,m}\left(\theta,\phi\right) \tag{24}$$

For large values of the plate thickness, for the coherent part $N_{c,m}^{\infty}\left(\theta,\phi\right)=\lim_{l\to\infty}N_{c,m}\left(\theta,\phi\right)/l$, from (17) one gets

$$N_{c,m}^{\infty}\left(\theta,\phi\right)=\frac{e^2}{\hbar c}\frac{\varepsilon_1\beta_1^2k_s\sin^3\theta\cos\theta}{\varepsilon_0\sqrt{\varepsilon_0-\varepsilon_1\sin^2\theta}W^2}F_x\left(k_x\right)F_y\left(k_y\right)C_m\left(\omega_m\right)\left|m\right|J_m^2\left(a_1\right) \tag{25}$$

We consider the electron distribution function having the asymmetric Gaussian form

$$f_z\left(Z\right)=\frac{N_b}{\sqrt{2\pi}\left(1+p\right)b_z}\left[\exp\left(-\frac{Z^2}{2p^2b_z^2}\right)\theta\left(-Z\right)+\exp\left(-\frac{Z^2}{2b_z^2}\right)\theta\left(Z\right)\right] \tag{26}$$

For the coherent part one gets

$$N_{c(aG)}^{\infty}\left(\theta\right)=\frac{\alpha\omega^2\varepsilon_1^{3/2}V\sin^3\left(\theta\right)\cos\left(\theta\right)}{4\sqrt{\pi}c^2\varepsilon_0\sqrt{\frac{\varepsilon_0}{\varepsilon_1}-\sin^2\left(\theta\right)}\left(1+p^2\right)}\int_{-\infty}^{+\infty}d\tau W\left(\tau,p\right)$$
$$\sum_{m=-\infty}^{+\infty}J_m^2\left(a_1\sin\left(\frac{b_z\omega_s}{2V}\tau\right)\right)\cos\left(\frac{b_z}{V}\tau\left(m\omega_s-\omega\right)\right) \tag{27}$$

where

$$W(\tau,p)=\exp\left(-\frac{\tau^2}{4}\right)\operatorname{erfc}\left(\frac{|\tau|}{2}\right)+\exp\left(-\frac{\tau^2}{4p^2}\right)\operatorname{erfc}\left(\frac{|\tau|}{2p}\right)$$
$$+\frac{\sqrt{2}\exp\left(-\frac{\tau^2}{2\left(1+p^2\right)}\right)p\left(\operatorname{erf}\left(\frac{-\left(-1+p^2\right)\tau+\left(1+p^2\right)|\tau|}{2\sqrt{2}p\sqrt{1+p^2}}\right)+\operatorname{erf}\left(\frac{\left(-1+p^2\right)\tau+\left(1+p^2\right)|\tau|}{2\sqrt{2}p\sqrt{1+p^2}}\right)\right)}{\sqrt{1+p^2}} \tag{28}$$

p determines the degree of bunch asymmetry, b_z the correspond characteristic sizes of the bunch.

In figure 1 we have plotted the quantity (25) for $m=-1$ as a function of $\sigma_z k_s$ and θ for the electron energy 17.5 MeV and for the longitudinal distribution function (22) with $d_b=0.5$, $\beta=0$, $\sigma_z=3\times10^{-2}cm$. We assumed that the plate is made from fused quartz and $\varepsilon_1=1$. For the velocity of the acoustic wave one has $v_s=5.6\times10^5 cm/s$ and we have taken $\Delta\varepsilon=0.02$. For the left plot $\sigma_z k_r=5$ and for the right one $\sigma_z k_r=10$. For the transverse part of the distribution function we have taken $F_x\left(k_x\right)F_y\left(k_y\right)=1$. With increasing $\sigma_z k_s$ the separation between the peaks and the height of the right peak increase. In addition, the right peak exhibits microstructure. We have numerically checked that the contributions of the higher harmonics $m=-2,-3,...$ are small compared to the one for $m=-1$.

In figure 2 graphics shows that for asymmetric bunch the coherent part of the radiation can be essentially larger than for symmetric case.

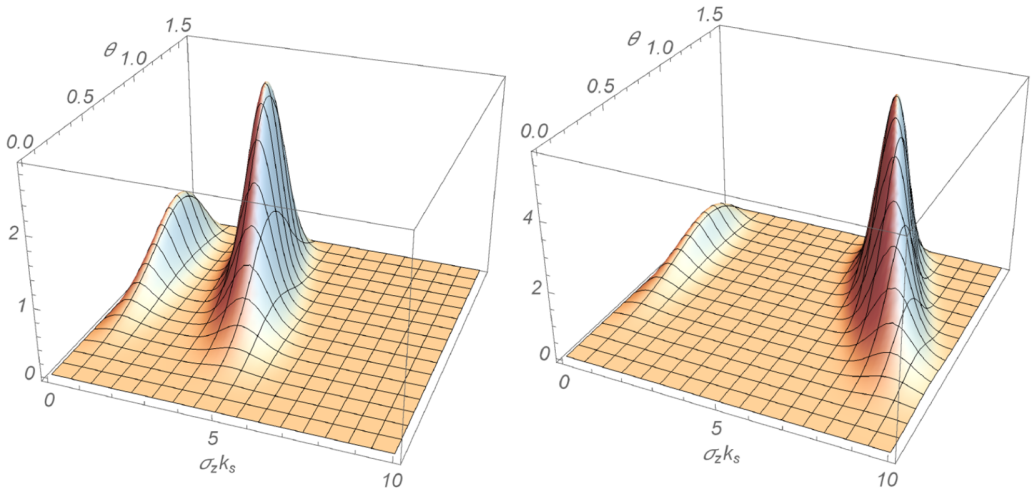

Fig. 1. Coherent part in the number of the radiated quanta, $10^8 N^{\infty}_{c,m}$ (see (25)) at a given harmonic corresponding to $m=-1$.

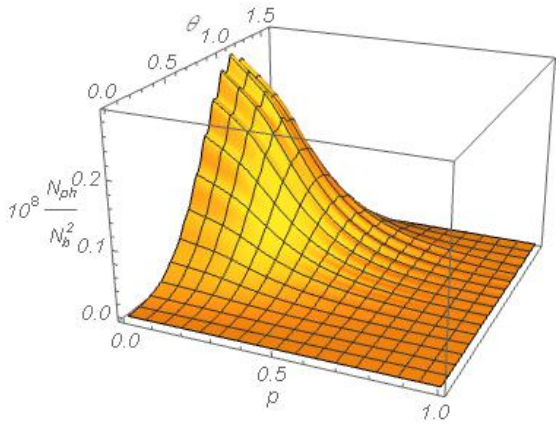

Fig. 2. Coherent part in the number of the radiated quanta $10^8 \dfrac{N_{ph}(\theta)}{N_b^2}$ at a given harmonic corresponding to $m=-1$, electron energy 17.5 MeV, $b_z = 3\times10^{-2} cm$, $\triangle\varepsilon = 0.02$, $\triangle\varepsilon = 0.02$,

5. Conclusion

In the present paper we have considered the coherence effects in the transition radiation of a microbunched electron beam on an acoustic superlattice excited in a finite thickness dielectric plate. Assuming that the amplitude of the modulation for dielectric permittivity is small, the spectral–angular density of the radiation intensity in the forward direction is given by formula (7). After averaging over the coordinates of particles in the bunch, it is presented as (10), where for the contribution of coherent effects one has the expression (12). Under the conditions $L_z \le \lambda_s$ and $m\omega_s \ll \omega$, the influence of the bunch structure on the radiation intensity is separated in the form of the form–factor (see (14)). For a thick plate, the general formula is further simplified to (15). In this formula, the $m=0$ term corresponds to the Cherenkov radiation in the plate which propagates in the region $z>0$ after the refraction at the plate boundary. As an application of the general expression for the transition radiation intensity, in section 4 we have considered a beam with Gaussian distribution functions in transverse directions and with modulated Gaussian distribution in the longitudinal direction. The spectral–angular distribution of the radiation intensity can be controlled by tuning the parameters of two periodic structures: the beam modulation wave number k_r and the acoustic wave number k_s.

References.

1. Ter–Mikaelian M L 1972 High Energy Electromagnetic Processes in Condensed Media (New York: Wiley Interscience)
2. Gharibian G M and Yan S 1983 Rentgenovskoye Perekhodnoye Izluchenie (Yerevan: Izdatelstvo AN Arm. SSR, in russian)
3. Ginzburg V L and Tsytovich V N 1990 Transition Radiation and Transition Scattering (Bristol: Adam Hilger)
4. Rullhusen P, Artru X and Dhez P 1998 Novel Radiation Sources Using Relativistic Electrons (Singapore: World Scientific)

5. Potylitsin A P 2009 Izluchenie Electronov v Periodicheskikh Structurakh (Tomsk: Izdatelstvo Nauchno– Tekhnicheskoi Literaturi, in russian)
6. Grigoryan L Sh, Mkrtchyan A H and Saharian A A 1988 Nucl. Instr. Meth. B145 197
7. Grigoryan L Sh, Mkrtchyan A R, Khachatryan H F, Arzumanyan S R and Wagner W 2010 J. Phys.: Conf. Ser. 236 012012
8. Mkrtchyan A R, Parazian V V and Saharian A A 2010 Mod. Phys. Lett. B 24 2693
9. [9] Mkrtchyan A R, Parazian V V and Saharian A A 2012 Int. J. Mod. Phys. B 26 1250036

Research of Acoustic Responses of Biological Objects for Detection of Malignancies

A.H. Mkrtchyan*, V. V. Nalbandyan, A. S. Hakobyan, H.T. Hovhannisyan, K.V. Avetisyan, V.S. Harutyunyan, A.A. Papazyan, E.S. Shadyan

Institute of Applied Problems of Physics NAS of the Republic of Armenia
25 Hrachya Nersissian Str., Yerevan, Republic of Armenia, 0014

***Abstract**: The technique of diagnosing of malignancies, in particular sarcomas like S–180, in biological objects (mice) utilizing the new contactless method of diagnostics developed on the basis of modulation acoustic spectroscopy which is carried out by scanning of objects by acoustic field formed by package of the modulated electromagnetic waves of different frequency is offered. Comparative analysis of the amplitude–frequency distributions of acoustic responses of the studied healthy and sick objects received as result of scanning gives the chance of detection and determination of prevalence of malignancies.*

1. Introduction

Medical diagnostics represents a complex of researches permitting to conclude about existence or probability of existence of a certain disease in an organism. Discovery new methods and improvement of the existing methods of medical diagnostics are the most important fields of investigation of modern sciences and technology. Diagnostics of oncological diseases at early stages of evolution is one of the most important problems of medicine, as it is important for forehanded and successful treatment of these diseases. The problem of forehanded detection of oncological diseases is directly connected with the existence of high–precision unique equipment and the possibility to develop new techniques of definition of existence of malignancies.

The existing diagnostic resources of oncological diseases [1–4] based generally on ultrasonic and x–ray techniques are not always safe as they can lead to emergence of side effects on organism and, besides, not all areas of organism can be explored thus because of impossibility of penetration of the corresponding radiations through certain types biological fabrics. Thus development of more comprehensive and safe systems of diagnosing at an early stage of disease based on use of ultrasonic waves is relevant.

Utilization of ultrasonic waves for diagnosing of the malignancies is based on property of their rectilinear distribution in organism and diverse reflection from the borders of biological fabrics of various density and internal structures depending on biomechanical characteristics of fabrics: density, structures, elasticity and viscosity.

The organism represents an anisotropic object with various internal structures. In healthy fabrics the anisotropy prevails, accurately there are reactions of dissymmetry [5.6]. The anisotropy defines dependence of properties of fabrics on the direction in an organism. The dissymmetry is the property of biological systems which is shown at the macroscopic and molecular levels to synthesize substance in one of two possible spatial configurations. At pathology in fabrics, in varying degree, properties of anisotropy and dissymmetry are broken. Cancer cells unlike healthy have pronounced property of an isotropy therefore ultrasonic waves

*E – mail: *amktychyan@sci.am*

interact with them differently, than with healthy. If the frequency of physical impact of standing acoustic waves on bodies and body tissues matches their natural frequency, then there is a phenomenon of a resonance which is understood as increase in the response of biological system, i.e. increase in processes of life activity of biological systems. The result of this influence is the response of system, which can be fixed by means of the registration unit.

Thus, the problem of diagnosing by means of standing acoustic waves, consists in definition of responses of biological fabrics depending on their state that will give the chance of differentiation of healthy fabrics from malignancies by comparison of their responses. The amplitude–frequency characteristic specter of responses of structures of body tissues bears information on interior and the condition of structure of fabrics. Registering variation of responses of while passing through fabrics or reflection from the relevant structures, it is possible to judge their functional state and to carry out diagnosing of malignancies.

This problem, is similar to the problem of propagation of ultrasonic waves in multilayer isotropic mediums with heterogeneous of certain type and geometrical form, which was successfully solved at Institute of applied problems of physics of NAS RA [14]. Utilizing some registration technique and methods of Acoustaphysics a new method of diagnostics of malignancies biological objects was developed [7.8].

2. Experimental setup

To carry out the experimental investigation an unique experimental setup was developed [8]. The schematic view of the experimental setup is presented in Figure 1.

Special high precision tunable generators of acoustic wave of $0.1 \div 30 \times 10^9$ Hz frequency rage and low noise linear amplifier for the same was frequency range were developed (Figure 1 2,3,4). A unique unit providing double modulation of acoustic fields was also developed (Figure 1 5)

By the aim to register the acoustic response of all presented in biological object anatomic parts a special high precision low noise registration unit with feedback was developed (Figure 1 8).

The measurements were conducted in specially designed experimental chamber (Figure 1 7), which have appropriate possibility for connection with electronic units.

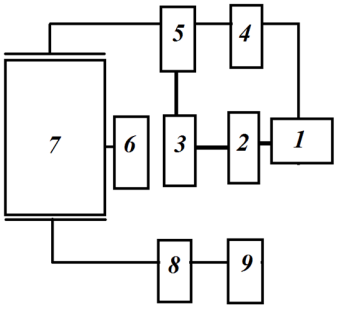

Fig. 1. Schematic view of the experimental setup. 1– Power supply, 2, 4 – fine tunable acoustic generators, 3 – linear low noise amplifier, 5 – special modulator, 6 – accelerating power supply, 7 – experimental chamber, 8 – registration unit, 9 –PC

As biological objects laboratory white mice were used.

Sarcoma C–180, as one of the most aggressive malignancies of the biological object was tested.

To obtain the amplitude–frequency characteristic specters of the studied biological object scanning in a frequency range $100 \div 30 \times 10^9$ Hz with step of 100 Hz was made. To gain more information about the state of organism of the studied biological object step of scanning was decreased up to 1 Hz.

3. The results of experimental investigations

To carry out the experimental investigation healthy and infected biological object were placed in the chamber of the experimental setup and by making scan in above mentioned frequency rage corresponding to the studied biological objects amplitude–frequency characteristic specters were obtained.

A series of experimental meserments on several groups of healthy and sick biological objects at various stages of disease were conducted. Obtained during each subsequent experiment on the same group of infected biological objects the amplitude–frequence characteristic specter of containing the acoustic responses of the biological object differed from early the obtained specters.

Relative analysis the amplitude–frequence characteristic specters obtained for the healthy and infected biological object yields the accurate information on the disease stage. Taking into account the temporary factor it is possible to elicit the dynamics of the pathology of disease.

In Figure 2 an amplitude–frequency characteristic specter for healthy biological object is presented.

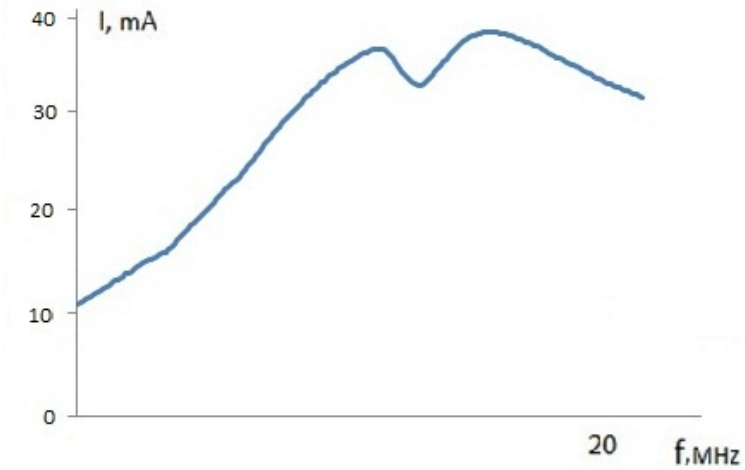

Fig. 2. Amplitude–frequency characteristic specter of healthy biological object

In Figure 3 an amplitude–frequency characteristic specter for healthy (a) and infected (b) biological object are presented. At the relative analysis of these spectrums changes caused by presence malignant formations in biological object are accurately observed. Depending on the stage of the disease the variations in amplitude–frequency charateristic specters become more valuable.

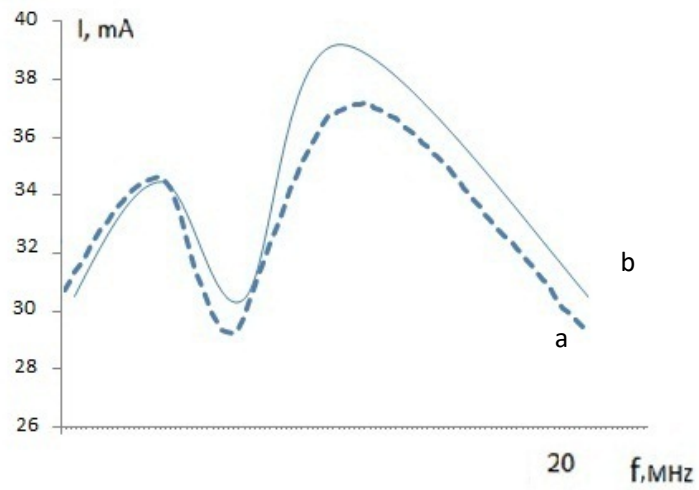

Fig. 3. Amplitude–frequency characteristic specters of healthy (a) and infected (b) biological objects.

At the last stage of disease sharp modification of relative amplitude–frequency characteristic specter of the responses (Fig. 4), which can be explained by detected high energy emission from the biological object.

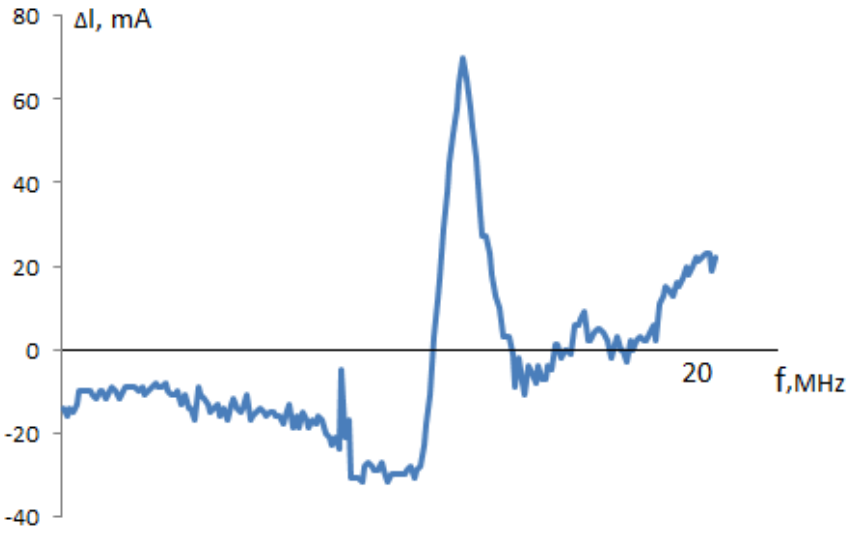

Fig. 4. Relative aamplitude–frequency characteristic specter of acoustic responces of the biological objects.

4. Conclusion

The developed method have a series advantages in comparison with existing ones [6,9]:

- possibility to make not only reliable, but also differential diagnostics of the pathological violations in tissues, by means of the analysis of spectrums of acoustic responses;
- possibility to conduct periodical safe diagnosing of malignant growths;
- possibility of achiving high accuracy diagnostics by reduction the step of scanning.

Utilization of the developed method gives the chance by means of exterior super week double modulated acoustic fields to carry out diagnostics of pathological violations in tissues of biological object. Experimental investigation in this field will be continued further on various biological objects by applying other malignant formations.

References.

1. Б.В.Акопян, Ю.А.Ершов. Основы взаимодействия ультразвука с биологическими объектами. Ультразвук в медицине, ветеринарии и экспериментальной биологии. М. Изд. МГТУ им Н.Э.Баумана, 2005, 224 .
2. М.Р.Бейли, В.А.Хохлова и др. Физические механизмы воздействия терапевтичес кого ультразвука на биологическую ткань (обзор) . Акустический журнал, 2003, том 49, №4, 447.
3. J.J. Cronan, R.K. Zeman, A.T. Rosenfield.Comparison of computerized tomography, ultrasound and angiography in staging renal cell carcinoma. J. Urol., 1982, V. 127, № 2,712–714.
4. И.Г. Фролова, О.В. Котова, Ю.И. Тюкалов, С.А. Величко, Е.Е. Боберь, Ж.А. Старцева, А.И. Коновалов, А.В. Богоутдинова. Возможности ультразвукового метода в диагностике сарком мягких тканей. Сибирский онкологический журнал. 2015, № 3, 82–89
5. Ю.А. Корнеев, А.П. Коршунов, В.И. Погадаев. Медицинская и биологическая физика. М. Наука, 2001.
6. М.В.Кутушов.Способ диагностики с помощью ультразвуковых и электромагнитных волн. № 2378989, 2, 2007.
7. А.Г. Мкртчян, А.Р. Мкртчян, В.В. Налбандян, В. Хачикян, Г. Базикян. Метод обнаружения злокачественной опухоли в живом организме. Авторское свидетельство № 2994 А,2015.
8. А.Г. Мкртчян, В.В. Налбандян, А.С. Акопян, М.М. Момджян . Исследования акустических откликов биологических объектов при отсутствии и наличии злокачественных образований. Международный научный журнал. Сборник научных трудов, Киев, №6, т.3, 2016, 25–27.
9. Г.Т. Синюкова, Л.А. Костякова, В.Н. Шолохов, П.А. Синюков. Ультразвуковая диагностика новообразований мягких тканей. Вестник РОНЦ им. Н. Н. Блохина РАМН, № 1–2, т. 15, 2004.
10. S.A. Mirakyan. Propagation of acoustic waves through elastic stratified medium with heterogeneity in the form of rectangular reservoir. Armenian Journal of Physics, 2014, vol. 7, issue 2, 102–105.
11. А.Г. Мкртчян, А.Р. Мкртчян, Х.В. Котанджян, А.А. Асланян, Э.М. Арутюнян, А.С. Арутюнян, Г.А. Айвазян, О.Р. Мурадян, В.Н. Агабекян, С.А. Миракян. О возможности определения параметров сейсмо–акустических волн методом обратных задач. Фундаментальные Исследования, № 8, 2014, 51–54.
12. А.Г. Мкртчян, А.Р. Мкртчян, А.С. Багдасарян, В.К. Сарьян, Х.В. Котанджян, А.А. Асланян, Г.А. Айвазян, О.Р.Мурадян, В.Н. Агабекян, С.А. Миракян. Определение параметров акустических колебаний методом обратных задач. Нелинейный Мир, № 6, Т.12, 2014,42–47.

13. А.Г. Мкртчян, А.Р. Мкртчян, А.С. Багдасарян, В.К. Сарьян, Х.В. Котанджян, А.А. Асланян, О.Р. Мурадян, С.А. Миракян. Накопления акустических волн при распространении в слоистых средах. Нелинейный Мир, № 8, Т.12, 2014, 16–22.
14. А.Р. Мкртчян, А.Г. Мкртчян, Э.М. Арутюнян, С.А. Миракян. Метод регистрации параметров акустических колебаний. Авторское свидетельство № 2863 А, 2014.
15. Т.Н.Пашовкин, Д.Г.Садикова. Расслаивание,разделение и концентрирование клеток в поле стоячих ультразвуковых волн. Акустический журнал, 2009, том 55, №4–5, 575.

Radiation of Surface Polaritons from a Charge Rotating Around a Dielectric Cylinder

A.A. Saharian[1,2,*], A.S. Kotanjyan[2], A.R. Mkrtchyan[1], V.Kh. Kotanjyan[1]

[1] Institute of Applied Problems of Physics NAS of the Republic of Armenia
25 Hrachya Nersissian Str., Yerevan, Republic of Armenia, 0014
[2] Department of Physics, Yerevan State University,
1 A. Manoogian Str., Yerevan, Republic of Armenia, 0025

Abstract. *We investigate the radiation of surface polaritons by a charged particle rotating around a dielectric waveguide embedded in a homogeneous medium. A formula is derived for the spectral distribution of the radiation intensity for surface–type modes. It is shown that the corresponding waves are radiated on the eigenmodes of the dielectric cylinder. The number of radiated quanta for surface polaritons of a given harmonic can be essentially larger than that for guiding modes.*

1. Introduction

The surface plasmon polaritons (SPPs, for reviews see [1]–[4]) are evanescent electromagnetic waves propagating along a metal–dielectric interface as a result of collective oscillations of electron subsystem coupled to electromagnetic field. They exist in frequency ranges where the real part of the permittivity undergoes a change of the sign at the interface. SPPs have been a powerful tool in the wide range of investigations including surface imaging, surface–enhanced Raman spectroscopy, data storage, biosensors, plasmonic waveguides, light–emitting devices, plasmonic solar cells, etc. Remarkable properties of SPPs include the possibility of concentrating electromagnetic fields beyond the diffraction limit of light waves and enhancing the local field strengths by orders of magnitude [1,2]. Depending on the dielectric properties of the active medium, other forms of surface polaritons may exist. In particular, other materials besides metals, such as semiconductors, organic and inorganic dielectrics, ionic crystals, can support surface polariton type waves. An important direction of recent developments is the extension of plasmonics to the infrared and terahertz ranges of frequencies. This can be done by a suitable choice of the active medium such as doped semiconductors and artificially constructed materials (metamaterials) by using various structures [5,6].

From the point of view of an understanding of the fundamental properties and practical applications, of particular interest is the investigation of the effects induced by the curvature of the interface on the generation and propagation of surface polaritons. In the present report we consider the generation of surface polaritons by a charge circulating around a cylindrical waveguide. We are interested in the electromagnetic fields and in the intensity of the radiated surface polaritons.

For a charged particle rotating around a dielectric cylinder, the spectral and angular distribution of the radiation intensity at large distances from the cylinder has been investigated in [7,8]. It was shown both analytically and numerically that if the Cherenkov condition for permittivity of the cylinder and for the velocity of the particle image on the cylinder surface is

[*] **E – mail**: *saharian@ysu.am*

obeyed then strong narrow peaks appear in the angular distribution of the radiation intensity on a given harmonic. At these peaks the radiated energy density may exceed the corresponding value for the radiation in the absence of the cylinder by several orders of magnitude. Similar features for the radiation from a charge moving along a helical trajectory around a cylinder have been discussed in [9]. The radiation of surface waves on the eigenmodes of a dielectric cylinder by a charge circulating around the cylinder is discussed in [10]. The interference effects between the synchrotron and Smith–Purcell radiations from a charge rotating around a cylindrical grating have been studied in [11]. In all these investigations it has been assumed that the dielectric functions for both the cylinder and surrounding medium are positive and, hence, the cylinder modes corresponding to surface polaritons are absent. The present paper aims to consider the radiation intensity on those modes.

2. Radiation fields for surface–type modes

Consider a point charge q circulating around a cylinder with dielectric permittivity ε_0. The cylinder is embedded in a homogeneous medium with permittivity ε_1. The radii of the rotation orbit and cylinder will be denoted by r_q and r_c, respectively. According to the problem symmetry we will use cylindrical coordinates (r,ϕ,z). In the absence of the cylinder, for a charge rotating in a homogeneous medium we would have two types of radiations: synchrotron radiation and Cherenkov radiation (if the corresponding condition is satisfied). The presence of the cylinder gives rise to new types of radiations propagating inside the cylinder (guiding modes) and along the surface (surface modes).

In the present report we are interested in the radiation of the surface polaritons. The corresponding intensity is expressed in terms the work done by the radiation field on the charged particle:

$$I_{(\mathrm{SP})} = -\int_0^\infty dr \int_0^{2\pi} d\phi \int_{-\infty}^{\infty} dz\, r\, \mathbf{j}\cdot\mathbf{E}^{(r)} \tag{1}$$

Here, the only nonzero components of the current density $\mathbf{j}$ is along the azimuthal direction, $\mathbf{j}=(0, j_\phi, 0)$, given by

$$j_\phi = \frac{q}{r} v\delta(r-r_q)\delta(\phi-\omega_0 t)\delta(z) \tag{2}$$

where v is the velocity of the charge and $\omega_0 = v/r_q$ is the corresponding angular velocity. In (1), $\mathbf{E}^{(r)}$ is the electric field corresponding to surface polaritons. In the problem at hand the azimuthal component $E_\phi^{(r)}$ of the radiation field is required only. For the electric field $\mathbf{E}(\mathbf{r},t)$ we can write the Fourier expansion

$$\mathbf{E}(\mathbf{r},t) = 2\mathrm{Re}\left[{\sum_{n=0}^{\infty}}' e^{in\phi - in\omega_0 t} \int_{-\infty}^{\infty} dk_z e^{ik_z z} \mathbf{E}_n(k_z, r) \right] \tag{3}$$

where the prime on the summation sign means that the term $n=0$ should be taken with an additional coefficient 1/2.

The Fourier components $\mathbf{E}_n(k_z,r)$ can be found by using the corresponding Green function (see [7]). Outside the cylinder, $r > r_c$, for the azimuthal component one gets

$$E_{n\phi}(k_z,r)=E_{n\phi}^{(0)}(k_z,r)+E_{n\phi}^{(c)}(k_z,r) \tag{4}$$

The part $E_{n\phi}^{(0)}(k_z,r)$ presents the field for a charge rotating in a homogeneous medium with permittivity ε_1 and the part $E_{n\phi}^{(c)}(k_z,r)$ is generated by the presence of the cylinder. Omitting the arguments, the separate contributions are presented

$$\begin{aligned} E_{n\phi}^{(0)} &= -\frac{qv}{8n\omega_0\varepsilon_1}\sum_{p,j=\pm1}\left(j\frac{n^2\omega_0^2}{c^2}\varepsilon_1+k_z^2\right)J_{n+jp}(\lambda_1 r_q)H_{n+p}(\lambda_1 r) \\ E_{n\phi}^{(c)} &= -\frac{iqv}{4\pi n\omega_0\varepsilon_1}\sum_{p,j=\pm1}\left(j\frac{n^2\omega_0^2}{c^2}\varepsilon_1+k_z^2\right)B_{n,jp}^{(c)}H_{n+p}(\lambda_1 r) \end{aligned} \tag{5}$$

where in the first expression it is assumed that $r>r_q$. The corresponding expression for $E_{n\phi}^{(0)}$ in the region $r<r_q$ is obtained by the replacements $J\rightleftarrows H$. In (5), $J_\nu(x)$ is the Bessel function and $H_\nu(x)=H_\nu^{(1)}(x)$ is the Hankel function of the first kind. Here and in what follows we define

$$\lambda_j^2=n^2\omega_0^2\varepsilon_j/c^2-k_z^2,\quad j=0,1 \tag{6}$$

The coefficients $B_{n,p}^{(c)}$ are given by

$$B_{n,p}^{(c)}=-\frac{\pi}{2i}H_{n+p}(\lambda_1 r_q)\frac{V_{n+p}^{J}}{V_{n+p}^{H}}+p\frac{\lambda_0 J_n(\lambda_0 r_c)}{2r_c\alpha_n}\frac{J_{n+p}(\lambda_0 r_c)}{V_{n+p}^{H}}\sum_{l=\pm1}\frac{H_{n+l}(\lambda_1 r_q)}{V_{n+l}^{H}} \tag{7}$$

where for $F=J,H$ we use the notation

$$V_n^F=\lambda_1 J_n(\lambda_0 r_c)F_n'(\lambda_1 r_c)-\lambda_0 F_n(\lambda_1 r_c)J_n'(\lambda_0 r_c) \tag{8}$$

and α_n is defined as

$$\alpha_n=\frac{\varepsilon_0}{\varepsilon_1-\varepsilon_0}-\frac{\lambda_0}{2}J_n(\lambda_0 r_c)\sum_{l=\pm1}l\frac{H_{n+l}(\lambda_1 r_c)}{V_{n+l}^{H}} \tag{9}$$

The eigenmodes of the cylinder is determined from the equation $\alpha_n=0$. The integration range in (3) is divided into two parts. The first one corresponds $k_z^2<n^2\omega_0^2\varepsilon_1/c^2$ and it describes the radiation propagating at large distances from the cylinder, $r\gg r_q$. For the second one, $k_z^2>\omega_n^2\varepsilon_1/c^2$, one has $\lambda_1=i|\lambda_1|$ and the corresponding Hankel functions are reduced to the Macdonald function $K_\nu(x)$. The respective electromagnetic fields are exponentially small at large distances from the cylinder. The modes with $k_z^2>\omega_n^2\varepsilon_1/c^2$ are further subdivided into guiding modes with $\lambda_0^2>0$ and surface–type modes with $\lambda_0^2<0$. We are interested in the radiation fields for the second subclass.

For the evaluation of the radiation intensity (1) we must separate the radiation field corresponding to surface–type modes. The exponent in (3) has no stationary points and for large values of z and for fixed r and the radiation field is determined by the contributions from the poles of the integrand. These poles correspond to the zeros of the function α_n. For the surface–type modes $\lambda_j^2<0$ and the corresponding expression is presented as

$$\alpha_n(k_z)=\frac{U_n^{(s)}(k_z)}{(\varepsilon_1-\varepsilon_0)\left(V_n^{(s)2}-n^2u^{(s)2}\right)},\ u^{(s)}=\frac{u_0}{u_1}-\frac{u_1}{u_0} \tag{10}$$

with the notations

$$U_n^{(s)}(k_z) = V_n^{(s)}\left(\varepsilon_0 u_1 \frac{I_n^{'}}{I_n} - \varepsilon_1 u_0 \frac{K_n^{'}}{K_n}\right) - \frac{n^4\omega_0^2}{c^2}\frac{r_c^4 k_z^2}{u_0^2 u_1^2}\left(\varepsilon_1 - \varepsilon_0\right)^2 \tag{11}$$

and

$$V_n^{(s)} = u_1 \frac{I_n^{'}}{I_n} - u_0 \frac{K_n^{'}}{K_n} \tag{12}$$

Here $I_n = I_n(u_0)$, $K_n = K_n(u_1)$, $I_n(x)$ is the modified Bessel function and

$$u_j = r_c\sqrt{k_z^2 - n^2\omega_0^2\varepsilon_j / c^2} \tag{13}$$

The expression for the functions V_{n+p}^H is presented as

$$V_{n+p}^H = \frac{2i}{\pi r_c} K_n I_n\left(V_n^{(s)} + pnu^{(s)}\right) \tag{14}$$

We note that the product $-iV_{n+p}^H$ is always positive and the function V_{n+p}^H has no zeros. Consequently, the only poles of the integrand in (3) correspond to the zeros of α_n. As seen from (10), the equation $\alpha_n(k_z) = 0$ is reduced to the equation

$$U_n^{(s)}(k_z) = 0 \tag{15}$$

This equation coincides with the equation for surface–type modes (on features of propagation and radiation of surface polaritons in cylindrically curved geometries of the interface see, for instance, Refs. [12]–[19] and references therein). From (15), as necessary condition for the presence of the surface–type modes with $\lambda_j^2 < 0$, we get $\varepsilon_1 / \varepsilon_0 < 0$. Hence, in order to have surface–type modes the dielectric permittivities of the cylinder and the surrounding medium must have opposite signs. This condition is the same as that for surface–type modes on a planar interface between two media.

We will denote by $k_z = \pm k_{n,s}$, $k_{n,s} > 0$, the roots of (15) with respect to k_z, where s enumerates the roots for a given n. In the presence of the poles $k_z = \pm k_{n,s}$, we need to specify the integration contour in (3). That is done by noting that in physically realistic situations one has $\varepsilon_j(\omega_n) = \varepsilon_j^{'}(\omega_n) + i\varepsilon_j^{''}(\omega_n)$. By taking into account that in physically realistic situations $\varepsilon_j = \varepsilon_j^{'} + i\varepsilon_j^{''}$, with $\varepsilon_j^{''}(\omega) > 0$ for $\omega > 0$, we can see that the contour should overcome the poles $k_z = k_{n,s}$ from below and the poles $k_z = -k_{n,s}$ from above. For the radiation fields in the region $z > 0$ we close the integration contour by a semicircle with large radius in the upper complex plane and the integral is expressed in terms of the residues of the integrand. The azimuthal component of the radiation field outside the cylinder is presented in the form

$$\begin{aligned} E_\phi^{(r)}(\mathbf{r},t) \;=\; & \sum_{n=1}^{\infty}\frac{qvr_c}{2n\omega_0\varepsilon_1}\sum_s \frac{\lambda_{n,s}^{(0)}}{I_n K_n^2 \alpha_n^{'}\left(k_{n,s}\right)}\sum_{l=\pm 1}\frac{lK_{n+l}(\lambda_{n,s}^{(1)} r_q)}{V_n^{(s)} + lnu^{(s)}} \\ & \times \sum_{p,j=\pm 1} p\left(k_{n,s}^2 + j\frac{n^2\omega_0^2\varepsilon_1}{c^2}\right)\frac{I_{n+jp}K_{n+p}(\lambda_{n,s}^{(1)} r)}{V_n^{(s)} + jpnu^{(s)}}\cos\left(n\phi + k_{n,s}z - n\omega_0 t\right) \end{aligned} \tag{16}$$

where $V_n^{(s)}$ and $u^{(s)}$ are defined by Eq. (12) with $u_j = r_c\lambda_{n,s}^{(j)}$, $I_n = I_n(\lambda_{n,s}^{(0)} r_c)$, $K_n = K_n(\lambda_{n,s}^{(1)} r_c)$, and

$$\lambda_{n,s}^{(j)} = |\,\lambda_j(k_{n,s})\,| = \sqrt{k_{n,s}^2 - n^2\omega_0^2\varepsilon_j/c^2} \tag{17}$$

The expression (16) corresponding to the surface–type modes is valid for all values of $z > 0$.

3. Radiation intensity

Having the radiation field (16), the radiation intensity is evaluated by using (1) with (2). The latter is presented as the sum of the intensities on separate harmonics $I_{(\mathrm{SP})} = \sum_{n=1}^{\infty} I_{(\mathrm{SP})n}$. After transformations, for the radiation intensity on a given harmonic n we get

$$I_{(\mathrm{SP})n} = -\frac{q^2 r_q^2 r_c \omega_0}{n(\varepsilon_1 - \varepsilon_0)} \sum_s \frac{\lambda_{n,s}^{(0)2}}{\alpha_n'(k_{n,s}) K_n^2} \left[\sum_{l=\pm 1} \frac{lK_{n+l}(\lambda_{n,s}^{(1)} r_q)}{V_n^{(s)} + lnu^{(s)}} \right]^2 \left(\lambda_{n,s}^{(0)} \frac{I_n'}{I_n} - \lambda_{n,s}^{(1)} \frac{K_n'}{K_n} \right) \tag{18}$$

For a given ω_0, the radius of the orbit enters in the form $r_q^2 K_{n+l}^2(\lambda_{n,s}^{(1)} r_q)$. From here it follows that at distances from the cylinder surface, $r_q - r_c$, much larger that the radiation wavelength the radiation intensity is suppressed by the factor $\exp[-2\lambda_{n,s}^{(1)}(r_q - r_c)]$. For values of ε_0 close to $-\varepsilon_1$ the roots $k_{n,s}$ are large. The leading term in the radiation intensity is presented as

$$I_{(\mathrm{SP})n} \approx \frac{4q^2 v^2 \varepsilon_0}{(\varepsilon_1^2 - \varepsilon_0^2) r_q^3 \omega_n} \exp\left[-2\frac{\omega_n}{c} \frac{\varepsilon_1 (r_q - r_c)}{\sqrt{-\varepsilon_0 - \varepsilon_1}} \right] \tag{19}$$

and, hence, the radiation intensity tends to zero in the limit $\varepsilon_0 \to -\varepsilon_1$. In the limiting case $\varepsilon_0 \ll -\varepsilon_1$ the surface polariton type modes are present for the main harmonic $n = 1$ only. In this range the roots for k_z are close to the limiting value $\omega_n \sqrt{\varepsilon_1}/c$ and one gets

$$I_{(\mathrm{SP})1} \approx \frac{q^2 c\,|\,\varepsilon_0\,|}{2\varepsilon_1^{5/2} r_q^2} \left(r_q^2/r_c^2 - 1 \right)^2 \exp\left(-\frac{c\sqrt{|\,\varepsilon_0\,|}}{\varepsilon_1 v_c} \right) \tag{20}$$

and the radiation intensity vanishes in the limit $\varepsilon_0 \to -\infty$. For $n > 1$ and $k_z \to \omega_n \sqrt{\varepsilon_1}/c$, the dielectric permittivity of the cylinder, determined from the mode equation for surface polaritons, tends to a finite limiting value, $\varepsilon_0 \to \varepsilon_{0n}^{(1)}$. Consequently, the quantity $\lambda_{n,s}^{(0)}$ in (18) tends to the finite limit $(\omega_n/c)\sqrt{\varepsilon_1 + |\,\varepsilon_{0n}^{(1)}\,|}$. The radiation intensity $I_{(\mathrm{SP})n}$ approaches a finite limiting value.

In Fig. 1 we have plotted the number of the radiated quanta in the form of surface polaritons on a given harmonic n per period of the charge rotation $T = 2\pi/\omega_0$,

$$N_{(\mathrm{SP})n} = T \frac{I_{(\mathrm{SP})n}}{\hbar n \omega_0} \tag{21}$$

as a function of ε_0 for $\varepsilon_1 = 1$, $r_c/r_q = 0.95$. The numbers near the curves correspond to the values of v/c and the full (dashed) curves correspond to $n = 1$ ($n = 2$). For the critical values of the cylinder dielectric permittivity in the case $n = 2$ one has $\varepsilon_{0n} \approx -1.52$ for $v/c = 0.5$ and $\varepsilon_{0n} \approx -3.44$ for $v/c = 0.9$.

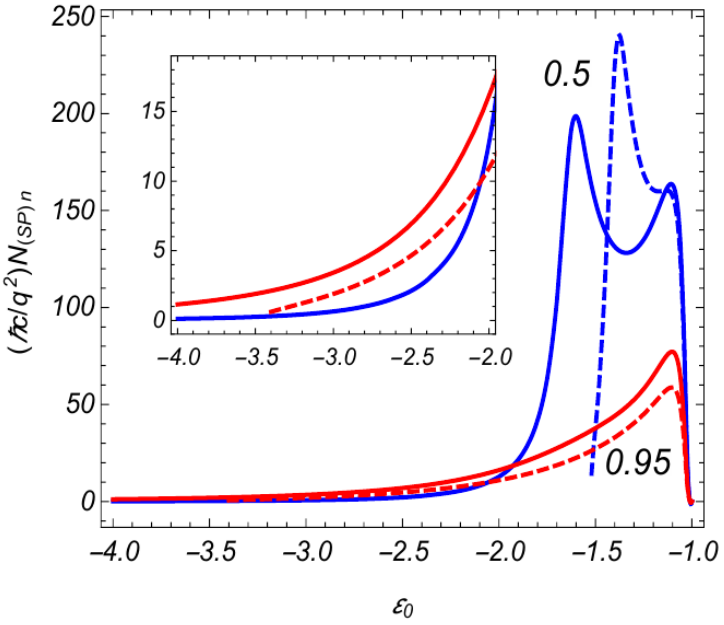

Fig. 1. The number of the radiated quanta in the form of surface polaritons versus the dielectric permittivity of the cylinder. The graphs are plotted for $v/c = 0.5, 0.95$ (numbers near the curves) and for $n = 1, 2$ (full and dashed curves, respectively).

In Fig. 2 we have plotted the dependence of the number of the radiated surface polaritons on the dielectric permittivity of the cylinder for $v/c = 0.5$ and for higher harmonics $n = 3, 5, 10$ (numbers near the curves). Again we see the presence of critical values of the dielectric permittivity for the radiation of surface polaritons on the harmonics with $n > 1$. The critical value increases with increasing n. For $n = 3, 5, 10$ one has $\varepsilon_{0n} \approx -1.37, -1.29, -1.26$, respectively. In these cases the critical values ε_{0n} coincide with the limiting values $\varepsilon_{0n}^{(1)}$.

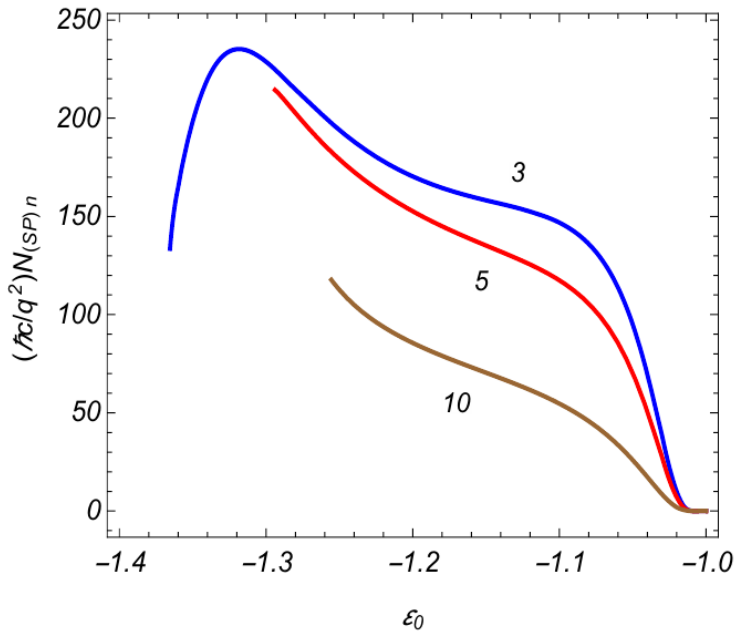

Fig. 2. The same as in Fig. 1 for $v/c=0.5$ and $n=3,5,10$ (numbers near the curves).

It is of interest to compare the radiation intensity for surface polaritons with the radiation for guiding modes ($\lambda_1^2<0<\lambda_0^2$) from a charge rotating around a cylinder having dielectric permittivity $\varepsilon_0>0$ in a given spectral range. The intensity for the part of the corresponding radiation propagating in the region outside the cylinder has been investigated in [10] (the radiation of guiding modes by a charge circulating inside the dielectric cylinder has been discussed in [20]). The numerical results were presented for a cylinder made of quartz. Note that for guiding modes, with increasing harmonic number n the number of roots $k_{n,s}$ increases for some critical values of the harmonic. For the example considered in [10], the number of roots was 1 for $1\le n\le 7$, 2 for $8\le n\le 12$, and 3 for $13\le n\le 16$. For the corresponding number of the quanta radiated on the guiding modes per period of the rotation by an electron of energy 2 MeV and for $r_c/r_q=0.99$ one has $N_{(\mathrm{GM})n}<0.25q^2/(\hbar c)$. The numerical data for these values of the energy and the ratio r_c/r_q, similar to those depicted in Fig. 1, show that for $-5<\varepsilon_0<0$ the number of the radiated surface polaritons is essentially larger. For example, in the case of $n=1$ one gets $N_{(\mathrm{SP})n}\approx 4.23q^2/(\hbar c)$ for $\varepsilon_0=-3$ and $N_{(\mathrm{SP})n}\approx 45.49q^2/(\hbar c)$ for $\varepsilon_0=-1.5$.

4. Conclusion

We have investigated the radiation of surface polaritons by a charge rotating around a dielectric cylinder with permittivity ε_0. For the corresponding waves the component of the wave vector along the cylinder axis obey the condition $k_z^2>\omega_n^2\varepsilon_1/c^2$ and they are radiated on the eigenmodes of the cylinder, determined by the zeros of the function $\alpha_n(k_z)$ for a given harmonic. For the existence of solutions to this equation the dielectric permittivities for the cylinder and surrounding medium should have opposite signs. We have considered the case $\varepsilon_0<0<\varepsilon_1$. The radiation intensity for surface waves on a given harmonic n is given by Eq. (18). For the main

harmonic $n=1$, the surface polaritons are radiated for all values of the cylinder dielectric function in the range $\varepsilon_0 < -\varepsilon_1$. For higher harmonics $n>1$, there exists a critical value ε_{0n} with the absence of surface polariton radiation in the range $\varepsilon_0 < -\varepsilon_{0n}$. The radiation wavelength increases with approaching ε_0 to the limiting value $-\varepsilon_1$. In that range, the wavelength of surface polaritons is much smaller that the wavelength of electromagnetic radiation in free space with the same frequency. We have also demonstrated that, for a given harmonic, the number of radiated quanta for surface polaritons can be essentially larger than that for guiding modes of the cylinder. For the problem under consideration, in addition to the radiation of surface polaritons, there is also radiation propagating at large distances from the cylinder. The latter corresponds to synchrotron radiation modified by the presence of the cylinder. For the respective electromagnetic fields one has $k_z^2 < \omega_n^2 \varepsilon_1 / c^2$ and their radial dependence is given by the Hankel functions $H_{n+p}(\lambda_1 r)$ with positive λ_1. The features of synchrotron radiation for a cylinder made of material with negative dielectric permittivity have been investigated in [21]. It has been shown that the radiation intensity on a given harmonic, integrated over the angles, can be essentially amplified by the presence of the cylinder.

Acknowledgement

A.A.S. has been supported by Grant No. 18T–1C397 from the Science Committee of the Ministry of Education and Science of the Republic of Armenia.

References.

1. V.M. Agranovich and D.L. Mills (Editors), *Surface Polaritons: Electromagnetic Waves at Surfaces and Interfaces* (North–Holland Pub. Co., Amsterdam, 1982).
2. S.A. Maier, *Plasmonics: Fundamentals and Applications* (Springer, 2007).
3. S. Enoch, N. Bonod (Editors), *Plasmonics: From Basics to Advanced Topics* (Springer, 2012).
4. M.I. Stockman *et al.*, Roadmap on plasmonics, J. Optics **20**, 043001 (2018).
5. P.R. West, S. Ishii, G.V. Naik, N.K. Emani, V.M. Shalaev, A. Boltasseva, Laser Photonics Rev. **4**, 795 (2010).
6. N.C. Lindquist, P. Nagpal, K.M. McPeak, D.J. Norris, Sang–Hyun Oh, Rep. Prog. Phys. **75**, 036501 (2012).
7. L.Sh. Grigoryan, A.S. Kotanjyan, A.A. Saharian, Izv. Nats. Akad. Nauk Arm., Fiz. **30**, 239 (1995) (Engl. Transl.: J. Contemp. Phys.).
8. A.S. Kotanjyan, H.F. Khachatryan, A.V. Petrosyan, A.A. Saharian, Izv. Nats. Akad. Nauk Arm., Fiz. **35**, 115 (2000) (Engl. Transl.: J. Contemp. Phys.).
9. A.A. Saharian and A.S. Kotanjyan, J. Phys. A **42**, 135402 (2009).
10. A.S. Kotanjyan, A.R. Mkrtchyan, A.A. Saharian, V.Kh. Kotanjyan, JINST **13**, C01016 (2018).
11. A.A. Saharian, A.S. Kotanjyan, A.R. Mkrtchyan, B.V. Khachatryan, Nucl. Instrum. Methods Phys. Res. B **402**, 162 (2017).
12. M.V. Berry, J. Phys. A **8**, 1952 (1975).
13. U. Schröter, A. Dereux, Phys. Rev. B **64**, 125420 (2001).

14. K. Hasegawa, J. U. Nöckel, and M. Deutsch, Phys. Rev. A **75**, 063816 (2007).
15. J.–W. Liaw, P.–T. Wu, Opt. Express **16**(7), 4945 (2008).
16. M. Guasoni, J. Opt. Soc. Am. B **28**(6), 1396 (2011).
17. J. Polanco, R. Fitzgerald, A. Maradudin, Opt. Commun. **316**, 120 (2014).
18. I.A. Kotelnikov, G.V. Stupakov, Phys. Lett. A **379**, 1187 (2015).
19. M.V. Berry, Eur. J. Phys. **39**, 045807 (2018).
20. A.A. Saharian, A.S. Kotanjyan, Int. J. Mod. Phys. B **26**, 1250033 (2012).
21. A.A. Saharian, A.S. Kotanjyan, L.Sh. Grigoryan, H.F. Khachatryan, V.Kh. Kotanjyan, arXiv:1908.10220.

Fermionic Condensate in Two–Dimensional Rings

A.A. Saharian*, A.Kh. Grigoryan, V.V. Parazian

Institute of Applied Problems of Physics NAS of the Republic of Armenia
25 Hrachya Nersissian Str., Yerevan, Republic of Armenia, 0014

Abstract. We investigate the fermionic condensate induced by an external magnetic flux in a two–dimensional circular ring. Both the irreducible representations of the Clifford algebra are considered. On the ring edges the bag boundary conditions are imposed for the field operator. The fermionic condensate is decomposed into the boundary–free and boundary–induced contributions. Both these contributions are even periodic functions of the magnetic flux with the period equal to the flux quantum.

1. Introduction

There has been a growing interest in recent years in models formulated on backgrounds with the number of spatial dimensions $D>3$. Aside from their role as simplified models in particle physics, field theories in lower dimensions serve as effective theories describing the long–wavelength properties of a number of condensed matter systems [1,2]. Examples for the latter are high–temperature superconductors, d–density–wave states, Weyl semimetals, graphene (and graphene related materials) and topological insulators. For these systems, the long–wavelength dynamics of excitations is formulated in terms of the Dirac–like theory living in (2+1)–dimensional space–time where the role of the velocity of light is played by the Fermi velocity. In topological insulators, $2D$ massless fermionic excitations appear as edge states on the surface of a $3D$ topological insulator. (2+1)–dimensional models also appear as high temperature limits of 4–dimensional field theories.

Among interesting features in (2+1)–dimensional models are flavor symmetry breaking, parity violation, fractionalization of quantum numbers, the possibility of the excitations with fractional statistics. Important new possibilities appear in gauge theories. In particular, the topologically gauge invariant terms in the action provide masses for the gauge fields. This leads to a natural infrared cutoff in the theory and to the solution for the infrared problem without changing the physics in the ultraviolet range [3]. A possible mechanism for the generation of gauge invariant topological mass terms is provided by quantum corrections [4]. The corresponding theories provide a natural framework for the investigation of the quantum Hall effect. Among the most interesting topics in the studies of (2+1)–dimensional theory is the parity and chiral symmetry–breaking. In particular, it has been shown that a background magnetic field can serve as a catalyst for the dynamical symmetry breaking [5, 6]. In addition, the background gauge fields give rise to the polarization of the ground state for quantum fields with the generation of various types of quantum numbers [4, 7]. In particular, charge and current densities are induced [8–11].

In a number of field theoretical models, including the ones describing the condensed matter systems at large length scales, additional boundary conditions are imposed on the field operator. These conditions can have different physical origins. For example, in graphene

*E – mail: *saharian@ysu.am*

nanotubes and nanoloops, because of the compactification of one or two spatial dimensions, the Dirac equation is supplemented by quasiperiodicity conditions along compact dimensions with phases depending on the wrapping direction (chirality of the nanotube). Another type of graphene made structures in which additional boundary conditions are imposed on the field wave functions are graphene nanoribbons, geometrically terminated single layers of graphite (see, for instance, [12]). The edge effects play a crucial role in electronic properties of nanoribbons. In particular, depending on the boundary conditions, a nonzero band gap may be generated. An important new thing is the possibility for the appearance of dispersive edge states.

For charged fields, among the most important characteristics of the ground state are the expectation values of the charge and current densities. Similarly, to the vacuum energy and stresses, the VEVs of these quantities are influenced by the change of spatial topology or by the presence of boundaries. The vacuum currents in spaces with nontrivial topology and with quasiperiodic boundary conditions on the field operator along compact dimensions have been investigated in [13] for the at background geometry and in [14] and [15] for locally de Sitter and anti–de Sitter backgrounds. For the special case $D=2$, the general results were applied to cylindrical and toroidal graphene nanotubes, within the framework of the effective Dirac theory. The influence of additional boundaries on the vacuum currents along compact dimensions has been discussed in [16] and [17] for locally Minkowski and anti–de Sitter backgrounds.

2. Fermionic modes on the ring

We consider a quantum fermionic field $\psi(x)$ in (2+1)–dimensional space–time in the presence of a classical gauge field A_μ. The corresponding dynamics is described by the Dirac equation

$$\left(i\gamma^\mu D_\mu - sm\right)\psi(x)=0 \tag{1}$$

where the gauge extended covariant derivative is defined as $D_\mu=\partial_\mu+\Gamma_\mu+ieA_\mu$, $\mu=0,1,2$, with Γ_μ being the spin connection and e is the charge of the field quanta. For a background geometry with the metric tensor $g_{\mu\nu}$ the Dirac matrices γ^μ obey the anticommutation relations $\left\{\gamma^\mu,\gamma^\nu\right\}=2g^{\mu\nu}$. In the irreducible representation of this Clifford algebra γ^μ are 2×2 matrices. In odd number of space–time dimensions, the Clifford algebra has two inequivalent irreducible representations and the parameter s in Eq. (1), with the values $s=+1$ and $s=-1$, corresponds to two different representations. With these representations, the mass term violates both the parity (P_-) and time–reversal (T_-) invariances. In the long wavelength description of the graphene, s labels two Dirac cones corresponding to $\boldsymbol{K}_+$ and $\boldsymbol{K}_-$ valleys of the hexagonal lattice.

In the present paper the geometry is at and in the polar coordinates $x^\mu=(t,\boldsymbol{r},\phi)$ one has $g_{\mu\nu}=\mathrm{diag}(1,-1,-r^2)$. For the Dirac matrices we will use the representation

$$\gamma^0=\begin{pmatrix}1 & 0\\ 0 & -1\end{pmatrix},\quad \gamma^l=\begin{pmatrix}0 & e^{-i\phi}\\ (-1)^{l-1}e^{i\phi} & 0\end{pmatrix} \tag{2}$$

for $l=1,2$. The corresponding spin connection vanishes, $\Gamma_\mu=0$. We assume that the field $\psi(x)$ is localized in the spatial region bounded by two concentric circles having radii a and b, $a<b$ (two–dimensional ring). On the edges the field operator obeys the MIT bag boundary conditions

$$\left(1+in_\mu\gamma^\mu\right)\psi(x) \tag{3}$$

with n_μ being the outward pointing unit vector normal to the boundaries. In the region $a\le r\le b$ one has $n_\mu=n_u\delta_\mu^1$ for the boundary at $r=u$ with

$$n_a=-1,\ n_b=1 \tag{4}$$

From the conditions (3) it follows that $n_\mu\overline{\psi}\gamma^\mu\psi=0$, where $\overline{\psi}=\psi^\dagger\gamma^0$ is the Dirac adjoin and the dagger denotes Hermitian conjugation. This means that the normal component of the fermionic current vanishes on the edges and the boundaries are impenetrable for the fermionic field. The boundary condition of the type (3) was used in the bag model of hadrons for the confinement of quarks [18]. The analog boundary condition in graphene physics is referred as the infinite mass boundary condition. It has been employed in (2+1)–dimensional Dirac theory for the breaking of time–reversal symmetry without magnetic fields [19].

For the vector potential we will consider a configuration corresponding to the presence of a magnetic flux located in the region $r<a$. In the region under consideration, $a\le r\le b$, for the covariant components in the coordinates (t,r,ϕ) one has $A_\mu=(0,0,A_2)$. Note that the physical azimuthal component for the vector potential is given by $A_\phi=-A_2/r$ and for the magnetic flux threading the ring we have $\phi=-2\pi A_2$. Though the magnetic field strength vanishes, the magnetic flux enclosed by the ring gives rise to Aharonov–Bohm–like effects on physical observables. In particular, the vacuum fluctuations of the field $\psi(x)$ in the region $a\le r\le b$ are influenced by the magnetic flux and the VEVs of physical quantities depend on the ux. Here we are interested in the fermionic condensate, defined as the VEV

$$\langle\overline{\psi}\psi\rangle\equiv\langle 0|\,\overline{\psi}(x)\psi(x)\,|0\rangle \tag{5}$$

Expanding the field operator in terms of the complete set of the positive– and negative–energy fermionic modes $\left\{\psi_\sigma^{(+)}(x),\psi_\sigma^{(-)}\right\}$ and using the commutation relations for the annihilation and

$$\langle\overline{\psi}\psi\rangle=-\frac{1}{2}\sum_{k=\pm}k\sum_\sigma\overline{\psi}_\sigma^{(k)}(x)\psi_\sigma^{(k)}(x) \tag{7}$$

Here σ corresponds to a set of quantum numbers specifying the solutions. The expression in the right–hand side of (7) diverges. In the problem under consideration the background space–time is at and in the region $a\le r\le b$ the field tensor for the external electromagnetic field is zero. As a consequence, the divergences at the points outside the boundaries are the same as those in Minkowksi space–time in the absence of the magnetic flux and the renormalization is reduced to the subtraction of FC corresponding to the latter geometry.

For the problem under consideration the mode functions are presented in the form

$$\psi_{\sigma}^{(k)}(x)=Ce^{-kiEt+ij\phi}\begin{pmatrix} g_{\beta_j,\beta_j}(\gamma a,\gamma r)e^{-i\phi/2} \\ \dfrac{e_j\gamma e^{i\phi/2}}{kE+sm}g_{\beta_j,\beta_j+\varepsilon_j}(\gamma a,\gamma r)\end{pmatrix} \tag{8}$$

where $E=\sqrt{\gamma^2+m^2}$, $\varepsilon_j=1$ for $j>-\alpha$, $\varepsilon_j=1$ for $j\le-\alpha$, and

$$\beta_j=|j+\alpha|-\varepsilon_j/2,\ \alpha=eA_2=-\phi/\phi_0 \tag{9}$$

with $\phi_0=2\pi/e$ being the flux quantum. In (8), for the Bessel and Neumann functions $J_\nu(x)$ and
$Y_\nu(x)$ we have defined

$$g_{\beta_j,\mu}(x,y)=Y_{\beta_j}^{(a)}(x)J_\mu(y)-J_{\beta_j}^{(a)}(x)Y_\mu(y) \tag{10}$$

with the notation

$$\begin{aligned} f_{\beta_j}^{(u)}(x)&=xf_{\beta_j}'(x)+\left[n_u\left(k\sqrt{x^2+m_u^2}+sm_u\right)-\varepsilon_j\beta_j\right]f_{\beta_j}(x) \\ &=n_u\left(k\sqrt{x^2+m_u^2}+sm\right)f_{\beta_j}(x)-\varepsilon_j xf_{\beta_j+\varepsilon_j}(x)\end{aligned} \tag{11}$$

for $u=a,b$, Y $f=J,Y$, and mu = mu $m_u=mu$.

The eigenvalues for γ are determined from the boundary conditions (3) and in the region $a\le r\le b$ are the roots of the equation

$$C_{\beta_j}(\eta,\gamma a)\equiv J_{\beta_j}^{(a)}(\gamma a)Y_{\beta_j}^{(b)}(\gamma b)-J_{\beta_j}^{(b)}(\gamma b)Y_{\beta_j}^{(a)}(\gamma a)=0 \tag{12}$$

with $\eta=b/a$. The positive roots with respect to γa will be denoted by zl, $l=1,2,\ldots$, $z_l<z_{l+1}$. For the eigenvalues of γ one has $\gamma=\gamma_l=z_l/a$. In this way, the mode functions are specified by the quantum numbers $\sigma=(l,j)$. Note that, the roots z_l depend on the value of j as well. In order to simplify the expressions below we do not write this dependence explicitly. For the energy one has $E=\sqrt{\gamma_l^2+m^2}$. The normalization coefficient is given by the expression

$$|C_k|^2=\frac{\pi z_l}{16a^2}\frac{E+ksm}{E}T_{\beta_j}^{ab}(\eta,z_l) \tag{13}$$

where

$$\begin{aligned} T_{\beta_j}^{ab}(\eta,z)&=z\left[D_bJ_{\beta_j}^{(a)2}(z)/J_{\beta_j}^{(b)2}(\eta z)-D_a\right]^{-1} \\ D_u&=u^2\frac{E+ksm}{E}\left[E\left(E+kn_u\frac{\varepsilon_j\beta_j}{u}\right)+kn_u\frac{E-ksm}{2u}\right]\end{aligned} \tag{14}$$

3. Fermionic condensate

Substituting the mode functions (8) into the mode–sum formula (7) we get

$$\langle\bar{\psi}\psi\rangle=-\frac{\pi}{32a^2}\sum_j\sum_{l=1}^{\infty}\sum_{k=\pm}kT_{\beta_j}^{ab}(\eta z_l)h(z_l) \tag{15}$$

$$h(z)=\frac{z}{E}\left[(E+ksm)g_{\beta_j,\beta_j}^2(z,zr/a)-(E-ksm)g_{\beta_j,\beta_j+\varepsilon_j}^2(z,zr/a)\right] \tag{16}$$

with $E=\sqrt{z^2/a^2+m^2}$. In (15), the eigenvalues zl are given implicitly, as roots of (12), and this representation is not convenient for the further evaluation of the VEV. Another disadvantage of the representation (15) is that the separate terms in the series are highly oscillating for large values of the quantum numbers.

These difficulties are overcome by using for the summation over l the Abel–Plana–type formula

$$\sum_{l=1}^{\infty}h(z_l)T_{\beta_j}^{ab}(\eta,z_l)=\frac{4}{\pi^2}\int_0^{\infty}dz\,\frac{h(z)}{J_{\beta_j}^{(a)2}(z)+Y_{\beta_j}^{(a)2}}-\frac{2}{\pi}\mathrm{Re}\,s\left[\frac{h(z)H_{\beta_j}^{1b}(\eta z)}{C_{\beta_j}(\eta z)H_{\beta_j}^{1a}(\eta z)}\right]$$
$$-\frac{1}{\pi}\int_0^{\infty}dz\sum_{p=\pm}\frac{h\left(ze^{i\frac{\pi}{2}}\right)K_{\beta_j}^{(bp)}(\eta z)/K_{\beta_j}^{(ap)}(z)}{K_{\beta_j}^{(ap)}(z)I_{\beta_j}^{bp}(\eta z)-I_{\beta_j}^{ap}(z)K_{\beta_j}^{(bp)}(\eta z)} \tag{17}$$

where $H_{\beta_j}^{(1)}(x)$ and $H_{\beta_j}^{(2)}$ are the Hankel functions. In (17), we have introduced the notation

$$f_{\beta_j}^{(up)}(x)=xf_{\beta_j}'(x)+\left\{n_u\left[k\sqrt{\left(xe^{p\pi i/2}\right)^2+m_u^2}+sm_u\right]-\varepsilon_j\beta_j\right\}f_{\beta_j}(x) \tag{18}$$

with $f=I,K$ for the modified Bessel functions $I_{\beta_j}(x)$ and $K_{\beta_j}(x)$. Note that $f_{\beta_j}^{(u+)}(z)=f_{\beta_j}^{(u-)}(z)$ for $z<m_u$. The summation formula (17) is obtained from the generalized Abel–Plana formula [20] (see also [21]).

Applying the formula (17) to the series over l in (15), the FC is decomposed as

$$\langle\bar{\psi}\psi\rangle=\langle\bar{\psi}\psi\rangle_a+\frac{1}{2\pi^2}\sum_j\int_0^{\infty}dxx\left\{\frac{sm}{\sqrt{x^2-m^2}}\right.$$
$$\times\mathrm{Re}\left[\Omega_{a\beta_j}(ax,bx)\left(G_{\beta_j,\beta_j}^{(a)2}(ax,rx)-G_{\beta_j,\beta_j+\varepsilon_j}^{(a)2}\right)\right] \tag{19}$$
$$\left.-\mathrm{Im}\left[\Omega_{a\beta_j}(ax,bx)\left(G_{\beta_j,\beta_j}^{(a)2}(ax,rx)+G_{\beta_j,\beta_j+\varepsilon_j}^{(a)2}\right)\right]\right.$$

where

$$\langle\bar{\psi}\psi\rangle_a=-\frac{1}{8\pi a^2}\sum_j\sum_{k=\pm1}\int_0^{\infty}dz\,\frac{kh(z)}{J_{\beta_j}^{(a)2}(z)+Y_{\beta_j}^{(a)2}(z)} \tag{20}$$

The notations used in (19) are defined as

$$\Omega_{a\beta_j}(ax,bx)=\frac{K_{\beta_j}^{(b)}(bx)/K_{\beta_j}^{(a)}(ax)}{K_{\beta_j}^{(a)}(ax)I_{\beta_j}^{(b)}(bx)-I_{\beta_j}^{(a)}(ax)K_{\beta_j}^{(b)}(bx)} \tag{21}$$

and

$$G_{\beta_j,\mu}^{(u)}(x,y)=K_{\beta_j}^{(u)}(x)I_{\mu}(y)-(-1)^{\mu-\beta_j}I_{\beta_j}^{(u)}(x)K_{\mu}(y) \tag{22}$$

with $u=a,b$. Here for the modified Bessel functions $f_{\beta_j}(z)=I_{\beta_j}(z),\ K_{\beta_j}(z)$ we define

$$f_{\beta_j}^{(u)}(z)=zf_{\beta_j}'(z)+\left[n_u\left(i\sqrt{z^2-m_u^2}+sm_u\right)-\varepsilon_j\beta_j\right]f_{\beta_j}(z)$$
$$=\delta_f zf_{\beta_j+\varepsilon_j}(z)+n_u\left(i\sqrt{z^2-m_u^2}+sm_u\right)f_{\beta_j}(z) \tag{23}$$

where $\delta_I = 1$ and $\delta_K = -1$.

Let us present the parameter α in the form

$$\alpha = N + \alpha_0, \ |\alpha_0| \leq 1/2 \tag{24}$$

where N is an integer. Redefining the summation variable j in accordance with $j + N \to j$ we see that the charge density does not depend on the integer part N. Then, separating the summations over negative and positive values of j, making the replacement $j \to -j$ in the part with negative j and introducing a new summation variable $n = j - 1/2$, the FC is presented as

$$\begin{aligned} \langle \bar{\psi}\psi \rangle = \langle \bar{\psi}\psi \rangle_a + \frac{1}{2\pi^2} \sum_{n=0}^{\infty} \sum_{p=\pm} \int_m^{\infty} dx x \left\{ \frac{sm}{\sqrt{x^2 - m^2}} \right. \\ \left. \times \mathrm{Re}\left[\Omega_{an_p}(ax, bx) \left(G^{(a)2}_{n_p, n_p}(ax, rx) - G^{(a)2}_{n_p, n_p+1}(ax, rx) \right) \right] \right\} \end{aligned} \tag{25}$$

with

$$n_p = n_p + p\alpha_0 \tag{26}$$

and now the notation (23) in the definitions (21) and (22) for $\Omega_{an_p}(ax, bx)$ and $G^{(a)}_{n_p, \mu}(ax, rx)$ is specified to

$$f^{(u)}_{n_p}(z) = \delta_f z f_{n_p+1}(z) + n_u \left(sm_u + i\sqrt{z^2 - m_u^2} \right) f_{n_p}(z) \tag{27}$$

for $f = I, K$. The representation (25) explicitly shows that the last term is an odd function of the fractional part α_0. The property that the VEVs do not depend on the integer part of the flux, in units of the flux quantum, is a general feature in the Aharonov–Bohm effect and is a consequence of that the flux enters through the phase of the wave function.

In order to clarify the physical meaning of the separate terms in (25) we note that in the limit $b \to \infty$ the last term vanishes. This shows that the part $\langle \bar{\psi}\psi \rangle_a$ presents the FC in the region $r \geq a$ for the geometry of a single boundary at $r = a$. It can be further decomposed as

$$\langle \bar{\psi}\psi \rangle_a = \langle \bar{\psi}\psi \rangle_0 + \langle \bar{\psi}\psi \rangle_a^{(b)} \tag{28}$$

where

$$\langle \bar{\psi}\psi \rangle_0 = -\frac{sm}{4\pi} \sum_j \int_0^{\infty} dx \frac{J^2_{\beta_j}(xr) + J^2_{\beta_j + \varepsilon_j}(xr)}{\sqrt{x^2 + m^2}} \tag{29}$$

and

$$\begin{aligned} \langle \bar{\psi}\psi \rangle_a^{(b)} = \frac{1}{2\pi^2} \sum_j \int_m^{\infty} dx x \left\{ sm \frac{K^2_{\beta_j}(rx) - K^2_{\beta_j + \varepsilon_j}(rx)}{\sqrt{x^2 - m^2}} \mathrm{Re}\left[\frac{I^{(a)}_{\beta_j}(ax)}{K^{(a)}_{\beta_j}(ax)} \right] \right. \\ \left. - \left[K^2_{\beta_j}(rx) + K^2_{\beta_j + \varepsilon_j}(rx) \right] \mathrm{Im}\left[\frac{I^{(a)}_{\beta_j}(ax)}{K^{(a)}_{\beta_j}(ax)} \right] \right\} \end{aligned} \tag{30}$$

with the notations (23). For the representation $s = 1$, this expression for a single boundary–induced
part coincides with the one given in [22].

In order to give a physical interpretation of the separate terms in Eq. (28) let us consider the limit $\alpha \to 0$. Note that the radius of the magnetic flux should also be taken to zero. For $j+\alpha \neq 0$ one has

$$\frac{I_{\beta_j}^{(a)}(ax)}{K_{\beta_j}^{(a)}(ax)} \approx \frac{i\sqrt{x^2-m^2}+\varepsilon_j sm}{x} \frac{2(ax/2)^{2|j+\alpha|}}{\Gamma^2(|j+\alpha|+1/2)} \tag{31}$$

and, hence, the part (30) vanishes as $a^{2|j+\alpha|}$. For half–odd integer values of α, the exceptional case

corresponds to the mode with $j=-\alpha$. For this mode $\beta_j = 1/2,\ \varepsilon_j = -1$, and we get

$$\frac{I_{\beta_j}^{(a)}(ax)}{K_{\beta_j}^{(a)}(ax)} \approx \frac{2}{\pi} \frac{i\sqrt{x^2-m^2}-sm}{x} \tag{32}$$

Note that for this special value of β_j, in (30) the coefficient of the term with the imaginary part of (32) vanishes.

Hence, if α is not a half–odd integer one has

$$\lim_{a\to 0}\langle\bar{\psi}\psi\rangle_a = \langle\bar{\psi}\psi\rangle_0 \tag{33}$$

In this case, the part (30) in the FC is induced by the presence of the boundary at $r=a$, whereas $\langle\bar{\psi}\psi\rangle_0$ gives the FC in the boundary–free geometry with a point like magnetic flux at $r=0$. For α being a half–odd integer one gets

$$\lim_{a\to 0}\langle\bar{\psi}\psi\rangle_a = \langle\bar{\psi}\psi\rangle_0 - \frac{m}{\pi^2 r}\int_0^\infty dy \frac{y^2 e^{-2mr\sqrt{y^2+1}}}{\sqrt{y^2+1}} \tag{34}$$

For a massless field, taking the limit $m \to 0$ we find

$$\lim_{a\to 0}\langle\bar{\psi}\psi\rangle_a = \langle\bar{\psi}\psi\rangle_0 - \frac{1}{2\pi^2 r^2} \tag{35}$$

The boundary–induced contribution (30) does not depend on the integer part N in (24). Redefining the summation variable in (30), this contribution is rewritten in the form

$$\begin{aligned}\langle\bar{\psi}\psi\rangle_a^{(b)} = \frac{1}{2\pi^2}\sum_{n=0}^{\infty}\sum_{p=-,+}\int_m^\infty dx x \\ \times\left\{ sm\frac{K_{n_p}^2(rx)-K_{n_p+1}^2(rx)}{\sqrt{x^2-m^2}}\mathrm{Re}\left[\frac{I_{n_p}^{(a)}(ax)}{K_{n_p}^{(a)}(ax)}\right]\right. \\ \left. -\left[K_{n_p}^{(a)}(rx)+K_{n_p+1}^{(a)}(rx)\right]\mathrm{Im}\left[\frac{I_{n_p}^{(a)}(ax)}{K_{n_p}^{(a)}(ax)}\right]\right\}\end{aligned} \tag{36}$$

with n_p given by (26). This explicitly shows that the single boundary–induced charge density is an odd function of α_0. The real and imaginary parts in (36) are explicitly given by the relation

$$\frac{I_{n_p}^{(u)}(z)}{K_{n_p}^{(u)}(z)} = \frac{W_{n_p}^{(u)}(z) - in_u\sqrt{1-m_u^2/z^2}}{z\left[K_{n_p+1}^2(z)-K_{n_p}^2(z)\right]-2sn_u m_u K_{n_p}(z)K_{n_p+1}(z)} \tag{37}$$

with $u=a,b$ and with the function

$$W_{\nu}^{(u)}(z)=z\left[I_{\nu}(z)K_{\nu}(z)-I_{\nu+1}(z)K_{\nu+1}(z)\right] \\ +\mathrm{n}_u sm_u\left[I_{\nu+1}(z)K_{\nu}(z)-I_{\nu}(z)K_{\nu+1}(z)\right] \tag{38}$$

Note that for $z\geq m_u$ the denominator in (37) is positive. For a massless field and at large distances
from the boundary, $r\gg a$, the dominant contribution to the boundary–induced part (36) comes from the term $n=0$ and this part decays as $(a/r)^{3-2|\alpha_0|}$ with the sign $\mathrm{sgn}(\alpha_0)\langle j^0\rangle_a^{(b)}/e<0$. For a massive field and for $r\gg a,m^{-1}$, the dominant contribution in (36) comes from the region near the lower limit of the integration and the boundary–induced charge density is suppressed by the factor $e^{-2mr}/r^{3/2}$.

From the consideration above it follows that, if $|\alpha_0|\neq 1/2$, the part $\langle\bar{\psi}\psi\rangle_0$ can be interpreted as the charge density in boundary–free two–dimensional space with a special type of boundary condition on the magnetic flux line at $r=0$. Namely, we impose the bag boundary condition at finite radius which is then taken to zero. Consequently, the part (36) is interpreted as the contribution induced in the region $a\leq r<\infty$ by the boundary $r=a$. The last term in (25) is the contribution in the charge density induced when we add the boundary at $r=b$ to the geometry with a single boundary at $r=a$. In this sense, this part can be termed as the second boundary–induced contribution.

The expression (29) for the boundary–free part can be further simplified. The first terms in the brackets of the coefficients of the functions $J_{\beta_j}^2(xr)$ and $J_{\beta_j+\varepsilon_j}^2(xr)$ are canceled for the contributions coming from the positive– and negative–energy modes. For the remaining part we get

$$\langle\bar{\psi}\psi\rangle_0=-\frac{sm}{4\pi}\sum_j\int_0^{\infty}dxx\frac{J_{\beta_j}^2(xr)+J_{\beta_j+\varepsilon_j}^2(xr)}{\sqrt{x^2+m^2}} \tag{39}$$

The corresponding renormalized VEV is presented in the form

$$\langle\bar{\psi}\psi\rangle_{0,ren}=-\frac{sm\sin(\pi\alpha_0)}{2\pi^2 r}\int_0^{\infty}dx\frac{\sinh x}{\cosh^2 x}\frac{\sinh(2\alpha_0 x)}{e^{2mr\cosh x}} \tag{40}$$

This expression with $s=1$ was obtained in [22]. Similarly, to the boundary–induced contributions,
this part is an even function of the parameter α_0. In the limit $\alpha_0\to 1/2$ one gets

$$\langle\bar{\psi}\psi\rangle_{0,ren}=-\frac{sm}{2\pi^2 r}\int_0^{\infty}dx\frac{\sinh^2 x}{\cosh^2 x}\frac{1}{e^{2mr\cosh x}} \tag{41}$$

For a massless field the boundary–free contribution in the FC vanishes for $r\neq 0$. In the case of a massive field, at large distances, the charge density $\langle j^0\rangle_0$ falls off as $e^{-2mr}/r^{3/2}$, whereas at the origin it diverges as $1/r$. At large distances, the decaying factor for a massive field is the same as that for the boundary–induced contribution (36).

4. Conclusion

Among the most important local characteristics of the fermionic vacuum is the FC. We have investigated the FC in two dimensional ring with the bag boundary conditions on its edges. The eigenvalues of the radial quantum number are roots of the equation (12). The mode sum for the FC contains series over those eigenvalues. For the summation we applied Abel–Plana type formula (17) that allowed to extract from the vacuum expectation value the edge induced contributions. In the corresponding integral representation explicit knowledge of the eigenvalues is not required. The FC is an even periodic function of the magnetic flux enclosed by the ring with the period equal to the flux quantum. It is decomposed as (25), where the first term in the right–hand side corresponds to the FC in the geometry with a single edge at $r = a$. The last term is induced by the external edge. The single edge part is further decomposed as (28) with the extracted boundary–free part. The renormalized boundary–free part is given by (40).

References.

1. E. Fradkin, Field Theories of Condensed Matter Systems (Addison–Wesley Publishing Company, Reading, 1991); Y. Imry, Introduction to Mesoscopic Physics (Oxford University Press, Oxford, 1997); G.V. Dunne, Topological Aspects of Low Dimensional Systems (Springer, Berlin, 1999).
2. V.P. Gusynin, S.G. Sharapov, J.P. Carbotte, Int. J. Mod. Phys. B **21**, 4611 (2007); A.H. Castro Neto, F. Guinea, N.M.R. Peres, K.S. Novoselov, A.K. Geim, Rev. Mod. Phys. **81**, 109 (2009); M.A.H. Vozmediano, M.I. Katsnelson, and F. Guinea, Phys. Rep. **496**, 109 (2010).
3. S. Deser, R. Jackiw, S. Templeton, Ann. Phys. (N.Y.) **140**, 372 (1982).
4. A.J. Niemi, G.W. Semenoff, Phys. Rev. Lett. **51**, 2077 (1983).
5. K.G. Klimenko, Z. Phys. C **54**, 323 (1992); K.G. Klimenko, Theor. Math. Phys. **90**, 1 (1992).
6. V.P. Gusynin, V.A. Miransky, I.A. Shovkovy, Phys. Rev. D 52, 4718 (1995); R.R. Parwani, Phys. Lett. B 358, 101 (1995); G. Dunne, T. Hall, Phys. Rev. D 53, 2220 (1996); A. Das, M. Hott, Phys. Rev. D 53, 2252 (1996); M. de J. Anguiano–Galicia, A. Bashir, A. Raya, Phys. Rev. D **76**, 127702 (2007); A. Raya, E. Reyes, Phys. Rev. D **82**, 016004 (2010).
7. A.N. Redlich, Phys. Rev. D **29**, 2366 (1984); R. Jackiw, Phys. Rev. D **29**, 2375 (1984); D. Boyanovsky, R. Blankenbecler, Phys. Rev. D **31**, 3234 (1985); R. Blankenbecler, D. Boyanovsky, Phys. Rev. D **34**, 612 (1986); A.P. Polychronakos, Nucl. Phys. B **278**, 207 (1986).
8. T. Jaroszewicz, Phys. Rev. D **34**, 3128 (1986).
9. P. Gornicki, Ann. Phys. (N.Y.) **202**, 271 (1990).
10. E.G. Flekkoy, J.M. Leinaas, Int. J. Mod. Phys. A **6**, 5327 (1991).
11. H.N. Li, D.A. Coker, A.S. Goldhaber, Phys. Rev. D 47, 694 (1993); V.B. Bezerra, E.R. Bezerra de Mello, Class. Qiantum Grav. 11, 457 (1994); E.R. Bezerra de Mello, Class. Qiantum Grav. **11**, 1415 (1994); Yu.A. Sitenko, Phys. Rev. D **60**, 125017 (1999); R. Jackiw, A.I. Milstein, S.–Y. Pi, I.S. Terekhov, Phys. Rev. B **80**, 033413 (2009); A.I. Milstein, I.S. Terekhov, Phys. Rev. B **83**, 075420 (2011).

12. C.W.J. Beenakker, Rev. Mod. Phys. 80, 1337 (2008); K. Wakabayashi, S. Dutta, Solid State Commun. **152**, 1420 (2012).
13. S. Bellucci, A.A. Saharian, Phys. Rev. D **79**, 085019 (2009); S. Bellucci, A.A. Saharian, V.M. Bardeghyan, Phys. Rev. D **82**, 065011 (2010).
14. S. Bellucci, A.A. Saharian, H.A. Nersisyan, Phys. Rev. D **88**, 024028 (2013).
15. E.R. Bezerra de Mello, A.A. Saharian, V. Vardanyan, Phys. Lett. B **741**, 155 (2015).
16. S. Bellucci, A.A. Saharian, Phys. Rev. D **87**, 025005 (2013); S. Bellucci, A.A. Saharian, N.A. Saharyan, Eur. Phys. J. C **75**, 378 (2015).
17. S. Bellucci, A.A. Saharian, V. Vardanyan, JHEP **11** (2015) 092; S. Bellucci, A.A. Saharian, V. Vardanyan, Phys. Rev. D **93**, 084011 (2016).
18. A. Chodos, R. Jaffe, K. Johnson, C. Thorn, V. Weisskopf, Phys. Rev. D **9**, 3741 (1974); K. Johnson, Acta Phys. Pol. B **6**, 865 (1975).
19. M.V. Berry, R.J. Mondragon, Proc. R. Soc. London, Ser. A **412**, 53 (1987).
20. A.A. Saharian, The Generalized Abel–Plana Formula with Applications to Bessel Functions and Casimir Effect (Yerevan State University Publishing House, Yerevan, 2008); Preprint ICTP/2007/082; arXiv:0708.1187.
21. E.R. Bezerra de Mello, A.A. Saharian, Class. Quantum Grav. **23**, 4673 (2006).
22. S. Bellucci, E.R. Bezerra de Mello, A. A. Saharian, Phys. Rev. D **83**, 085017 (2011).

Features of Synchrotron Radiation in Presence of a Medium with Negative Permittivity

A.R. Mkrtchyan[1], A.A. Saharian[1,2*], L.Sh. Grigoryan[1], H.F. Khachatryan[1], A.S. Kotanjyan[2]

[1] Institute of Applied Problems of Physics NAS of the Republic of Armenia
25 Hrachya Nersissian Str., Yerevan, Republic of Armenia, 0014
[2] Department of Physics, Yerevan State University,
1 A. Manoogian Str., Yerevan, Republic of Armenia, 0025

Abstract. We investigate the radiation from a charged particle rotating around a dielectric cylinder with a negative real part of dielectric permittivity. A formula is derived for the angular density of the radiation intensity on a given harmonic. Compared with the case of a cylinder with positive real part of the permittivity, new interesting features arise in the nonrelativistic limit and for the radiation at small angles with respect to the cylinder axis. Another feature is the appearance of sharp narrow peaks in the angular density of the radiation intensity for large harmonics. We show that the radiation intensity on a given harmonic, integrated over the angles, can be essentially amplified by the presence of the cylinder.

1. Introduction

The presence of medium may essentially influence the physical characteristics of radiation processes by charged particles moving through or near the medium. As a result of the interaction of the charge with medium, under certain conditions, new types of radiations appear. Examples are Cherenkov, diffraction and transition radiations. New interesting features in the radiation processes appear in spectral ranges where the real part of the dielectric permittivity of material becomes negative (for general consideration concerning the existence of a negative dielectric constant see [1]). For example, the metals exhibit a negative permittivity from the visible to microwave frequencies. Another example of material with negative real part of the dielectric permittivity is provided by doped semiconductors [2–4]. Compared to the metals, an advantage of the doped semiconductors is related to the possibility of small losses at infrared and longer wavelengths. In addition, the corresponding plasma frequency can be controlled by tuning the free carrier densities.

At interfaces between two media with positive and negative real parts of the dielectric permittivity new types of surface waves arise called surface polaritons. In particular, the surface plasmon polaritons (SPPs) have found a wide range of applications (see, for example, [5–8] and references therein). SPPs are evanescent electromagnetic waves propagating along a metal–dielectric interface as a result of collective oscillations of electron subsystem coupled to electromagnetic field. The surface polaritons can be excited by electron beams moving parallel or perpendicularly to the interface (see [9–14]). The radiation of surface polaritons by a charged particle rotating around a cylindrical dielectric waveguide recently has been considered in [15]. It has been shown that the radiation intensity for surface polaritons of a given harmonic can be

[*] **E – mail**: *saharian@ysu.am*

essentially larger than that for guiding modes of the cylinder (the radiation on guiding modes for a cylinder with positive dielectric permittivity is investigated in [16,17]).

For the problem considered in [15], in addition to the radiation of surface–type modes (surface polaritons) and guided modes, where will be radiation propagating at large distances from the cylinder. That corresponds to the synchrotron radiation influenced by the presence of the cylinder. For a cylinder with positive dielectric permittivity, in [18,19] it has been shown that under the Cherenkov condition for the velocity of the charge image on the cylinder surface and for the cylinder dielectric permittivity, strong narrow peaks may appear in that distribution (similar features for the radiation from a charge circulating around a dielectric ball were discussed in [20,21]). In the present report we consider the features for the radiation from a charge rotating around a dielectric cylinder in the frequency range with negative real part of dielectric permittivity of the cylinder material.

2. Electromagnetic fields in the exterior region

Let a particle with charge q moves along a circular trajectory of radius r_q around a cylinder with radius r_c and with dielectric permittivity ε_0. For generality we assume that the cylinder is embedded in a homogeneous medium with real and positive dielectric permittivity ε_1. For the material of the cylinder the general case of frequency dependent complex permittivity, $\varepsilon_0=\varepsilon_0^{'}(\omega)+i\varepsilon_0^{''}(\omega)$, will be considered. In the cylindrical coordinate system (r,ϕ,z), with the axis z along the cylinder axis, the components of the current density are written as

$$j_l=\frac{q}{r}v\delta_{l\phi}\delta(r-r_q)\delta(\phi-\omega_0 t)\delta(z),\ l=r,\phi,z, \tag{2.1}$$

where v is the particle velocity and $\omega_0=v/r_q$ is its angular velocity. We are interested in the radiation from the charge at large distances from the cylinder in the frequency range where $\varepsilon_0^{'}(\omega)<0$. There are two types of radiations: the radiation propagating at large distances from the cylinder and the radiation of surface–type modes localized near the cylinder surface. The first type of radiation corresponds to the synchrotron radiation influenced by the cylinder and by the host medium and the surface–type modes correspond to SPPs.

The electric, $\mathbf{E}(\mathbf{r},t)$, and magnetic, $\mathbf{H}(\mathbf{r},t)$, fields, created by the current density (2.1), are expanded in the Fourier series

$$\mathbf{F}(\mathbf{r},t)=\sum_{n=-\infty}^{\infty}e^{in\phi-i\omega_n t}\int_{-\infty}^{\infty}dk_z e^{ik_z z}\mathbf{F}_n(k_z,r) \tag{2.2}$$

with $\omega_n=n\omega_0$ and $\mathbf{F}=\mathbf{E},\mathbf{H}$. For the Fourier components one has $\mathbf{F}_{-n}(k_z,r)=\mathbf{F}_n^{*}(-k_z,r)$, with the star being the complex conjugate, and in what follows we will assume that $n>0$. The $n=0$ term in Eq. (2.2) is time independent and will not contribute to the radiation fields. The Fourier components of the fields can be found by using the Green function from [18] in a way similar to that presented in Refs. [18,19,22] for a cylinder with positive dielectric permittivity and in what follows we will present only the main steps.

Denoting the cylindrical components as $F_{nl}=F_{nl}(k_z,r)$, with $l=r,\phi,z$, for the magnetic field in the region $r>r_q$ one gets

$$H_{nl}=\frac{i^{2-\sigma_l}qvk_z}{2\pi c}\sum_{p=\pm1}p^{\sigma_l-1}B_{n,p}H_{n+p}(\lambda r),\ l=r,\phi,\ H_{nz}=-\frac{qv\lambda}{2\pi c}\sum_{p=\pm1}pB_{n,p}H_n(\lambda r) \tag{2.3}$$

where $\sigma_r=1$, $\sigma_\phi=2$, $H_n(x)\equiv H_n^{(1)}(x)$ is the Hankel function of the first kind and

$$\lambda^2=\omega_n^2\varepsilon_1/c^2-k_z^2 \tag{2.4}$$

The coefficients $B_{n,p}$ are given by the formula

$$B_{n,p}=\frac{\pi}{2i}J_{n+p}(\lambda r_q)-\frac{\pi}{2i}H_{n+p}(\lambda r_q)\frac{W^J_{n+p}}{W^H_{n+p}}+p\frac{\eta I_n(\eta r_c)}{2r_c\alpha_n}\frac{I_{n+p}(\eta r_c)}{W^H_{n+p}}\sum_{l=\pm1}l\frac{H_{n+l}(\lambda r_q)}{W^H_{n+l}} \tag{2.5}$$

Here, $J_n(x)$ and $I_n(x)$ are the Bessel and modified Bessel functions, and we have defined

$$\eta^2=k_z^2-\omega_n^2\varepsilon_0/c^2 \tag{2.6}$$

The other notations in (2.5) are defined as

$$\alpha_n=\frac{\varepsilon_0}{\varepsilon_1-\varepsilon_0}-\frac{\eta I_n(\eta r_c)}{2}\sum_{l=\pm1}\frac{H_{n+l}(\lambda r_c)}{W^H_{n+l}} \tag{2.7}$$

and

$$W^F_{n+p}=p\lambda I_{n+p}(\eta r_c)F_n(\lambda r_c)-\eta F_{n+p}(\lambda r_c)I_n(\eta r_c) \tag{2.8}$$

for the Bessel and Hankel functions $F_\nu(x)=J_\nu(x),H_\nu(x)$. The components for the electric field are found from (2.3) by using the Maxwell equation. In the region $r>r_q$ one gets

$$E_{nl}=\frac{i^{1-\sigma_l}qv}{4\pi\omega_n\varepsilon_1}\sum_{p=\pm1}p^{\sigma_l}\left[\left(\frac{\omega_n^2}{c^2}\varepsilon_1+k_z^2\right)B_{n,p}-\lambda^2B_{n,-p}\right]H_{n+p}(\lambda r),\ E_{nz}=\frac{iqv\lambda k_z}{2\pi\omega_n\varepsilon_1}\sum_{p=\pm1}B_{n,p}H_n(\lambda r) \tag{2.9}$$

where, as before, $l=r,\phi$.

The integration range in (2.2) can be divided into two parts. The radiation fields at large distances from the cylinder correspond to the range $k_z^2<\omega_n^2\varepsilon_1/c^2$, where λ is real. In the range $k_z^2>\omega_n^2\varepsilon_1/c^2$ the quantity (2.4) is purely imaginary and the fields induced by the cylinder depend on the radial coordinate through the Macdonald functions $K_{n+p}(|\lambda|r)$. These parts are exponentially small at large distances from the cylinder. For a cylinder with a negative real part of ε_0 they correspond to the surface–type modes. For the latter the eigenvalues of k_z are the roots of the equation $\alpha_n=0$. In what follows we are interested in the radiation at large distances from the cylinder.

3. Radiation intensity

The radiation propagating in the exterior medium at large distances from the cylinder correspond to the integration range in (2.2) with $\lambda^2>0$. The average energy flux per unit time through the cylindrical surface of radius $r>r_c$, coaxial with the dielectric cylinder, is presented as

$$I=\sum_{n=1}^{\infty}\int d\Omega\frac{dI_n}{d\Omega} \tag{3.1}$$

where $d\Omega = \sin\theta d\theta d\phi$ is the solid angle element and θ, $0 \le \theta \le \pi$ is the angle between the wave vector of the radiated photon and the cylinder axis. For the angular density of the radiation intensity on a given harmonic n one gets

$$\frac{dI_n}{d\Omega} = \frac{q^2 v^2 \omega_n^2 \sqrt{\varepsilon_1}}{2\pi^3 c^3}\left[\left|B_{n,1} - B_{n,-1}\right|^2 + \left|B_{n,1} + B_{n,-1}\right|^2 \cos^2\theta\right] \tag{3.2}$$

In the expression (2.5) for the functions $B_{n,p}$ we should take

$$\lambda = \frac{\omega_n}{c}\sqrt{\varepsilon_1}\sin\theta, \tag{3.3}$$

and

$$\eta = \frac{\omega_n}{c}\sqrt{\varepsilon_1 \cos^2\theta - \varepsilon_0}. \tag{3.4}$$

Formula (3.2) is valid for a general case of dispersion $\varepsilon_0 = \varepsilon_0(\omega_n)$ of the cylinder material with complex permittivity.

The general expression (3.2) is rather complicated and we its asymptotic in limiting regions of the parameters. For nonrelativistic velocities, under the condition $n\beta_1 << 1$, the main contribution comes from the terms with $B_{n,-1}$ and we get

$$\frac{dI_n}{d\Omega} \approx \frac{2q^2 c\left(n\beta_1/2\right)^{2n+2}}{\pi (n!)^2 \varepsilon_1^{3/2} r_q^2}\left|1 + \frac{\left(r_c/r_q\right)^{2n}}{2\alpha_n}\right|^2 \left(1+\cos^2\theta\right)\sin^{2n-2}\theta, \tag{3.5}$$

Where for $n \ge 2$

$$\alpha_n \approx \frac{1}{2}\frac{\varepsilon_1 + \varepsilon_0}{\varepsilon_1 - \varepsilon_0} + \frac{r_c^2}{8n}\left(\frac{\lambda^2}{n+1} + \frac{\eta^2}{n-1}\right), \tag{3.6}$$

and for $n = 1$

$$\alpha_1 \approx \frac{1}{2}\frac{\varepsilon_1 + \varepsilon_0}{\varepsilon_1 - \varepsilon_0} + \frac{r_c^2}{16}\left[-4\eta^2 \ln(\lambda r_c/2) + \lambda^2\right]. \tag{3.7}$$

Compared to the radiation on the main harmonic $n = 1$, the radiation on higher harmonics $n \ge 2$ is suppressed by the factor β_1^{2n-2}. In formula (3.5) the part with the first term in the expression under the absolute sign corresponds to the radiation in a homogeneous medium with permittivity ε_1.

For positive ε_0' we can keep the leading order terms and in (3.5) $\alpha_n \approx \left(\varepsilon_1 + \varepsilon_0\right)/[2(\varepsilon_1 - \varepsilon_0)]$. In this case, in the expression under the sign of modulus in (3.5) the contribution of the term induced by the cylinder is smaller than the one corresponding to the radiation in a homogeneous medium and the radiation intensity behaves as β_1^{2n+2}. A new qualitatively different feature arises for negative values of ε_0' and for small ε_0''. In this case, under the assumption $|\varepsilon_1 + \varepsilon_0'|, \varepsilon_0'' \lesssim \beta_1^2$, we see that $\alpha_n \propto \beta_1^2$ for $n \ge 2$ and $\alpha_1 \propto \beta_1^2 \ln(\beta_1)$. Now, the dominant contribution to the radiation intensity (3.5) comes from the part induced by the cylinder and one has $dI_n/d\Omega \propto \beta_1^{2(n-1)}$ for $n \ge 2$ and $dI_1/d\Omega \propto 1/\ln^2(\beta_1)$.

For small values of the angle θ and for fixed values of the other parameters, assuming that

$$\lambda r_q = n\beta_1 \sin\theta << 1, \tag{3.8}$$

for cylinder functions with the arguments λr_q and λr_c we use the expansions for small arguments. For the function α_n to the leading order we get

$$\alpha_1 \approx \frac{\varepsilon_1}{\varepsilon_1 - \varepsilon_0},\ \alpha_n \approx \frac{1}{2}\frac{\varepsilon_1 + \varepsilon_0}{\varepsilon_1 - \varepsilon_0} + \left[(n-1)\frac{2I_{n-1}(\eta r_c)}{\eta r_c I_n(\eta r_c)} + 1\right]^{-1} \tag{3.9}$$

where $n \geq 2$ and $\eta r_c \approx n(\omega_0 r_c / c)\sqrt{\varepsilon_1 - \varepsilon_0}$. In the limit $\theta \to 0$, one gets $dI_n / d\Omega \propto 1/\ln(\sin\theta)$ for $n = 1$ and $dI_n / d\Omega \propto \sin^{2n-2}\theta$ for $n \geq 2$. For small θ, assuming that $\varepsilon_0'' \lesssim \sin\theta$, in the leading terms (3.9) we can replace ε_0 by ε_0'. In this case, an interesting situation arises for $\varepsilon_1 + \varepsilon_0' < 0$ and $n \geq 2$ when the leading term in (3.9) (with the replacement $\varepsilon_0 \to \varepsilon_0'$) may become zero. For given n and $\omega_0 r_c \sqrt{\varepsilon_1} / c$, that condition can be considered as an equation for the corresponding value of the ratio $\varepsilon_0 / \varepsilon_1$. In this case the next–to–leading term should be kept in the asymptotic expansion of α_n over $\sin\theta$ and ε_0''. Near that specified value of $\varepsilon_0 / \varepsilon_1$ the decay of $dI_n / d\Omega$ in the limit $\theta \to 0$ is slower.

Another new qualitative feature in the radiation intensity, induced by the cylinder, is the possibility for the appearance of strong narrow peaks for large values of the radiation harmonic at specific values of the angle θ. For a transparent cylinder with a positive dielectric permittivity, this feature has been discussed in Refs. [19,22]. Here we consider the frequency range with $\varepsilon_0' < 0$. The contribution of the first term in the right–hand side of (2.5) (corresponding to the radiation in a homogeneous medium) is suppressed by the factor $e^{-n\zeta(\lambda r_q / n)}$, where

$$\zeta(y) = \ln\frac{1 + \sqrt{1 - y^2}}{y} - \sqrt{1 - y^2} \tag{3.10}$$

The contribution of the second term is suppressed by $e^{-n[2\zeta(\lambda r_c / n) - \zeta(\lambda r_q / n)]}$. By taking into account that for $y > 0$ we have $\zeta(\lambda r_q / n) < \zeta(\lambda r_c / n)$, the suppression of the second term is stronger than that for the first one. Let us denote by $\alpha_n^{(0)}$ the function that is obtained from α_n replacing the Hankel functions $H_{n+l}(\lambda r_c)$ by the Neumann functions $Y_{n+l}(\lambda r_c)$. For angles θ not too close to the ones determined by the zeros of $\alpha_n^{(0)}$, the function α_n is of the order of one and the contribution of the third term in (2.5) is of the same order as that for the second term. In this case the first term in (2.5) is dominant and the radiation intensity is close to the one for a homogeneous medium. The situation is essentially different for the radiation angles close to the ones determined by the zeros of $\alpha_n^{(0)}$. For these angles one has $\alpha_n \propto e^{-2n\zeta(\lambda r_c / n)}$ and the contribution of the last term in (2.5) is of the order $e^{n\zeta(\lambda r_q / n)}$. Hence, the angular density of the radiation intensity for the peak at $\theta = \theta_p$ is proportional to $e^{2n\zeta(\beta_1 \sin\theta_p)}$. For the peak in the region $z > 0$ ($0 < \theta_p < \pi / 2$) the height increases with decreasing θ_p. The angular width $\Delta\theta_p$ of the

peak is of the order $\exp[-2n\zeta(\beta_1(r_c/r_q)\beta_1\sin\theta_p)]$. With increasing height of the peak the corresponding width decreases.

In the numerical investigation we evaluate the angular density for the number of the quanta radiated on a given harmonic per period of the particle rotation:

$$\frac{dN_n}{d\Omega}=\frac{T}{\hbar\omega_n}\frac{dI_n}{d\Omega} \tag{3.11}$$

In Fig. 1 we have plotted this quantity (in units of $q^2/\hbar c$) versus θ for a transparent cylinder ($\varepsilon_0''=0$) with dielectric permittivity $\varepsilon_0=-3$ in the vacuum ($\varepsilon_1=1$). The graphs are plotted for $r_c/r_q=0.95$, $n=10$ and the numbers near the curves correspond to the values of v/c. For the cases $v/c=0.9,0.99$ we see the presence of the peaks described above analytically. For the angular locations of the peaks one has $\theta\approx 0.96$ for $v/c=0.9$ and $\theta\approx 0.75$ for $v/c=0.99$. With increasing v/c, the angular location of the peak in the region $0\le\theta\le\pi/2$ is shifted to smaller angles. For the solution of the equation $\alpha_n^{(0)}=0$ in the region $0<\theta<\pi/2$ one has $\theta\approx 0.965$ for $v/c=0.9$ and $\theta\approx 0.75$ for $v/c=0.99$. In agreement with the analysis given above, these roots coincide with the locations of the peaks in the radiation intensity with good accuracy.

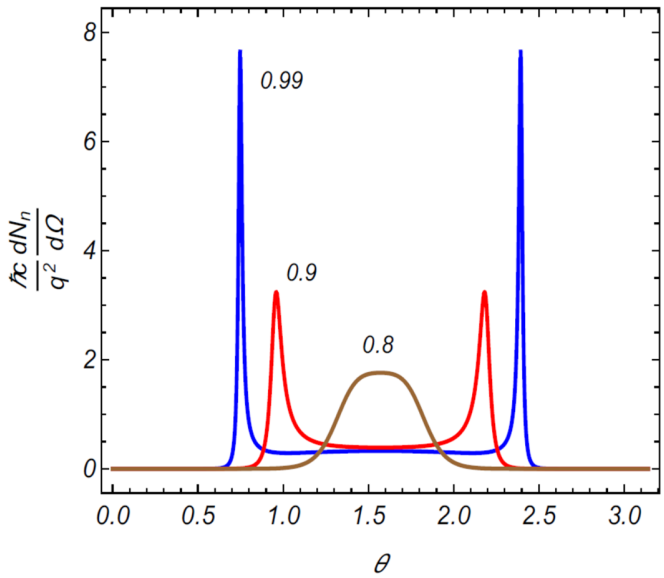

Fig. 1. The angular density of the number of the radiated quanta per rotation period versus the radiation angle θ for a cylinder with permittivity $\varepsilon_0=-3$ in the vacuum. The numbers near the curves correspond to the values of the ratio v/c and the graphs are plotted for $r_c/r_q=0.95$, $n=10$.

To see the effect of the cylinder on the radiation intensity, in Fig. 2 we display the corresponding quantity for the radiation intensity in the absence of cylinder ($\varepsilon_0=\varepsilon_1$) for the same values of the other parameters. As seen, the presence of the cylinder may lead to an essential increase in the angular density of the radiation intensity.

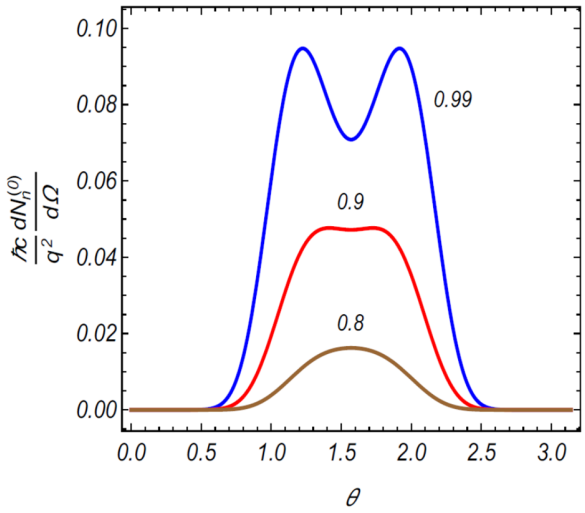

Fig. 2. The same as in Fig. 1 for the radiation of a charge in the vacuum ($\varepsilon_0 = \varepsilon_1 = 1$).

It is also of interest to see the influence of the cylinder on the total radiated energy on a given harmonic, obtained from (3.2) by integration over the angles θ and ϕ. Figure 3 presents the total number of the radiated quanta per period of charge rotation, $N_n = \int d\Omega (dN_n / d\Omega)$ (red circles), versus the number of the harmonic n, for $v/c = 0.8$ and for the same values of the parameters as in Fig. 2. The blue points present the same quantity for the radiation in the vacuum. As seen from Fig. 3, the radiation intensity on a given harmonic, integrated over the angles, can be essentially amplified by the presence of the cylinder. For large harmonics, $n >> 1/\zeta(v/c)$ the radiation intensity tends to the one for the radiation in vacuum. Physically, the latter feature is related to the fact that for those harmonics the Fourier components of the charge field are strongly localized near the particle trajectory and the corresponding polarization of the cylinder is week.

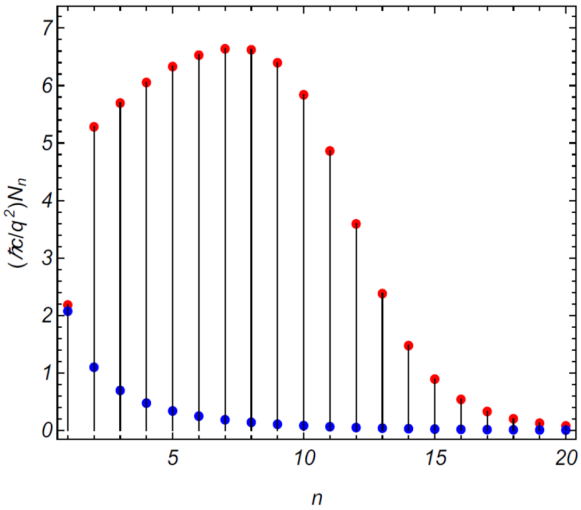

Fig. 3. The total number of the radiated quanta as a function of the harmonic n for $v/c = 0.8$. The values for the remaining parameters are the same as those in Fig. 2.

4. Conclusion

We have investigated the features of the synchrotron radiation from a charged particle rotating around a cylinder in the spectral range where the real part of the dielectric permittivity is negative. At large distances from the cylinder the angular density of the radiation intensity on a given harmonic is given by (3.2). Compared to the case of a cylinder with positive dielectric permittivity, a qualitatively new feature appears in the nonrelativistic limit when the real part of the permittivity is sufficiently close to $-\varepsilon_1$. In this region the angular density of the radiation intensity behaves as $\beta_1^{2(n-1)}$ for radiation harmonics $n \geq 2$ and like $1/\ln^2(\beta_1)$ for $n=1$. For $|\varepsilon_0' + \varepsilon_1| >> \beta_1^2$ the angular density decays as β_1^{2n+2} for $n \geq 1$. Similar differences from the case of a cylinder with positive dielectric permittivity arise in the behavior of the radiation intensity for small values of the angle θ. An interesting feature in the influence of the cylinder on the radiation at large distances from the cylinder is the possibility for the appearance of strong narrow peaks in the angular distribution of the radiation intensity on large harmonics. They are located in the angular region $\sin\theta < 1/\beta_c$, with β_c being the velocity of the charge image on the cylinder surface. With decreasing values of the angle θ in the range $0 < \theta < \pi/2$ the height of the peak increases, whereas the width decreases. Similar behavior takes place with increasing number of the radiation harmonic.

Acknowledgement

A.A.S., L.Sh.G. and H.F.Kh. were supported by Grant No. 18T–1C397 from the Science Committee of the Ministry of Education and Science of the Republic of Armenia.

References.

1. O.V. Dolgov, D.A. Kirzhnits, and E.G. Maksimov, Rev. Mod. Phys. **53**, 81 (1981).
2. P.R. West, S. Ishii, G.V. Naik, N.K. Emani, V.M. Shalaev, and A. Boltasseva, Laser Photonics Rev. **4**, 795 (2010).
3. G.V. Naik and A. Boltasseva, Phys. Status Solidi RRL **4**, 295 (2010).
4. D.M. Mittleman, Nat. Photonics **7**, 666 (2013).
5. V.M. Agranovich and D.L. Mills (Editors), *Surface Polaritons: Electromagnetic Waves at Surfaces and Interfaces* (North–Holland Pub. Co., Amsterdam, 1982).
6. K. Welford, Optical and Quantum Electronics **23**, 1 (1991).
7. S.A. Maier, *Plasmonics: Fundamentals and Applications* (Springer, 2007).
8. S. Enoch and N. Bonod (Editors), *Plasmonics: From Basics to Advanced Topics* (Springer, 2012).
9. H. Raether, *Surface Plasmons on Smooth and Rough Surfaces and on Gratings* (Springer–Verlag, Berlin, 1988).
10. F.J.G. de Abajo, Rev. Mod. Phys. **82**, 209 (2010).
11. M.V. Bashevoy, F. Jonsson, A.V. Krasavin, N.I. Zheludev, Y. Chen, and M.I. Stockman, Nano Lett. **6**, 1113 (2006).
12. S. Liu, P. Zhang, W. Liu, S. Gong, R. Zhong, Y. Zhang, and M. Hu, Phys. Rev. Lett. **109**, 153902 (2012).

13. S. Liu, C. Zhang, M. Hu, X. Chen, P. Zhang, S. Gong, T. Zhao, and R. Zhong, Appl. Phys. Lett. **104**, 201104 (2014).

14. S. Gong, M. Hu, R. Zhong, X. Chen, P. Zhang, T. Zhao and Sh. Liu, Optics Express **22**, 19253 (2014).
15. A.S. Kotanjyan, A. R. Mkrtchyan, A. A. Saharian, and V.Kh. Kotanjyan, Phys. Rev. Accel. Beams. **22**, 040701 (2019).
16. A.S. Kotanjyan, A.R. Mkrtchyan, A.A. Saharian, and V.Kh. Kotanjyan, JINST **13**, C01016 (2018).
17. A.A. Saharian, A.S. Kotanjyan, and V.Kh. Kotanjyan, J. Contemp. Phys. **54**, 111 (2019).
18. L.Sh. Grigoryan, A.S. Kotanjyan, and A.A. Saharian, Izv. Nats. Akad. Nauk Arm., Fiz. **30**, 239 (1995) (Engl. Transl.: J. Contemp. Phys.).
19. A.S. Kotanjyan, H.F. Khachatryan, A.V. Petrosyan, and A.A. Saharian, Izv. Nats. Akad. Nauk Arm., Fiz. **35**, 115 (2000) (Engl. Transl.: J. Contemp. Phys.).
20. L.Sh. Grigoryan, H.F. Khachatryan, and S.R. Arzumanyan, Izv. Nats. Akad. Nauk Arm., Fiz. **33**, 267 (1998) (Engl. Transl.: J. Contemp. Phys.).
21. L.Sh. Grigoryan, H.F. Khachatryan, S.R. Arzumanyan, and M.L. Grigoryan, Nucl. Instr. Methods B **252**, 50 (2006).
22. A.A. Saharian and A.S. Kotanjyan, J. Phys. A **42**, 135402 (2009).

Variety of Physical Vacuum or Worldwide. Interaction Form in a New Strengthening Space

A.M. Sedrakyan*

National Polytechnic University of Armenia
105 Teryan St., Yrevan, Republic of Armenia, 0009

AbstractIn the work a new type of space is offered which may be exists in the atomic systems and cosmic space. The new environment (vacuum) where strong interaction of the charged particles occurs than in the ordinary vacuum is called TeppArt environment. For such an environment where strong interactions between accurate charges occur, we have written the law of Coulomb in this way: $\vec{F}_{TerrArt}(r) = k\frac{q_1 q_2}{\varepsilon r^2}\exp(m/r)\frac{\vec{r}}{r}$.

1. Introduction.

As you know, the force acting on a charged point particle or material point (the concept of a point charge or material point is a physical abstraction in science) is called central if it depends only on the distance to the field source and is directed along the straight line connecting the material point to the field source. In a general form, the central force can be written in the form, $\vec{F} = F_r(r)\frac{\vec{r}}{r}$, where $F_r(r)$ is the projection of the force onto a straight line connecting the material point to the field source.

One of the most common types of central forces is a force whose projection is inversely proportional to the square of the distance from the field source to the material point $F_r(r) = \frac{\alpha}{r^2}$, where α is a constant, and depends on the nature of the interaction. An example of a central force of this kind is the Coulomb force [1, 2] or the gravitational interaction of two bodies by masses and when one of them acts as a field source for the other. In a physical vacuum (world ether), the Coulomb law is expressed in the form $\vec{F}_r(r) = k\frac{q_1 q_2}{r^2}\frac{\vec{r}}{r}$, and in a liquid and gaseous medium with a dielectric constant, which characterizes the electrical properties of the medium – (since the interaction depends on the physical properties of the medium). It shows how many times the interaction force of two point stationary charges in a vacuum is greater than their interaction forces in a medium $\beta = F_{вак}/F_{среда}$. Based on the concept of world ether or physical vacuum, below we will consider such media in which the interaction force between two charged particles increases compared to the interaction between the same particles at the same conditions in a vacuum about which we have a view, as well as we feel and can conduct experiments.

The concept of "ether" arose even in the days of the ancient Greeks: according to their mythology, this is the highest, cleanest and most transparent layer of air, the place where the gods stay. Aristotle (a student of Plato), in addition to the four elements – Fire, Water, Air, Earth,

*E – mail: *asedrakyan.phys@gmail.com*

introduced the fifth (the essence of all things) –a ether. Thus, the concept of "world ether" has entered into physics – a universal medium that fills all space, including the gaps between atoms and molecules in bodies. That is, we assume that the new ether, or physical vacuum, has such a physical property that enhances electromagnetic interaction between two charged particles without taking into account the polarization of the medium. Similarly, amplifying active media exist in optoelectronics and are used to enhance weak rotations forthe polarization plane angle of electromagnetic waves. In [3, 4], the mechanisms for amplifying the rotation of the plane of polarization of electromagnetic waves using various amplifying material media were theoretically investigated and compared.

2. Setting goals.

According to the general theory of relativity, space is unthinkable without ether. Suppose that a physical vacuum is an active medium with newphysicochemical properties, where an amplification of the interaction of charged particles takes place, and differs from the active media of electromagnetic waves. Such among the ambiguous, and physical interaction occurs in different ways. Therefore, in the model under consideration, we will conditionally call TerrArt a medium (a new medium in the space of world ether) in this model of active medium. In this work, we considered such media where the interaction gain is greater than in ordinary vacuum, and we do not consider the question of the polarization of the vacuum $(\beta = F_{TerrArt}/F_{вакуум} > 0)$ at strong interaction, as in [5]. By changing the input parameters in the law of Coulomb, have been obtained different types of physical vacuum.

3. The force of interaction of charged particles in a TerArt medium.

Let us consider the interaction of two charged particles in active amplifying media. The Coulomb law for strong interactions in a vacuum in this problem, we present the equation in the form

$$\vec{F}_{TerrArt}(r) = k\frac{q_1 q_2}{\varepsilon r^2}\exp(m/r)\frac{\vec{r}}{r} \tag{1}$$

where the exponent in the equation (1) is a dimensionless quantity having a dimension of length. The gain coefficient (the ratio of the force of interaction of two media) is equal to

The potential energy is equal to the force of interaction.

$$U(r) = -\int \vec{F}(r)d\vec{r} = -k\frac{q_1 q_2}{\varepsilon}\int\frac{\exp(m/r)}{r^2}d\vec{r} + const\,,\varepsilon = 1 \tag{2}$$

$$U(r) = k\frac{q_1 q_2}{m}\exp(m/r) + const \tag{3}$$

Since the electric field acts on the charged particles in it (see equation(1)), it does work when the charge moves in the electric field.

$$A(r_1 r_2) = k\frac{q_1 q_2}{m}\left[\exp(m/r_1) - \exp(m/r_2)\right] \tag{4}$$

Since the motion of the charge in the new space does not depend on the type of trajectory along which the charge moves, only the position of the starting and ending points of the path is determined.

As can be seen from the laws of the presented equations and general reasoning, the physical vacuum or type of world ether [6] where physical phenomena (material–energy processes) occur is ambiguous, the interaction force and other physical parameters strongly depend on the value of m in the exponent. The number m indicates the intensity of the interaction of the force (1), or potential energy (see (2)).We assume that the medium about what we discussed may exist in interatomic as well as in outer space. They also have the properties of matter and are continuable and transparent for the light. From this point of view, the physical vacuum in quantum physics is understood as the lowest energy state of a quantized field, which has zero momenta and angular momentum and other quantum numbers, etc. In mathematical modeling of the quantum–mechanical phenomenon in the description of the Hamiltonian equation, which in the simplest cases represents the energy $(H = T + U)$ of a physical system, the term of the potential energy included in it is expressed by the expression (3).

4. Conclusions.

In the considered media, well–known and generally understood parameters are introduced. When analyzing the results of this paper, it is clear for the concept of the ambiguity of the void or vacuum (in the space where it exists), similar to a multi–channel radio station. For example, we can say that in atomic systems there can be several different types of vacuums, based on equation (1). For different values of the number, different spaces are obtained in one system with different properties. This says that in the void, the boundary between two physical vacuums with different properties can be represented, and the void in this case is a superconducting layer between two media and the motion of two layers of vacuums (or ethers with different parameters) and can be independent in some stationary cases. Within the framework of this model, it is possible to explain some physical phenomena that entered into physics as a postulate (the Hartmann paradox) [6,7]. – the speed of light does not depend on the speed of the source in full accordance with Einstein's second postulate, there are existing problems of field space and ether in physics.

I thank to my co–author of the book, Professor Artie D Alexander, for valuable advice and support in carrying out this work.

References.

1. Sivukhin D.V. General course of physics.–M.: MIPT, 2004.–T.3, Electricity. – P. 17. 656 c. – ISBN 5–9221–0227–3
1. Gursky I.P. Elementary Physics.– M., 1976 .–. 223 p.
2. Patent No. AM20060077. The method of amplification of rotation of the plane of polarization electromagnetic waves and devices / A.A. Gevorgyan, A.M. Sedrakyan, A.Zh. Khachatryan. 05/06/2006
3. Sedrakyan A.M. Measurement of small rotations of the angle of rotation of the plane of polarization of an electromagnetic wave with an arbitrary orientation of the polarization of the optical elements of the polarimeter // Of state Enginering University of Armenia: Collection of scientific and methodical papers – 2011.– T.3, N1.–P. 56–61.

4. Whittaker E. History of the theory of ether and electricity. – M .: Regular and chaotic dynamics, 2001. – 512p.
5. Davidovich M.B. On the Hartman paradox, tunneling of electromagnetic waves and superluminal speeds // The success of the physical sciences. – M., 2009 (April). – Vol. 179.– P. 443.
6. Albert Einstein " Collection of scientific works " works on the theory of relativity, Moscow 1966. Volume 2.